

Overheating in the Attic Space Classroom in Summer

Dušan Katunský^{1*}, Marián Vertal¹, Silvia Zozuláková², Erika Dolníková¹, Kristián Hutkai¹

Technical University of Kosice, Slovakia
Faculty of Civil Engineering, ¹Institute of Architectural Engineering, ²CRIC – Center for Research and Innovation in Construction
*e-mail: dusan.katunsky@tuke.sk

Abstract

The presented study deals with the space located in the attic of an older building after reconstruction. Originally, the attic space was not used, as it did not have sufficient headroom. The reconstruction was designed in such a way that the entire original pitched roof was gradually raised by 1.2 meters in parts, creating a full-fledged space under the pitched roof. The visual connection of the interior space with the exterior was ensured by continuous strips of vertical windows around the perimeter of the building, each window measuring 600x600 mm. The space is also illuminated by several skylights at roof level, which, although they ensure sufficient penetration of daylight from above into the interior, at the same time allow for considerably unpleasant overheating. The task was to find a way to optimize the size of transparent surfaces and determine the accumulation of building structures in order to achieve an acceptable cumulative effect of daylight and overheating, i.e., permissible increase in indoor air temperature in summer. It means trying to theoretically design a suitable and comfortable interior space in the attic in an already existing building.

Keywords: roof windows, attic, simulation, overheating

1 Introduction

Old attic spaces, or lofts, are currently becoming an attractive object for creating a new living space. In this way, the attics of old buildings are used, or also new attic spaces can be created by extending the original building. This approach is mainly applied in historic city centers, where old attic spaces can be transformed into an attractive and valuable space. There is no need to occupy new land. It will be created above the existing floor of the original building. The content of the article follows on from [1], where the authors tried to find out and describe the influence of the size of roof windows, on the indoor climate of the attic. Assuming an adequate design of the heating system and the thermal insulation properties of the used dividing structures, an acceptable climate and well-being can be achieved in the attic during the winter. However, the situation in the summer season can be different, which also contributes to the cardinal direction of the space. The works published so far have taken the following approach. Gupta et al. [2] investigated the attic space from the point of view of parametric factors, of

thermal technology, and ultimately the theory that heat transfer inside the building is the most complicated for the attic space was confirmed. It is necessary to design an attic resistant to moisture [3] and well ventilated [4]. Ventilation is important both for the removal of moisture in the winter during heating and in case of excessive overheating and the effect of solar energy in the summer [5]. Recently, many articles [6, 7, 8, 9] have been published about overheating of attic spaces in the summer. So far, the authors have dealt with the problem of overheating from the point of view of the influence of various structural components that surround the interior space of the attic (roof shell, outer shell, skylights, partitions, ceiling). The increase in indoor air temperature in the summer season is influenced not only by structures, but also by several factors. These are mainly heat gains from solar radiation, air exchange, etc. There are several calculation methods for calculating overheating, while it is generally known that thermal comfort in the summer depends mainly on the heat accumulation of the building envelope and internal dividing structures. The effect of windows on increasing the internal air temperature is known. As the dimensions of the windows increase, illumination of the space increases, as well as the temperature of the internal air. Optimizing areas prone to overheating, such as attics, leads to finding the appropriate ratio of the total window area and the physical properties of other structures adjacent to the space to achieve visual comfort. At the same time, it is necessary to prevent glare and ensure little or no overheating. The concept of mitigating overheating can include elements of active shading of transparent structures, or the use of progressive types of glazing. Finally, cross ventilation of the attic space can be used to reduce the temperature in the summer.

2 Case Study

2.1 Chosen Building and Space

The subject of the contribution is the attic space, which is after renovation. The older brick three-story building with a traditional truss structure is located in the Košice in Slovakia. As part of the reconstruction of the building, the roof was raised by 1.2 meters in order to make full use of the spaces above the entire floor plan of the fourth floor. Rafters are placed only 0.5 meters above the ceiling level and tie beams did not allow creating a suitable space in the attic. The new premises created by the refurbishment and a view of the building are shown in Figure 1.



a)



b)

Figure 1: Subject of the assessment: a) building after refurbishment; b) assessed room

2.2 Evaluation of Measurements in Assessed Room

Measurement in classroom of dimensions 8.205 x 10.770 meters was realized in summer of 2020. Height of space is differing from 2.2 meters (in envelope wall) to 5.35 m (in the top of slope roof). The composition of individual constructions is shown in Table 1. Parameters of the indoor microclimate were measured: air temperature ($^{\circ}\text{C}$), relative air humidity (%), air flow rate (m/s), surface temperatures ($^{\circ}\text{C}$) and illuminances (lx), which can be seen in Figure 2.

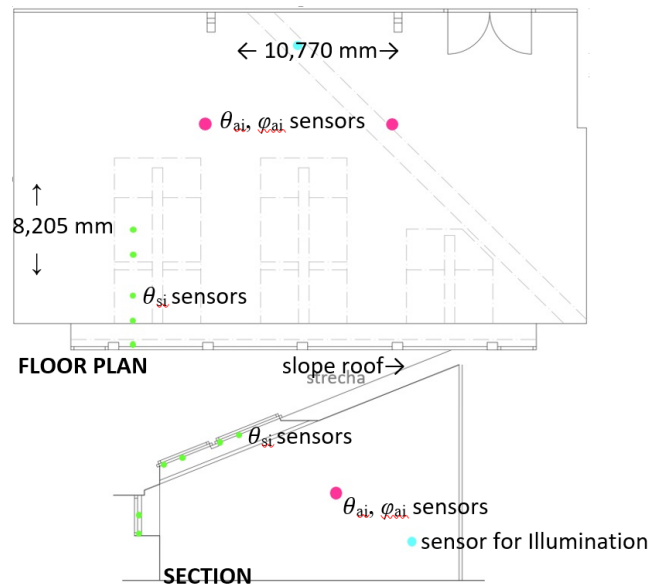


Figure 2: Assessed classroom space: a) sensors position on floor plan; b) sensors position in section

During very warm days in July the maximum indoor temperatures were recorded. The measurement was carried out from May to October. Analyzed period were set to 10 warm days that occurred from 15th to 25th of July 2020. The goal of this work is to monitor and assess thermal comfort during the selected period. Selected period was chosen because the weather was consistently very clear and warm, which causes thermal discomfort in terms of overheating in chosen attic space. It can be seen in Figure 3.

Considered time 1.5.-10.10.2020
 Time for simulation (hottest days) (15.7.-25.7.2020)
 Measurement time (28.8.-10.09.2020)

May 01.-08.	May 09.-15.	May 16.-29.	May 30.-6.6.	June 7.-26.	June 27.-10.7.	July 11.-24.	July 25.-7.8.	Aug 8.-21.	Aug 22.-4.9.	Sept 5.-18.	Sept 19-2.10.	Oct 3.-10.
simulation						July15.-25.						
measurement									August 28. - Sept. 10.			

Figure 3: Considered time periods

The resulting values of temperature and relative humidity are calculated as the average of two measured values. The second measuring set measured surface temperatures on transparent structures. The temperature was measured in one section on the surface of the frame and the surface of the glass in the plane of the facade and the roof. The entire measurement took place

from mid-April to mid-October therefore for the analyzed period was chosen a shorter period for simulation model evaluation. Two measuring sets were used to measure the mentioned parameters of the indoor environment. The first measuring set monitored air temperatures, relative air humidity and air flow speed. Two sensors were used, each placed at a height of 2 m above the floor in the room.

Table 1: Composition of the envelope structures of the assessed room

1	2	3	4
Parapet masonry	Roof structure	Ceiling structure	Partition wall
Cement lime Plaster Solid Brick Masonry	Roofing Air Layer 100 mm Low ventilated	Cement lime Plaster Steel-Concrete slab	Gypsum Board Air Layer 120 mm
Mineral Insulation Board Air Layer 50 mm	Mineral Insulation Board Alternative heavy insulation	Mineral Insulation Board Air Layer 70 mm	Mineral Insulation Board Gypsum Board
Gypsum Board	Vapour barrier Air Layer 50 mm Gypsum Board	Oriented Strand Board Oriented Strand Board	$U_4= 0.444 \text{ W}/(\text{m}^2\text{K})$ Partition wall – alternative 2 Steel-Concrete partition wall
$U_1= 0.285 \text{ W}/(\text{m}^2\text{K})$	$U_2= 0.211 \text{ W}/(\text{m}^2\text{K})$	$U_3= 0.472 \text{ W}/(\text{m}^2\text{K})$	$U_4= 2.662 \text{ W}/(\text{m}^2\text{K})$

Since the goal was to correctly describe mainly the external (and exterior) thermal load, while during the measurement occupants were not present in the room. Other factors affecting the overall thermal comfort in the room will be implemented in the simulations. Meteoblue climate diagrams based on 30 years of hourly weather model simulations were used as outdoor climate conditions in Košice (<https://www.meteoblue.com/sk>). Results can be seen in Figure 4.

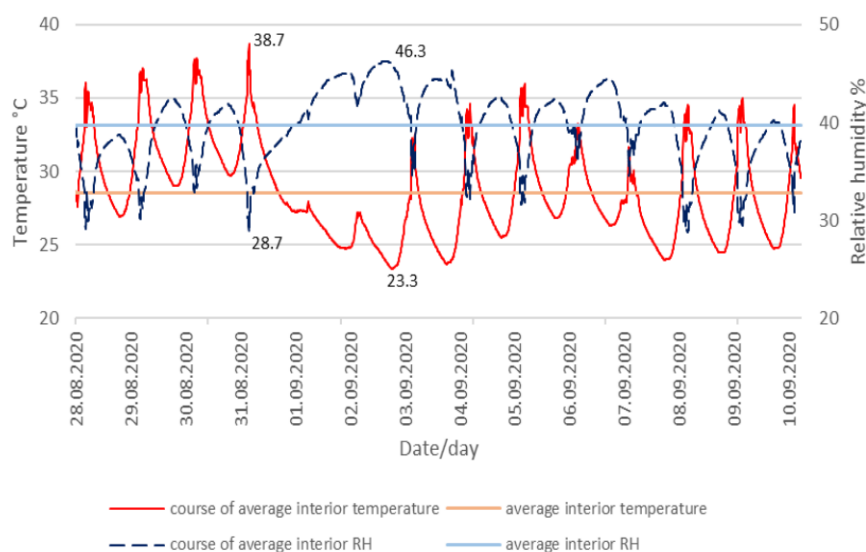


Figure 4: Results of indoor environmental conditions for period from 28th of August to 10th of September 2020

The resulting conditions of the indoor environment for period 28th of August to 9th of September 2020 which were used for numerical model verification can be seen in Figure 4. Concluded measured values were - minimum θ_{ai} = 23.33°C, average θ_{ai} = 28.6°C, maximum θ_{ai} = 38.68°C, average ϕ_i = 39.7 %.

2.3 Assessment of Overheating

The simulation calculation was carried out in the WUFI Plus tool. The model of the analyzed part of the building is in Figure 5.

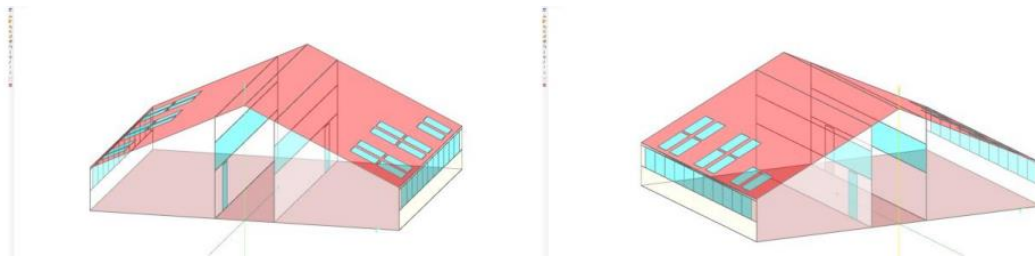


Figure 5: Simulation model geometry

For the assessment of overheating was selected a room in north-west orientation. Floor area of the room is 63.3 m², inner volume of the room 125.0 m³. As the boundary conditions for simulation were used IWEC climatic parameters for location of Košice (48.72°; 21.258056°). The simulated time for all calculation cases (Table 2) is from 1st of May to 10th of October 2020 with a time step of 1 hour (3889 hours). The shading model is set as 0%, 20%, 40%, 60%, 80% and 90% exclusively for roof windows. Description of roof and partitions is in Table 3.

Table 2: Description of individual calculation cases for simulation

case	roof insulation	partitions	skylights shaded	vertical windows	night ventilation	maximal temperature
1	light	light	no	no	no	45.9 °C
2	light	heavy	no	no	no	41.2 °C
3	heavy	light	no	no	no	42.8 °C
4	heavy	heavy	no	no	no	39.3 °C
5	light	light	yes	no	no	37.5 °C
6	heavy	heavy	yes	no	no	34.4 °C
7	light	light	yes	yes	no	34.9 °C
8	heavy	heavy	yes	yes	no	33.0 °C

Table 3: Description of light and heavy roof and partitions

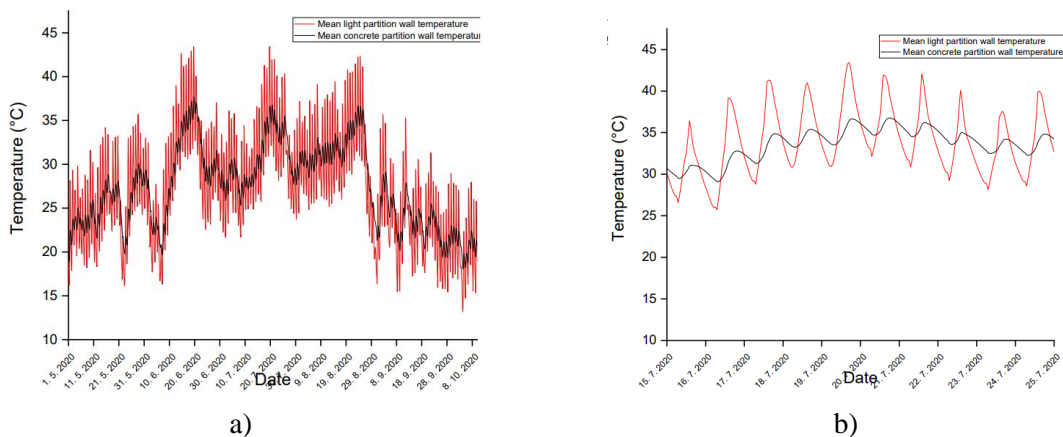
roof	partitions	description
light	light	published [1] (no position and number of windows adjusting);
light	heavy	area of partition of 32.5 m ² , change from the light sandwich to a reinforced concrete wall with same thickness of 0.185m;
heavy	light	heavy thermal insulation of the roof, same thickness, change of density from 115 kg/m ³ to 440 kg/m ³ ;
heavy	heavy	heavy partition, change from the light sandwich to a reinforced concrete wall of the same thickness; heavy thermal insulation of the

roof, identical thickness, change of density from 115 kg/m³ to 440 kg/m³.

3 Results and Discussion

The period of 10 critically warm days with high solar radiation from 15th to 25th of July 2020 was evaluated. The average temperatures of the partitions (Case 1 - light sandwich - and Case 2 - heavy reinforced concrete) were calculated. Based on the results, it is possible to point out the fact that in the evening, the heavier reinforced concrete wall contributes to the interior space air temperature. The course of average temperatures of the light partition (sandwich) and heavy partition (reinforced concrete) obtained by calculation is shown in Figure 5a,b, in a room with a western orientation for selected periods. It is possible to observe the shift of the temperature amplitudes for the cases of light and heavy partition structure, as well as the "sensitivity" of the light wall structure to changes in temperature, which changes rapidly (has a short phase shift) compared to the reinforced concrete wall. While the average temperature of the partition made of both materials is almost the same, the maximum temperature of the light dividing structure during the calculation rose to approximately 44°C, and in the case of the reinforced concrete partition the temperature rose to approximately 38°C (Figure 5c,d). The difference in their maximum temperatures is 6K. The accumulative capacity of concrete in this way can contribute to the resulting temperature in a given space after sunset and at night.

Calculated results of indoor air temperatures for simulation scenarios Case 1-8 in a west-facing classroom for the selected period of simulated time 15th to 25th of July 2020 presents Figure 6. The hot 10-day period with high solar radiation was selected for the assessment of overheating. During the analyzed period of 241 hours, the calculated average value of the indoor air temperature was 33.2°C (minimum of 23.9°C and a maximum of 45.9°C). After replacing the light dividing structure with a heavy one maximum calculated air temperatures dropped below 42°C (41.2°C).



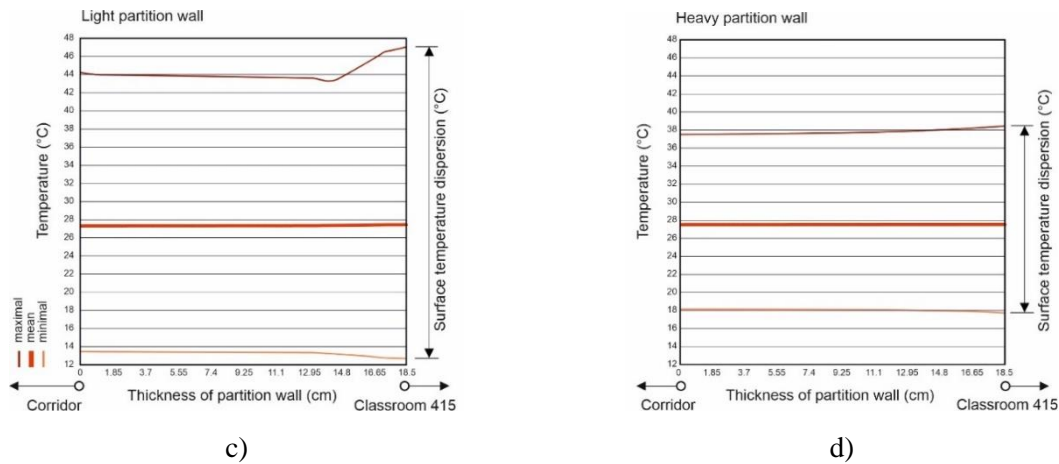


Figure 6: Results of temperatures for heavy and light partitions – **a)** the entire evaluation time from 1st of May to 10th of October; **b)** warm period from 15th to 25th of July; **c)** results of temperature dispersion in light partition; **d)** results of temperature dispersion in heavy (reinforced concrete) partition

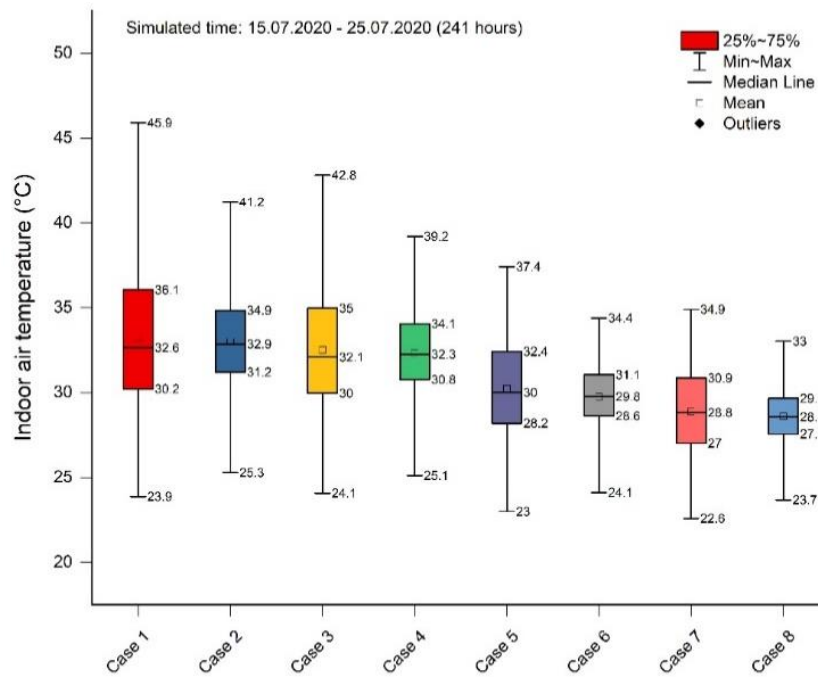


Figure 7: Results for Cases 1-8 for 10-day high solar radiation period 15th to 25th of July for Cases 1 and 2 (heavy and light partitions)

4 Conclusion

Several authors deal with the problem of overheating of spaces in the attic which makes the problem current. Considering the possibility of using old uninhabited attic spaces in buildings favorably located, it is needed to create a comfortable conditions in such space. Due to the insufficient heat accumulation capacity of the structural elements of the attic structures, there is

a risk of excessive overheating in the summer. In winter, this problem is less pronounced. The space chosen for research was originally an unused attic, which was increased by approx. 1.2 meters in restoration. This space is illuminated by one vertical row (connected) of windows and two rows of roof windows in the roof plane. The city of Košice is located in the central Europe, where the climate is continental - winters are cold and summers are warm. For a closer assessment, the 10 hottest days of the analyzed period were chosen. Measurements and calculations were compared and several variants of roof and vertical window shading were simulated afterwards. The following conclusions follow from the obtained results. In order to mitigate overheating, the roof shell and internal dividing structures were theoretically replaced with structural elements with greater heat accumulation, but this did not lead to a satisfactory degree of overheating. Even with the use of the heaviest constructions (which the building can structurally withstand) and the greatest shading of the windows, the internal temperature will decrease, but it will still not reach the required level below 27°C, which indicates an unsatisfactory condition. Although our standard says that in indoor areas with permanent human residence, the indoor temperature in summer should not exceed 27°C, it is allowed to exceed the limit by two degrees for several hours a day, which means that we could tolerate a temperature of 29°C for one or two hours a day. This condition is fulfilled only in some cases. Since the satisfactory solution were not found it is necessary to state that further attention should be paid to this issue. Based on the results of the authors dealing with the problem of overheating of buildings, it is clear that the required parameters can be achieved by combining suitable building structures with the necessary heat accumulation, window shading, the use of external reflective surfaces and the connection with environmental technology, i.e. ventilation and artificial ventilation and air conditioning.

Acknowledgments

This paper was elaborated with the financial support of the research project VEGA 1/0626/22 of the Scientific Grant agency, the Ministry of Education, Science, Research, and Sport of the Slovak Republic and the Slovak Academy of Sciences.

References

- [1] Dolnikova, E., Katunsky, D., Vertal, M., & Zozulak, M. (2020). Influence of Roof Windows Area Changes on the Classroom Indoor Climate in the Attic Space: A Case Study. *Sustainability*, 12(12), 5046.
- [2] Gupta, A., & Thakur, H. (2019, November). The Study of Parametric Factor in Attic Space for Winter Season. In IOP Conference Series: Materials Science and Engineering (Vol. 691, No. 1, p. 012091). IOP Publishing.
- [3] Richter, J., Staněk, K., Tywoniak, J., & Kopecký, P. (2020). Moisture-safe cold attics in humid climates of Europe and North America. *Energies*, 13(15), 3856.
- [4] Forest, T. W., & Walker, I. S. (1993). Attic ventilation and moisture. Canada Mortgage and Housing Corporation.
- [5] Chwieduk, D. A. (2018, August). Solar energy impact on space heating and cooling needs in moderate climate. In IOP Conference Series: Materials Science and Engineering (Vol. 415, No. 1, p. 012008). IOP Publishing.

- [6] Parker, D. S., & Sherwin, J. R. (1998). Comparative summer attic thermal performance of six roof constructions. *Transactions - American society of heating refrigerating and air conditioning engineers*, 104, 1084-1092.
- [7] Fantucci, S., & Serra, V. (2019). Investigating the performance of reflective insulation and low emissivity paints for the energy retrofit of roof attics. *Energy and Buildings*, 182, 300-310.
- [8] Lee, S. W., & Lim, C. H. (2016). Reflective thermal insulation systems in building: A review on radiant barrier and reflective insulation. *Renewable and Sustainable Energy Reviews*, 65, 643-661.
- [9] Piotrowski, J. Z., Stroy, A., & Olenets, M. (2015). Mathematical model of the thermal-air regime of a ventilated attic. *Journal of Civil Engineering and Management*, 21(6), 710-719.

Physical-mechanical Evaluation of Polyethylene Terephthalate Fiber Dune Sand Mortar Exposed to Elevated Temperature

A. Ghrieb^{1,2}, Y. Abadou^{2*}, T. Choungara^{1,2}, R. Bustamante³

¹Mechanical and Materials Development Laboratory, University Ziane Achour, Djelfa, Algeria

²Department of Civil Engineering, University Ziane Achour, Djelfa, Algeria

³ Technical School of Architecture of Universidad Politécnica de Madrid (ETSA-UPM), Spain

*e-mail: abadouyacine@gmail.com

Abstract

The mechanical properties of mortar containing Polyethylene Terephthalate (PET) as Strapping Band Fibers (SBF) replacing natural sand have been studied by many researchers. These studies indicate that when SBF is used as a substitute for sand in mortar, the characteristics in both the fresh and hardened states are altered. This experiment's purpose is to valorize local materials, which are abundant in the region of Djelfa (Algeria), in cement mortar manufacturing and to discuss the influence of these materials on the mechanical and physical characteristics of the resulting mortar at the room, and at the high temperature. This study presents the results of an experimental investigation into the effects of high temperatures on the properties of dune sand mortar made with strapping band fibers. The method for formulating the mortar mixes was based on the progressive replacement of dune sand by PET fibers, with weight contents of 0%, 0.5%, 1%, 1.5%, 2%, and 2.5%. Several tests have been carried out to study the evolution of the different characteristics of mortar mixtures. The workability, bulk density, compressive and tensile strengths, and all samples were subjected to temperatures of ambient, 100 °C, 200 °C, and 400 °C. The results demonstrate that the inclusion of the recycled fibers and the preservation mode had remarkable effects on the characteristics of the mortar obtained.

Keywords: dune sand, mortar, elevated temperature, mechanical strength

1 Introduction

The process of valorizing local and waste materials in mortar production is among the most effective ways to solve the issue of a lack of sources of building materials and pollution in urban and rural areas. The use of Polyethylene Terephthalate band fibers as incorporation into dune sand mortar not only contributes to the exploitation of worn strapping bands, but it can also have a positive role in improving the performance of mortar.

Many investigations have been conducted on this topic. The results of the experiments showed that the incorporation of PET as a fiber, bond, or aggregate could have a significant influence

on cementitious materials' properties, mechanical strength, deformability, and durability [1-9]. According to Hacini et al. [1], the use of PET aggregates as a replacement for natural sand allows reducing the density of reinforced mortars. Umasabor et al. [2] investigated the effects of using PET as an additive on the mechanical strength of concrete and reported that there was a progressive decrease in the flexural strength of the concrete as the PET content increased in the concrete. Martinez-Barrera et al. [3], Meza de Luna et al. [4], and Kutum et al. [5] concluded that the size and concentration of PET flakes had a significant impact on the compressive strength of concrete. The results obtained by Singh et al. [6] showed that the addition of PET waste to concrete as a fine aggregate replacement increased the mechanical strength of the concrete. On the other hand, Lin et al. [7] and Uddin et al. [8] reported that the use of PET fiber reinforcement enhances the interfacial properties between fiber and matrix. Alaloul et al. [9] studied the effects of PET and polyurethane (PU) on the mechanical and thermal properties of interlocking bricks, and they reported that adding PET and PU improved the impact strength.

The use of PET as mechanical reinforcement in concrete and as an enhancement in elasticity for concrete structures would not only assist in addressing the issue of environmental impact, but it could also have a positive and significant effect on the ductility behavior of beam structures and improve the electrochemical properties of reinforcing steel in concrete. [10-12]. The use of PET-FRP (Fiber Reinforced Polymer) in the production of reinforced concrete (RC) structures is a relatively recent technique. The use of PET fiber concrete with FRP reinforcement systems and techniques to retrofit RC structures has significantly increased the ultimate load, giving PET-FRP a great advantage over conventional materials. [13,14].

Mohammad et al. [15] studied the impact of the partial replacement of natural aggregates by recycled fine PET aggregates. Various incorporations of PET fine aggregates ranging from 10 to 50% were used in concrete. The optimum percentage of admixture was found to be 10% of PET, which improved the qualities of fresh and hardened concrete.

Ayush et al. [16] replaced recycled Polyethylene Terephthalate fiber in the concrete with fine aggregate and investigated workability, and mechanical properties. Their study concluded that plastics can be used in concrete up to 3% as a partial substitution for fine aggregate, as they reduce workability, increase compressive strength, and also decrease concrete density.

Haikuan et al. recently investigated the erosion resistance of normal concrete (NC) and recycled plastic concrete (RPC) in a solution of sodium sulfate at concentrations of 3%, 5%, and 7% [17]. According to the results, as the erosion concentration and time increase, the mass increase rate of RPC and NC also increases. Under 3% and 5% concentration erosion, the compressive strength increases and then decreases as the rate of mass changes and the speed of the ultrasonic waves' velocity changes.

On the other hand, PET-modified concrete is appropriate for structural uses due to its acceptable fresh, mechanical, microstructural, and thermal properties [18,19]. This study examines the compressive strength and flexural strength of dune sand (DS) mortar that contains varying amounts of PET strapping band fibers that have been exposed to elevated temperatures. The performance of the reinforced dune sand mortar was compared to that of an alluvial sand (AS) mixture and a DS-based mortar without fiber (the control mix).

The main objective of the experimental work presented in this paper is to examine the possibility of applying mortar containing dune sand and PET scrap waste fiber for building construction. This experimental study also looked at the effects of using PET Strapping Band Fibers (SBF) at progressive levels (0%, 0.5%, 1.0%, 1.5%, 2.0%, and 2.5% by weight) on the physical and mechanical characteristics of the obtained mortar at ambient and elevated temperatures.

2 Experimental Program

2.1 Materials

The type of cement used in the present study was Composite Portland Cement (CEM II/A 42.5) brought from the BISKRIA CEMENT factory, Biskra (Algeria). The cement used has a bulk and a specific gravity of 1.96 g/cm^3 , and 3.11 g/cm^3 , respectively, and Blaine fineness of $3225 \text{ cm}^2/\text{g}$.

In the present research, two different sorts of sand have been employed; dune sand, denoted by (DS), and alluvial sand denoted by (AS). These sands are from the Djelfa region (Algeria). The physical specifications of each sand are given in Table 1. DS and AS sands have grain sizes of $0/0.315 \text{ mm}$ and $0/4 \text{ mm}$, respectively (Figure 1). The X-ray diffraction (XRD) analysis shows the presence of SiO_2 (Quartz) as the main component, which indicates the siliceous nature of the sands used (Figure 2).

Table 1: Physical properties of the sands used

Property	AS	DS
Apparent density (g/cm^3)	1.61	1.46
Specific gravity (g/cm^3)	2.60	2.53
Total porosity (%)	38	43
Compactness (%)	62	57
Water absorption capacity (%)	0.87	2.35
Visual sand equivalent (%)	81	79
Sand equivalent with the piston (%)	80	75
Fineness modulus	2.36	0.86

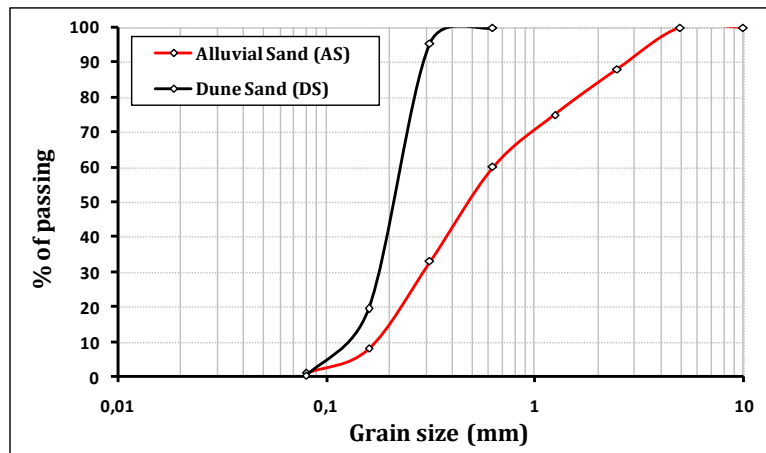


Figure 1: Particle size distribution of the sands studied

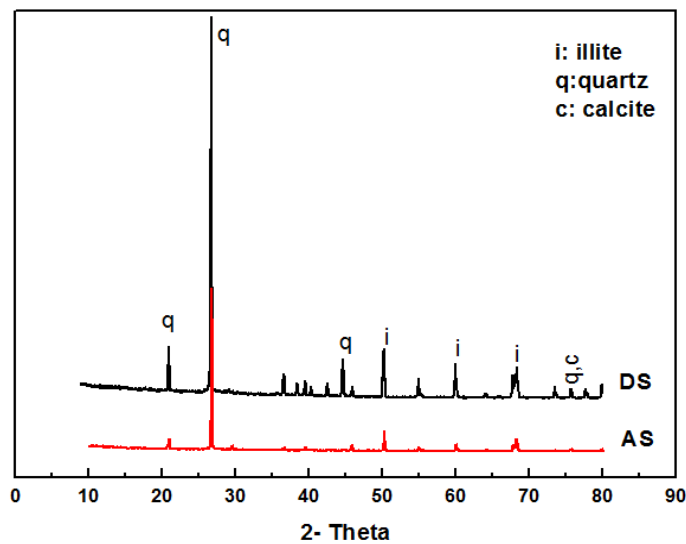


Figure 2: X-ray diffraction patterns of sands used

Polyethylene terephthalate (PET) waste used in this study has a tensile strength of up to 36 MPa, a melting point of 255-265°C, and a range of glass transition temperatures between 70°C and 80°C. The used Polyethylene Terephthalate fibers, designated by (F), were obtained manually by cutting packaging straps. Their dimensions are between 15 and 20 mm in length, 1.0 and 1.5 mm in width, and 0.55 mm in thickness. The fibers used have a density of 1.29. Figure 3 shows a sample of the PET fibers used.



Figure 3: PET strap waste fibers used

2.2 Mix Proportions and Sample Preparation

The experimental procedures applied in this work to determine the mechanical resistance employed prism samples measuring $4 \times 4 \times 16 \text{ cm}^3$. Dune sand mortar mixtures with various amounts of PET-SBF fibers were prepared and performed according to the NF EN 196-1 standard (Table 2). In order to assess the impact of fiber inclusion on the different physical and strength characteristics of the mortar, the dune sand was substituted by 0%, 0.5%, 1.0%, 1.5%, 2.0%, and 2.5% PET fibers.

Table 2: Mix composition of designed mortars

Mixture	Composition	Cement (g)	DS (g)	AS (g)	F (g)	W/C
M _{AS}	100% AS	450	-	1350	0	0.7
M _{DS}	100% DS	450	1350	-	0	0.7
M ₁	84.5% DS + 0.5% F	450	1343.3	-	6.7	0.7
M ₂	84% DS + 1% F	450	1336.5	-	13.5	0.7
M ₃	83.5% DS + 1.5% F	450	1329.8	-	20.2	0.7
M ₄	83% DS + 2% F	450	1323	-	27	0.7
M ₅	82.5% DS + 2.5% F	450	1316.3	-	33.7	0.7

After mixing is complete, the fresh mixtures were molded, and they were then subjected to 20 to 30 seconds of vibration on a vibrating table. During the first 24 h, the samples were stored in ambient laboratory conditions of temperature ($23 \pm 2^\circ\text{C}$) and relative humidity ($50\% \pm 10\%$). They were then demolded and kept submerged in drinking water until the test day.

2.3 Testing Procedures and Heat Treatment Process

For fresh mortar, the workability was determined using an LCPC mortar maniabilimeter, (NF P18-452 standard). The experiment consists of determining the consistency of a fresh mortar subjected to specified vibrations. For hardened mortar samples, the mechanical characteristics were evaluated at 28 days before and after the heat treatment process, using mortar prism samples of $4 \times 4 \times 16 \text{ cm}^3$ in dimension (NF EN 196-1 standard). The three-point bending test was used to assess the flexural strength. After that, the half-samples resulting from the flexural test were tested in axial compression. The water absorption capacity and apparent density of mortar in the hardened state were investigated according to the European standards NF EN 1015-18 and NF EN 1015-10 respectively.

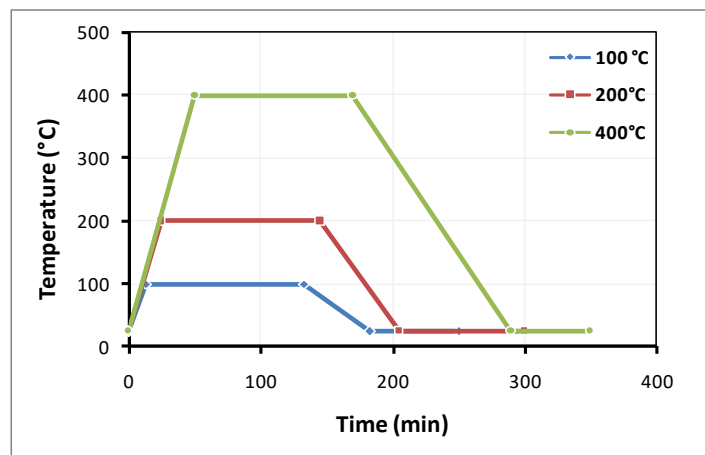


Figure 4: Heat treatment process diagram

To evaluate the effect of elevated temperature on the mechanical characteristics of the mortar studied, the samples were heated in an electric furnace laboratory (FOURS ME brand) for 2 hours at temperatures of 100 °C, 200 °C, and 400 °C, with an increment rate of 7.84 °C per minute (Figure 4). After that, the samples were allowed to cool to room temperature (23 ± 2 °C). It should be noted that when raising the temperature from 200°C to 400°C, we observed the melting of the PET fibers appearing on the faces of the samples. Figure 5 illustrates the state of the mixture M₂ when the temperature reaches 200°C and 400°C.



Figure 5: The visual state of the mortar M₂ at a temperature of 200°C and 400°C

3 Results and Discussion

3.1 Consistency of Fresh Mortar

The results of the flow time of PET fiber-reinforced mortar mixtures with different fiber contents are plotted in Figure 6. The results of this experiment showed that the incorporation of PET fibers with substitution rates less than or equal to 1.5% does not have a substantial impact on the consistency of the mixes; the consistency shows a constant value (4 seconds) for 0%, 0.5%, 1%, and 1.5% PET fibers. On the other hand, it is found that beyond 1.5%, the flow time decreases progressively with the number of fibers added, to reach a minimum value (one second) for 2.5% of PET fibers. The substitution of 2.5% dune sand with PET waste fibers makes it possible to achieve consistencies equal to those of alluvial sand mortar (MAS); which shows that the incorporation of 2.5% fibers results in a considerable increase in workability.

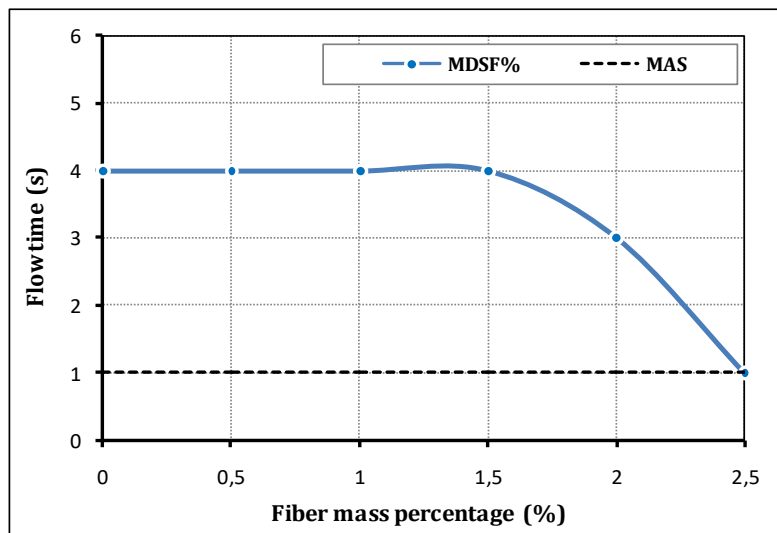


Figure 6: Evolution of the consistency as a function of PET fibers amount

The increase in consistency may be attributed to the distinction in water absorption capacity between DS and fibers, which increased the amount of excess water and therefore the workability. The decrease in flow time is also attributed to the longitudinal shape of PET waste fibers, which assist the mixed particles to flow over each other [20].

3.2 Bulk Density of a Hardened Mortar

The results presented graphically in Figure 7 show that at room temperature, the inclusion of recycled fibers results in a significant enhancement in bulk density for a reinforcement rate of 0.5% (the case of the mixture M_1). This replacement ratio allows for a bulk density comparable to that of alluvial sand mortar (1.98 g/cm^3). Beyond this percentage, a general decrease in apparent density was observed. The mortar specimens with recycled fibers exhibited apparent densities varying from 1.95 to 1.79 g/cm^3 at room temperature. The reinforcement of dune sand mortar with 1%, 1.5%, 2%, and 2.5% PET strap waste fibers induces reductions of 0.5%, 2.1%, 1.6%, and 5.8%, respectively, in comparison to a mortar without fibers. This might be related

to PET fibers' specific gravities which are relatively low compared to those of dune sand (1.29 and 2.53, respectively).

The findings demonstrate that the exposure of the investigated mortar specimens to high temperatures has an important effect on the bulk density; for 0%, 0.5%, 1%, 1.5%, and 2% of PET fibers, the increase in temperature significantly decreases this characteristic. For 0.5% of fibers, treatment of the mortar samples at temperatures of 100°C, 200°C, and 400°C causes reductions of 3.6%, 5.1%, and 5.6%, respectively, in comparison to the bulk density at room temperature.

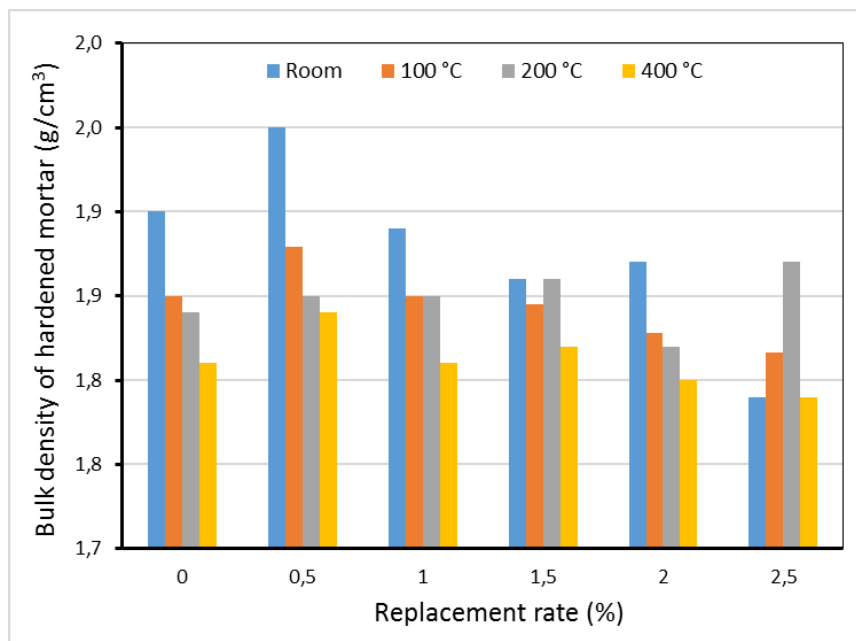


Figure 7: The influence of replacement rate on mortar dry bulk density at room and high temperatures

These results coincide with those obtained by other authors who have studied the thermo-mechanical characteristics of mortars containing expanded vermiculite powder at high temperatures [21]. On the other hand, for 2.5% fibers, we notice improvements of 1.5% and 4.5% for 100°C and 200°C, respectively.

3.3 Water Absorption at Room Temperature

Figure 8 illustrates the impact of the fiber ratio on the water absorption of dune sand mortar. From the results obtained, it should be noted that the reinforcement of the DS-mortar by the introduction of PET fibers results in a continuous increase in the water absorption capacity, which shows that these fibers do not participate in improving the compactness of mortar mixes.

The samples of the dune sand mortar with PET fibers exhibited water absorption capacities varying from 11% to 15.5%. The minimum value of water absorption capacity (11%) was observed at 0% and 0.5% replacement levels. The maximum value is given by the mixture containing 2.5% PET fibers (mixture M₅); the incorporation of PET fibers can generate an important increase in water absorption of the order of 40% in comparison to the mortar without

fibers. The reinforcement of dune sand mortar with PET strap waste fibers does not allow obtaining water absorption values close to those of the SA-based mortar (MAS); this might be attributed to the AS sand's better particle size distribution as compared to the DS sand.

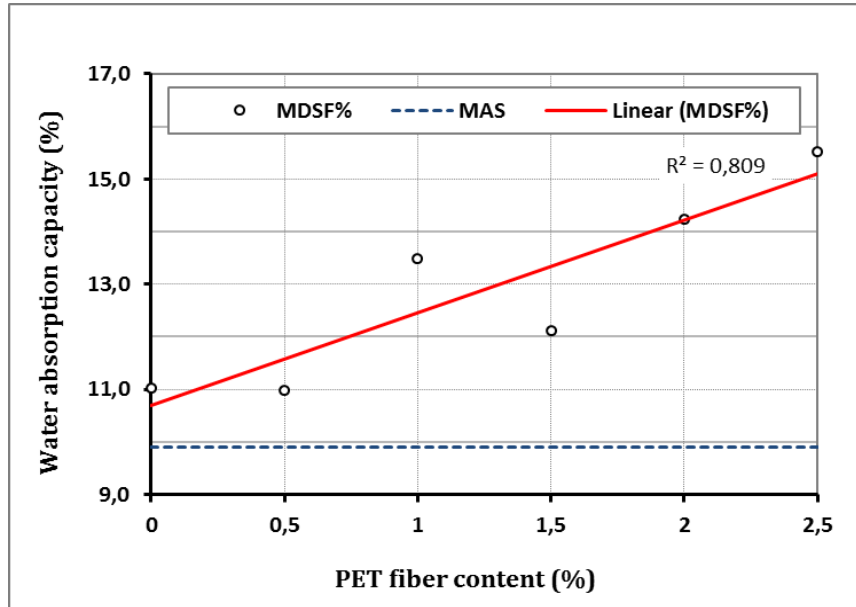


Figure 8: Impact of the PET replacement ratio on the water absorption capacity

3.4 Compressive Strength of Hardened Mortar

Figure 9a depicts the results of the compressive strength test on mortar specimens after exposure to temperatures ranging from room temperature to 400 °C. Figure 9b depicts the changes in compressive strength at temperatures of 100 °C, 200 °C, and 400 °C. As it appears, the mortar samples treated with recycled fibers developed compressive strengths ranging from 17.8 to 21.2 MPa at room temperature. Under these storage conditions, the fiber reinforcement of the dune sand mortar does not make it possible to give higher resistances than that of the AS-based mortar (MAS). of 21.2 MPa was achieved for a replacement rate of 2% (an improvement of 10.4%), and the minimum value of 17.8 MPa was noted for the mortar containing 1% PET fibers, i.e., a reduction of 7.3% in comparison with the control mortar (MDS). The factors that lead to a decrease in compressive strength were principally attributed to the increase in porosity and decrease in bulk density with increasing replacement ratio.

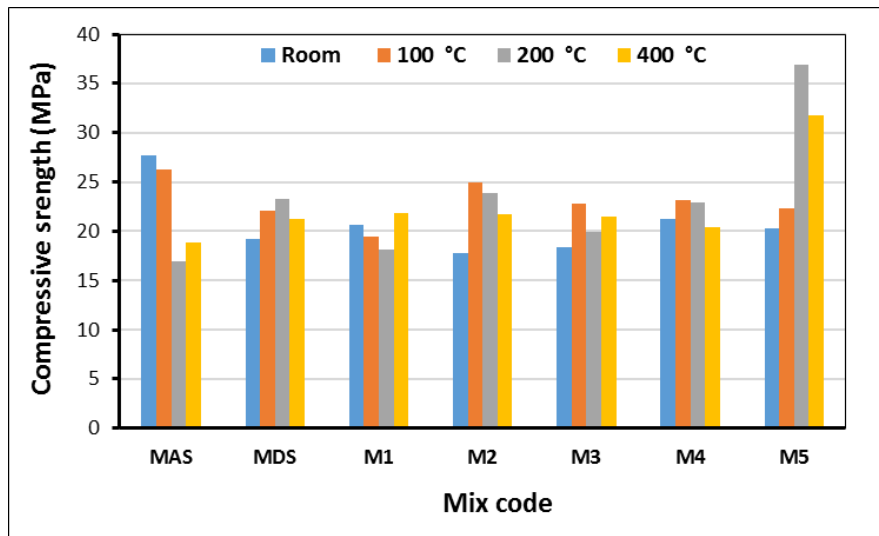


Figure 9a: Evolution of compressive strength as a function of the heating temperature

The inclusion of recycled fibers improved the mechanical performance of the reinforced mortar at 100°C, 200°C, and 400°C. At 100 °C, the incorporation of 1%, 1.5%, 2%, and 2.5% PET fibers showed good performance with improvements in compressive strengths of 40%, 24%, 9%, and 10%, respectively, as compared to the control mortar (MDS). However, a reduction in strength of 6% was recorded at 0.5% of fibers. The improvement in compressive strength can be attributed to reactions that occur during the heating process. [22]. At 200 °C, a very high compressive strength enhancement (82%) was recorded at a replacement rate of 2.5%. However, at 0.5% PET fibers, there is still a strength reduction of 6%; it seems that the behavior of the fibers is better when they overlap or intersect than when they are isolated.

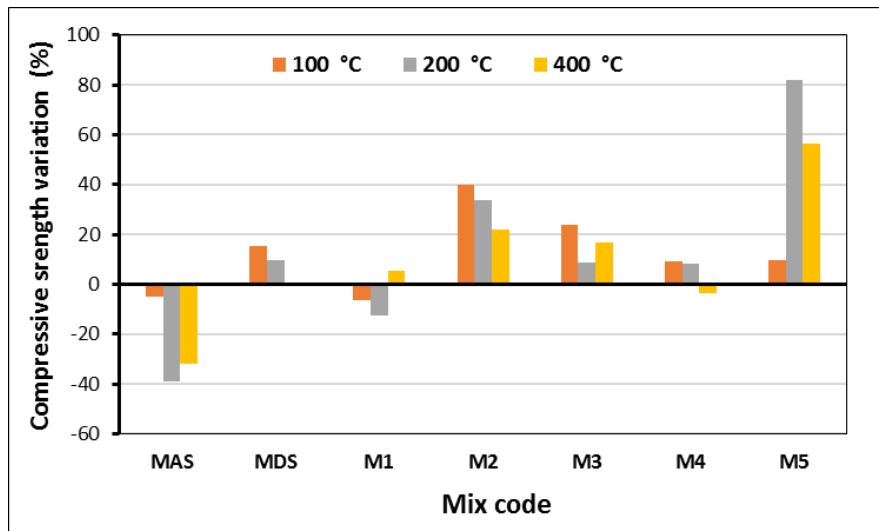


Figure 9b: Influence of heating temperature on compressive strength variations

At 400 °C, improvements in compressive strength were observed for fiber contents of 0.5%, 1%, 1.5%, and 2.5%. The results also show that adding 2.5% PET fibers to dunes sand mortar results in the highest compressive strength. It is also noted that the DS-based mortars, with or without PET fibers, exhibit better high-temperature resistance performance than AS-based

mortar; it appears that the illite of DS is a refractory or heat-resistant component that contributes to this enhancement at high temperatures. The AS-based mortar exhibited compressive strength reductions of 5.1%, 39.1%, and 32.1% at 100°C, 200°C, and 400°C temperatures, respectively.

3.5 Flexural Strength of Hardened Mortar

Figure 10a shows the experimental results obtained from the bending test of the samples studied after being subjected to heating temperatures ranging from room temperature to 400 °C. Figure 10b illustrates the improvements and losses in flexural strength values at different temperatures. As shown, the dune sand mortars reinforced with PET strap waste fibers exhibited bending strengths ranging from 1.23 to 1.72 MPa at ambient temperature. Similar to the results for compressive strength, the use of PET waste fibers as mortar reinforcement does not make it possible to achieve higher flexural strengths than that of the AS-based mortar. The greatest value (1.72 MPa) was achieved for 0.5% PET fiber (an improvement of 11%). The significant gain in strength is the result of the bonding force between the fibers and the mortar matrix. In comparison to the control mortar (MDS), the bending strength decreased by 20.6%, reaching its lowest value of 1.23 MPa. This reduction in strength is mainly related to the decrease in compactness with increasing fiber content; the water absorption values (Figure 8) show the impact of PET fiber inclusion on compactness.

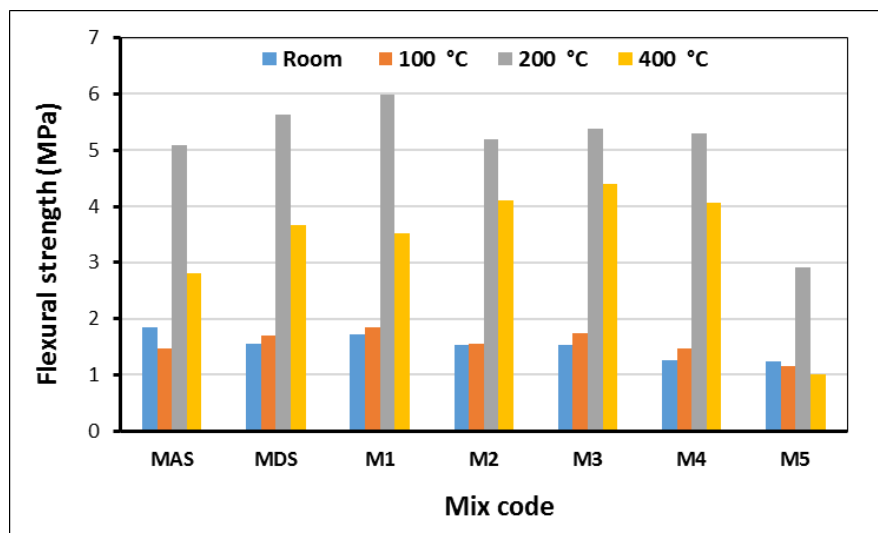


Figure 10a: Effect of temperatures rate on flexural strength

At 100°C and 200°C, the best flexural strength results were obtained for the fiber content of 0.5%; the improvements recorded for this replacement rate are respectively 8.9% and 6% in comparison to the DS-based mortar without fiber (MDS). For mortar specimens heated at 400 °C, a decrease in flexural strength was noticed compared to those heated at 200 °C. These samples exhibited strength reductions of 44.7%, 35.1%, 41.3%, 21.0%, 18.3%, 23.4%, and 65.7% for MSA, MSD, M1, M2, M3, M4, and M5, respectively. These important reductions may be associated with the cracking in the mortar matrix and with the voids created after the melting of the PET fibers. Also, this would coincide with the melting temperature of the fibers (Figure 11). It is also noted that the mortar with 2.5% PET fibers (M5) has the lowest flexural

strength values when compared to other mixes; this is primarily due to the high content fiber, which reduces adhesion between fiber and matrix, resulting in poor tensile stress transfer.

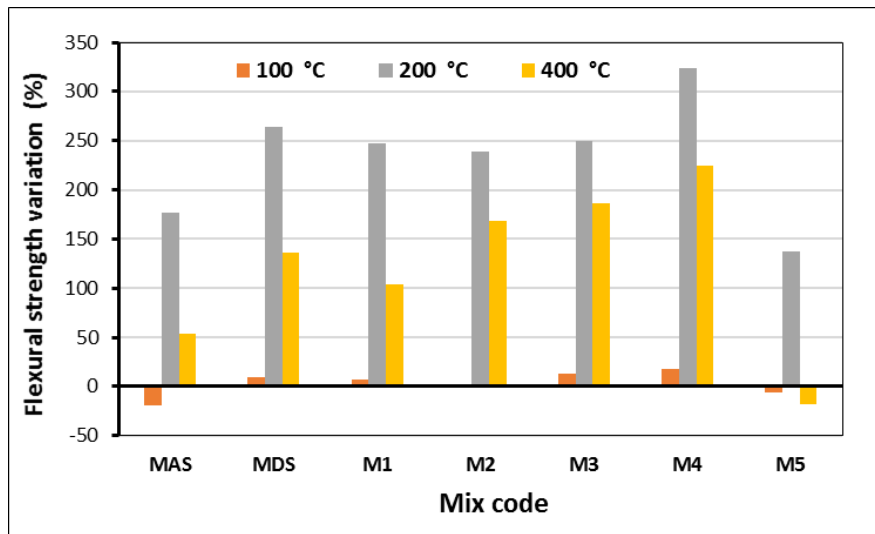


Figure 10b: Effect of temperatures rate on flexural strength variations



Figure 11: Formation of voids in the M5 mortar matrix after heating at 400 °C

4 Conclusions

Many experiments on PET fiber-reinforced dune sand mortar have been conducted. According to the findings of this study, adding recycled PET fiber to mortar had a significant impact on the physical and mechanical characteristics of the mortar obtained in both fresh and hardened states.

The research's conclusions may be summarized as follows:

- The incorporation of PET fiber with replacement rates less than or equal to 1.5%, has little impact on the mortar consistency. However, beyond 1.5% the flow time decreases with the percentage of fibers until it reaches the lowest value (at 2.5% of PET).

- The inclusion of 0.5% PET waste fibers results in a significant increase in bulk density at room temperature. After this percentage, a general decrease in apparent density was observed.
- The use of PET strap waste fibers improves the behavior of reinforced dune sand mortar at 100°C, 200 °C, and 400°C. Compared to AS-based mortars, DS-based mortars have much higher mechanical performance at high temperatures.
- The best flexural strength results measured after heating at 100 °C and 200 °C were obtained for 0.5% fiber. For mortar samples exposed to 400 °C, a decrease in flexural strength is observed compared to samples exposed to 200 °C.

References

- [1] M. Hacini, A.S. Benosman, N.K.Tani, M. Mouli, Y. Senhadji, A. Badache, N. Latroch. (2021). Utilization and assessment of recycled polyethylene terephthalate strapping bands as lightweight aggregates in Eco-efficient composite mortars. *Construction and Building Materials*. 270, 121427. DOI: 10.1016/j.conbuildmat.2020.121427.
- [2] R.I. Umasabor, S.C. Daniel. (2020). The effect of using Polyethylene Terephthalate as an additive on the flexural and compressive strength of concrete. *Heliyon*. 6, e04700. DOI: 10.1016/j.heliyon.2020.e04700.
- [3] G. Martínez-Barrera, L. Ávila-Córdoba, F. Ureña-Núñez, M. Alonso Martínez, F. P. Álvarez-Rabanal, O. Gencel. (2021). Waste Polyethylene terephthalate flakes modified by gamma rays and its use as aggregate in concrete. *Construction and Building Materials*. 268, 121057. DOI: 10.1016/j.conbuildmat.2020.121057.
- [4] A. Meza de Luna, F.U.A. Shaikh. (2020). Anisotropy and bond behaviour of recycled Polyethylene Terephthalate (PET) fibre as concrete reinforcement. *Construction and Building Materials*. 265, 120331. DOI: 10.1016/j.conbuildmat.2020.120331.
- [5] R. Kutum, P. Singh, A. Saha. (2021). Experimental Study on Recycled Polyethylene Terephthalate (PET) Bottle Fibre Reinforced Concrete. In: Ajay S. Kalamdhad (eds), *Integrated Approaches Towards Solid Waste Management* (pp. 87–97). New Delhi, India: Springer, Cham. DOI: 10.1007/978-3-030-70463-6_9.
- [6] K. Singh. (2021). Partial replacement of cement with Polyethylene Terephthalate fiber to study its effect on various properties of concrete. *Materials today: proceedings*. 37, pp. 3270-3274. DOI: 10.1016/j.matpr.2020.09.111.
- [7] X. Lin, J. Yu, H. Li, J.Y.K. Lam, K. Shih, I.M.L. Sham, C. K.Y. Leung. (2018). Recycling Polyethylene Terephthalate wastes as short fibers in Strain-Hardening Cementitious Composites (SHCC). *Journal of Hazardous Materials*. 357, 40-52. DOI: 10.1016/j.jhazmat.2018.05.046.
- [8] F. Uddin, A. Shaikh. (2020). Tensile and flexural behaviour of recycled Polyethylene Terephthalate (PET) fibre reinforced geopolymer composites. *Construction and Building Materials*. 245, 118438. DOI: org/10.1016/j.jhazmat.2018.05.046.
- [9] W.S. Alaloul, V.O. John, M.A. Musarat. (2020). Mechanical and Thermal Properties of Interlocking Bricks Utilizing Wasted Polyethylene Terephthalate. *International Journal of Concrete Structures and Materials*. 14, 24. DOI: 10.1186/s40069-020-00399-9.
- [10] S.U. Khan, T. Ayu. (2020). Flexure and shear behaviour of self-compacting reinforced concrete beams with Polyethylene Terephthalate fibres and strips. *Structure*. 25, 200-211. DOI: 10.1016/j.istruc.2020.02.023.

- [11] H.M.Adnan,A.O.Dawood. (2020). Strength behavior of reinforced concrete beam using re-cycle of PET wastes as synthetic fibers. *Case Studies in Construction Materials*. 13, e00367. DOI: org/10.1016/j.cscm.2020.e00367.
- [12] Y.D. Blanco, E.C.M. Campos, C.I.R. Valdés et al. (2020). Effect of Recycled PET (Polyethylene Terephthalate) on the Electrochemical Properties of Rebar in Concrete. *Int J Civ Eng*. 18, 487–500. DOI: 10.1007/s40999-019-00478-3.
- [13] R.A. Hawileh, H.H. Mhanna, A. Al Rashed, J. A. Abdalla, M.Z. Naser. (2022). Flexural behavior of RC beams externally bonded with polyethylene terephthalate (PET) fiber reinforced polymer (FRP) laminates. *Engineering Structures*. 256, 114036 DOI: 10.1016/j.engstruct.2022.114036.
- [14] O.K. Ali, A.I. Al-Hadithi, A.T. Noaman. (2022). Flexural performance of layered PET fiber reinforced concrete beams. *Structures*. 35, 55–67. DOI: org/10.1016/j.istruc.2021.11.007.
- [15] M.E. Kangavar, W. Lokuge, A. Manalo, W. Karunasena, M.Frigione. (2022). Investigation on the properties of concrete with recycled Polyethylene Terephthalate (PET) granules as fine aggregate replacement. *Case Studies in Construction Materials*. 16, e00934. DOI: 10.1016/j.cscm.2022.e00934.
- [16] A.Meena, A. Surendranath, P.V. Ramana. (2022). Assessment of mechanical properties and workability for polyethylene terephthalate fiber reinforced concrete. *Materials Today: Proceedings*. 50, pp. 2307–2314. DOI: 10.1016/j.matpr.2021.10.054.
- [17] H. Wu, Y. Miao, H. Zhu, C. Zhao, Z. Shu, C. Liu. (2022). Erosion resistance behavior of recycled plastic concrete in sodium sulfate solution. *Construction and Building Materials*. 324, 126630. DOI: 10.1016/j.conbuildmat.2022.126630.
- [18] G. Bamigboye, K. Tarverdi, D. Adigun, B. Daniel, U. Okorie, J. Adediran. (2022). An appraisal of the mechanical, microstructural, and thermal characteristics of concrete containing waste PET as coarse aggregate. *Cleaner Waste Systems*. 1, 100001. DOI: 10.1016/j.clwas.2022.100001.
- [19] M. Chen, Z. Sun, W. Tu, X. Yan, M. Zhang. (2021). Behaviour of recycled tyre polymer fibre reinforced concrete at elevated temperatures. *Cement and Concrete Composites*. 124, 104257. DOI: 10.1016/j.cemconcomp.2021.104257.
- [20] T. Flexikala, P. Partheepan. (2010). Granite powder concrete. *Indian Journal of Science and Technology*. 3(3), pp. 311–317.
- [21] F. Koksai, et al. (2021). The effects of cement type and expanded vermiculite powder on the thermo- mechanical characteristics and durability of lightweight mortars at high temperature and RSM modelling. *Case Studies in Construction Materials*. 15, e00709. DOI: 10.1016/j.cscm.2021.e00709.
- [22] V. Pachta, S. Triantafyllaki, M. Stefanidou. (2018). Performance of lime-based mortars at elevated temperatures. *Construction and Building Materials*. 189, pp. 576–584. DOI: 10.1016/j.conbuildmat. 2018.09.027.



Assessment of Water Loss in the Water Distribution Network of Bendjerrah Using a Combination Approach of Fixed Area Variable Area Discharge, Minimum Night Flow, and Epanet Calibrator

Meriem Dorbani^{1*}, Rachid Mansouri¹, Faiza Balla¹, Mazouz Kherouf¹

University of 8 May 1945, Guelma, Algeria
Department of Civil Engineering and Hydraulics
*e-mail: dorbani.meriem@univ-guelma.dz

Abstract

Water losses due to leakage are a pernicious problem for water utilities. Understanding and quantifying Non-Revenue Water (NRW) and water loss components is the first step in the management of urban water losses. Hydraulic modeling is a powerful tool to predict the impacts of different management scenarios on the hydraulics of the Water Distribution Network (WDN). The water distribution network (WDN) can be divided into a number of District Meter Areas (DMAs) with suitable sizes in order to apply pressure management. In this study, the Fixed Area Variable Area Discharge (FAVAD) concept and the number of leaks were analyzed for a number of water network pressure management areas in the city of Bendjerrah – the district of Guelma, Algeria. The analysis identified some anomalies concerning the parameters of some networks; especially those related to leakage exponent N_l values greater than 1.5. The approach used in this framework is based on the estimation of the leakage from the Minimum Night Flow (MNF) and the burst frequency of Average Zonal Pressure (AZP). After the use of this approach and the calibration procedure using the Epanet-calibrator on real District Meter Areas, the obtained results are very close to the real state of the network. In addition, this paper studies the possibility of explicitly incorporating the variation of the leakage zone in the hydraulic modeling of the water distribution systems. The results show that the power equation leakage exponent N_l estimates the total system leakage with an error of up to 20%. From the Minimum Night Flow, obtained by using the South African Night Flow (SANFLOW) practical tool, it was found that the actual losses calculated for sectors 1, 2, and 3 are respectively 25%, 45%, and 30%.

Keywords: Minimum Night Flow (MNF), Fixed Area Variable Area Discharge (Favad), South African Night Flow (Sanflow), water losses, leakage, modulation of pressure

1 Introduction

Water is not a product or business asset; this is a resource that should be valued by mankind. The water shortage issue is put into the spotlight over most of the world and pushes many nations to re-planning their water resources in various aspects. Providing data on water's economic value assists policymakers to make informed decisions regarding water distribution. Additionally, addressing the increasing demand for all uses and building a sustainable future of agricultural and water policies [1].

Non-revenue water in Algeria is estimated between 40 and 50% and is divided into two categories: technical losses and commercial losses. In fact, because of technical and economic reasons, a leak-free network is not realizable, but the amount of water loss should be kept as low as possible. The distribution network undergoes degradation over time, which can easily lead to leaks. A whole range of factors is, to varying degrees in space and time, responsible for water loss.

Sustaining water services is challenging for every water utility. The goal of this effort is to make sure that water losses are kept at a minimum. Water losses, non-revenue water, and unaccounted-for water are the most commonly used terms to address the wastage occurring in the supply network. The term nonrevenue water has substituted the term 'Unaccounted for Water as suggested by International Water Association (IWA), and as recommended by American Water Work Association "AWWA, (2014)" [2]. Generally, NRW is an indicator of the operational efficiency of WDS. Precise knowledge of water consumption allows for quantifying the water lost volumes on the network. But even an exact assessment of losses is still not enough to eliminate all the leaks on the network.

Due to the huge economic impact of water losses, several approaches, that deal with this problem, have been proposed. Many water loss management studies assess non-revenue water without evaluating the contribution of leakages to total water losses. Consequently, total water losses are not partitioned accordingly. Therefore, there is an urgent need for specialized application tools for assessing partitions of non-revenue water. One such tool is the Pressure management scheme.

Pressure pipelines with a variable flow rate of fluid along the path are widely used in many industrial processes - pipeline-collector (PC) and distribution pipeline (DP). PCs are widespread in water supply (water-intake structures with tubular heads), amelioration (drainage systems), water supply, etc. [3].

Pressure management can be defined as "the practice of managing system pressures to an optimum level of service ensuring sufficient and efficient supply to legitimate users and consumers, while eliminating or reducing pressure transients and variations, faulty level controls and reducing unnecessary or excess pressures, all of which cause the distribution system to leak and break unnecessarily" [4], [5].

There are several methods for regulating pressure in the WDNs [6], [7]. In addition, regulating the water pressure in distribution networks is usually achieved by partitioning the

complex networks into smaller sub-networks known as the District Meter Areas (DMAs) [8], [9]. The water pressure in these areas is regulated by installing network elements such as control valves at the inlet of the zones. Ryma Fares [10] developed a theoretical approach linking the reduction in leak flow rate with the pressure reduction in the network. The proposed approach counts explicitly and separately the leaks and rigidity of the pipe materials in the network. The pressure management proposed by Liberatore and Sechi [11] is carried out by means of control valves. This method consists of the pressure constraint at (pseudo-valves) nodes and determines the valve optimum calibration value. Another powerful tool is the South African Night Flow (SANFLOW) Analysis Model. The SANFLOW analysis model is an alternative tool, relevant and highly adaptable to the developing world. This model [12] uses the Minimum Night Flow (MNF) method based on the inflow measurement at the MNF time.

Apart from the MNF data, the SANFLOW model also uses basic infrastructure variables such as length of mains, number of connections, number of properties, estimated population, average zone night pressure, and major water users. It is important to note that if there was no data such as leakage coefficients and pressure correction factors, some assumptions were made and SANFLOW default values which were recommended by McKenzie [12] were used. The SANFLOW model is based directly on the BABE (burst and background estimate) with Fixed and Variable Area Discharges (FAVAD) principles and is written in DELPHI computer language for the Windows operating system [13].

The present work focuses on the development of an approach to WDN using Rossman's Epanet software and the South African Night Flow (SANFLOW) Analysis Model. This study proposes the use of a calibration technique to assess the leaks in each network sector. In addition, the results of the calibration model were compared with the results estimated from the MNF method targeting the validation of the computational approach. A calibration with (Epanet Calibrator) was particularly used as a calculation tool. Field measurements were carried out in a real system in order to collect the pressure and flow rate data. The scarcity of data is a real problem in network modeling. In an attempt to overcome this difficulty, a new approach has been proposed. One of the simplest ways of tackling this problem is to develop a model that can be used for pressure management rather than for assessing the background leaks in the networks. This study has been conducted by considering the frequency of burst pipes caused by high pressure at the most unfavorable points (critical points), based on the minimum night flow rate, in order to quantify the leak flow rate at specific locations.

2 Materials and Methods

2.1 Real Loss Assessment Using Minimum Night Flow (MNF) Rate

The scarcity of measured data is a real obstacle to network modelers. To overcome this difficulty, a new approach is proposed. The steps are described in the detailed flowchart below (Figure 1).

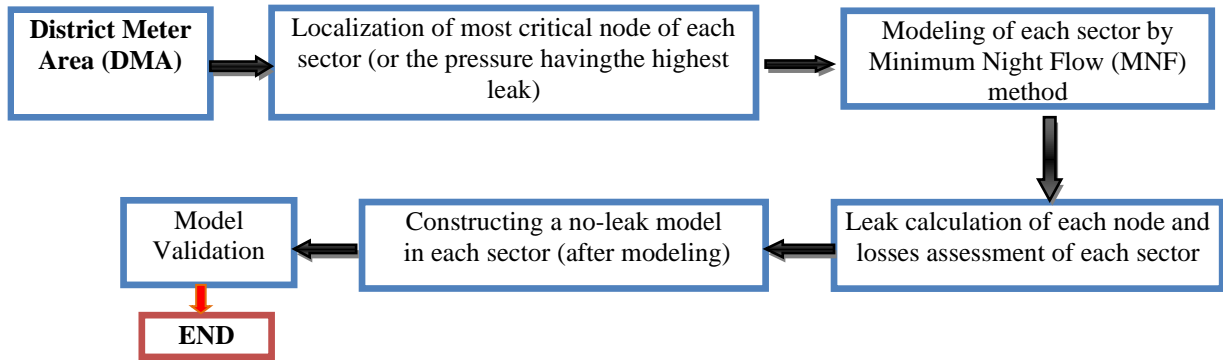


Figure 1: Flowchart of the proposed approach

The idea is to develop a model that can be used for pressure management rather than for assessing the background leaks in the networks. The study was conducted considering the frequency of pipe bursts caused by high pressure at the most unfavorable points (critical points), and by using the minimum night flow rate, to quantify the leak flow rate at specific locations.

The MNF is the lowest flow entering a water supply area during 24-hours, assuming that the availability of water during this period is sufficient to meet the required demands [14]. Since the pressure during the night is usually the largest and the pressure varies throughout the day, the real loss value of the whole day cannot be determined by extrapolating the real loss value measured during the MNF. According to the study carried out by Marzola et al. [15] the MNF analysis can only be performed in the District Meter Area.

During the analysis of MNF, the flow is considered to consist of three main components namely: normal legitimate night use, background leakage, and burst leakage (or excess night flow) as mentioned by AL-Washali et al. [16]. Utility managers should also determine a pressure factor that creates a true average 24-hour leakage value when applied to the Net Night Flow (NNF). "Morrison et al.[17] proposed that the Minimum Night Flow (MNF) should comprise the Legitimate Night Flow (LNF) of household and non-household and abnormal night flow on account of background losses and bursts, i.e., the physical losses. As leakage is proportional to pressure, the average leakage can be represented throughout the day and the Utility Net Night Flow (UNNF) should be corrected with respect to the pressure factor. Typical values of the Night Day Factor (NDF) range from 20 or less in gravity fed systems to over 30 hours per day in pressure management areas with flow modulated systems [18].

A leak in a pipe can be considered an orifice. The hydraulics of orifices is well understood and clearly described by Torricelli's Law. Experimental research has shown that the discharge in orifices varies greatly with pressures depending on the pipe material, called the Fixed and Variable Area Discharges (FAVAD) principle, as described by the following relationship [19]:

$$\frac{Q_i}{Q_{MNF}} = \left(\frac{P_i}{P_{MNF}} \right)^{N_1} \quad (1)$$

where,

Q_i , leakage rate in DMA at time i [m^3/h], Q_{MNF} , leakage rate in DMA at time MNF [m^3/h], P_i , average zonal pressure (AZP) in DMA at time i [m], P_{MNF} , average zonal pressure (AZP) in DMA at time MNF [m]; N_i , leakage exponent [-].

Empirically N_i values are 0.5 for metallic pipes and between 1.5 to 2.5 for plastic pipes [19]. There is a relative abundance of data concerning the associated leakage exponents of individual leaks tested under laboratory conditions compared to field data of District Metered Area (DMA) level leakage exponents [19]. In order to calculate a daily leakage rate, a NightDay Factor (NDF) is introduced by Equations 2 and 3.

$$Q_{RL} = NDF * Q_{MNF} \quad (2)$$

$$Q_{RL} = NDF * Q_{MNF} \quad (3)$$

$$NDF = \sum_{i=1}^{i=24} \left(\frac{P_i}{P_{MNF}} \right) * P^{N_i} \quad (4)$$

where,

Q_{RL} , Real losses inside DMA [m^3/day]

Q_{MNF} , Net Night Flow in DMA [m^3/h]

NDF , Night Day Factor [h/day]

Apparent losses can be written as follows:

$$Q_{AL} = NRW - Q_{RL} \quad (5)$$

where,

Q_{AL} , Apparent losses inside DMA [m^3/day]

NRW , Non-revenue water inside DMA [m^3/day]

Q_{RL} , Real losses inside DMA [m^3/day]

2.2 Calibration Model

The Epanet Calibrator allows for establishing regressive models aimed to correlate the invisible leaks and pressures. In order to assess the real losses from Epanet Calibrator, first, the DMA sector should be modeled, and then the flow rate and pressure data observed would be entered into the software with regard to calibrating the network. Based on this research, it is important to take into consideration the frequency of burst pipes of high pressure for the most critical points of the area of study, along with the minimum Night Flow Rate in order to quantify the leakage rate at specific locations.

3 Case Study

The methodology is applied to a real network located northeast of Algeria (Guelma district); it is the WDN of the Bendjerrah municipality. It comprises 270 nodes. The total connection number is 1 923, with a network length of 36 km. The system of average flow rate is about

2174 m³/day. The DMAs synoptic in the latter case is composed of 03 sectors, each one fed by an HDPE supply pipe of 150, 200, and 200 mm in diameter, collected from a 1500 m³ semi-buried reservoir supplied by pumping. Using the AWWA-WAS-v5-09152014 software a water balance calculation is carried out. The overall results are summarized in Table 1. Over the past two years, which are 2018 and 2019, the real loss has averaged out to around 0.73, indicating a high proportion of the NRW, therefore, there is an urgent need to reduce leakages. The increase in the levels of NRW could be related to a number of factors such as: the age of the supply infrastructure, increased number of illegal connections, inaccurate billing, reservoir overflows, and vandalism of pipelines.

Table 1: Results of the water balance obtained by using the AWWA-WAS-v5-09152014 software

Year	2017	2018	2019
System Volume Input	181 189	198 609	210 060
Authorized Consumption	159 579	163 050	168 539
Billed Authorized Consumption	157 439	160 567	166 399
Unbilled Authorized Consumption	2 140	2 483	2 140
Billed Metered Consumption (inc. water exported)	157 439	160 567	166 399
Non-Revenue-water	23 750	38 042	43 661
Unauthorized Consumption	453	497	525
Apparent Losses	10 453	10 497	10 525
Real Losses	11 157	25 063	30 996
Water Losses	21 654	35 560	41 512
(Real Losses / Water Losses)	0.51	0.71	0.75

The district metering areas (DMAs) are shown in Figure 2. The DMA contains a total of 1020 residential connections, where three sectors were created, namely: sector 1, 450 residential connections, sector 2, 350 residential connections, and 220 residential connections in sector 3. Figure 2 represents the model EPANET for the three sectors as well as the locations of the monitored points (critical point/sector).

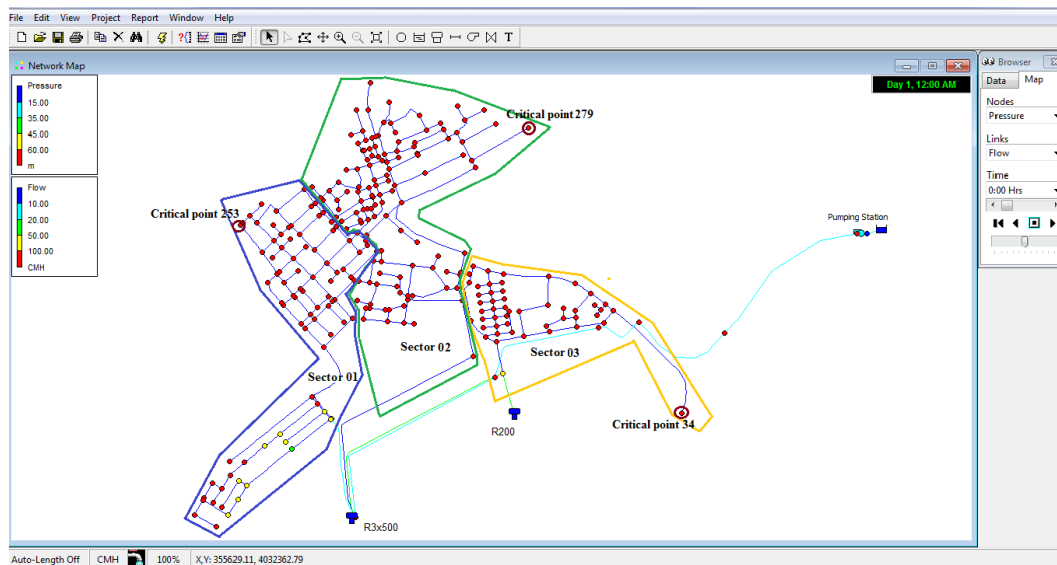


Figure 2: Parameterized model of Bendjerrah municipality WDN using Epanet Calibrator

Minimum night flow rate measurements (MNF) were carried out between 01:00 am and 05:00 am at the monitored points in each sector. In order to obtain the variations in flow rate and pressure, the computed values vary every 30 minutes. Figure 3 illustrates the excel spreadsheet charts of pressure versus leakage and they were plotted by using all the available chart types such as power, exponential, and polynomial (best fit) so as to establish a chart type with a good correlation coefficient (R^2). The follow-up of the weekly average night flow rate, $Q_{night}(s)$ clearly highlighted the correlation between the leak flow rate and pressure. Additionally, the pressure impact on the occurrence of the leak was confirmed by a strong flow rate increase, related to one or many new leaks, when the pressure was significantly increased.

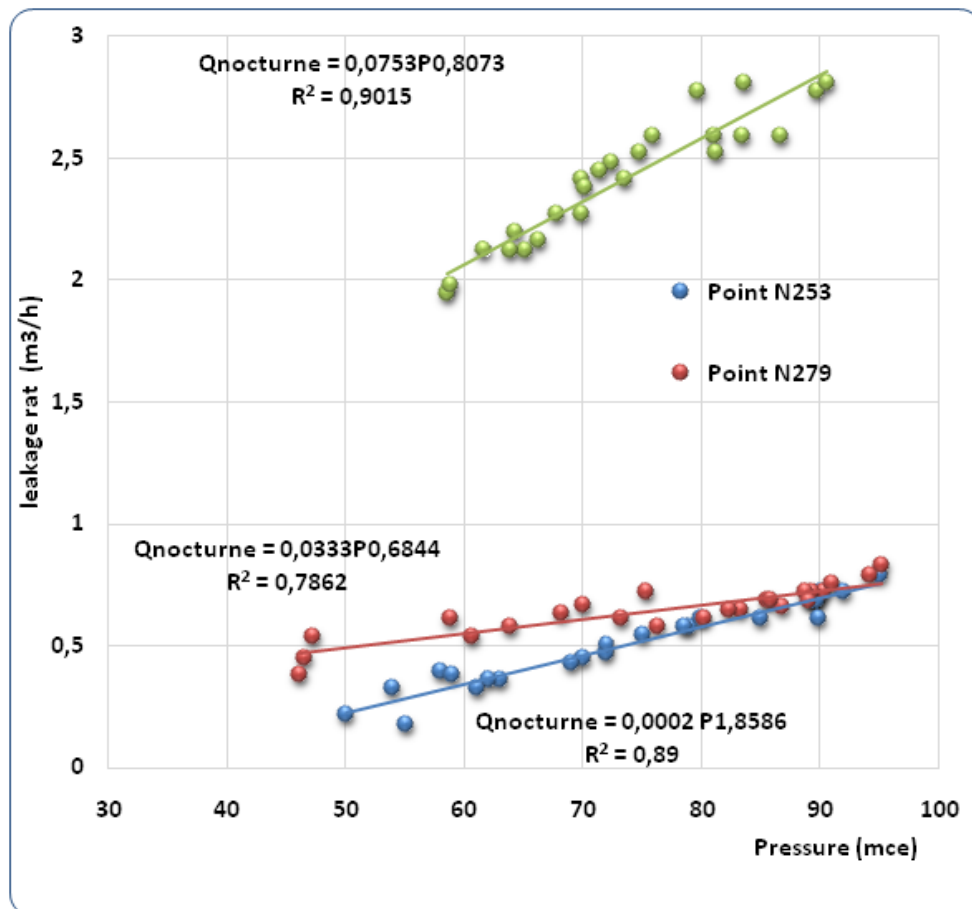


Figure 3: Night flow rate model of the 3 sectors critical points

4 Results and Discussion

The minimum Night Flow Rate methodology (MNF) was applied to the system of the network studied on Epanet as shown in Figure 2. After the valve (downstream) has been installed and handled which is located at the inlet of each sector, in order to urge small disruptions in the system, it was possible to assess the N_I value as shown in Table 2 and to use the hourly pressure values according to the studied points (critical points) from data recorders.

Table 2: N_I calculated for each point monitored during minimum night flow rates

	Time	Critical points 253 in sector 1		Critical points 279 in sector 2		Critical points 34 in sector 3	
		Pi/P _{MNF}	Qi/Q _{MNF}	Pi/P _{MNF}	Qi/Q _{MNF}	Pi/P _{MNF}	Qi/Q _{MNF}
Day 1	01:00-01:30	0.011	1.364	1.25	1.86	1.02	1.20
	01:30-02:00	0.013	1.889	1.26	1.82	1.01	1.36
	02:00-02:30	0.017	3.333	1.27	1.73	0.96	1.26
	02:30-03:00	0.013	1.810	1.00	1.45	0.90	1.07
	03:00-03:30	0.010	1.151	0.78	1.17	0.80	0.97
	03:30-04:00	0.011	1.600	0.84	1.23	0.75	0.86
	04:00-04:30	0.009	1.240	0.85	1.19	0.71	0.80
	04:30-05:00	0.008	1.083	0.91	1.14	0.73	0.83
Day 2	01:00-01:30	0.010	1.500	0.95	1.30	0.83	0.94
	01:30-02:00	0.013	3.400	0.80	1.34	0.93	1.22
	02:00-02:30	0.014	2.222	0.69	1.42	0.76	1.05
	02:30-03:00	0.011	1.462	0.65	1.24	0.70	0.94
	03:00-03:30	0.009	1.094	0.69	1.23	0.67	0.89
	03:30-04:00	0.008	0.941	0.66	1.14	0.69	0.92
	04:00-04:30	0.007	0.816	0.62	0.95	0.74	0.89
	04:30-05:00	0.006	0.650	0.61	0.79	0.81	0.90
Day 3	01:00-01:30	0.008	0.882	0.65	0.98	0.86	1.03
	01:30-02:00	0.009	1.063	0.68	1.20	1.02	1.32
	02:00-02:30	0.012	1.429	0.72	1.44	1.03	1.28
	02:30-03:00	0.009	1.000	0.74	1.45	1.06	1.31
	03:00-03:30	0.008	0.875	0.77	1.46	0.96	1.18
	03:30-04:00	0.007	0.727	0.71	1.26	0.88	1.05
	04:00-04:30	0.007	0.816	0.65	1.09	0.84	0.92
	04:30-05:00	0.006	0.765	0.64	0.87	0.80	0.86
		$N_1=1.54$		$N_2 = 0.73$		$N_3 = 1.05$	
		$R^2=$	0.88	$R^2=$	0.76	$R^2=$	0.81

At the network inlet, the data recorder presents the average flow rate of each of the three sectors respectively 12.82 m³/h, 8.23 m³/h, and 5.51 m³/h. From the minimum night flow rate (MNF), the average night-day factor NDF is calculated for each sector by means of Equation 3 and Q_{RL} by using equation 2. The results are presented in Table 3. Regarding the values obtained from the recorder, the N_I values are satisfactory (according to the correlation factor R^2).

Table 3: Real losses and NDF factor calculated for each point monitored during minimum night flow rates

	Real losses m ³ /24h	Real losses %	NDF
Sector 1	2373.51	25	0.79
Sector 2	4300.74	45	0.97
Sector 3	2828.46	30	0.94

5 Intervention Tools for Water Losses Management

Figure 4 presents the EPANET model for each sector and the location of the monitored points. The equipment was set up in residential flow meters aiming to continuously measure the network pressure.

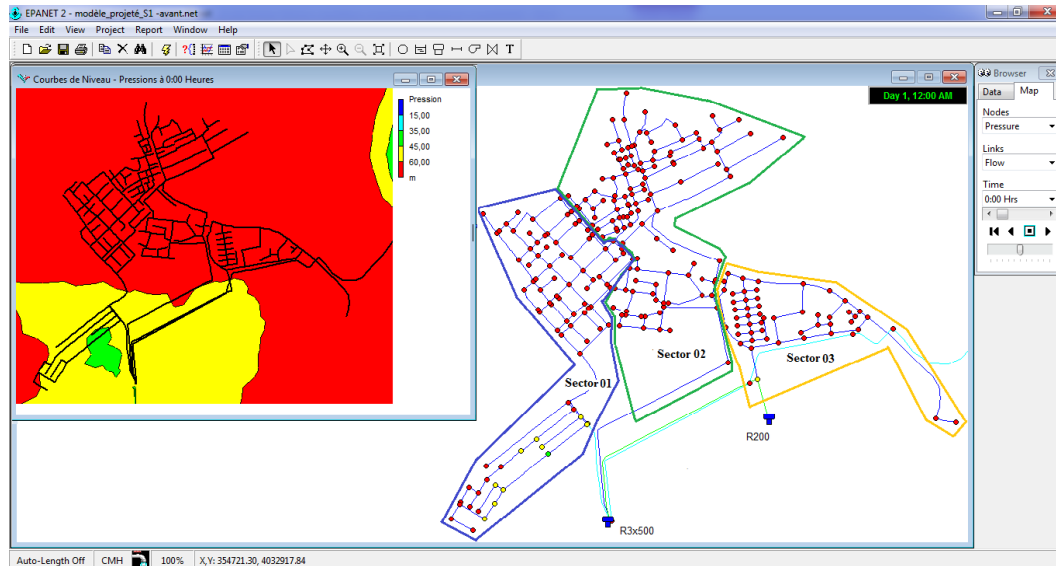


Figure 4: Pressure representation before modulation of valve less network

Continuous pressure sensors were set up for each pipe group (see Figure 3) in order to collect the real data system. The observed flow rate and pressure were used as input data for Epanet as illustrated in Figure 5.

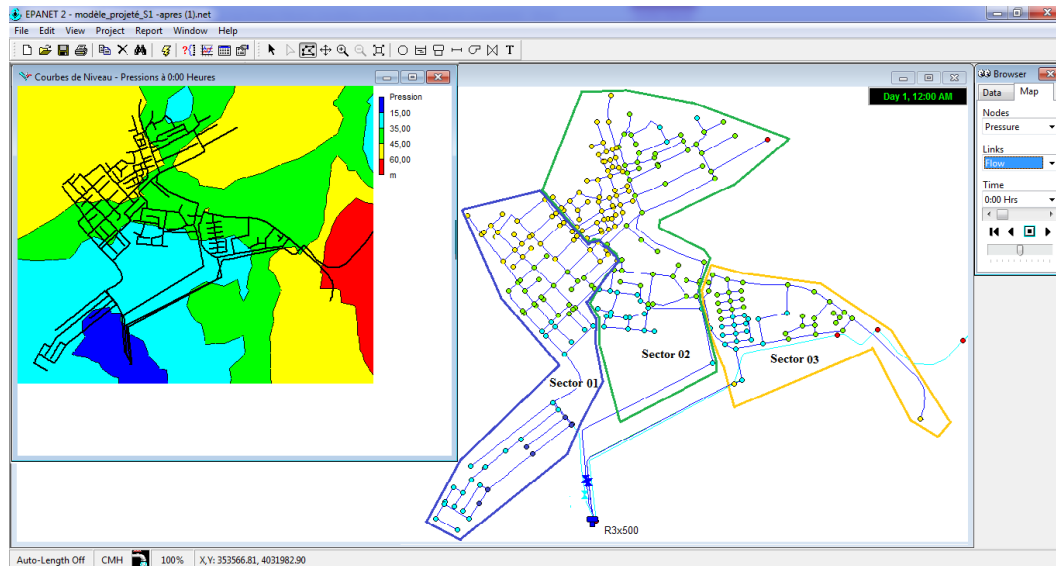


Figure 5: Pressure representation after modulation of network with pressure-reducing stab valve

From the flow rate diagram in Figure 5, the results of the 3 values ((a) observation, (b) simulation, an (c) calibration) can be represented. The operational roles seem to be inverted such as:

- (a) the observed flow rates during 4 days at the 3 critical points for each sector;
- (b) the simulated flow rates during 4 days at the 3 critical points for each sector;
- (c) the calibrated flow rates during 4 days at the 3 critical points for each sector.

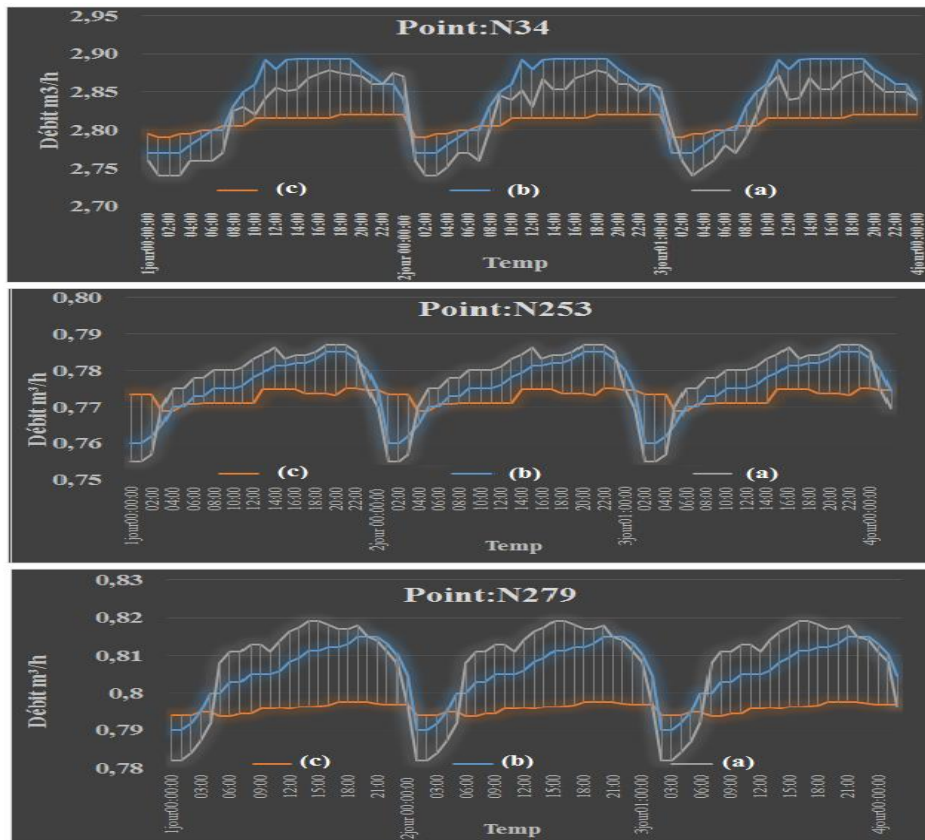


Figure 6: Flow rate (cubic meter per hour) at a critical point in each sector (a) valve less sector, (b) sector with valve fitted to outlet, (c) sector with valve modulated over time (pressure reducer)

From the data in Figure 6, it can be concluded that the demand at the critical points of the 3 sectors is decreased and is satisfactory at the calibrated sector (c), compared to other models (a) observed and (b) simulated where the demand and pressures are high. This indicates that the pressure is detected at the critical point and conveyed to PRV (pressure-reducing stab valve) which, in turn, adjusts the inlet pressure in order to keep the minimum pressure during the day.

Table 4 presents the coefficient calibration of Hazen-Williams. As long as the Epanet Calibrator simulates the leaks, as a result, the flow rates increased with respect to the observed values by the Epanet Calibration process.

Table 4: Hazen-Williams calibration coefficient

	Sector 1	Sector 2	Sector 3
Before calibration	160	160	160
After calibration	83.2	85	87.9

6 Zone Pressure Management

Reducing the pressure at a critical point either in a sector or in a network at a certain level triggers a significant pressure reduction at the network inlet. The tool does not depend on the network hydraulic representation; it rather compromises the MNF analysis and the most in-depth analysis of pressure measures, friction factors, and head losses at 3 DMA key points: inlet point, average zone point (elevation), and critical point, point(s) of the sector, the pressure of which is the lowest during the day as illustrated in Figure 7.

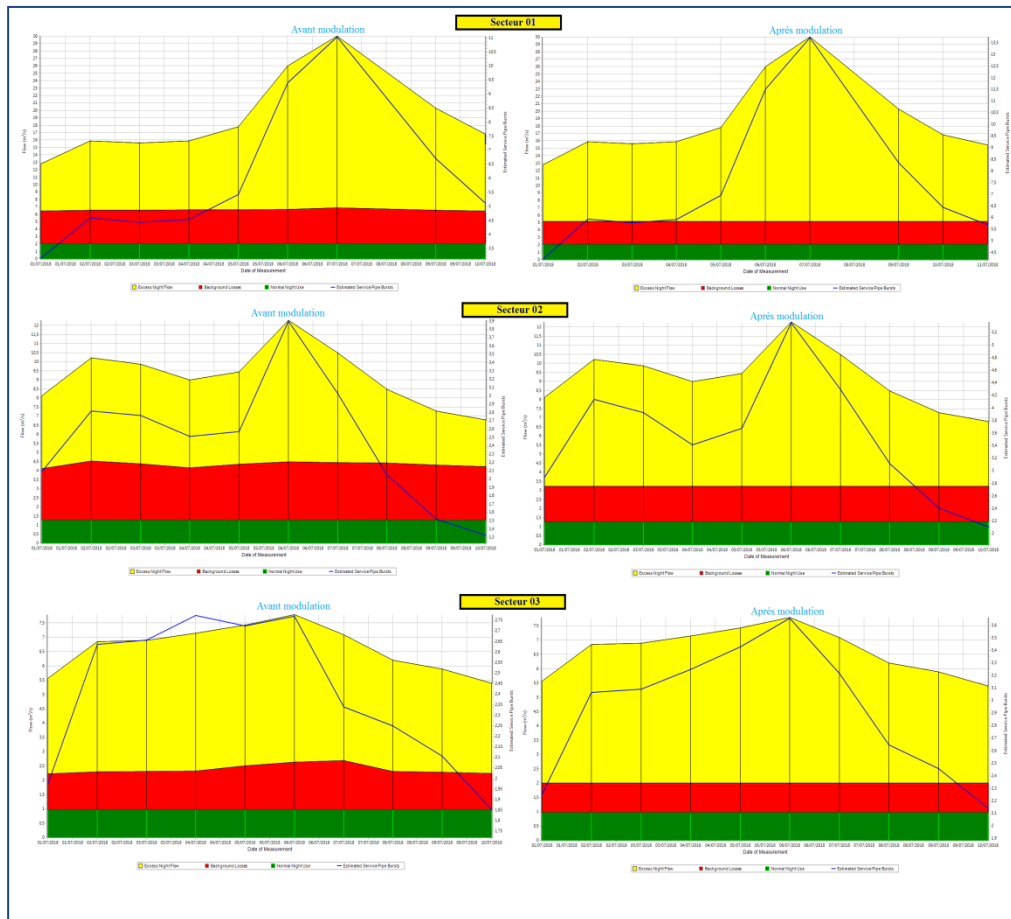


Figure 7: Leak, background losses and night use of the 3 sectors, Source: Sanflow v4.6

7 Model Validation

Sanflow deals with the analysis of each sector before and after calibration (reducing stab). The obtained results are summarized in Table 5. It is worth noting that the loss reduction (background losses) after calibration is observed; thereby allowing the protection of each network sector and minimizing the leaks. After having measured (assessed) the different components of normal night use, figures were added and then subtracted from the minimum night flow rate measured. The difference lies in the unexpected losses attributable, either to unreported bursts or to errors in the hypotheses made during the calculation. The probability of errors in the hypotheses will be treated separately and the remainder of this section considers the difference as a leak.

Table 5: Background loss assessment for night flow rate, Source: Sanflow v4.6

	S1	S2	S3
network losses (m ³)	0.34	0.22	0.16
connection losses (m ³)	1.35	1.05	0.66
property losses (m ³)	0.48	0.37	0.24
Total background leakage P =50 m	2.17	1.64	1.06
correction factor	2.08	1.86	1.33
Final total background leakage (m ³ /h) P = 50 m	4.52	3.06	1.41

The use of different loss parameter values in the analysis is shown in Table 6. It is based on the previous experiment, which can be taken into account, when the loss parameters determination comprises pipe material, age, soil conditions, implementation quality, etc. A pressure correction factor is then necessary to assess the background losses since the loss parameters are always specified at the standard pressure of 50 m. In this research, the average zone night pressure is located at 63 m, which requires a correction in order to reduce the losses. After assessing the two components, the connections background leak and network (BLCONN/ BLMAIN) and the installation background leak (BLINST)) can be determined. It is then possible to calculate the difference between the Minimum Night Flow rate measured and the legitimate use assessed with the results are presented in Table 6.

Table 6: Bursts assessment of each sector/night flow rate. Source: Sanflow v4.6

	S1	S2	S3
Unaccounted loss	6.4	4.7	2.6
Standard service pipes burst	0.80	0.76	0.48
Pressure correction factor	1.28	1.23	1.10
Burst equivalent service Pipes leak	1.02	0.93	0.53
Bursts expected number of equivalent service pipes	6	4	1

Based on the results obtained in Table 6, the majority of leaks are assumed to be of fixed zone type. In addition, the losses and bursts are not as pressure dependent as the background leak. From this Table, it can also be deduced that the bursts expected number of the service pipes, corresponding to the first sector is in the order of 6 bursts, with respect to the second and third sectors which have 4 and 1 burst, respectively.

8 Conclusion

Finding approaches toward water sustainability is crucial for national economic and social development. To reach water sustainability, water losses represented in Non-Revenue Water should be reduced. Many attempts have been made to reduce water losses in water distribution systems and as such many methodologies and tools have been applied to minimize water losses. These tools range from computational approaches, legal and policy implementation, economic approaches, and infrastructural rehabilitation approaches. A water balance is the best practice approach that can be used to partition various components of Non-Revenue Water. However, a water balance approach would not be able to forecast leakage as it only gives a general overview of water loss. Therefore, there is a need for specialized application tools for assessing partitions of non-revenue water. One such tool is the South African Night Flow (SANFLOW) analysis model, for analyzing flows and pressure within district-metered areas. In this study, the SANFLOW analysis model was found to be suitable for partitioning water leakages. The water losses that result only from leakages were determined by identifying the minimum night flow in the district metered areas.

The introduced case study represents an example of a high water loss area with, poor data availability. The semi-urban Municipality of Ben Djerrah has recorded in recent years an increasing Non-Revenue Water. The pressure impact on the occurrence of the leak was confirmed by a strong flow rate increase, linked to one or many new leaks when the pressure was significantly increased. A combination approaches of Rossman's Epanet software and the South African Night Flow (SANFLOW) Analysis Model and the minimum Night Flow Rate methodology were applied to the system of the network studied on Epanet. It was possible to determine the N_1 value from data records after having installed and managed the valve (downstream), situated at the inlet of each sector, to encourage minor disruptions in the system. The calculated N_1 values ranged between 0.5 and 2.5 (two outliers were determined as $N_1=8.9$ and $N_1=10.77$ but these are not impossible and can be explained through physical issues with the pressure management zone). The relationship between the calculated Leakage Exponent (N_1) and the Leakage Number (LN) was determined to be consistent with theoretical studies. The variation in N_1 values shows that leakage in water distribution systems is more sensitive to pressure than conventionally assumed. The importance of N_1 is demonstrated through the calculation of the percentage of the reduction in leaks. The obtained values for the latter ranged from 29% to 82%. At the network inlet, the data recorder, respectively, presents the average flow rate of each of the three sectors respectively 12.82 m³/h, 8.23 m³/h, and 5.51 m³/h. From the minimum night flow rate, the average night-day factor is calculated for each sector. Regarding the values obtained from the recorder, the N_1 values are satisfactory (according to determination factor R^2).

Acknowledgements

The authors very much appreciate the support by the university 8 May 1945 Guelma, Algeria and Ministry of Higher Education and Scientific Research.

References

- [1] Eldeeb H. and Zelenakova M. (2019). *Assessment of the economic value of irrigation water considering achieve main crops self-sufficiency: Case study Sharkia Governorate, Egypt*. SSP - JOURNAL OF CIVIL ENGINEERING Vol. 14, Issue 2, 2019
- [2] AWWA (American Water Works Association) (2014). *AWWA Free Water Audit Software, Version 5.0*. <http://www.awwa.org/home/awwa-news-details/articleid/2641/awwa-free-water-audit-software-version-5-0-now-available.aspx>.
- [3] Cherniuk V.V., Riabenko O.A., Ivaniv V.V. (2017) *Influence of transit water flow rate on its dispensation and on inflow through nozzles in pressure pipeline under action of external pressure*. SSP - JOURNAL OF CIVIL ENGINEERING Vol. 12, Issue 2, 2017
- [4] Ulanicki, B., Bounds, P., Rance, J.P. & Reynolds, L. (2000). *Open and closed loop pressure control for leakage reduction*. *Urban Water*, 2, 105-114.
- [5] Thornton J., and A. Lambert. (2006). *Memorandum: Update note for IWA Water Losses task Force Members, July 13th 2006*. IWA Water Loss Task Force.
- [6] Xylem Gould Water Technology (2016). *Aquavar e-ABII*. Xylem Inc., Rye Brook, New York, USA. [Online]. Available from: <http://goulds.com/pump-controllers/aquavar-abii-pump-controller-aqua-boostresidential/> [Accessed: 15/8/2020].
- [7] Hou Yukun, Yingying Wang, Yuexia Xu and Chunhui Zhao, (2011). *The Manager's Non-Revenue Water Handbook- A guide to understanding Water Losses*. Tongji University Press.
- [8] Wu, Z.Y., Farley, M., Turtle, D., Kapelan, Z., Boxall, J., Mounce, S.R., Dahasahasra, S., Mulay, M. & Kleiner, Y. (2011). *Water loss reduction*. 1st ed. USA: Bentley Institute Press: 1-68.
- [9] Araujo, L.S., Ramos, H., & Coelho, S.T. (2006). *Pressure control for leakage minimisation in water distribution systems management*. *Water Resources Management*, 20, 133-149.
- [10] Ryma Fares, (2010). « *Modélisation théorique et validation expérimentale de la réduction des fuites par la modulation de la pression* ». Mémoire de maîtrise en génie de la construction.
- [11] Liberatore and Sechi (2009). *LIBERATORE, Saverio et SECHI, Giovanni Maria. and calibration of valves in water distribution networks using a scatter-search meta-heuristic approach*. *Water resources management*, 2009, vol.23, no 8, p. 1479-1495.
- [12] McKenzie, R.S., (1999). *SANFLOW User Guide*. South Africa Water Research Commission, WRC Report TT 109/99, Pretoria, South Africa.
- [13] Liemberger R., Kingdom, W., Marin, P. (2007). *Performance based Non-Revenue Water Reduction Contracts, Water Loss 2007 Int. Conf.*, Vol. 3, pp. 655-664, Bucharest.
- [14] Marzola, I.; Alvisi, S.; Franchini, M. (2020). *Minimum Night Flow Analysis and Application of the Fixed and Variable Area Discharges Model for Characterizing Leakage in the Gorino Ferrarese (FE-Italy) District*. *Environ. Sci. Proc.* 2020, 2, 8.
- [15] AL-Washali, T., Sharma, S., AL-Nozaily, F., Haidera, M., & Kennedy, M. (2018). *Modelling the Leakage Rate and Reduction Using Minimum Night Flow Analysis in an Intermittent Supply System Water*, 11(1). <https://doi.org/10.3390/w11010048>
- [16] Morrison, J.; Tooms, S.; Rogers, D. (2007). *District Metered Areas, Guidance Notes; International Water Association (IWA), Specialist Group on Efficient Operation and Management of Urban Water Distribution Systems*: London, UK, 2007.
- [17] Fallis, P., Baader, J., Happich L., Sorg, F., Trujillo, R., Ziegler, D., (2011). *Guidelines for water loss reduction - A focus on pressure management*, Deutsche Gesellschaft Für Internationale Zusammenarbeit (GIZ).
- [18] Schwaller, J. & van Zyl, J. (2014). *Modeling the Pressure-Leakage Response of Water Distribution Systems Based on Individual Leak Behavior*. *Journal of Hydraulic Engineering*, 141(5).
- [19] Farely, M. & Trow, S. (2003). *Losses in Water Distribution Networks: A Practitioner's Guide to Assessment, Monitoring and Control*. IWA publishing.

Coconut Oil as Bio-based PCM: Characteristics and Compatibility with Plastics

Milan Ostrý¹, Sylva Bantová¹, Veronika Řezáčová^{2*}

¹ Brno University of Technology, Czech Republic
Faculty of Civil Engineering, Institute of Building structures
e-mail: ostrym@fce.vutbr.cz; bantova.s@fce.vutbr.cz

² Brno University of Technology, Czech Republic
Faculty of Chemistry, Institute of Chemistry and Technology of Environmental Protection
*e-mail: rezacova@fch.vut.cz

Abstract

The current use of buildings is facing an unprecedented increase in energy costs, especially in the European Union. The energy costs can be reduced by energy savings and by increased use of renewable energy represented mostly by energy converted from solar radiation. When solar energy is considered to be utilized in buildings, the mismatch between energy availability and energy demand must be solved by energy storage. This paper describes the principles of the use of latent heat thermal energy storage and the possibility of using bio-based phase change materials as heat storage media. Because the latent heat storage media undergo a change of phase during the charging and discharging, proper encapsulation is necessary. The paper presents the main findings of a study focused on the compatibility between coconut oil and selected plastics as materials of encapsulation. The compatibility of selected plastics and Coconut oil was evaluated by laboratory experiment based on the immersion of plastic samples in coconut oil and calculation of change in weight of samples within 17 weeks lasting test. The negligible weight changes were occurred for polycarbonate and polyethylene terephthalate which proves excellent compatibility with Coconut oil.

Keywords: latent heat storage, phase change material, coconut oil, plastics

1 Introduction

The reduction of non-renewable energy use for heating and cooling of buildings is an urgent priority, especially due to the turbulent prices of natural gas and electricity generated from fossil fuels and the global tendency to reduction of CO₂ emissions. Many building owners consider quick transformation from fossil fuels to renewable energy sources. In the residential sector, renewable energy is mostly represented by biomass, ambient or geothermal energy (with the use of a heat pump) or solar radiation (in a passive or active way). Passive utilization of solar radiation means that the solar radiation penetrating the building envelope is directly used for space heating and the rest of the energy is stored in exposed building structures for later radiant heating. The active way is mostly represented by the installation of photovoltaic systems on the

roof or walls enabling the conversion of solar radiation into electricity or solar thermal collectors integrated into domestic hot water technology systems. However, this active use of solar radiation assumes the possibility of energy storage from production peak hours for the later use. When the energy storage density is required to be higher than the sensible heat thermal energy storage (SHTES) capacity of water or heavy-weight building material than the latent heat thermal energy storage (LHTES) using a suitable storage medium should be taken into account.

The principle LHTES is energy absorption or energy release if the medium undergoes a change in its phase [1]. The significant advantages of LHTES over SHTES include absorption or release of thermal energy at a narrow temperature range and reduction of heat storage medium weight. Phase Change Materials (PCMs) are latent heat storage media which could be divided into organic PCMs (paraffins and non-paraffins – fatty acids, esters, and alcohols), inorganic PCMs (salt hydrates, metals, alloys) and eutectics (mixture of two or more components) [2]. Organic PCMs, especially paraffins are rather popular due to their chemical stability, durability and a low cost. On the other hand, the density of organic PCMs is lower compared to inorganic PCMs, thus heat storage density related to the volume of the storage medium is lower. Inorganic PCMs represented mainly by salt hydrates are characterized by high volumetric heat storage density, inconsistent melting, corrosive effects, and a tendency to subcooling.

Current PCM development is focused on the investigation of associated environmental impacts with the life cycle assessment methodology [3]. A relatively novel group of PCMs is bio-based PCMs. Bio-based PCMs are the results of investigations focused on renewable LHTES media. Bio-based PCMs could be mixtures manufactured from organic raw materials such as [4]:

- soya bean
- coconut oil
- palm oil
- pork lard
- beef tallow.

Because LHTES technology is often designed for renewable energy systems the bio-based PCMs represent an environmentally friendly, non-toxic and reusable alternative to artificial organic and inorganic PCMs available in nature in large quantities [5]. The combination of renewable energy and bio-based PCMs is therefore advantageous from the environmental point of view. For example, the temperature range of coconut oil is 20–25 °C which is suitable for use as a temperature regulator for indoor air integrated in building structures. On the other hand, energy release takes place in the temperature interval 16–18 °C and night cooling with intensive ventilation must be employed [5].

PCMs are often integrated into building materials. Building integrated PCMs (BIPCMs) prevent the indoor environment from overheating on hot and sunny days because melt during the daytime and solidify at nighttime when the space temperature reaches the solidification temperature. Thus, LHTES reduces the energy need for cooling. On the other hand, BIPCMs increase the possibility to store solar gains on cold but sunny days for later free spatial radiant heating.

Generally, PCMs must be encapsulated and hermetically sealed because the leakage of storage medium and undesirable integration with building materials and indoor environment must be avoided. Encapsulation means shelling the PCMs with suitable coating material [6]. The material of encapsulation ensures heat transfer, thermal and mechanical stability. Possible incompatibility of PCMs and the material of the capsule is crucial for the estimation of the

service life of LHTES systems. Metals and plastics are often used as materials for encapsulation. The application of metals for PCM encapsulation is attractive because of their high thermal conductivity. Plastics are cheaper compared to metals, but their thermal conductivity is much lower. This leads to the design of very thin capsule walls.

The motivation behind this study is to identify the most suitable combination of bio-based PCM (coconut oil) and low-cost plastic encapsulation with minimal undesirable interactions.

2 Materials and Methods

The aim of this study was to investigate the compatibility of selected plastics and coconut oil, which represents bio-based PCMs. The idea of its application in the Central European climate is to replace heavy-weight structures with light-weight structures with enhanced heat storage capacity by integrated bio-based PCMs.

The experiment is based on the gravimetric analysis which is generally recommended for the evaluation of the most suitable combination of PCMs and material for encapsulation [6].

Four types of plastics were selected for the test of their compatibility with bio-based PCM Coconut oil:

- polycarbonate (PC),
- polypropylene (PP),
- polyethylene (PE 500),
- natural polyethylene terephthalate (natural PET).

The reasons for the selection were wide availability on the global market, low costs, and existing applications in the building industry. The selection was based on earlier studies related to the compatibility of organic PCMs as LHTES media and materials for encapsulation [7, 8]. Typical characteristics of selected plastics are presented in Table 1.

Table 1: Characteristics of plastic samples

Material	Thermal conductivity [W·m ⁻¹ ·K ⁻¹]	Density [g·cm ⁻³]	Melting point [°C]	Long-term service temperature [°C]	Yield point [MPa]
	Test method				
	DIN 52612	DIN EN ISO 1183-1	ISO 11357	-	DIN EN ISO 527
PC	0.21	1.20	-	- 40 to 115	65
PP-H	0.22	0.92	166	0 to 100	33
PE 500	0.40	0.96	135	- 100 to 80	27
PET natural	0.28	1.38	255	- 20 to 115	85

Bio Coconut oil Purity Vision® was selected from the group of bio-based PCMs. It is 100% coconut oil (*Cocos nucifera*) and it is imported from the Philippines. Coconut oil was subjected to characterization using Differential Scanning Calorimeter DSC 2500 (TA Instruments) with an applied heating rate of 10 °C/min (temperature range -5 °C to 35 °C) and cooling rate 5 °C/min (temperature range 35 °C to -5 °C).

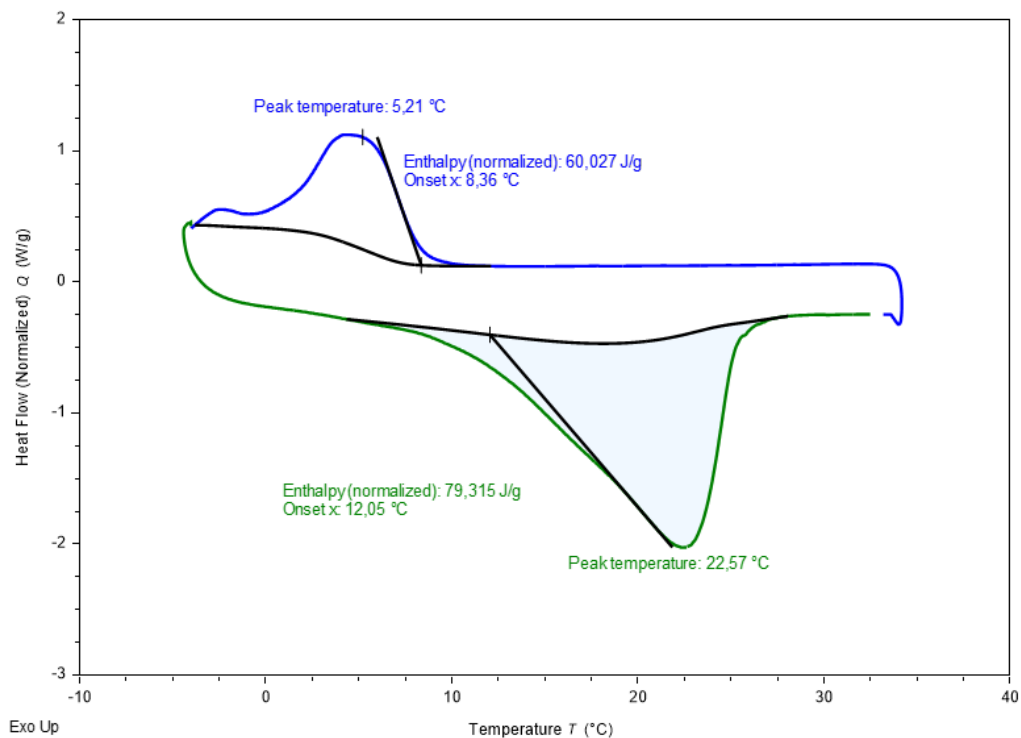


Figure 1: DSC record for Coconut oil

DSC curves are plotted in Figure 1 and important characteristics are shown in Table 2. Other important characteristics listed in the literature are the mean specific heat of the solid is $3.2 \text{ kJ}\cdot\text{kg}^{-1}\cdot\text{K}^{-1}$ and the mean of specific heat of liquid is $4.1 \text{ kJ}\cdot\text{kg}^{-1}\cdot\text{K}^{-1}$ [9]. Because the solid-liquid phase change of coconut oil is in the range of thermal comfort the potential use of coconut oil for temperature control was investigated in the past [5, 10]. The most important effect of coconut oil is the ability to control daytime indoor air temperatures [10]. The typical undesirable characteristic of coconut oil is low thermal conductivity which negatively influences heat transfer between the heat storage medium and the surrounding environment.

Table 2: Characteristics of Coconut oil

		Heating	Cooling
Peak temperature	[°C]	22.57	5.21
Onset temperature	[°C]	12.05	8.36
Enthalpy	[J·g ⁻¹]	79.32	60.03

The importance of this study arises from the consequences of possible negative interactions between coconut oil and proposed plastics as encapsulation material. In case of incompatibility of PCMs and plastics, there is a risk of change in properties of the container wall which should lead to loss of mechanical strength and leakage of PCMs.

The presented study consists of two phases. The test procedure (the first phase) is based on the test methodology of The American Society for Testing and Materials G1-03 [11] and a description of each part is shown in Figure 2.

The Evaluation procedure (the second phase) is adopted from ISO 175:2010 [12]. It is based on the monitoring of mass changes with the calculation of an evaluation parameter for each sample. The percentage change in mass was calculated for each plastic sample using Equation (1):

$$\Delta m = \frac{(m_t - m_{t_0})}{m_{t_0}} \cdot 100 \quad (1)$$

where Δm is the percentage change in mass [%], m_t is the weight of the sample after removal from PCM [mg] and m_{t_0} is the initial weight of the sample before immersion in PCM [mg].

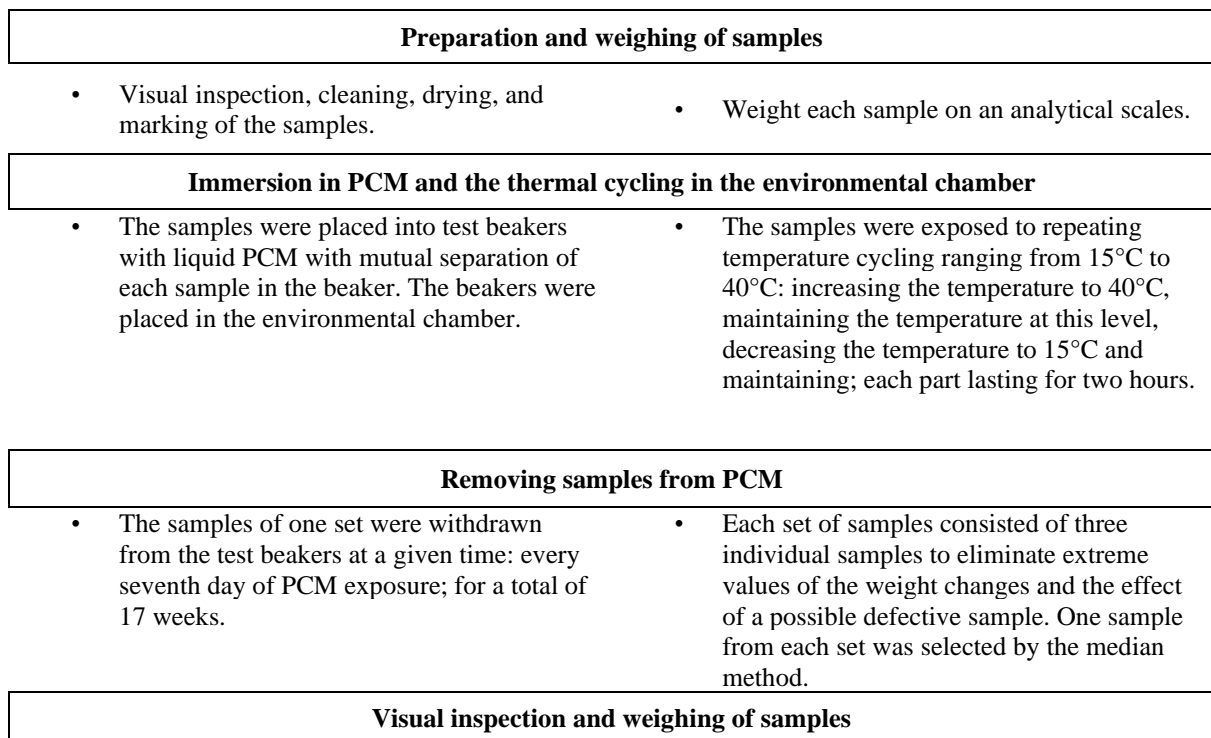


Figure 2: Test procedure

Figure 3 shows that the design of the test ensures the complete immersion of the plastic samples in coconut oil in a vertical position with almost the same distance due to their anchoring in special foam.



Figure 3: Plastic samples in the test beakers: (a) Samples before immersion in coconut oil and thermal cycling; (b) Samples immersed in coconut oil placed in a small environmental chamber

3 Results and Discussion

The mutual compatibility of selected plastics and bio-based PCM Coconut oil was verified by a long-term experiment. Plastic samples were immersed in liquid PCM with mutual separation of each sample in the test beaker and gradually withdrawn at the given periods. During the immersion in PCM, the samples were exposed to given temperature cycles for 17 weeks. After each plastic sample was withdrawn from the liquid PCM, the sample was cleaned, washed, if necessary, visually inspected and weighed.

The evaluation procedure included not only a visual inspection of all samples but also monitoring of the mass changes of tested plastic samples before and after removal from the PCM. From a visual point of view, the samples were monitored for any surface and shape changes. The result is that no visual changes occurred on the surface of the plastic samples during testing. The values of percentage change in mass were calculated according to equation (1) from the mass change of each sample before and after exposure to PCM, the values of Δm in % for the immersion period are shown in Table 3.

Table 3: Percentage changes in mass Δm [%] of plastic test samples exposed to coconut oil

Selected immersion period [days]	Mass changes of tested materials Δm [%]			
	PC	PP-H	PE 500	PET natural
7	0.0000	0.0099	0.1369	0.0000
28	0.0000	0.0253	0.2000	0.0000
49	0.0000	0.0000	0.3816	0.0000
70	0.0000	0.0952	0.3705	0.0000
91	0.0000	0.1110	0.7508	0.0000
112	0.0000	0.3275	0.7658	0.0000

The time dependence of the percentage change in mass of plastic samples immersed in Coconut oil is shown in Figure 3. Generally, the weight changes of plastic samples are relatively low depending on the length of the immersion time in PCM. The low mass variation means low infiltration of the coconut oil into the plastic. This confirms the compatibility of these materials for the encapsulation of the PCM. The curves of Δm values and trend lines demonstrate a low

initial penetration of coconut oil into PE 500 and PP-H and a subsequent slow increase over time. Contrary to this behavior, the PC and PET natural samples showed negligible weight changes. This indicates the excellent compatibility of these two plastics with coconut oil. A significant mass increase occurred in the case of PE 500 samples; the highest values were achieved for samples with longer immersion time in PCM. In this case, Δm exceeded 0.84% (for 15th weeks) with a mass increase of 18.4 mg.

Maximum mass changes calculated for the experiment presented in Table 3 and Figure 4 proved that all tested plastics are suitable for the encapsulation of coconut oil because the maximum values are below 1%.

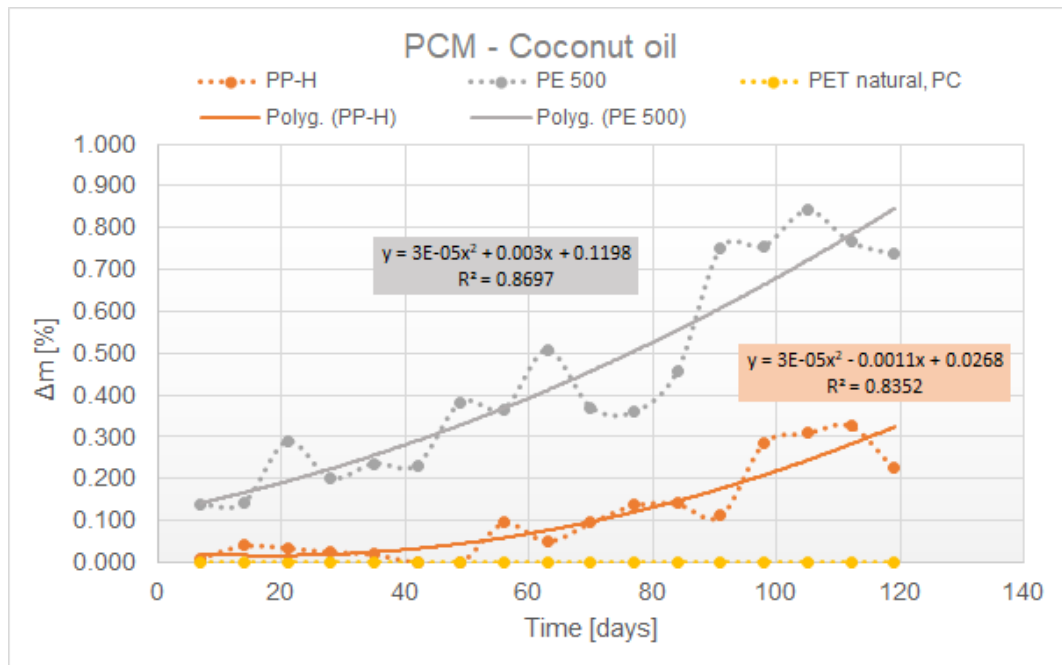


Figure 4: Comparison of the dependence of Δm value [%] of selected plastics immersed in bio-based PCM Coconut oil (the yellow curve shows the Δm values for both PC and PET natural materials, the Δm values are almost zero)

4 Conclusion

The compatibility of selected plastics and bio-based PCM Coconut oil was evaluated by laboratory experiments. The experiment proved the excellent compatibility of PC and PET natural samples with Coconut oil. Unfortunately, the results are not directly comparable with studies presented in the past because in the literature there are no experimental studies of Coconut oil migration in plastics and effects on plastics' properties. The future work will be focused on the determination of changes in the mechanical properties of selected plastics immersed in Coconut oil before and after test periods.

Acknowledgments

This research was funded by Czech Science Foundation, grant number 19-20943S "Compatibility of plastics and metals with latent heat storage media for integration in buildings".

References

- [1] Sarbu, I., Sebarchievici, C. (2018). A comprehensive Review of Thermal Energy Storage. *Sustainability*. 10 (191), 1-32. <https://doi.org/10.3390/su10010191>.
- [2] Tyagi, V.V., Buddhi, D. (2007). PCM thermal storage in buildings: A state of art. *Renewable and Sustainable Energy Reviews*. 11, 1146-1166. <https://doi.org/10.1016/j.rser.2005.10.002>.
- [3] Fabiani, C., Pisello, A.L., Barbanera, M., Cabeza, L.F. (2020). Palm oil-based bio-PCM for energy efficient building applications: Multipurpose thermal investigation and life cycle assessment. *Journal of Energy Storage*. 28, 101129. <https://doi.org/10.1016/j.est.2019.101129>
- [4] Saleel, A.C. (2022). A review on the use of coconut oil as an organic phase change material with its melting process, heat transfer, and energy storage characteristics. *Journal of Thermal Analysis and Calorimetry*. 147, 4451-4472. <https://doi.org/10.1007/s10973-021-10839-7>
- [5] Khan, Z., Khan, Z., Ghafoor, A. (2016). A review of performance enhancement of PCM based latent heat storage system within the context of materials, thermal stability and compatibility. *Energy Conversion and Management*. 115, 132-158. <https://doi.org/10.1016/j.enconman.2016.02.045>
- [6] Ostrý, M., Bantová, S., Struhala, K. (2019). Tests on Material Compatibility of Phase Change Materials and Selected Plastics. *Molecules*. 24 (7), 1398. <https://doi.org/10.3390/molecules24071398>
- [7] Lázaro, A., Zalba, B., Bobi, M., Castellón, C., Cabeza, L.F. (2005). Experimental study on phase change materials and plastics compatibility. *Environmental and Energy Engineering*. 52 (5), 804-808. <https://doi.org/10.1002/aic.10643>
- [8] Castellón, C., Martorell, I., Cabeza, L.F., Fernández, A.I., Manich, A.M. (2011). Compatibility of plastic with phase change materials (PCM). *International Journal of Energy Research*. 35, 765-771. <https://doi.org/10.1002/er.1723>
- [9] Putri, W.A., Fahmi, Z., Sutjahja, I.M., Kurnia, D., Wonorahardjo, S. (2016). Thermophysical parameters of coconut oil and its potential application as the thermal energy storage system in Indonesia. *Journal of Physics: Conference Series*. 739, 012065. doi:10.1088/1742-6596/739/1/012065
- [10] Wonorahardjo, S., Sutjahja, I.M., Kurnia, D., Fahmi, Z., Putri, W.A. (2018). Potential of Thermal Energy Storage Using Coconut Oil for Air Temperature Control. *Buildings*. 8, 95. <https://doi.org/10.3390/buildings8080095>
- [11] ASTM G1 - 03 Standard Practice for Preparing, Cleaning, and Evaluating Corrosion Test Specimens. Available online: <http://materialstandard.com/astm-g/> (accessed on September 10th, 2021)
- [12] ISO 175 (2010) Plastics - Methods of test for the determination of the effect of immersion in liquid chemicals

Durability of Different UHPFRCs, Made from Pozzolan as a Substitute for Portland Cement and Immersed in Two Aggressive Environments of Hydrochloric and Sulfuric Acids

Farida Ait Medjber^{1, 2*}, Mohammed Saidi², Brahim Safi²

¹Mouloud Mammeri University, Laboratory LEMM, Algeria.

²M'Hamed Bougara University, Faculty of Technology, Process Engineering Department, Research unit: Materials, Processes and Environment, Algeria.

*e-mail: farida.pcmc@gmail.com

Abstract

The objective of this study is to evaluate the effect of pozzolan on the durability of high-performance fiber concretes in two aggressive environments. For this, prismatic test pieces were made at (0%, 10%, 20%, and 40%) of pozzolan and immersed in two acids, hydrochloric and sulfuric. Then characterizations were carried out, such as the loss of mass, the depth of degradation and the mechanical resistance. The results obtained show that with the substitution rate of pozzolan, the loss of mass and the depth of degradation increase in the two acids, while the mechanical strength increases in hydrochloric acid and decreases in sulfuric acid.

Keywords: pozzolan, durability, chemical attack, loss of mass, hydrochloric acid and sulfuric acid

1 Introduction

For several decades, the concrete industry has developed the use of artificial and natural pozzolans in hydraulic concretes to increase their mechanical performance and durability properties [1]. This durability also guarantees considerable savings in the long term because such works will require little or no repairs, hence saving costs induced by repairs, which can be very high and can even exceed the initial construction costs [2].

Recent research has shown that the introduction of ultra-fine additives in the manufacture of UHPFCs is doubly beneficial from the point of view of resistance to chemical attacks and the economy [3].

Natural pozzolans have a positive influence on the durability of mortars against sulphate attacks. It is generally accepted that pozzolans require less grinding energy and that the use of pozzolanic materials in cement or concrete results in many beneficial properties, such as low heat of hydration, strength compression, low permeability, high sulphate resistance and low alkali-silica activity. The use of Portland cement with natural pozzolana generates a reaction

between the calcium hydroxide, produced by the hydration of Portland cement and the amorphous SiO₂ of the vitreous phase of the pozzolana [4].

Sulfuric acid (H₂SO₄), as well as hydrochloric acid (HCl), are classified as the most aggressive natural threats. When concrete is exposed to an environment containing sulfuric acid, it undergoes strong degradation due to neutralization reactions [5].

2 Materials and Experimental Methods

2.1 Used Materials

Cement: The cement used is a CPA (95% clinker+5% gypsum), prepared in the laboratory, with a density of 3.25 g/cm³ and a specific surface of 4004 cm²/g.

Pozzolan: In this study, finely ground pozzolan up to 3703 cm²/g was introduced as a substitute in the cement to manufacture the different UHPFC compositions. The physical, chemical, and mineralogical characteristics according to standard NF EN 197-1 [6] are given in Table 1.

Table 1: Characteristics of cementitious materials

Minerals %	Clinker	Gypsum	Pozzolana (PZ)
SiO ₂	21.79	12.44	41.00
Al ₂ O ₃	4.77	3.58	14.58
Fe ₂ O ₃	2.93	1.27	10.83
CaO	64.50	29.30	11.08
MgO	-	4.02	4.22
SO ₃	-	30.03	-
K ₂ O	-	-	-
Na ₂ O	-	-	-
P ₂ O ₅	-	-	-
TiO ₂	-	-	-
L. O. F	0.50	19.30	12.80
LSF	94.09	-	-
MS	2.83	-	-
MA	1.63	-	-
C ₃ S	55.65	-	-
C ₂ S	20.53	-	-
C ₃ A	7.68	-	-
C ₄ AF	8.91	-	-
P/Liter	1286	-	-
CaO free	1.24	-	-

Dune Sand: In this work, finely ground dune sand with a fineness of 2652 cm²/g was used as added fines in the formulation of concretes. The results of its chemical analysis by fluorescence are shown in Table 2.

Table 2: Fluorescent chemical analysis of dune sand

Elements (%)	Dune Sand (DS)
SiO ₂	94.40
Al ₂ O ₃	2.23

Fe ₂ O ₃	0.33
CaO	0.45
MgO	0.06
SO ₃	0.17
K ₂ O	1.13
Na ₂ O	0.36
P ₂ O ₅	0.01
TiO ₂	0.04
loss of fire	0.82

Fine sand: For the sand, washed sand from the Baghlia region was chosen, sifted through a 2 mm sieve, with an equivalent of 75%, and an expansion of 11%.

Adjuvant: In order to reduce the W/L ratio and increase the fluidity of the concretes for ease of implementation, a high water-reducing superplasticizer of the Tempo 12 type from Sika and compliant with standard EN 934-2 [7] was used.

Polypropylene fibers: The synthetic fibers marketed by Sika have been added to have better concrete resistance. Their characteristics are given in Table 3.

Table 3: Characteristics of polypropylene fibers

Properties	Polypropylene fibers
Fiber length (mm)	12
Density (g/cm ³)	0.90
Fusion point (°C)	150
Young's modulus (kN/m ³)	3
Elongation at break (mm)	50
Fiber section (microns)	30
Color	White

2.2 Methodology of Work

This study was carried out in two parts. In the first part, UHPFC specimens were made at 0%, 10%, 20% and 40% of pozzolan, as a substitution in the cement, and mechanical tests were carried out. In the second part, the specimens made in the previous part were followed for the study of the durability in immersion in two acidic media (HCl and H₂SO₄) for up to 28 days.

2.3 Test Methods

Mechanical tests: The specimens were made according to standard NF EN 196-1[8], cast in prismatic molds (4x4x16 cm) then unmolded after 24 hours and kept in a water bath until the days of mechanical crush. The compressive and flexural strengths of the specimens were tested at 7, 14 and 28 days using an "IBERTEST" type device with a capacity of 200 kN and controlled by computer. Three-point bending tests were performed on prismatic samples according to ASTM C348 [9]. The half-samples were subjected to compressive stress, in accordance with the ASTM C349 standard [10].

3 Results and Discussion

3.1 Effect of Pozzolan on the Mechanical Performance of UHPFC

Ultra-high-performance fiber-reinforced concretes at different percentages of pozzolan have been developed. The various concrete compositions studied are illustrated in Table 4. Then, the mechanical strengths were measured at 7, 14 and 28 days and the results obtained are illustrated in Table 5 and shown in Figure 1.

Table 4: The different UHPFC compositions in 1m³

Constituents	UHPFC00	UHPFC10	UHPFC20	UHPFC40
Cement [kg]	1000	900	800	600
Pozzolana %	0	10	20	40
Dune Sand [kg]	222.6	222.6	222.6	222.6
Fine sand [kg]	1029.9	1029.9	1029.9	1029.9
Adjuvant [kg]	25	25	25	25
Polypropylene fibers [kg]	2.6	2.6	2.6	2.6
Total water [kg]	280	280	280	280
W/L	0.229	0.229	0.229	0.229

Table 5: Mechanical resistance of UHPFC with age (days)

	Bending strengths (MPa)			Compressive Resistances (MPa)		
	07D	14D	28D	07D	14D	28D
UHPFC00	7.12	8.44	9.81	77.14	89.05	99.02
UHPFC10	7.46	8.91	10.54	75.52	90.33	103.23
UHPFC20	6.97	8.33	10.08	69.94	86.39	92.35
UHPFC40	5.52	6.88	8.36	67.26	86.24	89.01

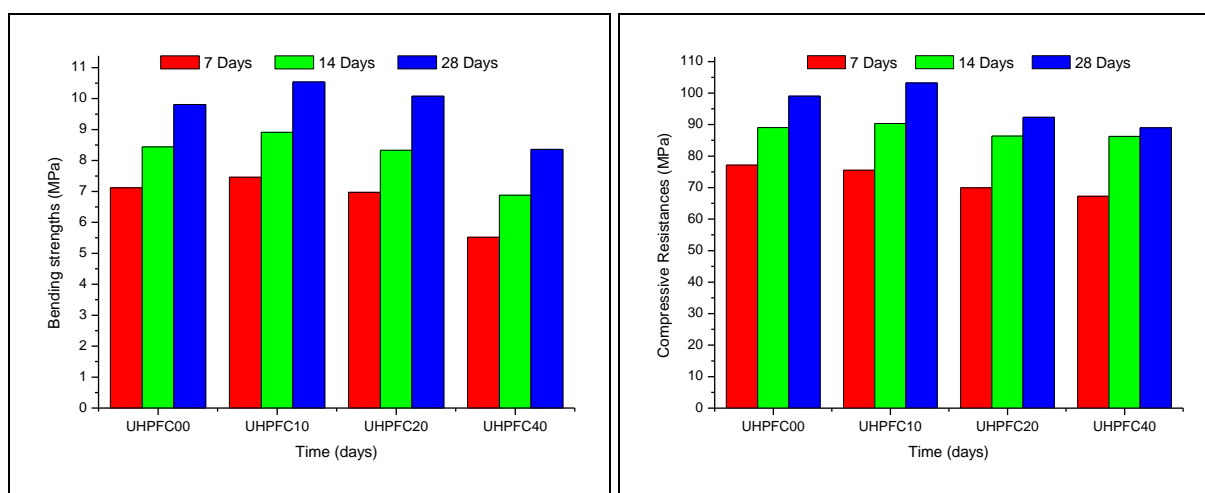


Figure 1: Evolution of the mechanical resistance of UHPFCs with age

According to Figure 1, the substitution of 10% of the cement by the pozzolan has a beneficial effect on the mechanical performance and displays a clear improvement in the mechanical resistances compared to the control concrete (UHPFC00). This is explained by the fact that the

introduction of pozzolana acts on the hydration reactions by pozzolanic reactions of well-dispersed cement grains with portlandite ($(Ca(OH)_2)$), thus modifying their speed of growth and morphology [11-15].

3.2 Durability of UHPFC Specimens

All these compositions were reformulated according to the same procedure followed in the previous part and were stored in a water bath at 20 ± 2 °C. After maturation, the specimens were removed from the water bath, dried in the air and then in an oven at 105 °C for 24 hours until constant masses. Two solutions of hydrochloric acid (HCl, pH = 1.34) and sulfuric acid (H_2SO_4 , pH = 1.6) were prepared. Then, three specimens of each variant were immersed in each solution. The chemical attack was monitored for 28 days, and the solutions were renewed each week at the same pH.

3.2.1 Loss of Mass

The chemical resistance was evaluated according to the ASTM C267 standard [17] by measuring the loss of mass of the specimens, calculated by the following formula:

$$\text{Mass Variation (\%)} = \left[\frac{M_1 - M_2}{M_1} \right] * 100 \quad (1)$$

With: M_1 : dry mass of the specimens before immersion.

M_2 : dry mass of the specimens after immersion.

The results obtained are shown in Figure 2.

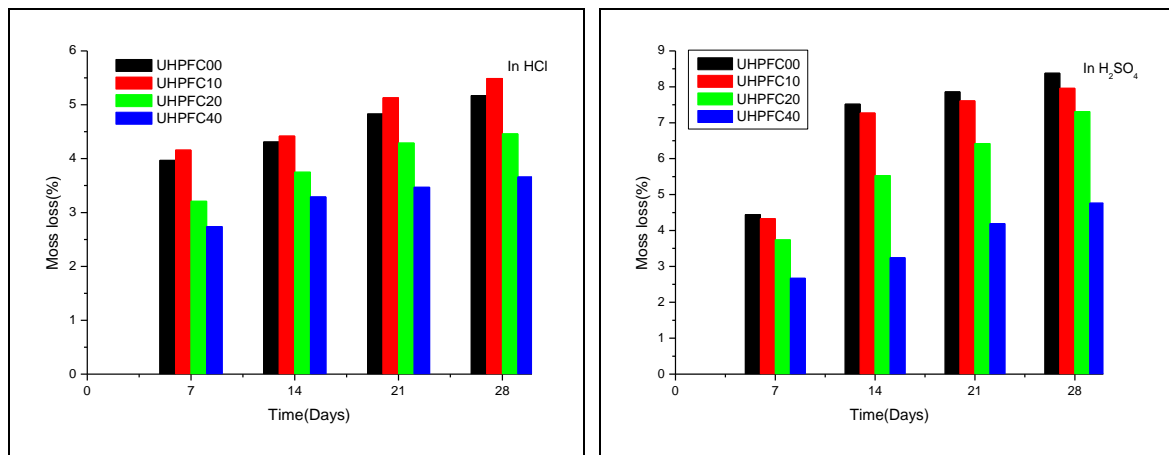


Figure 2: Mass loss as a function of the immersion time of the specimens in the two acids

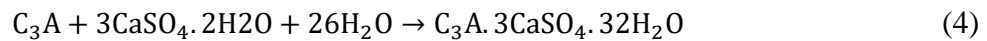
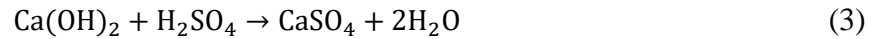
Figure 2 shows that the mass losses of the different UHPFRCs increase in both acids with immersion time and decrease with increasing pozzolan content from 10 to 40% in hydrochloric acid and from 0 to 40% in sulfuric acid.

A considerable part of free calcium hydroxide ($Ca(OH)_2$), released after hydration of the cement, will be leached out when subjected to attack by hydrochloric acid (HCl) giving the calcium hydroxide, according to the following chemical reaction [5]:



Calcium chloride (CaCl_2), obtained after the reaction of hydrochloric acid with cement lime, is a very soluble salt and very aggressive towards Portland cement [17, 18].

The reaction of sulfuric acid with the lime of the cement leads to the formation of expansive salts of secondary gypsum and secondary ettringite according to these two reactions:



3.2.2 Degradation Depth Measurements

Determination of the depth of degradation was carried out by measuring the difference between the thickness of the colored zone (which indicates the non-degraded basic part) and the initial thickness of the specimen. The staining test was carried out using phenolphthalein as shown in Figure 3 and the results obtained are shown in Figure 4.

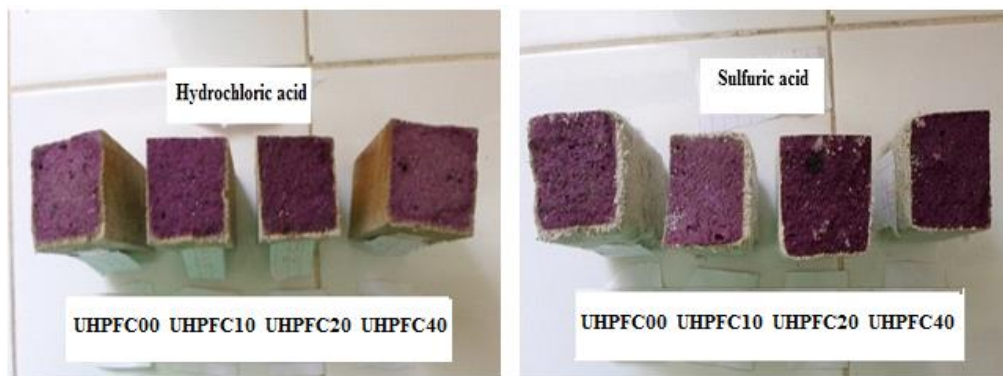


Figure 3: Staining of specimens attacked by the two acids HCl and H_2SO_4

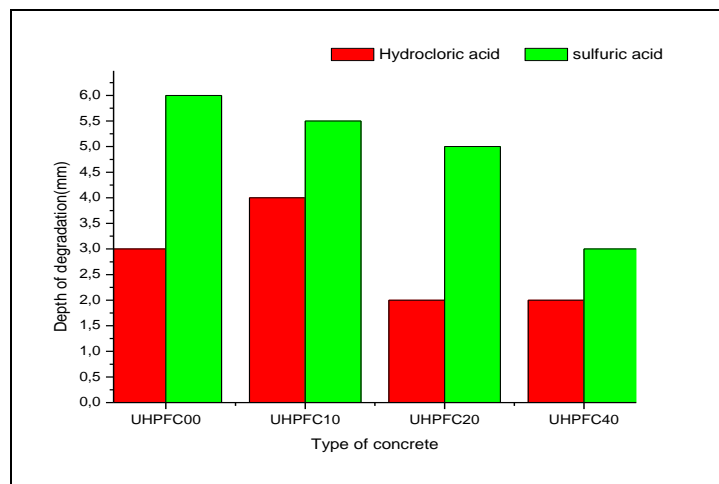


Figure 4: Depth of samples degradation in the two aggressive environments

Figure 4 shows that the degradation thickness of specimens immersed in sulfuric acid is greater than that of specimens immersed in hydrochloric acid while the lowest degradation thicknesses in the two acids are attributed to specimens made with 40% of pozzolan.

3.2.3 Mechanical Performance

Knowing that the degradation of concretes and mortars has a negative influence on the mechanical behavior of the latter, compression tests were carried out and the evaluation of the degrees of degradation of the specimens of different variants of UHPFC was carried out according to the following formula:

$$\text{Resistance difference (\%)} = \left[\frac{R_d - R_{28}}{R_{28}} \right] * 100 \quad (5)$$

With: R_{28} : The resistance of the specimens at 28 days

R_d : The resistance of the specimens after degradation

The results obtained are illustrated in Figure 5.

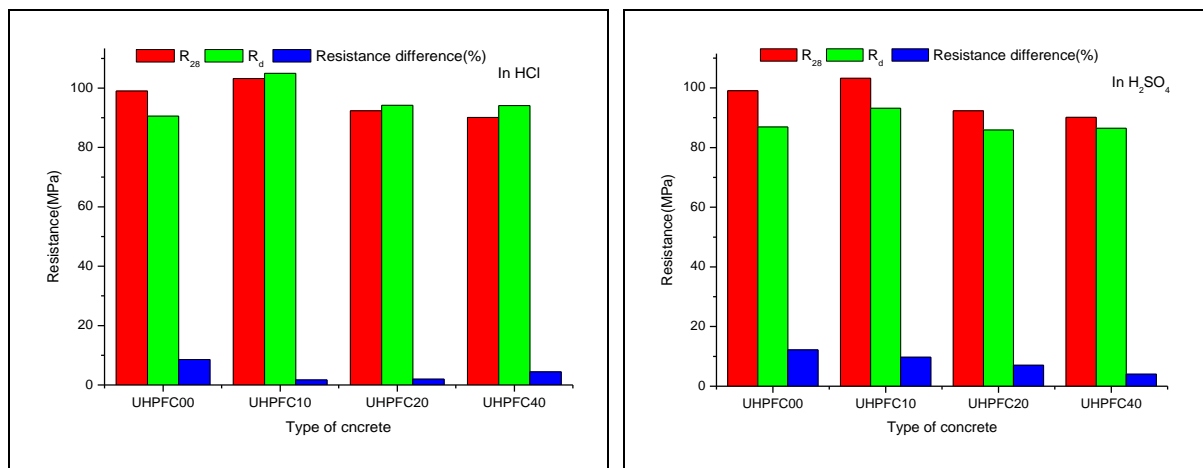


Figure 5: Degree of degradation of specimens of different UHPFC

From the mechanical resistances of the specimens immersed in the two aggressive environments we found:

- An increase in the mechanical resistance against attack by hydrochloric acid of all the variants except the control specimens (UHPFC00). This increase is directly proportional to the pozzolan substitution rate. This can be explained by the long-term pozzolanic activity [19].
- A decrease in the mechanical resistance of the different variants following the attack by sulfuric acid.
- After degradation, the best mechanical resistances in the two acids are attributed to the composition named UHPFC10.

4 Conclusion

This study informs us about the possibility of manufacturing a high-performance fiber-reinforced concrete based on Portland cement substituted by the natural pozzolan. The latter presents very important interests from the point of view of mechanical resistance, economy, ecology, and durability. The experimental results obtained through this study lead to the following conclusions:

- The mechanical resistances of UHPCs made from Portland cement substituted with 10% pozzolana are better. This means that the pozzolana substitution rate must be optimized to react with the portlandite and form a hydrated calcium silicate (C-S-H);
- The mass loss results showed that sulfuric acid is more aggressive than hydrochloric acid, however, the best chemical resistance is given by the specimens prepared with 40% pozzolan;
- The degradation thickness of specimens immersed in sulfuric acid is greater than that of specimens immersed in hydrochloric acid.
- The mechanical strengths after degradation show a decrease in sulfuric acid and an increase in hydrochloric acid.

What makes and according to these results, we deduce that the optimized substitution of cement by pozzolan in UHPCs is beneficial from the point of view of the economy, resistance and durability and that sulfuric acid is more aggressive than hydrochloric acid.

References

- [1] Rakotoelson, T. H. & Ramaroson, M. (2017). Composite based on pouzzolane and wood sawdust. *American Journal of Innovative Research and Applied Sciences*. 5 (6), 454-461.
- [2] Neville, AM. (2000). Propriétés des bétons. Paris: Edition Eyrolles.
- [3] Ait Medjber, F. & Saidi, M. (2021). Durabilité des bétons fibrés à ultra hautes performances élaborés à base de matières premières locales, dans deux milieux agressifs d'acide chlorhydrique et de sulfates de barium. *Romanian Journal of Civil Engineering*. 12(1), 33-44.
- [4] Laoufi, L., Senhadji, Y., Benazzouk, A., Langlet, T., Mouli, M. & Laoufi, I. (2016). Durability of Natural Pozzolan-based mortar exposed to sulfate attack. *Journal of Fundamental and Applied Sciences*. 8(2), 268-279.
- [5] Laoufi, L., Senhadji, Y., Benazzouk, A., Langlet, T., Mouli, M., Laoufi, I., & Benosman, A. S. (2016). Assessment of pozzolanic mortars sustainability exposed to chemical attack. *Journal of Materials and Environmental Science*. 7 (5), 1835-1845.
- [6] NF EN 197-1. (2012). Ciment - Partie 1 : composition, spécifications et critères de conformité des ciments courants.
- [7] NF EN 934-2-A2. (2006). Adjuvants pour béton, mortier et coulis-Partie 2: Adjuvants pour béton - Définitions, exigences, conformité, marquage et étiquetage.
- [8] NF EN 196-1. (2016). Méthodes d'essais des ciments-Partie1: Détermination des résistances.
- [9] ASTM C348-08. (2008). Standard Test Method for Flexural Strength of Hydraulic-Cement Mortars.
- [10] ASTM C349. (2018). Standard Test Method for Compressive Strength of Hydraulic-Cement Mortars (Using Portions of Prisms Broken in Flexure).

- [11] Zeghad, M., Mitterpach, J., Safi, B., Amrane, B. & Saidi, M. (2017). Reuse of refractory brick wastes (RBW) as a Supplementary cementitious material in a concrete. *Periodica Polytechnica Civil Engineering*. 61(1), 81-87.
- [12] Yu, R., Tang, P., Spiesz, P., & Brouwers, H. J.H. (2014). A study of multiple effects of nano-silica and hybrid fibres on the properties of Ultra-High Performance Fibre Reinforced Concrete (UHPC) incorporating waste bottom ash (WBA). *Construction and Building Materials*. 60, 98-110.
- [13] Arel, H. S. (2016). Effects of curing type, silica fume fineness, and fiber length on the mechanical properties and impact resistance of UHPC. *Results in Physics*. 6, 664-674.
- [14] Yi, N. H., Kim, J. H. J., Han, T.S., Cho, Y.G. & Lee, J.H. (2012). Blast-resistant characteristics of ultrahigh strength concrete and reactive powder concrete. *Construction and Building Materials*. 28 (1), 694-707.
- [15] Richard, P. (1996). *Reactive Powder Concrete: A New-Ultra High Strength Cementitious Material*. Proceedings of the Fourth International Symposium on the Utilization of High-Strength/High- Performance Concrete, 29-31 May (1343-1350). Paris: Edition de Larrard, F. & Lacroix, R.
- [16] ASTM C267-01. (2012). Standard Test Methods for Chemical Resistance of Mortars, Grouts, and Monolithic Surfacing and Polymer Concretes.
- [17] Zivica, V., Bajza, A. (2001). Acidic attack of cement based materials- a review. Part1: Principle of acidic attack. *Construction and Building Materials*. 15(8), 331-340.
- [18] Zivica, V., Bajza, A. (2002). Acidic attack of cement based materials- a review. Part2: Factors of rate of acidic attack and protective measures. *Construction and Building Materials*. 16(4), 215-222.
- [19] Gabrysiak, F., (2013). *Les Bétons*. Matériaux (1-28).

Assessing Photopic and Melanopic Daylighting Performance of Special Glazing System: A Full-scale Experiments

Jozef Hraška^{1*}, Peter Hartman¹

¹Slovak University of Technology in Bratislava, Slovakia
Faculty of Civil Engineering, Department of Building Construction
*e-mail: jozef.hraska@stuba.sk

Abstract

Comparative research on the influence of daylight and visual environment on melatonin oscillations and the performance of space users was realized in two identical rooms with different glazing at the Faculty of Civil Engineering of the Slovak Technical University in Bratislava. The glazing in the windows had significantly different transmittances of melanopic light. This article presents measured changes in the intensity of photopic and melanopic daylighting values inside the rooms on horizontal and differently oriented vertical plane. Photopic and melanopic illuminances were measured under cloudy and partly clear skies during several months in 2021 and 2022. The article is also partially devoted to the effect of light from a computer monitor on the spectral composition of light on the eye of a person working with a computer. The article also analyzes the problems associated with the evaluation of non-visual aspects of daylighting of the interior spaces of buildings.

Keywords: daylighting, melanopic light, glazing, illuminance, health

1 Introduction

When designing the daylighting of buildings, attention is primarily paid to the amount of photopic light in the interiors, which depends mainly on the photopic transmittance of the glazing and the size of the glazing. If we work with spectrally neutral glazing and spectrally neutral internal and external surfaces, the above approach is understandable. Currently, there are many glazing and shading devices on the construction market, which significantly change the spectral composition of daylight [1]. This may have an impact on the non-visual effects of light, which are strongly associated with the light regulation of the circadian biological clock [2–4]. Non-visual photoreception is essentially associated with the intrinsically photosensitive retinal ganglion cells that contain the photoreceptor melanopsin. In [5], the sensitivity of melanopsin to light was standardized, and the terms "melanopic illuminance" or "melanopic light" are gradually becoming established in the literature. According to [6] "...our data demonstrate the widespread utility of melanopic illuminance as a metric for predicting the circadian impact of environmental illumination". If there is little light in the indoor environment of buildings and it has an inappropriate spectral composition, hormonal processes in the human

body (e.g., melatonin, cortisol, serotonin) are disrupted, which affects both physiological and mental health. Health disorders are manifested in changes in the temperature of the human body, fatigue, depression, problems with natural sleep cycles, heart disease, obesity and even some types of cancer [7–8].

Prevention of the mentioned problems is enough intense and dynamic daylight that enters the eyes. In localities where cloudy skies dominate, it is important to ensure enough daylight in the interior of buildings, especially when the sky is overcast. Non-visual effects depend on the intensity, duration, timing, spectral composition, directionality and history of light entering a person's eyes. Circadian light is usually quantified in practice by the levels of melanopic illuminance on vertical planes, usually at a height of 1.2 m above the floor of the room, which represents the height level of the eyes of a seated person. The evaluation of vertical illuminance within climate-based daylight modeling, which uses annual daylight performance metrics, represents a radical change in the way of evaluating the indoor light environment. Various computer simulations of the illumination of the eyes of the building's users are rarely verified by measurements [8–10]. The high dynamic of natural light, variations in brightness and spectrum of the internal light environment, movement of users in space and changes in view directions basically do not even allow verification of annual simulation calculations.

This article presents part of the measured data on the photopic and melanopic light conditions in two identical and adjacent rooms, in which research was conducted in the winter months of 2021 and 2022 on the influence of different daylight on the oscillations of melatonin in the bodies of the experiment participants and also on their work performance and sleep quality. From the point of view of the goals of the experiment, very different optical properties of the glazing in the rooms were chosen. Here we present some measured data on the lighting environment in rooms only in relatively stable conditions of the outdoor daylight climate. In this study, we also marginally address the issue of circadian (melanopic) illuminance metrics.

2 Methodology

In this paper, the authors realized a full-scale experimental study to investigate horizontal and vertical daylight illuminance in two rooms with identical geometries and different glazing in conditions of cloudy and partly clear skies in Bratislava. In overcast sky conditions, horizontal and vertical illuminance was measured in several places in a room with glazing that significantly reduces the transmittance of the blue component of light (tested room). Horizontal illuminance was measured at a height of 0.85 m above the floor and vertical illuminance at a height of 1.2 m. The lighting of the occupant's eyes while working on a laptop at several computer workstations in the room was also measured. In the conditions of mostly clear days, the daily photopic light was continuously measured on the outer surface of the window and in the middle of the depth of both rooms and their longitudinal axis. The sensor measuring photopic and melanopic light was at a height of 1.2 m above the floor and was oriented perpendicular to the window. Illumination was taken at intervals of several tens of seconds.

At the time of measurements, the sun did not shine directly into the rooms. Blinds were not used during all measurements. During the presented measurements in clear sky conditions, there were 6 occupants in the room who worked with notebooks.

2.1 Rooms Description

The measured rooms are located on the 21st floor of the Faculty of Civil Engineering of the Slovak University of Technology in Bratislava, Slovakia. The basic geometric dimensions of the room are shown in Figure 1. The clear height of the rooms is 2.67 m. The windows of the rooms are oriented to the north-east (the deviation of the normal of the windows from the north is 29°). The window in each room is 2.8 m wide, 1.65 m high, and its lower profile is 0.90 m above the floor. The window frames are made of aluminium and have a light gray color. Buildings or terrain orography practically does not at all shade the windows of the rooms. The building surfaces of the room are spectrally neutral. The walls and ceiling are white, the carpet on the floor is dark gray, and the window frames are light gray. The coating of the walls and ceiling has a photopic light reflectance value of 0.75 and melanopic light reflectance is about 0.74. Carpet and window frames have the same photopic and melanopic light reflectance, with carpet 0.32 and window frames 0.49. There was a minimum of furniture in the room, the surfaces of which had an other color. A room with a standard triple-glazed window is called the "reference room" within the experiment. A room with a window with special glazing is called a "tested room".

Measurements were made on the axis of the room and at the working positions numbered in Figure 1.

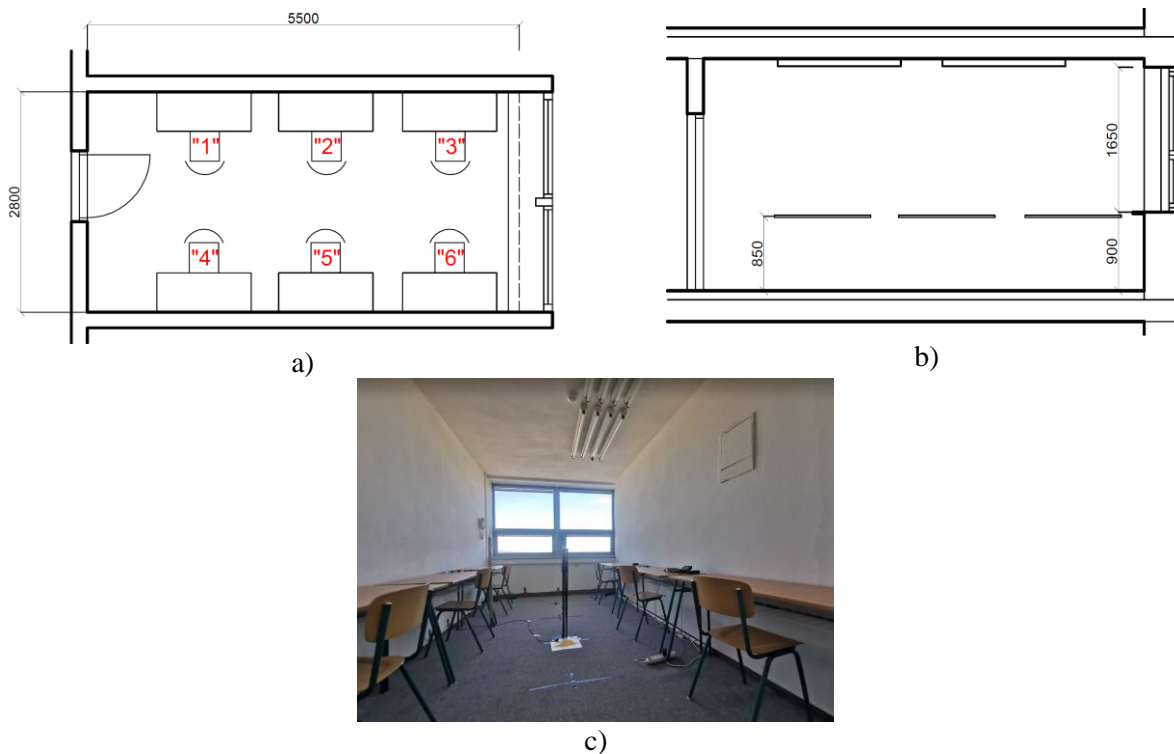


Figure 1: The room where the measurements were taken

a) floor plan of the office with marked workplaces, b) longitudinal section of the office, c) view of the office in the state of preparation of measurements

2.2 Main Measuring Devices

The new MSC 15 light spectrum meter from Gigahertz-Optik GmbH (Figure 2a) was used for the measurement of the photopic and melanopic illuminance and other spectral characteristics of light. MSC15 covers a spectral range between 360 nm and 830 nm with a spectral bandwidth of 10 nm and offers a wide measurement range for illuminance and color between 1 lx and 350,000 lx. The device can be operated manually, or measured data can also be stored in a computer running Windows as GOS extension source files, which are exported in ASCII and Excel™ formats. This device was used in experiments to measure melanopic and photopic parameters, especially in measurements under overcast sky conditions.

The compact illuminance spectrophotometer CL-500A (Figure 2b) can measure illuminance, color temperature, color rendering index, chromaticity, and spectral power distribution. The spectral irradiance is measured at 1 nm pitch from 360 to 780 nm. The measuring range is from 0.1 to 100,000 lx, with accuracy for illuminance $\pm 2\%$. The data management software CL-s10w is included as a standard accessory. These devices were located in the center of the rooms at a height of 1.20 m over the floor and were oriented toward the window.

The probe for measuring illuminance FLA 623 VL (Figure 2c) has spectral sensitivity from 380 to 720 nm and a measuring range from 0 to 170,000 lx. The absolute error of measured data is less than 5%. This photometer was placed on the outside of the window frame in a vertical position and in short time intervals, the intensities of the photopic illumination of the window were recorded by the computer.

The CM-5 spectrophotometer (Figure 2d) makes it possible to measure the spectral reflectance of opaque materials or the transmittance of transparent samples, including liquid ones, in the wavelength range of 360 to 740 nm with a pitch of 10 nm. The photopic light transmittance and reflectance of room materials were measured with this device.

Melanopic (circadian) parameters were measured in accordance with the CIE S 026/E:2018 [5].



Figure 2: The main devices used in the measurements

a) Gigahertz-Optik MSC15 spectral light meter, b) Konica Minolta illuminance color meter CL 500A, c) Ahlborn Almemo FLA 623 VL radiation probe for measuring illuminance, d) Konica Minolta spectrophotometer CM-5

2.3 Photopic and Melanopic Properties of the Windows

In the tested room, Orange 50 UV foil [11] was added to the window glazing. The spectral light transmittance of this foil is in Figure 3. The photopic light transmittance of the foil Orange 50 UV is 0.51 and melanopic light transmittance of the foil is 0.11.

The clear triple glazing in the reference room has a visible light transmittance of 0.70 (diffuse photopic light transmittance is 0.64). The diffuse melanopic light transmittance of clear triple glazing is 0.67.

The triple glazing with added foil Orange 50 UV in the tested room has a diffuse photopic light transmittance value of 0.39 and diffuse melanopic light transmittance is 0.10. Typical spectral irradiance leaving clear triple glazing under an overcast sky and spectral irradiance leaving triple glazing supplemented with foil Orange 50 UV are shown in Figure 4.

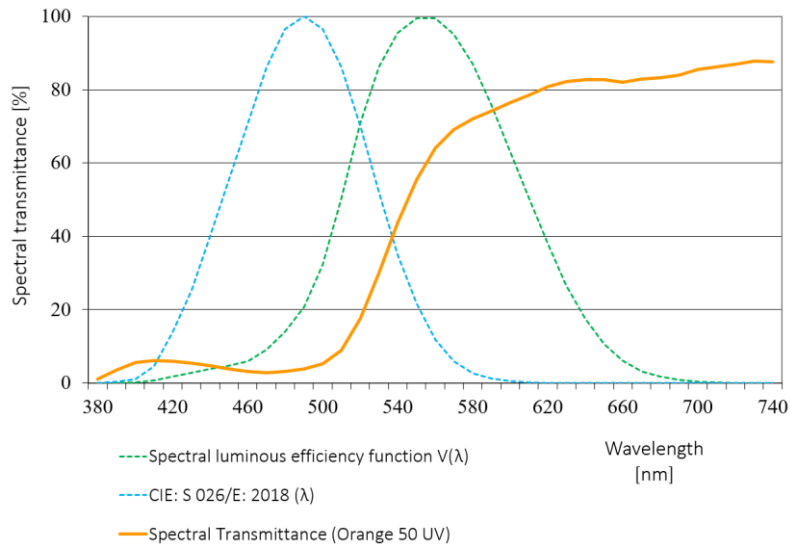


Figure 3: Spectral light transmittance of the foil Orange 50 UV and the CIE photopic and melanopic functions

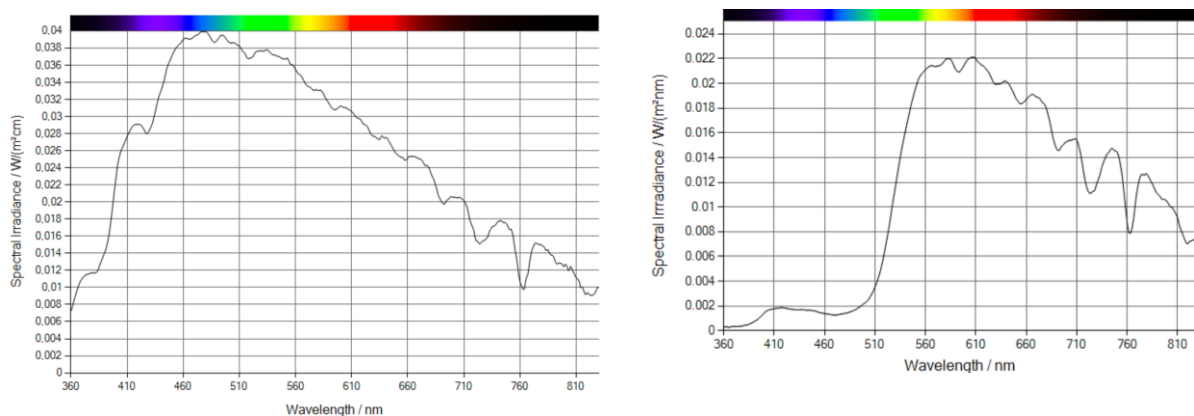


Figure 4: Typical spectral irradiance leaving clear triple glazing at the time of measurement under the overcast sky (left – ratio $E_{vp} / E_{vm} = 1.01$) and spectral irradiance leaving triple glazing supplemented with foil Orange 50 UV (right – ratio $E_{vp} / E_{vm} = 4.18$)

3 Results and Discussion

Only a small part was selected from the measured data on the light environment in the reference and tested room. However, the presented data provide a sufficient idea of how problematic it is

to evaluate photopic and melanopic light that reaches the eyes of users of building interiors, even in relatively stable conditions of the outdoor daylight climate. We have divided the analysis of the results into three sections - a part of the measured data under an overcast sky in an unoccupied tested room, a part under conditions of predominantly clear sky when people were working in the rooms, and a part in which we compare the measured data with current circadian metrics, especially melanopic illuminance.

3.1 Daylighting of the Tested Room under the Overcast Sky

The measurement results presented here are from the morning hours of a cloudy day on November 3, 2021. In the morning around 9:00 a.m., it was foggy. Then it was evenly cloudy until about 11:00 a.m. when very thick to black clouds arrived. Subsequently, the state of the sky returned to a uniformly cloudy sky, and around noon, the vertical illuminance of the window reached a level of illuminance similar to what it was at approximately 10:30 a.m. The illumination levels of the window of the tested room during the measurements are shown in Figure 5.



Figure 5: Vertical photopic illuminance of the window during measurements on November 3, 2021

Table 1: Photopic and melanopic illuminance in the axis of the tested room in a place 2.3 m and 4.1 m from the window – 11/3/2021

Measured location / direction of view	Time [h]	Illuminance 2.3 m from the window [lx]		Time [h]	Illuminance 4.1 m from the window [lx]	
		Photopic	Melanopic		Photopic	Melanopic
Horizontal 0.85 m above the floor	10:15	175.5	43.5	10:53	62.4	15.5
Vertical 1.2 m above the floor / view towards the window	10:20	287.0	73.4	10:56	107.3	27.3
Vertical 1.2 m above the floor / view towards the side wall	10:22	72.5	17.3	10:58	39.5	9.6
Vertical 1.2 m above the floor / view towards the back wall	10:23	42.3	10.2	11:00	24.5	5.9

Horizontal and vertical photopic and melanopic illuminances in the axis of the tested room in a place 2.3 m and 4.1 m from the window are in Table 1. Table 1 also shows the times of recording the illuminances. Vertical illuminances in the direction of the window are significantly higher than horizontal illuminances in the same place. In the deeper parts of the room, vertical illuminances are almost twice as high as horizontal ones. The mutual ratios between the illuminances of different oriented vertical planes and the horizontal illuminance change significantly with the orientation of the vertical planes and with the depth of the measured location in the room.

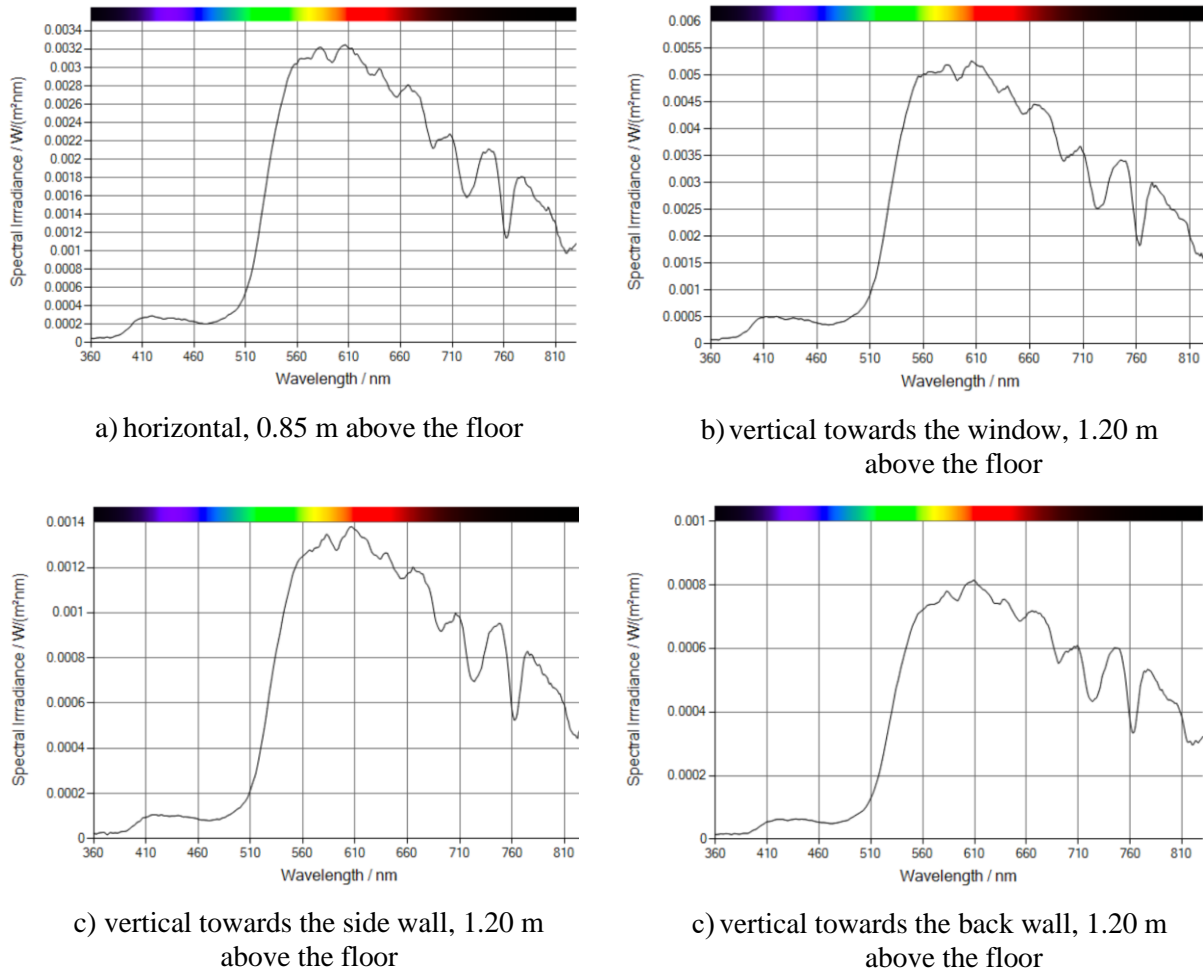


Figure 6: Spectral irradiance levels of daylight received on horizontal and vertical surfaces in the axis of the tested room at a distance of 2.3 m from the window

Figure 6 documents that in an empty room with spectrally neutral surfaces, the spectral composition of light is the same and does not depend on the orientation of the vertical plane. Of course, the intensity of spectral irradiance changes significantly with a change in the orientation of the measured vertical plane.

Characteristic spectral irradiance of the eyes of a person working with a laptop at workplace no. 3 (see Figure 1) at a distance of 2 m from the window of the tested room is in Figure 7 (left). At workplace no. 3 the photopic illuminance on the eyes of a person working on a laptop at a distance from the screen around 0.5 m was $E_{vf} = 67$ lx and the melanopic illuminance was

$E_{vm} = 23$ lx, the ratio E_{vf} / E_{vm} is 2.9. Characteristic spectral irradiance of the eyes of a person working with a laptop at workplace no. 1 at a distance of 4 m from the window is in Figure 7 (right). At workplace no. 1 the photopic illuminance on the eyes of a person working on a laptop at a distance from the screen around 0.5 m was $E_{vf} = 37$ lx and the melanopic illuminance was $E_m = 17$ lx. The ratio of photopic and melanopic illuminance of the eyes is $E_{vf} / E_m = 2.2$. At a workplace 4 m away from a window, the total illuminance on the eyes of a person working on a computer will decrease. The light falling from the computer screen on the eyes at the workplace no. 1 is the same as at workplace no. 3. The intensity of daylight at workplace no. 1 is significantly lower than at workplace no. 3. The blue part of the screen's light spectrum will improve the ratio of photopic to melanopic illuminance in favor of melanopic illuminance.

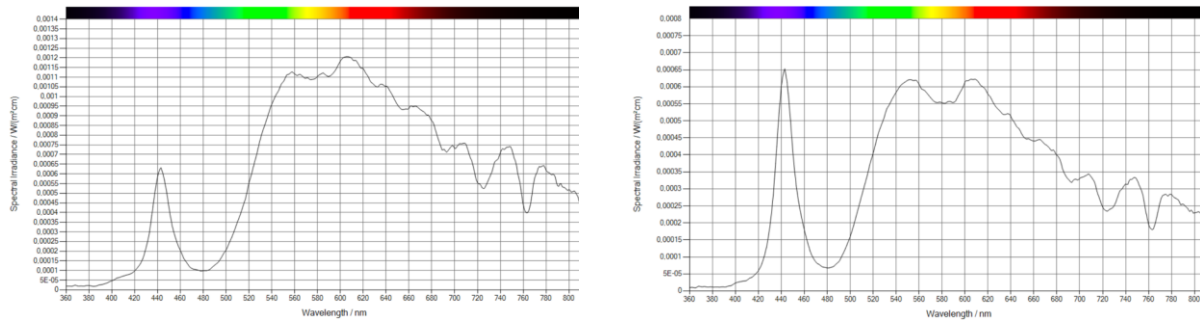


Figure 7: Characteristic spectral irradiance of the eyes of a person working with a laptop at workplace 3 (see Figure 1; left – ratio $E_{vp} / E_{vm} = 2.9$) and spectral irradiance of the eyes of a person working with a laptop at workplace 1 (right – ratio $E_{vp} / E_{vm} = 2.2$)

3.2 Daylighting of Both Rooms in Conditions of Partly Clear Sky

During the days from 1/18/2022 to 1/21/2022, in mostly clear sky conditions, several parameters of daylighting were continuously measured in both rooms. In this article, we only report the measured illuminances on the outer surface of the windows and the vertical illuminances in the center of the room towards the windows. At the time of measurements, 6 people were working on laptops in both rooms.

The vertical illuminances on the outer surface of the windows of the rooms are in Figure 8.

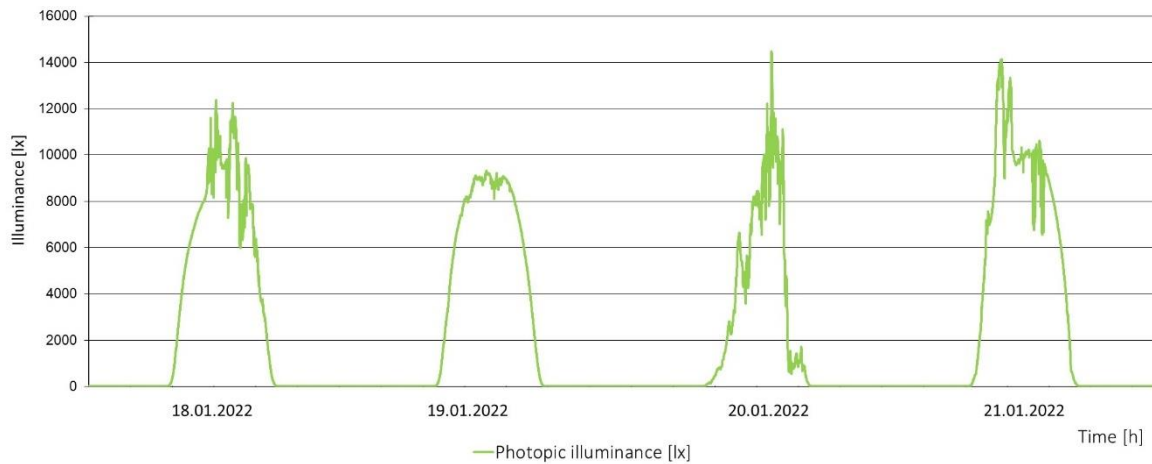


Figure 8: Vertical photopic illuminance on the external side of rooms windows

Figure 8 shows the sky lighting and the reflected light from the buildings and the terrain below the windows. Due to the relatively intense direct sunlight falling on the buildings and terrain, the reflected component of light has a significant share in the total illumination of the windows. Reflected light from buildings and terrain also has a slightly different spectral composition than a skylight.

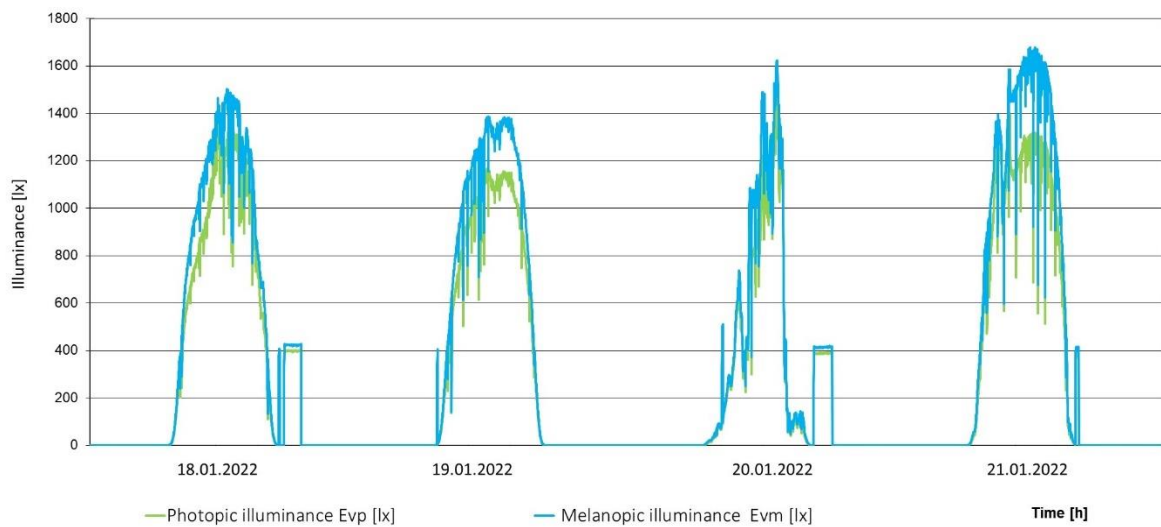


Figure 9: Photopic and melanopic illuminances of the vertical plane in the center of the reference room at a height of 1.2 m above the floor towards the window

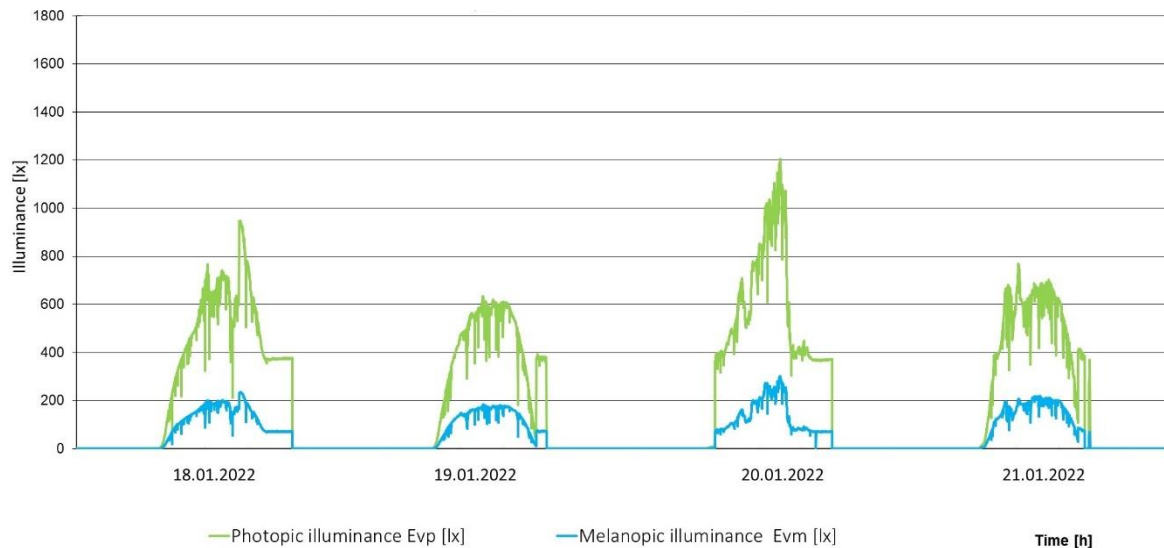


Figure 10: Photopic and melanopic illuminances of the vertical plane in the center of the tested room at a height of 1.2 m above the floor towards the window

Photopic and melanopic illuminance of a vertical plane in the center of the reference room at a height of 1.2 m above the floor towards the window is shown in Figure 9. Melanopic illuminance is higher than photopic for several reasons. The triple glazing in the window has a slightly higher transmittance of melanopic light than photopic light, and the share of blue light in the room also slightly increases the light from computer screens. However, the main reason for higher melanopic illuminance than photopic illuminance is that light from a clear sky contains more melanopic than photopic component. The rectangles in Figure 9 at the end of days 18 and 20 January 2022 are created by artificial lighting. At this time, at the end of daylight, instruments were checked under artificial lighting and other work was carried out that required experiments.

The difference between photopic and melanopic illumination in the tested room is significant due to the low transmittance of the blue component of the light spectrum - Figure 10. In the tested room, the blue component was not increased by the light from the computer screens, because for the purpose of the experiments, the computer screens were covered with a foil that does not transmit blue light.

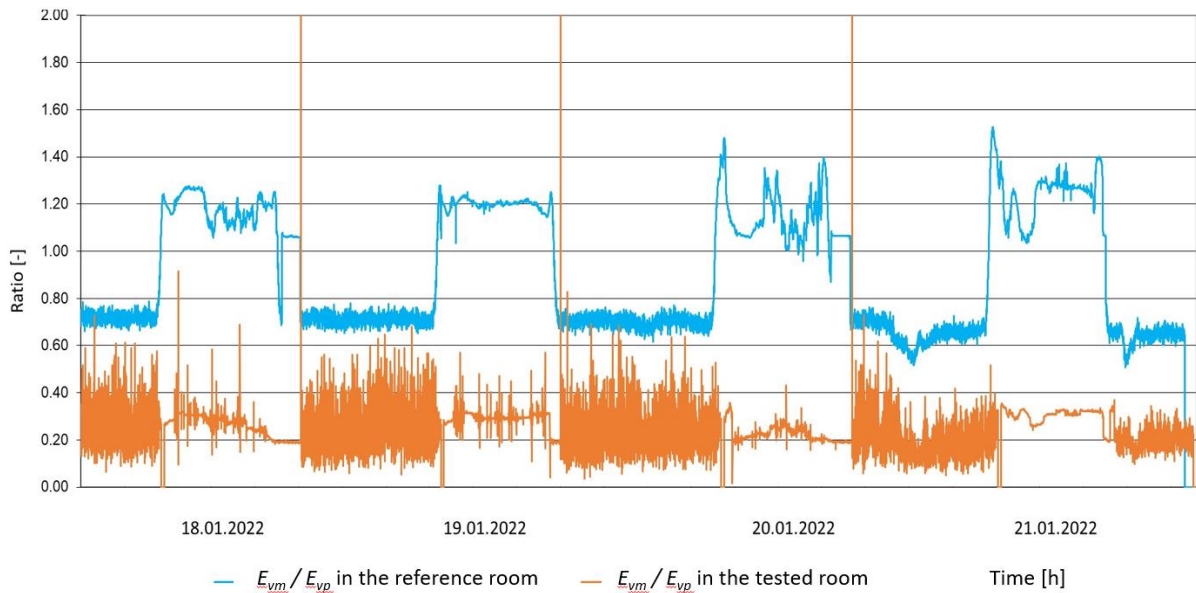


Figure 11: Ratio of melanopic illuminance to photopic illuminance in both measured rooms

Figure 11 shows that on clear days there is about 20% more melanopic light than photopic light in the center of the reference room at a height of 1.2 m above the floor towards the window. Conversely, in the tested room, the melanopic light level is only about 25% of the photopic light level. The measured rooms are located in the central part of Bratislava, where many light sources shine at night. The ratio of melanopic to photopic night light is approximately 0.70 in the reference room. The high oscillation of the melanopic to photopic night light ratio in the tested room is a consequence of the low light transmission through the windows and the light produced by the measuring devices in the room.

3.3 Performance Criteria for Non-Visual Light Evaluation

In the field of research into the non-visual effects of light, the greatest attention is paid to artificial light and its influence on the circadian stimulus. For artificial lighting, several methods and criteria for evaluating circadian (melanopic) lighting are recommended [for example in 12–14], but they differ from each other and are often fundamentally modified in short time intervals. Although these metrics are used to assess circadian aspects of daylighting, such a procedure cannot be considered correct. The reason for this statement is the high dynamics of the intensities and spectral composition of daylight. Despite the fact that assessing and evaluating melanopic daylighting is problematic, we will compare the measured illuminance in both rooms with the criteria [15]. According to [15], the melanopic equivalent daylight illuminance (M-EDI) sufficiently describes human circadian light responses and throughout the daytime, the recommended minimum M-EDI is 250 lx in the vertical plane at approximately 1.2 m height. Unfortunately, this metric, as well as other recommendations for minimum levels of melanopic light in building interiors, does not say in which places the proposed criteria should be achieved and in which direction the vertical plane should be oriented. In a reference room with standard spectrally neutral glazing, M-EDI values in the center of the room on clear days reach significantly higher levels than 250 lx (Figure 9). In the middle of the tested room with glazing with very low melanopic light transmittance, the minimum M-EDI values are not reached under

clear skies at all (Figure 10). No direct sunlight penetrated the room during the measurements. In the tested room with glazing that transmits approximately 40% of photopic light, illuminances higher than 250 lx are achieved only near the window (Table 1). At a depth of 4 m from the window, the photopic illuminance of the vertical plane at a height of 1.2 m above the floor is only around 100 lx. Due to the very low transmittance of melanopic light through the glazing, the M-EDI values are well below the recommended minimum levels.

4 Conclusion

This article presents the results of photopic and melanopic illuminance measurements in two rooms under limited daylight conditions. Due to the objectives of the scientific study, within which the measurements of daylighting conditions were carried out, the melanopic transmittance of the glazing in one of the measured rooms was extremely low. Nevertheless, we can state that when evaluating the circadian effects of daylight, it is essential to take into account the spectral properties of glazing and indoor opaque surfaces. The measurements showed that even in conditions of relatively steady skylight, it is very problematic to evaluate the melanopic illuminance on the eyes of the users of the interior space. Light from computer screens increases the overall melanopic illumination on the eyes of a person working with a computer. This effect is quite pronounced in the depth of a room with very low melanopic daylight. The intensity of the illuminance of the eyes from the computer screen can be significantly higher in the depth of the room than the illuminance of the eyes with only daylight. The presented measurements show that spectrally neutral glazing with high photopic light transmittance has a high non-visual potential. In cloudy locations, in regularly occupied indoor spaces, the photopic light transmittance of 0.40 can be considered insufficient in most cases. The measurements carried out also raised the question of whether, instead of year-round simulations with a range of subjective assumptions and their interpretations, it is not enough to adapt some of the traditional methods of designing and evaluating the daylighting of buildings in such a way that, in addition to the required photopic illuminance, the level of daytime melanopic illuminance is also guaranteed.

Acknowledgments

This article has been supported by the Ministry of Education, Science, Research and Sport of the Slovak Republic under VEGA contract 1/0042/21 and by the Slovak Research and Development Agency under contract APVV-18-0174.

References

- [1] Xiaodong, Ch., Xin, Z. & Jiangtao, D. (2019). Glazing type (colour and transmittance), daylighting, and human performances at a workspace: A full-scale experiment in Beijing. *Building and Environment*. 153 (18), 168-185. DOI: 10.1016/j.buildenv.2019.02.034.
- [2] Berson, D.M., Dunn, F.A. & Takao, M. (2002). Phototransduction by retinal ganglion cells that set the circadian clock. *Science*. 295 (5557), 1070-1073. DOI: 10.1126/science.1067262.
- [3] Al Enezi, J., Revell, V., Brown, T., Wynne, J., Schlangen, L. & Lucas, R. (2011). A melanopic spectral efficiency function predicts the sensitivity of melanopsin photoreceptors to

- polychromatic lights. *Journal of Biological Rhythms*. 26 (4), 314–323. DOI: 10.1177/0748730411409719.
- [4] Song, H., Jiang, W. & Cui, P. (2022). A Study on Nonvisual Effects of Natural Light Environment in a Maternity Ward of a Hospital in Cold Area. *BioMed Research International*. Volume 2022, Article ID 8608892, 16 pages, DOI: 10.1155/2022/8608892.
- [5] CIE Central Bureau. (2019). *CIE Position Statement on Non-Visual Effects of Light - Recommending Proper Light at the Proper Time. 2nd Edition*. Vienna: CIE Central Bureau.
- [6] Brown, T. M. (2020). Melanopic illuminance defines the magnitude of human circadian light responses under a wide range of conditions. *Journal of Pineal Research*. 69 (1), e12655. DOI: 10.1111/jpi.12655.
- [7] Pyeritz, R., Korf, R. & Grody, W. (editors). (2019). *Emery and Rimoin's Principles and Practice of Medical Genetics and Genomics. Clinical Principles and Applications. (7th Edition). Chapter 11 – Circadian Rhythms and Disease, authors: Zhang S.L. and Sehgal A., pp. 299-314*. Academic Press. DOI: 10.1016/B978-0-12-812536-6.00011-0.
- [8] Amundadottir, M. L., Lockley, S. W. & Andersen, M. Unified framework to evaluate non-visual spectral effectiveness of light for human health, *Lighting Research and Technology*. 49 (6), 673–696. DOI: 10.1177/1477153516655844
- [9] Inanici, M., Brennan, M. & Clark, E. (2015). Spectral daylighting simulations: Computing circadian light. In Proceedings of 14th Conference of International Building Performance Simulation Association, Dec. 7-9 (1245–1252). Hyderabad, India: IBPSA.
- [10] Saiedlue, S., Amirazar, A., Hu, J. & Place, W. (2019). Assessing circadian stimulus potential of lighting systems in office buildings by simulations. In ARCC 2019 International Conference “The Future of Praxis: Applied Research as a Bridge Between Theory and Practice”, May29 – June 1 (719-727). Toronto: Ryerson University.
- [11] <https://www.autolekaren.sk/produkt/anti-uv-interierova-fovia-oranzova-152cm-x-30-5m-orange-50-uv> (In Slovak.)
- [12] International WELL Building Institute. (2022). "WELL v2 Building Standard, Light, Feature L03, Circadian Lighting Design". <https://v2.wellcertified.com/en/wellv2/light/feature/3>
- [13] DIN SPEC 67600:2013-04 Biologisch wirksame Beleuchtung – Planungsempfehlungen. 68 p. (In German.)
- [14] UL DG 24480. Edition 1. (2019). “Design Guideline for Promoting Circadian Entrainment with Light for Day-Active People”.
- [15] Brown, T. M., Brainard, G.C., Cajochen, C., Czeisler, C.A., Hanifin, J.P., Lockley, S.W., et al. (2022). Recommendations for daytime, evening, and nighttime indoor light exposure to best support physiology, sleep, and wakefulness in healthy adults. *PLoS Biology* 20 (3): e3001571. DOI: 10.1371/journal.pbio.3001571.

Optimization of the Combined Effect of Lime and Ground Granulated Blast-furnace Slag on Clayey Soil

Diaf Nasreddine^{1*}, Hidjeb Mustapha¹, Boudjellal Khaled¹, Boudiaf Mohamed², Lamri Ihcene¹

¹University of 20 Août 1955 - Skikda, Algeria, Faculty of Technology
Department of Civil Engineering, Laboratory LMGHU

²University of 20 Août 1955 - Skikda, Algeria, Faculty of Technology
Department of Mechanical Engineering, Laboratory LMGHU

*e-mail: nasrodiaf@yahoo.fr

Abstract

This work investigates the behavior of a silty clay stabilized with 3, 6, 9, and 12 % of ground granulated blast-furnace slag (GGBS), respectively, and 1 % of quicklime used as an activator. The influence of the composite (Quicklime - GGBS) on the immediate behavior of the silty clay is studied by examining the Atterberg limits, the maximum dry density, the optimum moisture content, and the immediate bearing index. The evolution, at different curing periods (1, 7, and 28 days), of the mechanical characteristics of the treated soil, namely unconfined compressive strength, cohesion, and internal angle of friction is also studied. The increase, up to a dosage of 9%, of the GGBS content, leads to an increase in the optimum moisture content, the immediate bearing index, the unconfined compressive strength, and shear strength parameters. Paradoxically, a decrease in the plasticity index and the maximum dry density was observed.

Keywords: optimization, silty clay, GGBS, quicklime, strength parameters

1 Introduction

Clay soils, as in the case of dams, embankments, and roads, are often the site of vertical and horizontal deformations which can generate serious problems of stability and settlement, leading to very important economic damages. In the United States, annual losses due to structural damage from expansive soils are estimated at \$ 2.3 billion [1]. Keeping this global issue in mind and meeting the technical and economic needs, clay soil stabilization techniques are more than necessary. Stabilization of clay soils, through the addition of hydraulic binders such as cement [2], lime [3], and fly ash [4], is an old practice. However, in road geotechnics, the application of GGBS is so far not widely used. On the other hand, the use of GGBS as the main component of alkali-activated cement or as a partial replacement for Portland cement (PC) is widely used [5]. Today, the increasing demand for GGBS is due to economic and

technical reasons and environmental concerns associated with its production. A comparative study between the environmental impacts associated with the production of GGBS and those associated with the production of PC [6] showed that the production of one ton of GGBS at an energy consumption of 1300 MJ results in only 0.07 tons of CO₂ emissions while the production of one ton of PC results in 0.95 tons of CO₂ emissions and high energy consumption of 5000 MJ. GGBS, a co-product of the steel industry, is formed when molten blast-furnace slag is rapidly cooled by immersion in water. GGBS is available in large quantities worldwide. In Algeria, the annual production of slag is estimated at 500,000 tons [7]. In addition, global crude steel production reached 200 million tons in 2015, of which five million tons of slag were produced in France alone [7]. In the United States, steel industries generate 10-15 million tons of steel slag each year, while about 15-40 % of steel slag production is sent to slag disposal sites [8]. GGBS is chemically composed of four main oxides: lime (CaO), silica (SiO₂), alumina (Al₂O₃) and magnesia (MgO). GGBS contains the same major oxides as Portland cement (PC) which, in the presence of water, forms cementitious hydrates similar to those forming during the hydration of PC [9]. The GGBS rate of hydration is very slow compared to that of clinker of PC because, once the slag grains come into contact with water, low basicity and low permeability gelling layer, forms around the grains preventing the dissolution of the slowing down the hydration kinetics [10]. Hence, the addition of an appropriate activator is necessary to dissolve the layer covering the GGBS grains, thus accelerating the hydraulic setting. Chemical activation of GGBS is usually performed using either calcium activation [11] or alkaline activation [12] or PC activation [9] and finally sulfate activation [13]. Thus, some studies have shown that CaO has a better potential for GGBS activation than some activators [9]. The high CaO content in GGBS, added to the clayey soils and the presence of water and calcium activator, trigger quick hydration reactions resulting in the formation of a large quantity of calcium cations Ca⁺² and hydroxyls (OH⁻). The Ca⁺² cations react with the surfaces of clay minerals through the process of cation exchange leading to the flocculation of the particles in the form of water-insensitive lumps that result geotechnically in the decrease of plasticity of the treated soil [14]. The calcium hydrates (C-S-H, C-A-H, and C-S-A-H), occurring over time, result from two different reaction mechanisms. The first is a direct result of the hydration reaction between GGBS grains and water, which leads to the appearance of primary cementitious products in the form of gels coating the lumps [15]. The second mechanism appears thanks to the pozzolanic reaction from where, thanks to a high level of PH that increases with the increase of hydroxyl ions concentration [16], silica (SiO₂) and alumina (Al₂O₃) contained in the clay particles, react with the excess of calcium brought by GGBS and the activator forming insoluble calcium hydrates that are responsible for the increase in strength [17, 18]. GGBS as a binder is well established in many soil mixing applications. The effects of GGBS on the swelling properties of lime-stabilized sulfate-bearing clay soils were the concern of several studies [19, 20]. These studies showed that partial substitution of GGBS with lime in sulphate bearing soils produced significant improvements in strength development and reduced the expansion. Celik and Nalbantoglu [19] reported that, in the presence of 6 % GGBS, the swell potential of the lime-treated soil with 10,000 ppm sulfate concentration decreased from 8 % to 1 %. The potential of using other binders as an alternative to lime with GGBS for the stabilization of expansive soils was also evaluated [17, 21]. Guda [21] revealed that GGBS with 2 % of cement as an activator can be used as cushioning material to minimize the heave of expansive soil. The use of lime-activated GGBS to stabilize acid sulfate soils (ASS)

containing pyrite is another application [22, 23, 24, 25]. The effect of pyrite (FeS_2) content on the strength behavior of EngClay (an artificial clay prepared by mixing 85 % kaolin and 15 % bentonite) using lime activated GGBS was investigated [24, 25]. The results indicated that the negative effect of pyrite (FeS_2) could be reduced in acid sulfate soils (ASS) by using lime-activated GGBS and the formation of thaumasite-ettringite, a deleterious mineral, is deemed to be responsible for the degradation of strength in treated ASS. Lime-GGBS stabilized clay was also used to reduce the harmful effect of flooding in road structures and embankments [15, 26, 27]. They suggested that in roads and embankments, built on floodplains, GGBS reduced the water absorption and increased the formation of the CSH gel matrix responsible for the improvement of densification, strength, and durability. To reduce the use of PC in soft-clay stabilization, many studies investigated the efficiency of Lime-GGBS, Carbide Slag (CS)-GGBS and Alkali-GGBS compared with that of PC [18, 28]. Yi et al [18] found that the UCS after 90- a day cure, with a lime/GGBS ratio of 0.10, was 1.7 times that of PC stabilized marine soft-clay. Recently, the effectiveness of the GGBS using different types of activators in treating petroleum hydrocarbons and heavy metals contaminated soils was the subject of some studies [29, 30, 31, 32]. These studies showed that GGBS activated by different binders (Lime, PC, MgO , CaSO_4 , fly ash) would reduce the leachability of contaminants and enhance the physical and mechanical properties in contaminated soils using stabilization / solidification technology. The objective of this research is to promote the use of GGBS, a by-product of the steel industry, in the field of civil engineering and public works which will reduce the use of traditional binders such as cement and lime. In this research, the stabilization of silty clay using a composite (lime and GGBS) will be investigated.

2 Materials Used

The soil studied in this work comes from Laghdir deposit, located about 30 km east of Skikda (Algeria), and used to build a section of the East-West highway. According to the GTR (A French guide for road earthworks, backfills and subgrade layers), the soil taken from a depth of about 2 m is a silty clay (SC) characterized by high plasticity which, at medium and low water contents, becomes highly coherent, sticky, and slippery. The plasticity index (PI) and the activity coefficient of the studied soil are respectively 30.18 % and 0.75. Based on these results, and according to Skempton's correlation [33] and Mitchell [34] between the type of clay mineral and the activity coefficient, and according to the activity classification of Skempton [33], the predominant mineral in the studied clay is mainly composed of illite as the normal active clay mineral. The GGBS is a greenish-grey color. It was kindly provided by the El Hadjar steel complex of Annaba (Algeria). It was ground with a ball mill to increase the specific surface and thus increase the hydraulic power of the slag. The value of the basicity index (BI) being superior to the unit ($\text{BI} = 1.22 > 1$), the GGBS used is thus basic [35]. The physico-chemical properties of soil, GGBS and the activator namely quicklime from the SODEPAC plant in Saida (Algeria), are presented in Table 1. Figure 1 shows the particle size curve of the studied soil.

Table 1: Materials properties used in the study

Materials Properties	Value		
	Soil	GGBS	Quicklime
GTR Classification guide	SC	/	/

Percent passing 80 μm sieve (%)	50	98	95
Specific surface Blaine (cm^2/g)	/	4100	/
Basicity index	/	1.22	/
The product A.C (A is the Al_2O_3 content and C is the CaO content)	/	439.91	/
Natural moisture content (%)	19.55	/	/
Methylene blue value (cm^3)	7.01	/	/
Liquid limit (%)	56.54	/	/
Plastic Limit (%)	26.36	/	/
Plasticity index (%)	30.18	/	/
Consistency index	1.22	/	/
Optimum moisture content (%)	17.55	/	/
Maximum dry density (g/cm^3)	1.69	/	/
Immediate bearing index (%)	3	/	/
Organic matter (%)	1.80	/	/
Activity	0.75	/	/
CaO (%)	4.79	45.92	> 83.5
Al_2O_3 (%)	17.72	9.58	< 1.5
Fe_2O_3 (%)	6.80	5.45	< 0.5
SiO_2 (%)	51.65	37.58	< 2.5

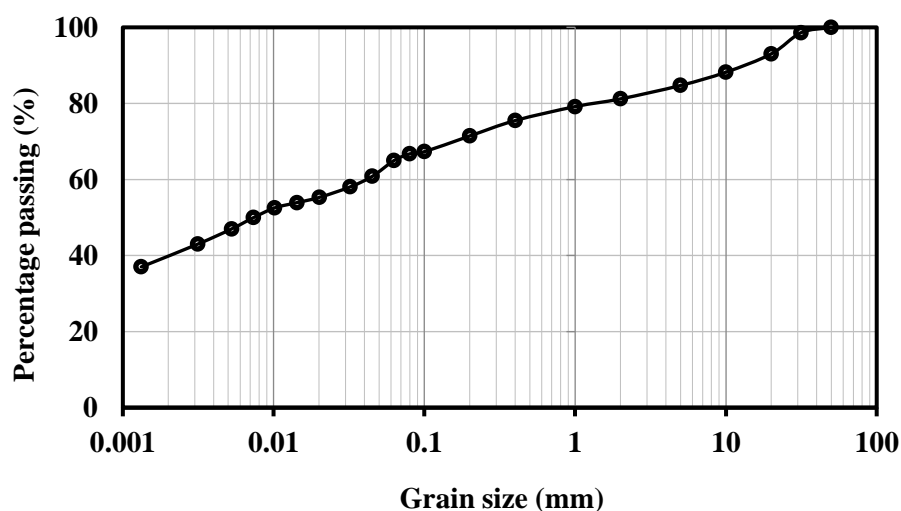


Figure 1: Grain-size curve of soil used

3 Testing Program and Sample Preparation

Several series of physico-chemical, mechanical and identification tests were carried out in accordance with French standards (AFNOR), at the university laboratory (see Figure 2, 3). The behavior of the treated soil, at different curing periods (0, 1, 7 and 28 days) was investigated using the following tests: - Atterberg limits [36] - Standard Proctor [37] - California Bearing Ratio (CBR) [38] - Unconfined compressive [39] - Direct shear [40]. After drying the samples at 105°C , passing materials are mixed with 3, 6, 9 and 12 % GGBS and 1 % quicklime, used as an activator (Table 2). In order to perform CBR, unconfined compressive

and direct shear tests, the composite samples (Quicklime - GGBS - Soil) are wetted to an optimum moisture content (OMC) determined by a standard Proctor compaction test. The treated samples are compacted in molds 101 mm in diameter and 117 mm in height [37]. For direct shear tests, specimens 60 mm x 60 mm in section and 30 mm in height are carried out under vertical loads of 50, 100, and 150 kPa. The drying of the specimens for the unconfined compressive and direct shear tests was carried out in the laboratory (average humidity of 65 % and a temperature of $20^{\circ}\text{C} \pm 2^{\circ}\text{C}$).

Table 2: Formulations of the samples

Tests	Sieve ϕ (mm)	Mass of the sample (g)	GGBS (%)	Quick lime (%)	Specimen (ϕ , h, L, ℓ) (mm)	Curing time (days)
Atterberg limits	0.4	200	0, 3, 6, 9 and 12	1	/	0
Compaction	20	2500	0, 3, 6, 9 and 12	1	$\phi = 101$; h= 117	0
CBR	20	5500	0, 3, 6, 9 and 12	1	$\phi = 152$; h= 152	0
Unconfined compressive	20	2500	0, 3, 6, 9 and 12	1	$\phi = 101$; h= 117	1, 7 and 28
Direct shear	2	400	0, 3, 6, 9 and 12	1	$\ell = 60$; L= 60 ; h = 30	1, 7 and 28



Figure 2: General view of the soil mechanics laboratory



Figure 3: Simple compression device

4 Results and Discussion

4.1 The Limits of Atterberg

Figure 4 shows that the increase in GGBS content leads to a change of the consistency of the silty clay. This change results in an increase in the plastic limit (PL) and a slight increase in the liquid limit (LL) inducing hence, a reduction of the plasticity index (PI) is observed. For 3 % GGBS content, a decrease of 17 % in PI is observed. For higher dosages, i.e., 6 and 9 %, reductions in PI of 27 and 41 % are respectively observed. Despite the large reductions in PI, 10 % with 6 % GGBS and 24 % with 9 % of GGBS, compared to the 17 % reduction in PI with 3 % GGBS content (Table 3) and, for economic reasons, a dosage of 3 % is considered as the optimum GGBS value. Nevertheless, the importance of the effect of 3 % of GGBS on IBI (Immediate Bearing Index) must be further looked over.

In its natural state, the liquid limit (LL) of the silty clay is 56.5 % and increases to 60.1 % for 12 % GGBS content. This small variation in LL may be explained by the increase in the specific surface of the silty clay due to the addition of GGBS powders. This phenomenon leads to an increase in the cation exchange capacity which increases the water adsorption capacity. The immediate changes occurring after the addition of GGBS to the soil could be explained by the hydration process of quicklime contained in GGBS and the quicklime used as a basic activator. This process would give rise to calcium Ca^{+2} cations responsible for bonding clay mineral layers called the flocculation phenomenon [41]. Flocculation, occurring after mixing, leads to the appearance of water-insensitive lumps [42].

It can be seen in Figure 4 that from 9 % GGBS onwards, no significant variation of the Atterberg limits is observed. This could probably be explained by the fact that the soil has reached its optimal lime fixation point defined by the condition: $\text{PH} = 12.4$ corresponds to a solution saturated with lime [43].

The addition of 9 % GGBS would therefore be more than sufficient to improve the short-term consistency of the silty clay.

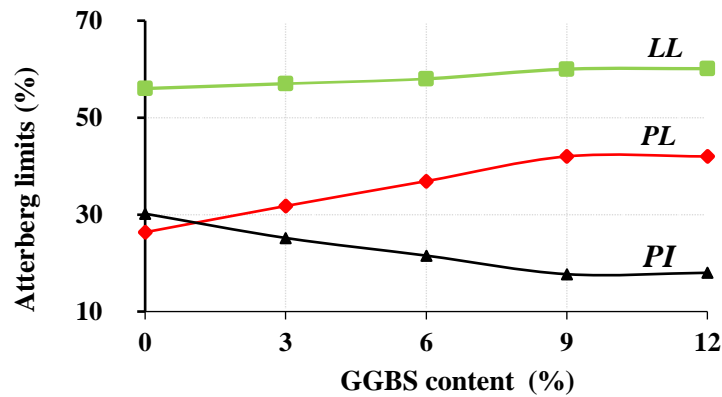


Figure 4: Effect of GGBS content on Atterberg limits

Table 3: Rate of decrease in PI for different increments of GGBS

GGBS (%)	Rate of decrease of PI (%)
0 to 3	17
0 to 6	27
0 to 9	41
3 to 6	10
3 to 9	24

4.2 Compaction Test

The compaction curve of the soil in its natural state, figure 5, shows a significant concavity, which may be due to the high sensitivity of the soil to water. On the other hand, the increase of GGBS (3, 6, 9, and 12 %) induces a progressive reduction of the soil's sensitivity to water, which results in flattening the compaction curves of the composites to a gradual decrease in slope. Furthermore, it is observed that the compaction curves of the GGBS treated specimens are located below and shifted to the right of the Proctor curve of the untreated soil. Thus, the GGBS treatment may reduce the maximum dry density (MDD) and increases the optimum moisture content (OMC). It can also be observed, in Figure 5, that an increase in the dosage of GGBS (3, 6, 9, and 12 %) induces a reduction in the MDD (3.5, 8, 11 and 12 % respectively). These reductions may be due to the following phenomenon:

- The granulometric modification, by the flocculation of the particles due to the immediate action of the quicklime contained in the GGBS and the activator, allows the lumps to occupy a larger space leading thus to an increase in the volume of the soil structure.
- The low density of GGBS also contributes to the reduction of the MDD of the composite (Quicklime - GGBS - Soil).

On the other hand, for 3, 6, 9 and 12 % of GGBS content (Figure 5), the OMC is 18.7, 19.9, 21.1 and 21.2 % respectively. These increases could be justified by the increase in the specific surface of the soil due to the addition of GGBS powders and therefore, in an increase in the water adsorption capacity.

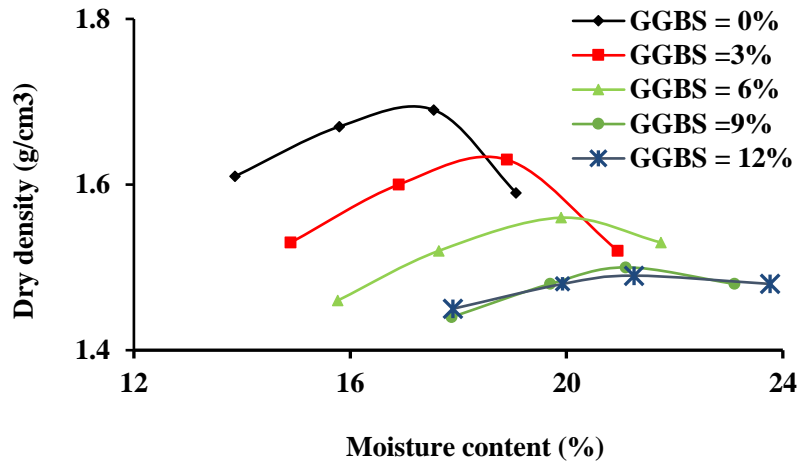


Figure 5: Effect of GGBS content on dry density

4.3 California Bearing Ratio (CBR) Test

To assess the ability of the treated soil to withstand the movements of road works construction machinery, CBR tests were performed to determine the immediate bearing index (IBI). It can be seen in Figure 6 that the IBI = 3 % of the untreated soil is lower compared to those of the treated soil samples whose increase in GGBS content (3, 6, 9 and 12 %) induced a significant increase in immediate bearing indexes (13, 21, 31 and 33 %, respectively). For a GGBS dosage of 3 %, the soil shows an IBI of 13, which satisfies the GTS [44] following criteria: $-5 < \text{IBI} < 10$ for embankments; $-\text{IBI} > 10$ for platforms.

Hence, a GGBS content, even lower than 3 %, could ensure proper implementation of the backfill, which governed the choice of 3 % of GGBS in the formulation of the soil-GGBS-Quicklime composite. The increase in soil bearing capacity is mainly due to immediate chemical reactions, including cation exchange and flocculation, which result in a reorganization and a better distribution of the particles.

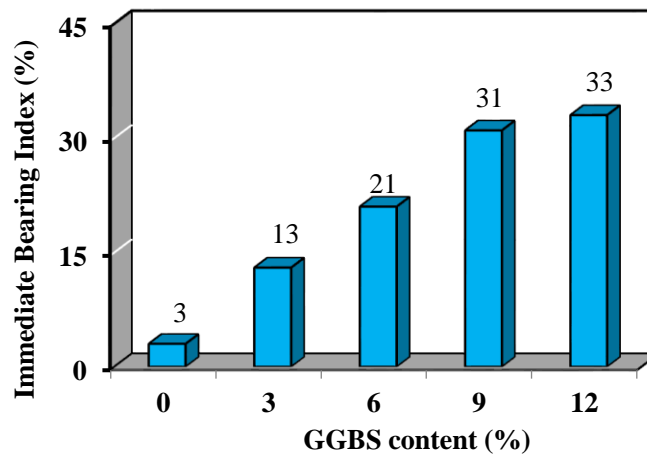


Figure 6: Evolution of the immediate bearing index as a function of GGBS content

4.4 Unconfined Compressive Test

Up to 9 % GGBS content, the unconfined compressive strength (UCS) increases progressively with the maturation of the soil-quicklime-GGBS composite (Figure 7). The addition of 3 % GGBS induces an increase in UCS of 113 % and 255 % at 7 and 28 days respectively. For 9 % GGBS content, increases in UCS of 86 % at 7 days and 280 % at 28 days are observed. However, for 3 % GGBS content and 28 days of age, the traffic criterion (According to GTS [44]), is verified: $UCS = 1.09 \geq 1$ MPa. Once again, the latter result justifies the choice of 3 % of GGBS. Increasing the dosage of GGBS from 9 % to 12 %, for different curing periods, does not provide any additional strength gain, which may mean that the silty clay has probably reached its lime fixation point. The gain in UCS of the GGBS treated soil samples could be explained by the following chemical phenomena:

- The immediate actions of calcium (Ca^{+2} cations) allow the flocculation of the clay particles in the shape of water-insensitive lumps [41] favoring, the reorganization and redistribution of soil particles and therefore improving its mechanical strength.
- The hydraulic reaction of GGBS fines with water leads to the appearance of the first generation of calcium hydrates (CSH, CAH and CSAH) in the shape of gel coating the lumps. The latter favors bonding between the lumps during compaction [15]. As the hardening of the gel takes place, a rigid shell forms [15]. This phenomenon could explain the increase in compressive strength at 7 and 28 days.
- We may consider that a pozzolanic reaction is originated by the PH increase of the medium, made possible by the hydroxide ions (OH^-) contained in the quicklime and GGBS [16]. A high PH level favors the dissolution of silica and alumina in the clay particles. These particles in solution react with the excess calcium provided by the GGBS and the activator by forming insoluble calcium hydrates which in the presence of water form crystals, thus creating bonds of the same nature as those of the first generation [16, 17]. The appearance of these types of second generation hydrates depends on the temperature, the PH of the medium and the nature of the clay minerals [43].

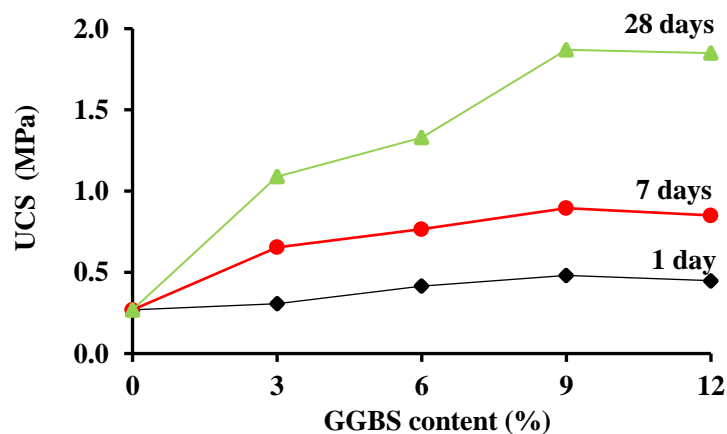


Figure 7: UCS versus GGBS for treated and untreated soil samples at different curing periods

4.5 Direct Shear Test

It can be seen in figure 8 that during the first week of cure, the increase in cohesion is slow to become faster till the 28th day. These variations over time may also be due to hydration and pozzolanic reactions [15, 17]. Regarding to the internal angle of friction (figure 9), an opposite tendency as that of the variation of the cohesion is observed. Indeed, the rate of increase of ϕ , during the first 7 days of treatment is fast to become slow till 28th days. This increase in the internal angle of friction would also be due to the phenomenon of flocculation responsible for the transformation of the silty clay into a lumpy structure. This reinforces the idea that the flocculation phenomenon, appearing approximately after two hours of treatment, is very significant. Nevertheless, this phenomenon begins to subside very quickly, becoming almost insignificant, after 7 and 28 days.

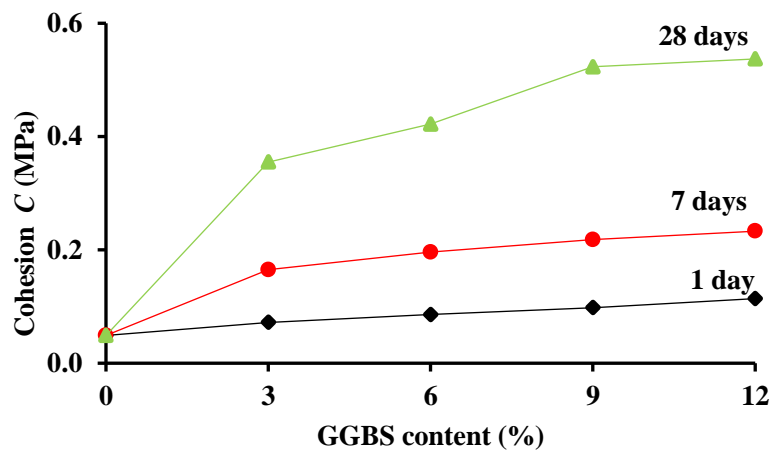


Figure 8: Cohesion versus GGBS for treated and untreated soil samples at different curing periods

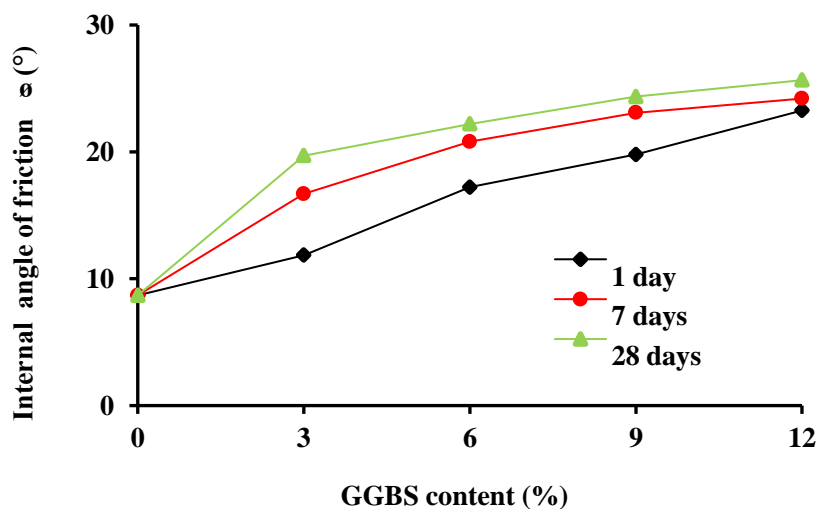


Figure 9: Internal angle of friction versus GGBS for treated and untreated soil samples at different curing periods

5 Conclusion

The use of large quantities of GGBS in the field of construction, will contribute to solving economic and environmental problems related to its storage such as well as the contamination of the water table. The use of GGBS as a hydraulic binder in the stabilization of silty clay would also reduce the use of traditional binders such as cement and lime. The aim of this work is to evaluate the hydraulic power of GGBS and highlight possible correlations between the chemical actions and the development of the physical and mechanical parameters of silty clay in road works and embankments. Several series of physico-chemical and mechanical tests were carried out and the following conclusions may be drawn:

- The addition of GGBS and quicklime to the silty clay generates immediate chemical reactions promoting the flocculation phenomenon which in turn creates lumpy structures. These observations could, possibly, be confirmed by physical and mechanical characterization tests such as the plasticity tests, the standard Proctor compaction test and the CBR test.
- For a variation of the GGBS content from 0 to 9 %, the plasticity index decreases while the consistency index of the composite (Quicklime - GGBS - Soil) increases.
- Due to the flocculation phenomenon, the granulometric modification allows the lumps to occupy a larger space, thus leading to an increase in the volume of the structure of the composite. Therefore, treatment of silty clay by adding GGBS reduces the maximum dry density and increases the optimum moisture content of the composite (Quicklime - GGBS - Soil).
- The increase of GGBS dosage leads to a significant increase in the immediate bearing index of the composite (Quicklime - GGBS - Soil), thus verifying the criterion of trafficability in the first day (IBI = 13) for a GGBS dosage of 3 %.
- Cementitious hydrates (C-S-H, C-A-H, and C-S-A-H), occurring over time, may result from two different reactions. The first one is the direct result of the hydration reaction between GGBS fines and water leading to the appearance of the first generation of calcium hydrates in shape of gel coated lumps. The second produces the second generation of calcium hydrates as a result of the pozzolanic reaction, between the clay minerals and the excess of calcium brought both by the GGBS and the activator. The development of cementitious hydrates is confirmed by the response of the following strength parameters:
 - The UCS increases progressively with the age of maturation of the composite (Soil + 3 % GGBS + 1 % Quicklime), thus verifying the trafficability criterion (1MPa at 28 days).
 - During the first week of cure, the variation in the cohesion of the composite (Quicklime - GGBS - Soil) is slow then faster till the 28th day.
 - The variation in the angle of internal friction of the composite (Quicklime - GGBS - Soil) increases quite rapidly, especially during the first 7 days of curing, then more slowly till the 28th day.

References

- [1] Shalabi, F. I., Asi, I. M., & Qasrawi, H. Y. (2017). Effect of by-product steel slag on the engineering properties of clay soils. *Journal of King Saud University-Engineering Sciences*. 29(4), 394-399. <https://doi.org/10.1016/j.jksues.2016.07.004>.
- [2] Mousavi, S., & Wong, L. S. (2015). Mechanical behavior of compacted and stabilized clay with kaolin and cement. *Jordan Journal of Civil Engineering*. 9(4), 20-32.
- [3] James, J., & Pandian, P. K. (2018). Select geotechnical properties of a lime stabilized expansive soil amended with bagasse ash and coconut shell powder. *Selected Scientific Papers-Journal of Civil Engineering*. 13(s1), 45-60. <https://doi.org/10.1515/sspjce-2018-0005>.
- [4] Bera, A. K., & Kundu, S. (2016). Influence of fly ash content on compaction characteristics of fly ash clay mixture. *Jordan Journal of Civil Engineering*. 10(1), 55-66.
- [5] Oravec, J., & Eštoková, A. (2017). Comparison of Hexavalent Chromium Leaching Levels of Zeolite and Slag-based Concretes. *Selected Scientific Papers-Journal of Civil Engineering*. 12(1), 29-36. <https://doi.org/10.1515/sspjce-2017-0003>.
- [6] Higgins, D. (2007). Briefing: GGBS and sustainability. *Constr. Mater.* 160 (3), 99 – 101. <https://doi.org/10.1680/coma.2007.160.3.99>.
- [7] Hadidane, H., Oucief, H., & Merzoud, M. (2018). Improving the behaviour of roads underlays by the use of industrial waste (blast furnace slag). *Journal of Materials and environmental Sciences*. 9 (3), 887-893. <https://doi.org/10.26872/jmes.2018.9.3.98>.
- [8] Yildirim, I. Z., & Prezzi, M. (2011). Chemical, mineralogical, and morphological properties of steel slag. *Advances in Civil Engineering*. 2011, 1-14. <https://doi.org/10.1155/2011/463638>.
- [9] Kim, M. S., Jun, Y., Lee, C., & Oh, J. E. (2013). Use of CaO as an activator for producing a price-competitive non-cement structural binder using ground granulated blast furnace slag. *Cement and Concrete Research*. 54, 208-214. <https://doi.org/10.1016/j.cemconres.2013.09>.
- [10] Häkkinen, T. (1993). The influence of slag content on the microstructure, permeability and mechanical properties of concrete. Part 1: Microstructural studies and basic mechanical properties. *Cement and Concrete Research*. 23(2), 407-421. [https://doi.org/10.1016/0008-8846\(93\)90106-J](https://doi.org/10.1016/0008-8846(93)90106-J).
- [11] Yum, W. S., Jeong, Y., Yoon, S., Jeon, D., Jun, Y., & Oh, J. E. (2017). Effects of CaC₁₂ on hydration and properties of lime (CaO)-activated slag/fly ash binder. *Cement and Concrete Composites*. 84, 111-123. <https://doi.org/10.1016/j.cemconcomp.2017.09.001>.
- [12] Tashima, M. M., Reig, L., Santini, M. A., Moraes, J. B., Akasaki, J. L., Payá, J., & Soriano, L. (2017). Compressive strength and microstructure of alkali-activated blast furnace slag/sewage sludge ash (GGBS/SSA) blends cured at room temperature. *Waste and Biomass Valorization*. 8(5), 1441-1451. <https://doi.org/10.1007/s12649-016-9659-1>.
- [13] Rashad, A. M., Bai, Y., Basheer, P. A. M., Milestone, N. B., & Collier, N. C. (2013). Hydration and properties of sodium sulfate activated slag. *Cement and concrete composites*. 37, 20-29. <https://doi.org/10.1016/j.cemconcomp.2012.12.010>.
- [14] Rani, T. G., Tulasi, K., & Krishna, Y. S. R. (2017). Ground granulated blast furnace slag as an expansive soil stabilizer. *VFSTR Journal of STEM*. 3(1), 2455-2062.
- [15] Obuzor, G. N., Kinuthia, J. M., & Robinson, R. B. (2011). Utilisation of lime activated GGBS to reduce the deleterious effect of flooding on stabilised road structural materials: A laboratory

- simulation. *Engineering geology*. 122(3-4), 334-338. <https://doi.org/10.1016/j.enggeo.2011.06.010>.
- [16] Sekhar, D., & Nayak, S. (2019). SEM and XRD investigations on lithomargic clay stabilized using granulated blast furnace slag and cement. *International Journal of Geotechnical Engineering*. 13(6), 615-629. <https://doi.org/10.1080/19386362.2017.1380355>.
- [17] Vindula, S. K., Chavali, R. V. P., Reddy, P. H. P., & Srinivas, T. (2019). Ground granulated blast furnace slag to control alkali induced swell in kaolinitic soils. *International Journal of Geotechnical Engineering*. 13(4), 377-384. <https://doi.org/10.1080/19386362.2017.1359901>.
- [18] Yi, Y., Gu, L., & Liu, S. (2015). Microstructural and mechanical properties of marine soft clay stabilized by lime-activated ground granulated blastfurnace slag. *Applied Clay Science*, 103, 71-76. <https://doi.org/10.1016/j.clay.2014.11.005>.
- [19] Celik, E., & Nalbantoglu, Z. (2013). Effects of ground granulated blastfurnace slag (GGBS) on the swelling properties of lime-stabilized sulfate-bearing soils. *Engineering Geology*. 163, 20-25. <https://doi.org/10.1016/j.enggeo.2013.05.016>.
- [20] Wild, S., Kinuthia, J. M., Jones, G. I., & Higgins, D. D. (1999). Suppression of swelling associated with ettringite formation in lime stabilized sulphate bearing clay soils by partial substitution of lime with ground granulated blastfurnace slag (GGBS). *Engineering geology*. 51(4), 257-277. [https://doi.org/10.1016/S0013-7952\(98\)00069-6](https://doi.org/10.1016/S0013-7952(98)00069-6).
- [21] Guda, S. (2016). Efficacy of cement-stabilized GBS and GGBS cushions in improving the performance of expansive soils. *Jordan Journal of Civil Engineering*. 10(4), 529-542.
- [22] Islam, S., Haque, A., & Bui, H. (2016). 1-D compression behaviour of acid sulphate soils treated with alkali-activated slag. *Materials*. 9(4), 289. <https://doi.org/10.3390/ma9040289>.
- [23] Islam, S., Haque, A., Wilson, S. A., & Ranjith, P. G. (2015). Time-dependent strength and mineralogy of Lime-GGBS treated naturally occurring acid sulfate soils. *Journal of Materials in Civil Engineering*. 28(1), 04015077. [https://doi.org/10.1061/\(ASCE\)MT.1943-5533.0001333](https://doi.org/10.1061/(ASCE)MT.1943-5533.0001333).
- [24] Islam, S., Haque, A., Wilson, S. A., & Ranjith, P. G. (2014). Improvement of acid sulfate soils using lime-activated slag. *Proceedings of the Institution of Civil Engineers-Ground Improvement*. 167(4), 235-248. <https://doi.org/10.1680/grim.12.00033>.
- [25] Islam, S., Haque, A., & Wilson, S. A. (2013). Effects of curing environment on the strength and mineralogy of lime-GGBS-treated acid sulphate soils. *Journal of Materials in Civil Engineering*. 26(5), 1003-1008. [https://doi.org/10.1061/\(ASCE\)MT.1943-5533.0000887](https://doi.org/10.1061/(ASCE)MT.1943-5533.0000887).
- [26] Khayat, N., Nazarpour, A., & Ganjipour, S. S. (2021). Application of lime ground-granulated basic furnace slag (GGBS) in improving geotechnical properties of clayey soils in floodplain area, case study, Khuzestan plain. *Journal of Advanced Applied Geology*. 10(4), 669-682. DOI: 10.22055/AAG.2020.31309.2045.
- [27] Obuzor, G. N., Kinuthia, J. M., & Robinson, R. B. (2012). Soil stabilisation with lime-activated-GGBS- A mitigation to flooding effects on road structural layers/embankments constructed on floodplains. *Engineering Geology*. 15(1), 112-119. <https://doi.org/10.1016/j.enggeo.2012.09.010>
- [28] Seco, A., Del Castillo, J. M., Espuelas, S., Marcelino, S., & García, B. (2020). Sulphate soil stabilisation with magnesium binders for road subgrade construction. *International Journal of Pavement Engineering*. 1-11. <https://doi.org/10.1080/10298436.2020.1825711>.

- [29] Zhang, Y., Ong, Y. J., & Yi, Y. (2022). Comparison between CaO-and MgO-activated ground granulated blast-furnace slag (GGBS) for stabilization/solidification of Zn-contaminated clay slurry. *Chemosphere*. 286, 131860. <https://doi.org/10.1016/j.chemosphere.2021.131860>.
- [30] Wang, F., Xu, J., Zhang, Y., Shen, Z., & Al-Tabbaa, A. (2021). MgO-GGBS Binder–Stabilized/Solidified PAE-Contaminated soil: strength and leachability in early stage. *Journal of Geotechnical and Geoenvironmental Engineering*. 147(8), 04021059. [https://doi.org/10.1061/\(ASCE\)GT.1943-5606.0002569](https://doi.org/10.1061/(ASCE)GT.1943-5606.0002569).
- [31] Li, J. S., Chen, L., Zhan, B., Wang, L., Poon, C. S., & Tsang, D. C. (2021). Sustainable stabilization/solidification of arsenic-containing soil by blast slag and cement blends. *Chemosphere*. 271, 129868. <https://doi.org/10.1016/j.chemosphere.2021.129868>.
- [32] Keramatikerman, M., Chegenizadeh, A., & Nikraz, H. (2018). Effect of slag on restoration mechanical characteristics of Ethanol Gasoline–Contaminated Clay. *Journal of environmental engineering*. 144(7), 06018001. [https://doi.org/10.1061/\(ASCE\)EE.1943-7870.0001386](https://doi.org/10.1061/(ASCE)EE.1943-7870.0001386).
- [33] Skempton, A. W. (1953). The colloidal activity of clays. *Selected papers on soil mechanics*. 106-118.
- [34] Mitchell, J.K. (1976). *Fundamentals of Soil Behavior*. University of California., Berkeley. John Wiley & Sons, Inc., New-York, NY, 422 p.
- [35] AFNOR NF 14227 - 2. (2005). Mixtures treated with hydraulic binders. Specification. Part 2: Mixture treated with slag.
- [36] AFNOR NF P 94-051. (1993). Soils: Reconnaissance and tests – Determination of the Atterberg limits – Liquid limit to the cupel - Plasticity limit to the roller.
- [37] AFNOR NF P 94-093. (1999). Soils: Reconnaissance and Tests – Determination of the compaction references of a material – Normal Proctor test – Modified Proctor test.
- [38] AFNOR NF P 94-078. (1997). Soils: Reconnaissance and tests - CBR index after immersion - Immediate CBR index - Immediate bearing index - Measurement on sample compacted in the CBR mould.
- [39] AFNOR NF P 94-077. (1997). Soils: Reconnaissance and tests – Uniaxiale compression tests.
- [40] AFNOR NF P 94-071-1. (1997). Soils: Reconnaissance and tests – Box straight shear tests – Part 1: Direct shear.
- [41] Goodarzi, A. R., & Salimi, M. (2015). Stabilization treatment of a dispersive clayey soil using granulated blast furnace slag and basic oxygen furnace slag. *Applied Clay Science*. 108, 61-69. <https://doi.org/10.1016/j.clay.2015.02.024>.
- [42] Al-Rawas, A. A. (2002). Microfabric and mineralogical studies on the stabilization of an expansive soil using cement by-pass dust and some types of slags. *Canadian geotechnical journal*. 39(5), 1150-1167. <https://doi.org/10.1139/t02-046>.
- [43] Al-Mukhtar, M., Lasledj, A., & Alcover, J. F. (2010). Behaviour and mineralogy changes in lime-treated expansive soil at 20 C. *Applied clay sciences*. 50(2), 191-198. <https://doi.org/j.clay.2010.07.023>
- [44] GTS. (2000). The technical guide, soils treatment with lime and/or hydraulic binders in backfill and subgrade. LCPC-SETRA, France.

Prediction of Deflection Behavior of NSM Strengthened Reinforced Concrete Beam Using Fuzzy Logic

K. M. Darain^{1,3*}, M.A. Hossain², M.Z. Jumaat³, M. Arifuzzaman⁴

¹Science, Engineering and Technology School, Khulna University, Bangladesh

²Department of Nuclear Science & Engineering, Military Institute of Science and Technology, Dhaka, Bangladesh

³Department of Civil Engineering, Faculty of Engineering, University of Malaya, Malaysia

⁴Civil and Environmental Engineering, King Faisal University, KSA

* e-mail: kmdarain@arch.ku.ac.bd

Abstract

This paper aims to present a deflection prediction model of Near Surface Mounted (NSM) Reinforce Concrete (RC) beams using the Fuzzy Logic Expert System (FLES) with different types of membership functions (MF). The absence of a complete theoretical deflection prediction model of NSM-strengthened RC beams persuades this research to develop an Artificial Intelligence (AI) based prediction model using FLES. The proposed model uses triangular and trapezoidal MF to predict the deflection behavior of six NSM-strengthened RC beams. The research variables are strengthening materials and NSM bar length. In this study, two inputs (applied load and variable length) were used to predict two outputs (deflection of two types of strengthened RC beams). The relative error of predicted values was within 5% and the suitability of fit was close to 1.0 which affirms the efficacy of the FLES. Besides, a tiny difference was detected using triangular and trapezoidal MF for the prediction model.

Keywords: Artificial Intelligence, fuzzy logic, CFRP, prediction model

1 Introduction

Structural strengthening can upgrade the existing underperforming structural system to carry additional loads and lengthen the service life. Various strengthening approaches are being used in professional works and Externally Bonded Reinforcement (ERB) is the most familiar among these techniques. However, EBR demonstrated premature debonding failure due to excessive shear stresses at the interface of the strengthening material and concrete [1, 2]. On the other hand, the Near Surface Mounted (NSM) technique is comparatively effective due to its superior flexural and shear stress along with better bonding arrangement with the concrete substrate [3, 4]. In this technique, the Carbon Fiber Reinforced Polymer (CFRP) bar or strip is fixed in the groove of the concrete cover with epoxy [5-8]. A superior concrete cutter with a diamond cutting edge was operated to create the essential NSM grooves in the longitudinal direction at the bottom side of the RC beam. The special epoxy adhesive was used to cover the CFRP or steel bar in the groove. The resulting assemblage of the NSM system demonstrates less possibility of early failures and improves the safety for fire and vandalism [9].

Deflection is the most important parameter to determine the serviceability of a structural element. It is essential to predict the deflection behavior of a new structural technique to make it popular in professional applications. However, there is a lack of a complete mathematical model for NSM-strengthened RC beams to predict the load-deflection behavior. To address this gap, the present study is proposing a deflection prediction model using the Fuzzy Logic Expert System (FLES) which is a simple, rapid, reliable, and artificial intelligence-based alternative method. Already a number of researchers have used this technique in similar applications [10-13]. FLES utilizes expert judgments with a rational system that is very close to human reasoning rather than a huge experimental output [14, 15].

The present study has a goal to develop a simple but accurate deflection prediction model of NSM strengthened RC beam using FLES. Another aim is to assess and compare the efficacy of triangular and trapezoidal Membership Function (MF) which was used in this FLES. It is expected that the approach could be directly applied to real applications without solving complex mathematical models.

2 Methodology of the Experimental Part

2.1 Test Matrix

Two parameters have been used in this study. They were: types of strengthening materials (CFRP and steel) and bond lengths (1600 mm, 1800 mm, and 1900 mm). For each type of CFRP or steel material, their bond lengths were varied to 1600 mm, 1800 mm, and 1900 mm. In total seven RC beams were experimented with in a four-point bending loading condition. For all the cases, the groove dimension of the NSM-strengthened RC beams was 24 mm × 24 mm. The matrix of the laboratory testing is shown in Table 1.

Table 1: The experimental test matrix

Sl. no.	Identification of beam	Description	Total bond length (mm)
1	CB	Control RC beam	-
2	N1.9F	NSM 12 mm CFRP bar	1900
3	N1.9S	NSM 12 mm Steel bar	1900
4	N1.8F	NSM 12 mm CFRP bar	1800
5	N1.8S	NSM 12 mm Steel bar	1800
6	N1.6F	NSM 12 mm CFRP bar	1600
7	N1.6S	NSM 12 mm Steel bar	1600

2.2 Experimental Materials and Set-up

RC beam specimens were prepared in the laboratory with 28 days' cube compressive and flexural strength of 43.24 MPa and 5.01 MPa, respectively. The yield stress of the 12 mm diameter deformed RC beam and NSM reinforcement were 400 and 520 MPa respectively having a common Modulus of Elasticity E of 200 GPa. The ultimate strength and E of a 12 mm diameter sand-treated CFRP bars were 2400 MPa and 165 GPa, respectively.

The experimental set-up includes under-reinforced RC beams which were 2.3 m long and had a 2 m effective span with a rectangular cross-section of (125x250) mm (Figure 1). The main

bar, top hanger bar, and shear reinforcement were 12 mm, 10 mm, and 8 mm in diameter, respectively. The experiments were arranged in a 500 kN capacity Universal Testing Machine (UTM) where a four-point bending load was applied to the specimen.

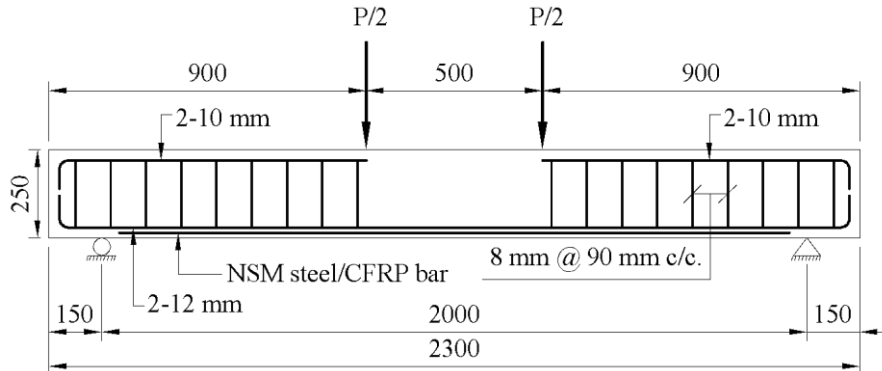


Figure 1: RC beam specimen with NSM reinforcement

3 Fuzzy Logic Expert System Prediction Model

3.1 Fuzzy Inference System

The basic Mamdani type two-dimensional FLES comprises four major elements [16]. These are: (1) Fuzzification gets crisp numeric inputs and translates the data into the fuzzy form required by the decision-making logic, (2) Rule base elements occupy an array of if-then rules. This measures the information that human connoisseurs have collected about resolving a particular glitch, (3) Inference generates a control action agreeing to the data delivered by the fuzzification component and by utilizing knowledge, and (4) Defuzzification analyzes the real output. It exchanges fuzzy output for an exact numerical value (crisp value).

3.2 Membership Function

MF refers to the approach that every single location in the input area is diagrammed to a membership value (or level of membership) stuck between 0 and 1. The input area is sometimes denoted as the universe of discourse, a decorative term for a simple idea [17, 18]. The μ_A is generally denoted as MF of a fuzzy set. For component x of X in a fuzzy set, the membership degree of x is termed $\mu_A(x)$. According to different graphical shapes, several MFs are developed. The Fuzzy Logic Toolbox in MATLAB operates with eleven built-in MF. Beginning from several basic functions, those eleven functions are formed. Those basic functions are the Gaussian distribution, the piecewise linear function, the quadratic & cubic polynomial curves, and the sigmoid curve. The membership with piecewise linear functions is the simplest. Among this category, a triangular function is mostly used due to its simplicity and rigorousness. Basically, these choices of the MF depend on the nature of the work [19]. Figure 2 showed the triangular and trapezoidal MF which were used in this study.

The triangular MF is expressed by three parameters a , b , and c assumed by the expressions, where the a and c parameters are positioned at the feet of the triangle and b at the peak.

$$f(x, a, b, c) = \max \left\{ \min \left(\frac{x-a}{b-a}, \frac{c-x}{c-b} \right), 0 \right\} \quad (1)$$

The trapezoidal MF is designated by four parameters a , b , c , and d assumed by the expressions; where the a and d parameters are positioned at the bases of the trapezoid and b and c are placed at the top.

$$f(x; a, b, c, d) = \max \left\{ \min \left(\frac{x-a}{b-a}, 1, \frac{d-x}{d-c} \right), 0 \right\} \quad (2)$$

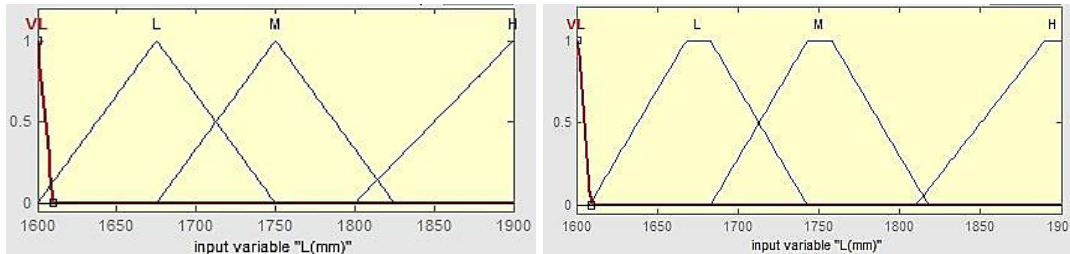


Figure 2: Example of MF for input variable (left) Load F ; Length L (right)

3.3 Fuzzy Logic Development

Two input parameters were used in this study. They were: monotonic applied load F and variable bond length L . From the experimental results, it was observed that the input parameters F and L significantly influenced the deflection of NSM steel (DS) and FRP (DF) strengthened RC beams, and hence these two types of deflection were considered as two output parameters. The developed FLES model consisting of input parameters of applied load F and bond length L has been considered with six linguistic variables such as very low (VL), low (L), low medium (LM), medium (M), high (H), and very high (VH). However, the output parameters of deflection for steel bar (DS) and CFRP (DF) have been considered with four linguistic variables such as low (L), medium (M), high (H), and very high (VH). The applied load F is considered within the range from 0 to 100 kN, whereas the bond length L is between 1500 mm and 1900 mm. The Fuzzy Inference System (FIS) has been developed based on the Mamdani max-min inference approach considering the center of gravity defuzzification method [14]. A total of 36 fuzzy inference rules have been formed based on experiences and knowledge. For instance, some of the rules were shown in Table 2.

Table 2: Fuzzy Rules for the Deflection model

Rule no.	Variables (Input)		Yield variables	
	F	L	DS	DF
1	VL	VL	L	L
6	VL	VH	L	L
....
15	LM	LM	M	M
20	M	L	M	M
....
35	VH	H	H	H
36	VH	VH	VH	VH

For example, an explanation of IF-THEN rules is described as follows:

- Rule 1: If applied force F is very low (VL), and bond length L is very low (VL) then deflection for steel bar strengthened beams (DS) is low (L), and deflection for CFRP bar strengthened beams (DF) is low (L).
- Rule 36: If applied force F is very high (VH), and bond length L is very high (VH) then deflection for steel bar strengthened beams (DS) is very high (VH), and deflection for CFRP bar strengthened beams (DF) is very high (VH).

3.4 Mathematical Error Criterion

The following statistical indicators were picked to assess the efficacy of the FLES. The relative error (ε) of the deflection prediction system using FLES was calculated using Equation 3.

$$\varepsilon = \sum_{i=1}^n \left| \frac{y_i - \hat{y}_i}{y_i} \right| \frac{100\%}{n} \quad (3)$$

Furthermore, the following Equation 4 was used to compute the suitability of fit (η) of this FLES prediction system.

$$\eta = \sqrt{1 - \frac{\sum_{i=1}^n (y_i - \hat{y}_i)^2}{\sum_{i=1}^n (y_i - \bar{y})^2}} \quad (4)$$

Here, n is the number of data, y_i is the assessed value, \hat{y}_i is the predicted value, and \bar{y} is the mean of assessed values. The number for the relative error presents the deviation between the predicted and assessed values. A flawless system should be the same as a null number. The suitability of fit offers the capacity of a formed system where the maximum value is 1.

4 Results and Discussion

4.1 Experimental Results

Experimental results of the NSM-strengthened RC beams with variable bond lengths and strengthening materials are summarized below in Table 3.

Table 3: Summary of experimental test results of NSM beams

Beam ID	P_{cr} (kN)	Δ_{cr} (mm)	P_y (kN)	Δ_y (mm)	P_u (kN)	Δ_u (mm)
CB	10.6	0.3	61.0	7.7	64.4	24.7
N1.9F	15.0	0.3	104.5	10.7	133.2	19.2
N1.9S	23.0	0.7	101.3	10.0	103.8	12.4
N1.8F	14.0	0.6	110.6	13.0	130.8	18.6
N1.8S	15.5	1.0	94.7	10.8	99.6	16.8
N1.6F	17.5	0.4	83.6	8.5	109.5	13.6

N1.6S	14.4	0.7	88.7	8.3	94.1	9.4
-------	------	-----	------	-----	------	-----

Table 3 demonstrated three distinct phases of strengthened RC beams where the load was gradually increased from zero to the highest magnitude where the beams failed. During the experimental program under increasing load, the first crack appeared which was termed as first crack load (P_{cr}) and its corresponding deflection was Δ_{cr} . The next phase was yielding where the beam showed significant deflection (Δ_y) and went to a plastic region under yield load (P_y). The last segment was ultimate load (P_u) which experienced the maximum stress that the beam could withstand and after this deflection (Δ_u) at the ultimate load point the beam started crushing and a non-linear response could be observed. If the strengthened beams were compared with the control RC beam it could be easily visualized that there was a significant improvement in first crack load, yield load, ultimate load, and their corresponding deflection over the control specimen.

4.2 FLES Model Analysis

The simulated output of the prediction model was checked thoroughly by changing the input values. In Figure 3, the rule viewer is presented where F and L were 50 kN and 1750 mm respectively. The corresponding strengthened RC beams deflection of steel bar (DS), and CFRP bar (DF) were found 4.1 mm and 4.99 mm, respectively. The input data (F and L) in the fuzzy inference system generated numerous fuzzy rules and these rules were assessed and the predicted output (DS and DF) was generated.

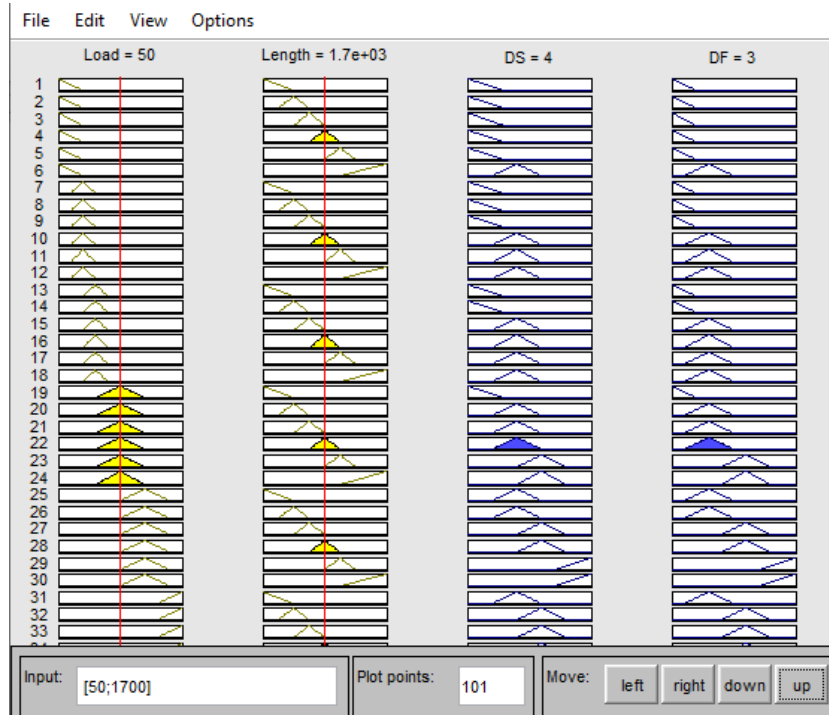


Figure 3: Input and output parameters in rule viewer

The Fuzzy Logic Toolbox in MATLAB was used to develop the deflection prediction of strengthened RC beams. The output of the model has been checked thoroughly by changing the input values. An example has been shown in Figure 3 as a rule viewer of how the parameters

are changed using IF-THEN rules. In case of the applied load F is close to 50 kN and the length of rod L is 1700 mm, then all the thirty-six rules are assessed simultaneously to determine the outputs namely deflection for steel bar strengthened beams (DS), and deflection for CFRP bar strengthened beams (DF) as 4 mm and 3 mm, respectively.

Several fuzzy control surfaces were simulated and depicted in Figure 4 and Figure 5. It demonstrated the dynamic nature of the fuzzy simulation over time which synchronized with the input and output parameters. These 3D diagrams were exercised to validate the rules and the MF. It is also important to monitor the parameters which could significantly improve the output. The incremental trend of the control surface demonstrated the impact of the increasing load on both steel and CFRP-strengthened RC beams.

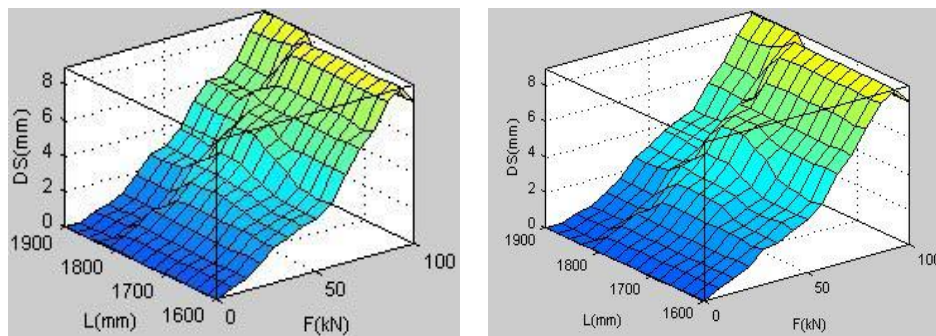


Figure 4: Control surface for deflection of NSM steel beam using (a) triangular MF, and (b) trapezoidal MF

Deflection increased gently at the initial phase while the applied load was also escalating till a particular value. It grasped to its peak once applied load and bar length were also at their maximum stages. Due to the growing stiffness of the RC beam, the percentage increase of deflection was insignificant for the case of extended steel and CFRP bar length. Therefore, the deflection was not as much for a reduced level of F and L and that is quite expected.

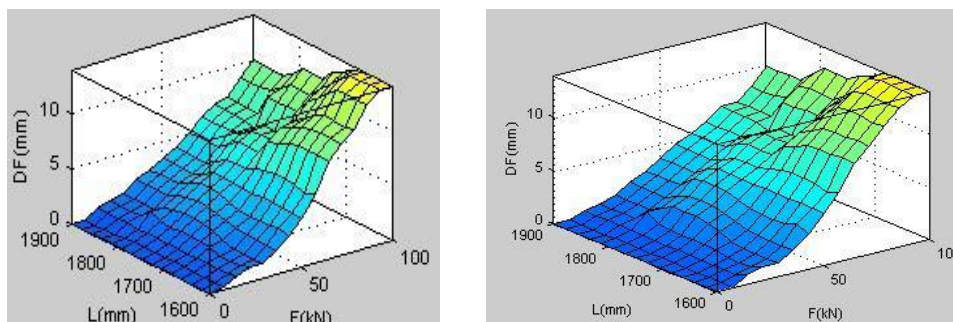


Figure 5: Control surface for deflection of NSM CFRP beam using (a) triangular MF, and (b) trapezoidal MF

If these control surfaces are analyzed carefully, it can be easily understood that the difference between the triangular and trapezoidal MF is negligible, and their effect is also less significant. It was early mentioned that the selection of MF and its performance is dependent on the nature of the work and the data pattern. Some researchers also agreed that the triangular MF gave a better response, and the trapezoidal MF showed an identical result [19]. However, those works are involved with the induction motor drive controller. So, the present study of the deflection prediction model and its results also support the same hypothesis as others postulated.

4.3 Analysis of Error and Discussion

By using Equations 3 and 4, the variation between experimental output and fuzzy predicted results could be understood properly. These two results were investigated considering gradually varying load and NSM bond length. Figures 6 and 7 illustrated the correlations among experimental and predicted outputs for the deflection of steel and CFRP bar. For the deflection of RC beam using an NSM steel bar, the correlation coefficient and mean relative error were 0.9712 and 10.20% for the triangular membership function, and 0.984 and 8.75% for the trapezoidal membership function, respectively (Figure 6). For CFRP bar deflection, the correlation coefficient and mean relative error were 0.9809 and 9.24% for triangular MF and 0.9788 and 8.04% for trapezoidal MF, correspondingly (Figure 7).

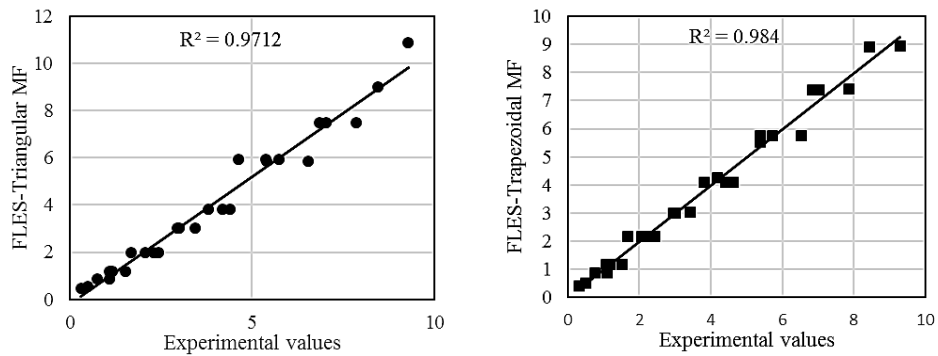


Figure 6: Correlation between experimental and fuzzy output of steel bar deflection with (a) triangular MF; (b) trapezoidal MF

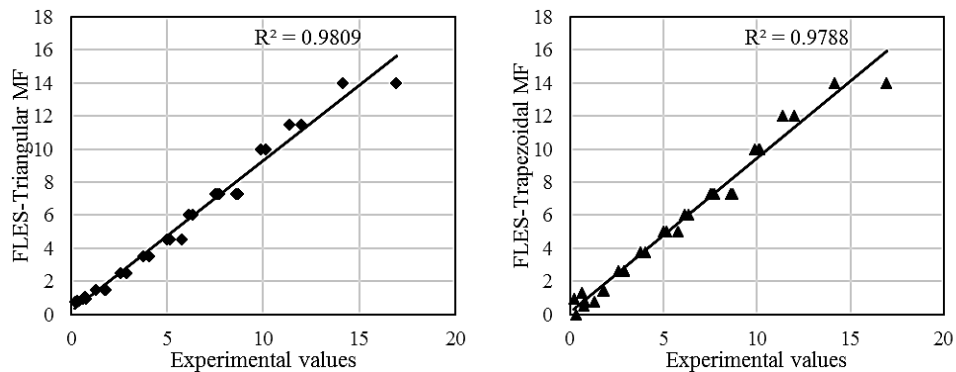


Figure 7: Correlation between experimental and fuzzy output of CFRP bar deflection with (a) triangular MF; (b) trapezoidal MF

The experimental outcomes confirmed the good prediction accuracy of the fuzzy inference model. From Figure 6 and 7, it was observed that the correlation coefficient for both steel and CFRP NSM beam showed similar superior performance which was very close to 1. However, trapezoidal MF showed slight improved correlation over triangular MF for steel bar. However, in case of CFRP bar the correlation of triangular MF was improved than trapezoidal MF. The relative error of trapezoidal MF was less compared to the triangular MF for both steel and CFRP NSM beam.

5 Conclusion

This study developed a deflection prediction model for NSM-strengthened RC beams. Variable applied load and various bond lengths of NSM reinforcement were the input parameters to attain the deflection of NSM-strengthened RC beams having steel and CFRP bars as output. The triangular and trapezoidal MFs were considered for the fuzzification process in this analysis. These MFs were chosen deliberately to check whether there was any significant difference and impact on the fuzzification process or not. The conclusions are as follows:

- The outputs of the suggested FLES model conformed well to the experimental results. The experimental and predicted deflection showed a good correlation between steel and CFRP-strengthened RC beams. The relative error of the predicted values was obtained to be inside the standard ceiling of 5% and the suitability of fit was very close to 1.0. These outcomes indicate the excellent functioning of the developed model.
- No significant difference was observed for the triangular and trapezoidal MF for the prediction model using FLES. The variance of the correlation coefficient and relative errors were also negligible. The slight differences in these statistical parameters would not affect the performance of the proposed model. This observation is also supported by different researchers who worked in other areas of soft computing research.

Acknowledgments

The authors gratefully acknowledge the support given by University of Malaya (UM) for funding the study through the High Impact Research Grant UM.C/HIR/MOHE/ENG/36 (D000036-16001).

References

- [1] Lousdad A, Megueni A and Bouchikhi AS 2010 Geometric edge shape based optimization for interfacial shear stress reduction in fiber reinforced polymer plate retrofitted concrete beams *J. Comp. Mat.* **47** 911-8
- [2] Abdallah M, Al Mahmoud F, Khelil A and Mercier J 2021 Efficiency of EB CFRP composites for flexural strengthening of continuous RC beams: A comparative study with NSM CFRP rods *J. Struc.* **34** 1567-88
- [3] Zhang S S, Yu T and Chen G M 2017 Reinforced concrete beams strengthened in flexure with near-surface mounted (NSM) CFRP strips: Current status and research needs *J. Comp. Part B: Engg.* **131** 30-42
- [4] Farahi B, Esfahani M and Sabzi J 2019 Experimental investigation on the behavior of reinforced concrete beams retrofitted with NSM-SMA/FRP *Amirkabir J. Civil Eng.* **51** 685-98
- [5] Lorenzis L De and Teng J G 2007 Near-surface mounted FRP reinforcement: An emerging technique for strengthening structures *J. Comp. Part B: Eng* **38** 119-43
- [6] Al-Obaidi S, Saeed Y M and Rad F N 2020 Flexural strengthening of reinforced concrete beams with NSM-CFRP bars using mechanical interlocking *J. Build. Eng.* **31** 101422
- [7] Barris C, Sala P, Gómez J and Torres L 2020 Flexural behaviour of FRP reinforced concrete beams strengthened with NSM CFRP strips *J. Comp. Struct.* **241** 112059
- [8] Haddad R H and Yaghmour E M 2020 Side NSM CFRP strips with different profiles for strengthening reinforced concrete beams *J. Build. Eng.* **32** 101772
- [9] Bilotta A, Ceroni F, Ludovico M Di, Nigro E, Pecce M and Manfredi G 2011 Bond efficiency of EBR and NSM FRP systems for strengthening concrete members *J.Comp. Const.* **15** 757-72

- [10] Darain K M U, Jumaat M Z, Hossain M A, Hosen M A, Obaydullah M Huda M N 2015 Automated serviceability prediction of NSM strengthened structure using a fuzzy logic expert system *J. Exp. Sys. App.* **42** 376-89
- [11] Darain K M U, Shamshirband S, Jumaat M Z and Obaydullah M 2015 Adaptive neuro fuzzy prediction of deflection and cracking behavior of NSM strengthened RC beams *J. Const. Build. Mat.* **98** 276-85
- [12] Akintunde O P 2021 Fuzzy logic design approach for A singly reinforced concrete beam *J. Civil Engg. Res. Tech.* **SRC/JCERT-111** 3
- [13] Govardhan P, Kalapatapu P, and Pasupuleti V D K 2021 Identification of multiple cracks on beam using fuzzy logic *Proc. Int. Conf. on Emerging Techniques in Computational Intelligence* (Hyderabad, India: IEEE) p 165-69.
- [14] Hossain A, Rahman A and Mohiuddin A 2012 Fuzzy evaluation for an intelligent air-cushion tracked vehicle performance investigation *J. Terramechanics* **49** 73-80
- [15] Hossain A, Singh R, Choudhury I A and Bakar 2013 A Energy efficient wind turbine system based on fuzzy control approach *J. Proc. Engg.* **56** 637-42
- [16] Passino K M, Yurkovich S and Reinfrank M 1998 *Fuzzy control* (California: Addison-Wesley)
- [17] Zadeh L A 1965 Fuzzy sets *J. Inf. Cont.* **8** 338-53
- [18] Shukla K 2000 Neuro-genetic prediction of software development effort *J. Inf. Soft. Tech.* **42** 701-13
- [19] Zhao J and Bose B K 2002 Evaluation of membership functions for fuzzy logic controlled induction motor drive *Proc. Annual Conf. on the Industrial Electronics Society* vol 1 (Seville, Spain: IEEE) p 229-34

Explicit Modeling of the Cyclic Behavior under a Large Number of Cycles: Application to the Case of Sand

Djessas Imed Eddine¹, Amrane Moussa^{2*}, Messast Salah¹

¹Department of Civil Engineering, Laboratory LMGHU, University 20 August 1955 of Skikda, BP 26, Road Elhadeik, 21000 Skikda, Algeria

²Department of Civil Engineering, Laboratory LGC-ROI, University of Batna 2, 53, Road of Constantine Fesdis, 05078 Batna, Algeria

*e-mail: moussa.amrane@univ-batna2.dz

Abstract

The estimation of deformations after a large number of cycles is a major concern of geotechnical engineers. This paper presents an explicit formulation of the accumulated cyclic volumetric strain. This study is concerned with cyclic triaxial tests simulated through the calculation by the Finite Element Method. The parameters of identification of the first cycle (loading-unloading) are determined step by step, using, as a soil behavior model, the Soft Soil Hardening Model, then, the behavior of the soil after N cycles ($N > 1000$) is simulated through the formulation proposed as a pseudo-creep. The comparison of the proposed method with several cyclic triaxial tests and a shallow foundation under cyclic loading approves the good compatibility of the proposed formula for this type of problem. This study does not take into account the effect of the grain size and the void ratio, things that can be translated by the coefficients $C1$ and $C2$.

Keywords: cyclic, volumetric strain, triaxial test, drained condition, sand

1 Introduction

It is very important to know the prediction of the irreversible cyclic deformations of the soil and their accumulation which may require important maintenance [1-6], to properly measure the dimensioning of structures subject to or located near cyclical excitation such as offshore structures, wind turbine foundations, silos, bridges, industrial installations, railways, tanks.

However, the complexity of mastering the problem of modeling the cyclic behavior of structures, mentioned above, has rendered many Geotechnical researchers interested in finding reliable solutions [7-9]. Among them, a lot of research is concentrated on the behavior of granular material under cyclic loading [10, 11]. Different studies are based on the test from the cyclic triaxial test and focus on the permanent displacements of sand with cyclic loading [3, 13–17, 18–20]. Other researchers have concentrated on the modeling of cyclic behavior under a large number of cycles [21–26]. Several researchers are interested in the settlement of shallow foundations under a high number of cycles [27-31].

There are two methods to predict the cyclic behavior of soil: the implicit method (incremental) and the explicit method. The implicit method is not recommended [11, 12, 17, 32]. The importance of explicit models appears especially in a large number of cycles ($N > 1000$). In such models, only one or a few initial cycles are calculated using an incremental calculation (implicit method), and the remaining cycles are treated as pseudo-creep.

This paper presents a simpler explicit model for the prediction of volumetric strains after a large number of cycles. The presented model in this work is an improvement from the one presented by [21]. This formulation offers a hyperbolic curve volumetric deformation based on the identification parameters of the average cyclical path and those of the first cycle which will be processed by the finite element calculation using the Plaxis program, in which the behavior of soil is modeled through the hardening soil model (HSM).

Furthermore, this formulation is compared with the measured value applied on a shallow foundation [33].

2 Research Background

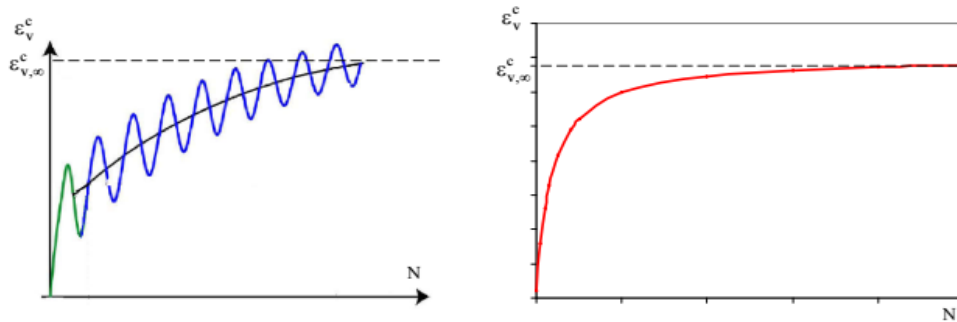
In such models, only one or a few first cycles are calculated using an incremental calculation, and the rest of the cycles will be treated as pseudo-creep. Several works have been concentrated in this direction, to better establish models which provide an estimate as faithful as possible to the cyclic behavior of the soil.

Thanopoulos [34] presented a hyperbolic formulation for estimating the delayed axial strains and another for the volumetric strain by introducing the concept of voluminous Poisson's ratio. The model presented by [9], describes the accumulation of axial and volume deformation by means of a logarithmic formulation, although this model was invested with a high number of cycles, it presents some deficiencies according to [31] such as the cyclic flow rule along with the boost in the acceleration of accumulation with the upturn in the mean pressure turns out to be inconsistent with the empirical values of [10], [32] proposed a model for the prediction of the accumulation of volumetric and deviatoric deformations depend on a power formulation, this model doesn't consider the amplitude of the deformation volume and the shape of the cyclic loading loop [7] proposed a model describing the densification of sands, using a logarithmic formulation, his disadvantage is that it is founded on a limited number of cycles and that it doesn't consider the amplitude of the volumetric strain and the shape of the cyclic loading loop [8] proposed a model for the prediction of cumulative deformations based on the results of tests carried out by [32] on sand with a number of cycles of the order of 100.000, the downside of this model is that it calls for implicit models to calculate the parameters of the identification cycle which is the second cycle.

The present study presents a simpler explicit model for the prediction of axial deformations after a very high number of cycles and the constitutive modeling of the cyclic behavior of granular material in a drained condition. A hyperbolic formulation proposed for the axial deformation based on the identification parameters of the average cyclic path and those of the first cycle, which will be treated by a finite element calculation using the Plaxis calculation code and the material modeled by the Hardening Soil Model (HSM).

3 Proposed Model

In this study, the proposed formulation entails determining the evolution of the accumulated volumetric strain, according to the cyclic average path, which is referred to as the pseudo-cyclic (Figure 1). Firstly, the determination of the parameters of identification in the first cycle (load-unload) is achieved through step-by-step calculation by Plaxis 8.2. Secondary, conforming to the cyclic average level, the limit cyclic level η_l , the characteristic cyclic level η_c , and the cumulative strain ($\varepsilon_{v,\infty}^c$) when $N \rightarrow \infty$ are determined. With this approach, we consider that cyclic pseudo creep (the evolution of the strain, regarding the number of cycles) is controlled mainly by the effect of the irreversible deformation after the first cycle ($\varepsilon_{v,1}^c$), and the calculation of the cumulative strain ($\varepsilon_{v,\infty}^c$) when $N \rightarrow \infty$.



a- Complete cyclic path

b- Average cyclic path

Figure 1: Evolution of cumulative volumetric strain after N cycles

The formulation of the cumulative volumetric strain after N cycles $\varepsilon_{v,N}^c$ can be expressed as follows from Equation 1.

$$\varepsilon_{v,N}^c = \frac{\sqrt{N}}{\frac{1}{\varepsilon_{v,1}^c} + \frac{\sqrt{N}-1}{\varepsilon_{v,\infty}^c}} \quad (1)$$

This last formula is simple and makes it possible to express the cumulative volume strain; it depends on four parameters: The number of cycles N , the number of the basic identification cycle and the corresponding strain, as well as the strain for an infinite number of cycles.

$\varepsilon_{v,\infty}^c$: The cumulative strain when $N \rightarrow \infty$ from Equation 2.

$\varepsilon_{v,1}^c$: The irreversible deformation after the first cycle.

The cumulative volumetric strain at infinity ($\varepsilon_{v,\infty}^c$) can be expressed in terms of η_{av} , η_{car} and η_l [21]:

$$\varepsilon_{v,\infty}^c = \varepsilon_{v,0}^c \frac{\left(\frac{\eta_{av}}{\eta_{car}} - 1\right)}{\left(1 - \frac{\eta_{av}}{\eta_l}\right)} \quad (2)$$

$$\eta_{av} = \frac{q_{av}}{p_{av}} \quad (3)$$

where q_{av} : Average of deviator during the cycle

p_{av} : Average of mean pressure during the cycle.

$$\eta_{car} = \frac{6 \sin \phi_c}{3 - \sin \phi_c} \quad (4)$$

where ϕ_c : Critical friction angle.

$$\eta_l = \frac{6 \sin \phi_l}{3 - \sin \phi_l} \quad (5)$$

where ϕ_l : Limit friction angle.

$\varepsilon_{v,0}^\infty$ Function of $\Delta\eta$ from Equation 6.

$$\varepsilon_{v,0}^\infty = \frac{C_1 \Delta\eta}{\Delta\eta + C_2} \quad (6)$$

$$\Delta\eta = \eta_{max} - \eta_{min} \quad (7)$$

With: $\eta_{max} = \frac{q_{max}}{p_{max}}$, $\eta_{min} = \frac{q_{min}}{p_{min}}$, C_1 and C_2 obviously depend on η_{av} and other parameters such as porosity and particle size. It is proposed for sand $C_1=4$ and $C_2=0.3$ [21].

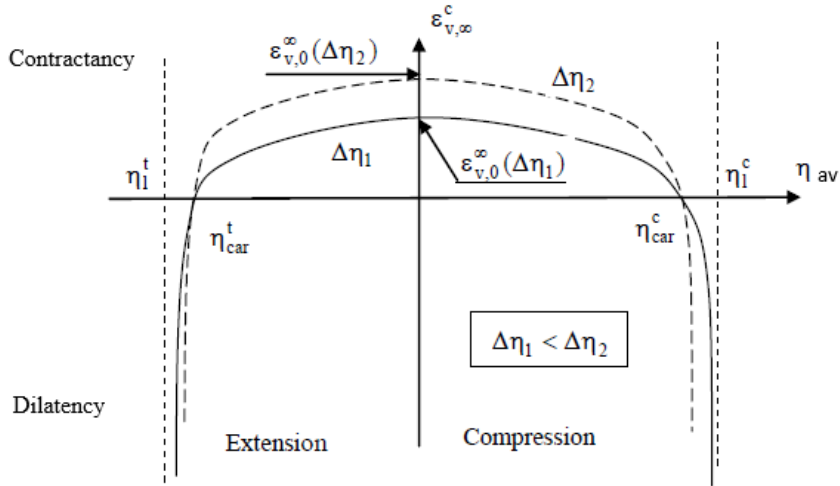


Figure 2: $\varepsilon_{v,0}^\infty$ in the function of $\Delta\eta$

Figure 2 illustrates the relationship between the different cyclic parameters where it represents the variation of the cumulative volumetric strain at infinity ($\varepsilon_{v,0}^\infty$) with terms of η_{av} , η_{car} and η_l in the contracting domain and the dilatancy domain.

4 Simulation and Results

To test the reliability of the proposed formulation, we proceed to the comparison of results obtained by this method with those presented in the work of [34].

Thanopoulos [34] has conducted cyclic tests on the sand of Plancoët relatively loose characterized by its dry unit weight of 12.5 kN/m^3 and the stress deviation - axial strain and volume strain - axial strain deflection curves for a monotonic triaxial test and three series of cyclic tests. Table 1 summarized the principal cyclical measured and calculated parameters for all tests. The behavior of the material will be reproduced using the HSM (Hardening soil model) model by representing the curves ε_v-N employing the finite element program Plaxis. Based on test 8 (monotonic test), the Plancoët sand will be characterized according to the HSM model:

$E_{50} = E_{oed} = 6689 \text{ kPa}$, $E_{ur} = 867.10^2 \text{ kPa}$, $\varphi = 37.6^\circ$, $C = 0$, $\psi = 6^\circ$, $R_f = 0.9$, $m = 0.4$ [21].

Table 1: Parameters of the cyclic tests in compression achieved on the fine sand of Plancoët, according to [34]

Test	σ_3 kPa	q_{max} kPa	q_{min} kPa	η_{moy}	$\Delta\eta$	ε_{v0}^∞	ε_v^∞ Calculated[%]	ε_v^∞ Test[%]	ε_{v1}^∞ Calculated [%]	ε_{v1}^∞ Measured[%]
2	40	56	38	0.84	0.23	1.75	1.46	1.60	0.48	0.50
4a	80	166	9	0.80	1.12	3.15	2.70	2.50	1.20	1.50
12	160	148	6	0.41	0.67	2.76	2.63	2.20	0.75	0.80
14a	160	154	37	0.50	0.51	2.53	2.36	1.40	0.79	0.70
14b	160	250	37	0.69	0.81	2.92	2.60	2.60	1.30	1.40
1	40	89	4	0.84	1.18	3.19	2.68	1.50	0.70	0.80
4b	80	237	115	1.27	0.52	2.53	0.91	2.70	1.10	2.50
7	80	166	67	0.98	0.57	2.62	2.01	3.60	1.00	2.00
9	80	172	116	1.13	0.27	1.91	1.21	2.60	1.10	2.30
11	40	125	37	1.21	0.82	2.93	1.47	2.10	0.84	1.60
13	160	323	3	0.76	1.19	3.19	2.78	4.50	1.50	2.60
16	80	182	143	1.21	0.17	1.47	0.73	1.60	1.20	0.95

According to [21], the tests of [34] representing coherence with the monotone test are 4a, 12, 14a, and 14b. For this purpose, this study is restricted to taking into account only those tests.

The simulation results are given in Figures 3 and 4.

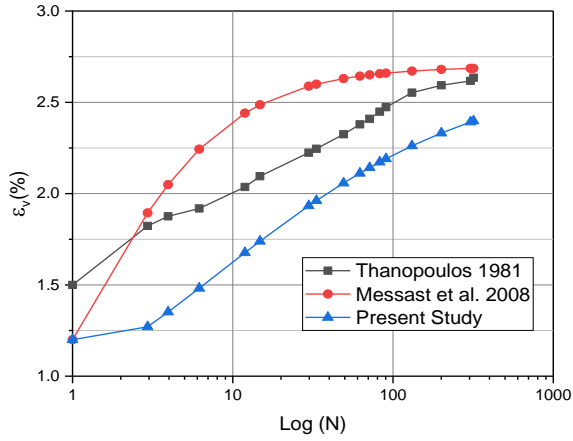


Figure 3: Curve ε_v^c versus $\log(N)$ for test 4a

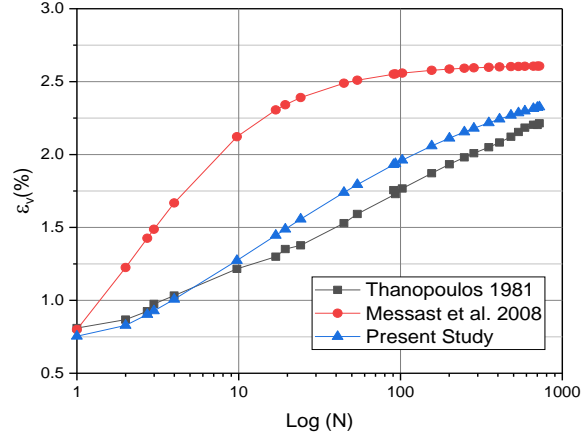


Figure 4: Curve ε_v^c versus $\log(N)$ for test 12

Figures 3 to 6 show a good improvement in the proposed model. The curves of this proposed formulation are similar to those measured by Thanopoulos [34].

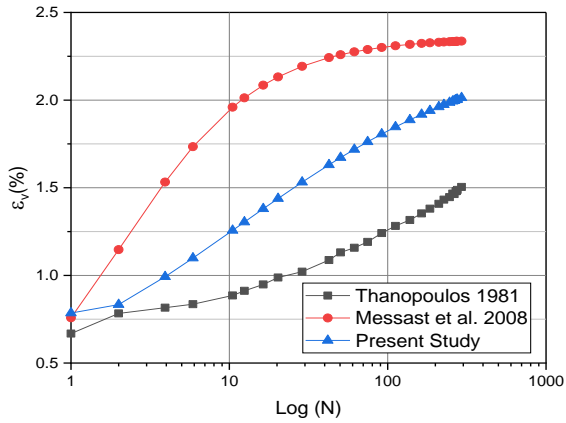


Figure 5: Curve ε_v^c versus $\log(N)$ for test 14a

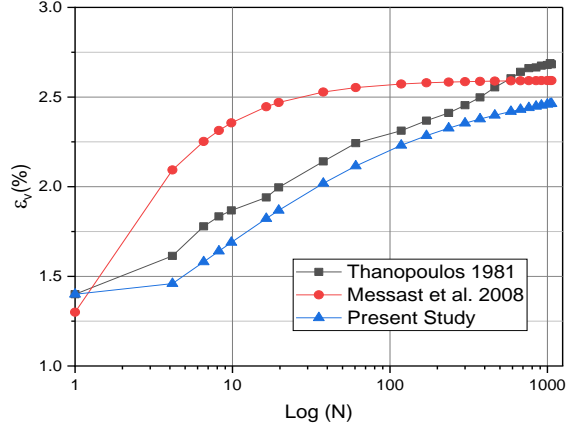


Figure 6: Curve ε_v^c versus $\log(N)$ for test 14b

5 Application to a Strip Foundation under Cyclic Loading

The numerical calculation of the settlement of shallow foundations using the PLAXIS package 2D version 8.2 is done after the calculation of the parameters q , p , $\Delta\eta$ and η_{av} of the model with the suggested formulations. In order to compare the ability of our numerical approach, we use the same set of parameters obtained from [21] and those found by the experimental test of [33]. The discretization was achieved by the triangular elements of 15 nodes to increase the accuracy of the calculation: the model has 964 triangular elements (average element size $255.64 \cdot 10^{-3}$ m) and 7910 nodes.

In the experimental centrifuge test of [33], fine sand (poorly graded) was used with these parameters: $\rho_s = 2.66 \text{ g/cm}^3$, $\varphi = 32.8^\circ$, $\Psi = 3^\circ$, $e_{max} = 0.908$, $e_{min} = 0.575$, $Cu = 2$, $d_{50} = 0.21$. The centrifuge test of [33] was simulated by Plaxis2D with the following boundary conditions:

- Material model of sand: hardening soil model (HSM).
- Dimensions of the test container: Using the symmetry, only half of the sand was discretized (9.05 m, 7.30 m), knowing that the real dimensions of the prototype were: width = 18.1 m, height = 7.3 m (Figure 7).

- Average load $\sigma_{av} = 89$ kPa, amplitude $\sigma_{ampl} = 75$ kPa.
- Boundary conditions are taken into account by blocking horizontal displacements on vertical faces and blocking horizontal and vertical displacements for the lower boundary.

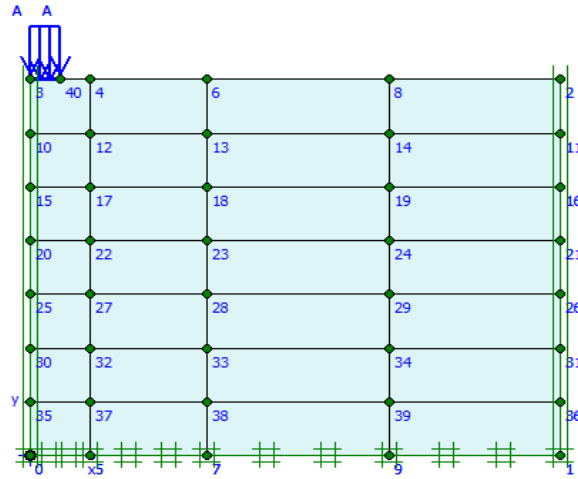


Figure 7: Geometry of the prototype (experimental test, height = 7.30 m, length = 9.05 m)

Table 2: Strip foundation dimension and material

width b (m)	height h (m)	depth of embedding t (m)	γ (g/cm ³)	E (GPa)	ν
1.00	0.60	0 m	2.70	25	0.30

The prototype of the sand studied in Plaxis is split into 28 clusters. After a charging cycle, stresses are created in each bunch whose stresses characterize the parameters of an equivalent triaxial test. The behavior of the global model will be defined by the application of cumulative volumetric strains of each cluster.

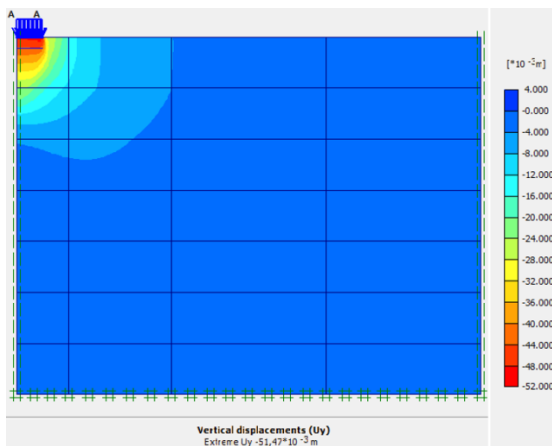


Figure 8: The shape and the field of settlement of the strip foundation (100 cycles)

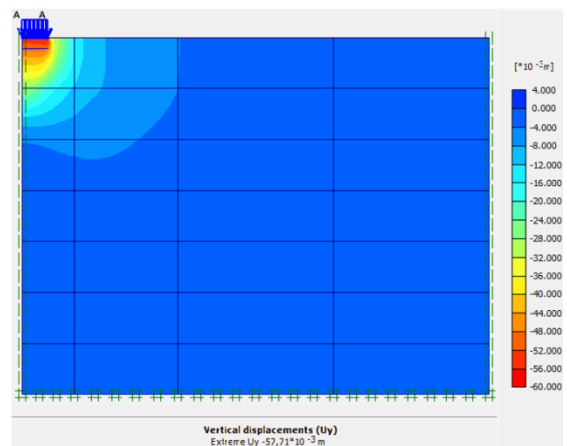


Figure 9: The shape and the field of settlement of the strip foundation (1000 cycles)

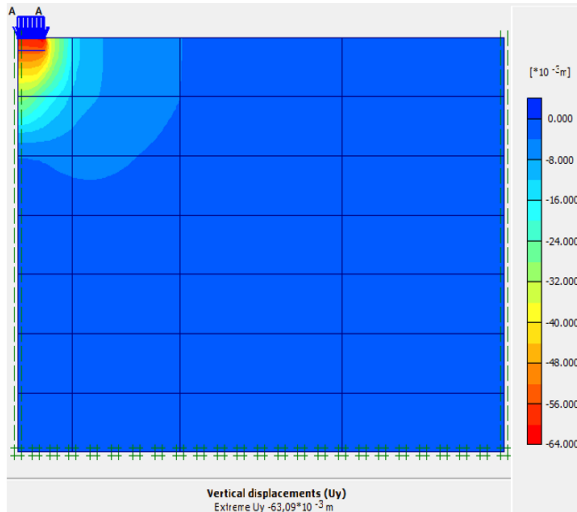


Figure 10: The shape and the field of settlement of the strip foundation (10000 cycles)

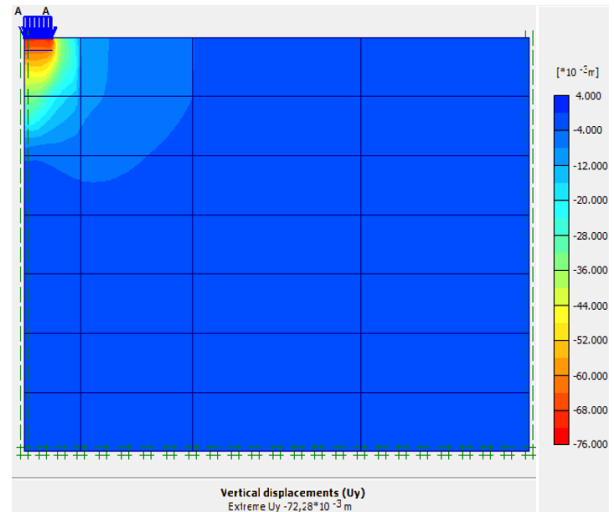


Figure 11: The shape and the field of settlement of the strip foundation (100000 cycles)

Figure 12 shows that the evolution of the settlement of the strip foundation presented in this research is very similar to the experimental curves of Helm et al. [33].

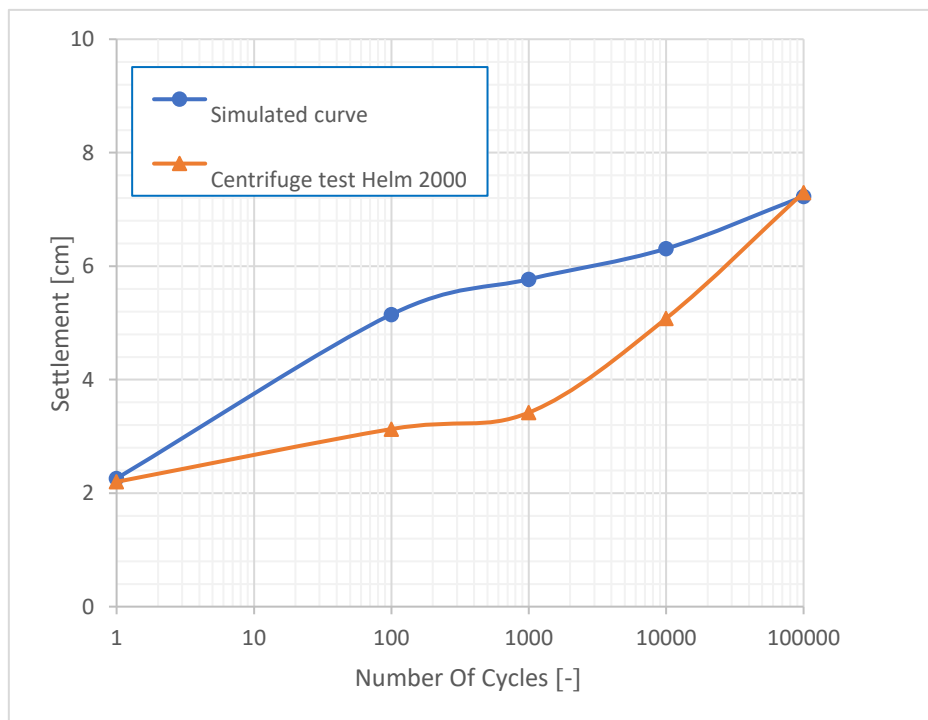


Figure 12: Comparison of the simulated curve with the centrifuge test [33]

6 Conclusion

This paper presents the modeling of the accumulation of volumetric deformations as a function of a large number of cycles. In this approach, the proposed model is based on the parameters of the first cycle (load-unload) and the cyclic parameters characterizing the average cyclic path. The calculation of the first cycle is achieved by a finite element calculation using the software

program Plaxis to simulate a triaxial test (load-unload). For this first cycle, the comportment of the material is described by the HSM model. The change of the volumetric deformations as a function of the number of cycles is formulated by a hyperbolic expression as a function of the number of cycles, the residual deformation after the first cycle, and the volumetric strain estimated at infinity.

The comparison of the results obtained with this formulation to the experimental curves presented by [30] shows a very good agreement, which confirms the reliability of the proposed model as well as its adaptation to this type of problem.

In the second part of this paper, the proposed model has been tested to determine the response of a strip foundation resulting from cyclic loading. The accumulation of deformation is detected at the center of the foundation.

Using the proposed method, a predicted settlement response equal to 7.30 cm of shallow foundation under large cyclic loading (after 10^5 cycles) was observed under the middle of the strip foundation [33]. The proposed approach predicts 7.23 cm. The comparison between the experimental values applied to a strip foundation [33] and those obtained by the proposed model confirms that the proposed model is well adapted to this type of problem.

As continuity of this work, we can cite the following perspectives:

- Examine the extension case.
- Apply this approach to clays.
- Generalize the approach to assess the response of geotechnical structures.
- Study of the cyclic response of interfaces.

References

- [1] Gu, C., Wang, J., Cai, Y., Yang, Z. & Gao, Y. (2012). Undrained cyclic triaxial behavior of saturated clays under variable confining pressure. *Soil Dynamics and Earthquake Engineering*, 40, 118-128.
- [2] Wang, J., Cai, Y. & Yang, F. (2013). Effects of initial shear stress on cyclic behavior of saturated soft clay. *Marine Georesources & Geotechnology*, 31(1), 86-106.
- [3] Wang, J., Guo, L., Cai, Y., Xu, C. & Gu, C. (2013). Strain and pore pressure development on soft marine clay in triaxial tests with a large number of cycles. *Ocean Engineering*, 74, 125-132.
- [4] Qian, J. G., Wang, Y. G., Yin, Z. Y. & Huang, M. S. (2016). Experimental identification of plastic shakedown behavior of saturated clay subjected to traffic loading with principal stress rotation. *Engineering Geology*, 214, 29-42.
- [5] Qian, J., Zhou, R., Chen, S., Gu, X., & Huang, M. (2018). Influence of pavement roughness on dynamic stresses in saturated subsoil subjected to moving traffic loading. *International Journal of Geomechanics*, 18(4), 04018012.
- [6] Guo, L., Cai, Y., Jardine, R. J., Yang, Z. & Wang, J. (2018). Undrained behaviour of intact soft clay under cyclic paths that match vehicle loading conditions. *Canadian Geotechnical Journal*, 55(1), 90-106.
- [7] Moussa, A., Salah, M. & Rafik, D.(2020). Improvement of a Hypoplastic Model for Granular Materials Under High-Confining Pressures. *Geotechnical and Geological Engineering* 38, 3761–3771. <https://doi.org/10.1007/s10706-020-01256-y>
- [8] Min, G., Fukuda, D., Oh, S., Kim, G., Ko, Y., Liu, H., Chung, M., Cho, S.(2020). Three-Dimensional Combined Finite-Discrete Element Modeling of Shear Fracture Process in Direct Shearing of Rough Concrete-Rock Joints. *Appl. Sci.* 10, 8033. <https://doi.org/10.3390/app10228033>

- [9] Bellayoune, A., Messast, S. & Boulon, M. (2021). Numerical Modeling of the Degradation of the Normal Stress Under Large Number of Shear cycles. *Civil and Environmental Engineering Reports*, vol.31. (3), pp.118-133. <https://doi.org/10.2478/ceer-2021-0037>
- [10] Sawicki, A., & Swidzinski, W. (1987). Compaction curve as one of basic characteristics of granular soils. In *4th colloque Franco-Polonais de mécanique des sols appliquée* (Vol. 1, pp. 103-115). Grenoble.
- [11] Niemunis, A., Wichtmann, T. & Triantafyllidis, T. (2005). A high-cycle accumulation model for sand. *Computers and geotechnics*, 32(4), 245-263.
- [12] Marr, W. A., & Christian, J. T. (1981). Permanent displacements due to cyclic wave loading. *Journal of the Geotechnical Engineering Division*, 107(8), 1129-1149.
- [13] Bouckovalas, G., Whitman, R. V. & Marr, W. A. (1984). Permanent displacement of sand with cyclic loading. *Journal of geotechnical engineering*, 110 (11), 1606-1623.
- [14] Ullidtz, P. (1993). Mathematical model of pavement performance under moving wheel load. *Transportation Research Record: Journal of the Transportation Research Board*, 1384: 94–99.
- [15] Gidel, G., Hornych, P., Chauvin, J. J., Breyse, D. & Denis, A. (2001). Nouvelle approche pour l'étude des déformations permanentes des graves non traitées à l'appareil triaxial à chargements répétés. *Bulletin de Liaison des laboratoires des ponts et chaussées*, 233, 5-21.
- [16] Chai, J. C. & Miura, N. (2002). Traffic-load-induced permanent deformation of road on soft subsoil. *Journal of geotechnical and geoenvironmental engineering*, 128(11), 907-916.
- [17] Wichtmann, T., Niemunis, A. & Triantafyllidis, T. (2005). Strain accumulation in sand due to cyclic loading: drained triaxial tests. *Soil Dynamics and Earthquake Engineering*, 25(12), 967-979.
- [18] Cai, Y., Chen, J., Cao, Z., Gu, C. & Wang, J. (2018). Influence of grain gradation on permanent strain of unbound granular materials under low confining pressure and high-cycle loading. *International Journal of Geomechanics*, 18(3), 04017156.
- [19] Ren, X. W., Xu, Q., Teng, J., Zhao, N. & Lv, L. (2018). A novel model for the cumulative plastic strain of soft marine clay under long-term low cyclic loads. *Ocean Engineering*, 149, 194-204.
- [20] Qian, J., Li, S., Gu, X. & Zhang, J. (2019). A unified model for estimating the permanent deformation of sand under a large number of cyclic loads. *Ocean Engineering*, 181, 293-302.
- [21] Messast, S., Boulon, M., Flavigny, E. & Labanieh, S. (2007). Modélisation constitutive du comportement cyclique des sables en condition drainée. In *Congrès français de mécanique*. AFM, Maison de la Mécanique, 39/41 rue Louis Blanc-92400 Courbevoie.
- [22] Papon, A. (2010). Modélisation numérique du comportement des sols sous très grands nombres de cycles: homogénéisation temporelle et identification des paramètres (Doctoral dissertation). Ecole centrale de Nantes.
- [23] Shariati, M., Hatami, H., Torabi, H. & Epakchi, H. R. (2012). Experimental and numerical investigations on the ratcheting characteristics of cylindrical shell under cyclic axial loading. *Structural Engineering and Mechanics*, 44(6), 753-762.
- [24] Dob, H., Messast, S., Boulon, M. & Flavigny, E. (2016). Treatment of the high number of cycles as a pseudo-cyclic creep by analogy with the soft soil creep model. *Geotechnical and Geological Engineering*, 34(6), 1985-1993.
- [25] Dob, H., Messast, S., Mendjel, A., Boulon, M. & Flavigny, E. (2016). Behavior of sand after a high number of cycles application to shallow foundation. *International Journal of Civil Engineering*, 14(7), 459-465.

- [26] Amrane, M., Messast, S. (2018) Modeling the Behavior of Geotechnical Constructions Under Cyclic Loading with a Numerical Approach Based on J. Lemaitre Model. *Indian Geotech J*, 48, 520–528. <https://doi.org/10.1007/s40098-017-0275-1>
- [27] Mohamed, F. M., Vanapalli, S. K. & Saatcioglu, M. (2013). Generalized Schmertmann Equation for settlement estimation of shallow footings in saturated and unsaturated sands. *Geomechanics and Engineering*, 5(4), 343-362.
- [28] Kim, T. H. & You, S. H. (2015). Settlement analysis considering sand mat induced initial settlement in soft ground improved by pbd. *International Journal of Civil Engineering*, 13(2), 146-152.
- [29] Lotfizadeh, M. R. & Kamalian, M. (2016). Estimating bearing capacity of strip footings over two-layered sandy soils using the characteristic lines method. *International Journal of Civil Engineering*, 14(2), 107-116.
- [30] Amrane, M.(2018). *Modélisation du Comportement des Ouvrages Géotechniques avec la Loi de J. Lemaitre*, PhD thesis. University of Skikda, Algeria. <http://ftech.univ-skikda.dz/doc2/2018/THESE%20Amrane%20Moussa.pdf>
- [31] Bellayoune, A. & Messast, S. (2021). Estimation of pile displacements anchored in sand after a large number of cycles. *Selected Scientific Papers-Journal of Civil Engineering*, 16(1), 35-44.
- [32] Wichtmann, T. (2005). *Explicit accumulation model for non-cohesive soils under cyclic loading*. Doctoral dissertation, Inst. Für Grundbau und Bodenmechanik).
- [33] Helm, J., Laue, J. & Triantafydillis, T. (2000). Untersuchungen an der RUB zur Verformungsentwicklung von Bödenunterzyklischen Beanspruchungen. *Bödenunter fast zyklischer Belastung: Erfahrungen und Forschungsergebnisse*, 109-133.
- [34] Thanopoulos, I. (1981). Contribution à l'étude du comportement cyclique des milieux pulvérulents (Doctoral dissertation). Université Scientifique et médicale & l'institut national polytechnique de Grenoble.

Experimental Research on the Thermal Instability of Fiber Polypropylene Concrete at 250 °C

Assia Aidoud^{1*}, Messaouda Bencheikh¹, Nacera Khaldi¹

¹University 8 May 1945 of Guelma, BP 401, Civil Engineering and Hydraulics Laboratory, Algeria

*e-mail: assia_aidoud76@yahoo.fr; aidoud.assia@univ-guelma.dz

Abstract

The high temperature in the concrete destroys the hydrates of the cement paste. This destruction means the weakness of the materials caused by the deterioration of their mechanical properties.

This work aims to study the behavior of high-performance fiber concrete sets at high temperatures; specifically, we used polypropylene fibers and studied their influence on deterioration behavior.

This study includes high performance concrete and three types of fiber concrete, each containing a specific ratio of polypropylene fibers (0.12 %, 0.18 %, and 0.24 %). Consequently, cubic test specimens (15 cm x 15 cm x 15 cm) were subjected to the temperature of 250 °C, with a speed of 2 °C/min followed by a step of one hour at the target temperature then cooling to the ambient temperature.

The results showed that fiber-reinforced concrete exhibited a better performance when exposed to the temperature studied. The mechanical properties were improved by up to 56% for compressive strength and 86% for tensile strength.

Key words: HPC, HPFC, fibers, high temperature, mechanical properties

1 Introduction

In recent years, several researches have been devoted to the development of the characteristics ultra-high-performance fiber-reinforced concrete (UHPC). This material has allowed the construction of several structures with complex architecture throughout the world [1]. Due to its durability on time [1]. In general, concrete is a composite material in which there are two phases: the matrix (hardened cement paste) and the aggregates (gravel and sand). Additionally, the paste/aggregate interface is present. This interface area is the strong point of High-Performance Concrete (HPC) which is characterized by better adhesion between the aggregates and the cement matrix. In addition, the resistance of the matrix is almost equal to the resistance of the aggregates and sometimes even higher [2]. Even if the mechanical resistance of HPC is significantly higher than that of ordinary concrete, there are other parameters to which the attention is drawn, and which have more advantages compared to ordinary concrete materials such as durability and fire strength [2].

However, when HPC is subjected to high temperatures, as in a fire situation, these dense concretes sometimes exhibit sensitive behavior, which results in damage to the microstructure and detachment of small or large fragments of concrete [3]. Several studies have reported the high risk of chipping of HPC during thermal stress [4, 5, 6, 7]. The best-known remediation process is the addition of polypropylene fibers (PPF) to improve the thermal stability of concrete and metallic fibers (MF) to increase residual mechanical performance [8, 9]. The properties of PPF fiber have great potential. Indeed, its major advantage is its ability to reduce plastic shrinkage and cracks by around 40% and more [10]. Their fusions occur at 160 – 171 °C, where they are completely or partially absorbed by the porous network of the cement matrix. A vacuum remains in the place of the fibers, providing additional space for the water vapor to circulate. Consequently, the risk of chipping decreases with the reduction of vapor pressures within the material [8].

The objective of this work is to improve the understanding of the behavior of high-performance concretes and concretes containing polypropylene fibers at high temperatures. For this, test specimens of different percentages of PPF were made, kept in water for 28 days, and then subjected to a heat treatment of up to 250 °C. This temperature was chosen because the major transformations of the different material characteristics are observed in several studies [9, 11] between 200 °C and 500 °C, whereas the first transformations are between 200 °C and 300 °C. Mass loss, ultrasonic velocity, compressive, and tensile strength tests and measurements were made before the heating and after the cooling, in order to assess the evolution of the mechanical and physical properties of fiber-reinforced concrete at high temperatures.

2 Experiment's Details

2.1 Materials

The materials used in this work for the preparation of the various concretes are of local origin (Figure 1) and their chemical compositions and their physical properties are shown in Table 1 and Table 2.



Figure 1: The materials used for making the various concretes studied. (a) Dune sand, (b) Natural sand, (c) Quarry sand, (d) Gravel 15/25, (e) Gravel 5/15, (f) Cement CPJ-CEM II/ A 42.5, (g) MEDAPLAST H silica fume, (h) MEDAPLAST-SP 40 super-plasticizer, (i) SIKAFIBRE Polypropylene 12/32

Table 1: Chemical compositions of cement, mineral addition, and sands

	CaO %	SiO ₂ %	Al ₂ O ₃ %	Fe ₂ O ₃ %	MgO %	K ₂ O %	Na ₂ O %	SO ₃ %	Cl- %	Loss on Ignition
Cement	58.6	24.92	6.58	3.65	1.21	0.85	0.08	2.17	-	1.7
Silica fume	0.2	93.7	0.6	0.3	0.2	0.5	0.2	<2.5	<0.5	2.9
Natural sand	0.23	97.97	0.58	0.26	0.05	0.29	0.06	0.03	-	0.46
Quarry sand	56.73	3.71	0.23	0.20	1.18	0.02	0.07	0.09	-	37.77
Dune sand	1.63	90.46	1.38	1.92	0.39	0.22	0.00	0.2	-	2.56

Table 2 : General material properties

	Unit	S _{natural}	S _{career}	S _{dune}	G _{5/15}	G _{15/25}	Cement	Silica Fume
Fineness modulus	%	3.04	3.51	0.84	-	-	-	-
Visual Sand Equivalent	%	78.07	80.61	99.56	-	-	-	-
Equivalent of sand per piston	%	71.92	76.53	85.97	-	-	-	-
Bulk density	g/cm ³	1.39	1.50	1.44	1.48	1.49	1.09	0.5
Absolute density	g/cm ³	2.83	2.71	2.51	2.46	2.71	3.11	-
Impurity	%	-	-	-	12.36	3.39	-	-
SSB	cm ² /g	-	-	-	-	-	3371	>15000

2.1.1 Sands

The three sand types used for making concrete have different classes and natures:

- Very clean dune sand (S_{dune}) of class 0/1. It is very fine with too tight a pace; its apparent and absolute densities are respectively 1.44 and 2.50 g/cm³.
- Clean natural sand (S_{natural}) of class 0/4 fine with a slightly spread appearance; its apparent and absolute densities are respectively 1.39 and 2.83 g/cm³.
- Clean, well-spread, class 0/5 quarry sand (S_{career}); its apparent and absolute densities are respectively 1.50 and 2.71 g/cm³.

2.1.2 Gravels

The two kinds of gravels used for making concrete have the following fractions: 5/15 and 15/25; their apparent and absolute densities are respectively 1.485; 2.46 g/cm³, and 1.49; 2.71 g/cm³. They are washed and air-dried before use.

2.1.3 Cement

The cement (C) used for all the concretes made in this study is a composite Portland cement of the type CPJ-CEM II/ A 42.5. This cement is mainly made of 75% Clinker, 5% gypsum, and 20% blast furnace slag.

2.1.4 Additive

The super-plasticizer (Sup) used is MEDAPLAST-SP 40 high water reducer per standard EN 934-2 [12] as well as the standards established by the (CNERIB) in January 2007 [12]. In the liquid form, it is brown-colored with a pH of 8.2 and a density of 1.20 ± 0.01 , and its chlorine content is less than 1g/L.

2.1.5 Addition

MEDAPLAST HP [NF P 18-502] is the addition of silica fume (SF) for making high-performance concrete (HPC). In the powder form, it has gray color; its density is 0.5 and its humidity in the oven at 105°C is less than one ($< 100\%$). The size of its products is less than 0.1 microns.

2.1.6 Polypropylene Fiber

We used synthetic fibers (12/32 polypropylene) marketed by the SIKA company called SIKAFIBRE based on specially treated polypropylene, presented in pre-dosed palpable sachets for 1 m^3 of concrete of density 0.91 g/cm^3 and length of 12 mm with a diameter of 32 μm . Their tensile strength f_t is 270 to 430 MPa and their Modulus of Elasticity E is 3000 to 6000 MPa.

2.1.7 Water

The water (W) used for making the mortar mixes is drinking water.

2.2 Method

A high-performance control concrete and three fiber-reinforced concretes with different dosages of polypropylene fiber PPF, 600 g/m^3 (0.12%), 900 g/m^3 (0.18%), and 1200 g/m^3 (0.24%) for each concrete (Table 3) were the subject of this comparative study. This choice of percentages was due to the method of introducing this type of fiber at the end of mixing, by a bag of 600 g/m^3 . The tests concerned the determination of the compressive strength, the tensile strength, the speed of ultrasound, therefore the dynamic Elastic Modulus and the loss of mass. All the tests were carried out on cubic specimens (15 cm x 15 cm x 15 cm). These residual properties were determined before and after subjecting the specimens to the study temperature of 250°C and their cooling to the environment. A temperature rise rate of 2°C/min was used to reach the target temperature followed by a 1-hour plateau for homogenization of the temperature in the test piece (Figure 2).

The compression and tensile tests (by splitting) were carried out by a maximum force of 2000 kN with speeds of 0.3 MPa/s and 0.05 MPa/s [13]. The ultrasound velocity measurements were carried out in direct transmission mode [14] by an ultrasonic tester [EN 12504-4] (brand controls) comprising a transmission head and a reception head of 54 kHz [15]. The compressive strength f_c was determined directly by the force used depending on the breaking force and the section (Equation 1), the splitting tensile strength was calculated by the formula of Equation 2 after the determination of the breaking force by the force used. For the dynamic elastic modulus E_d was calculated by an empirical formula (Equation 3) after the determination of the ultrasonic velocity by the ultrasound used.

$$f_c = F/S \quad (1)$$

f_c : Compressive strength (MPa),
 F : The breaking load (N),
 S : Section of the specimen (mm^2).

$$f_t = 2P/\pi DL \quad (2)$$

f_t : Tensile strength by splitting (MPa),
 P : The breaking load (N),
 L : Length of the contact line of the specimen (mm).
 D : Diameter of the specimen (mm).

$$E_d = \frac{(1+\nu)(1-2\nu)}{(1-\nu)} \cdot \rho \cdot V^2 \quad (3)$$

ν : Poisson's ratio,
 ρ : Density in kg/m^3 ,
 V : Speed of propagation of sonic waves in m/s.

Table 3: Composition of the concretes studied

Composition	Unit	HPC	HPFC1	HPFC2	HPFC3
S_{natural}	kg/m^3	76.49	76.49	76.49	76.49
S_{career}	kg/m^3	549.35	549.35	549.35	549.35
S_{dune}	kg/m^3	169.60	169.60	169.60	169.60
$G_{5/15}$	kg/m^3	216.09	216.09	216.09	216.09
$G_{15/25}$	kg/m^3	787.39	787.39	787.39	787.39
Cement	kg/m^3	500	500	500	500
Water	kg/m^3	193.05	193.05	193.05	193.05
Silica Fume	kg/m^3	75	75	75	75
Super-plasticizer	kg/m^3	10	10	10	10
Polypropylene fibers	kg/m^3	0	0.6	0.9	1.2
Water/Binder		0.336	0.336	0.336	0.336
Slump	(cm)	12	14	17	22

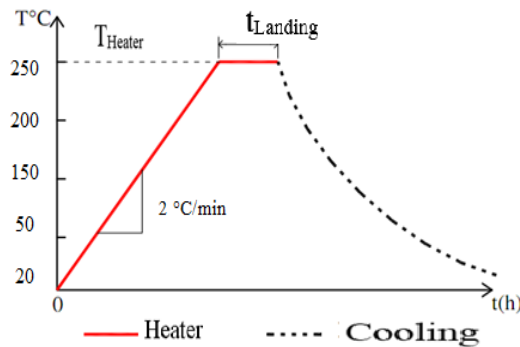


Figure 2: Heating cycle - cooling

3 Influence of Temperature on Fiber-reinforced Concrete

3.1 The Effect of Adding Fiber

The different results had grouped in Table 4 and illustrated by Figures 3, 4, 5, and 6 below.

Table 4: Effect of adding polypropylene fibers on the properties studied

20°C	Unit	HPC	HPFC1	HPFC2	HPFC3
Mass (m)	kg	7.993 ±	8.143 ±	8.101 ±	8.076 ±
		0.267	0.063	0.066	0.656
Modulus of dynamic elasticity (E_{dyn})	MPa	47860.135 ±	44810.508 ±	41821.248 ±	44496.768 ±
		1691.453	851.905	1985.935	2058.731
Compressive strength (f_c)	MPa	70.119 ±	68.424 ±	44.91 ±	62.694 ±
		5.0784	1.0234	6.143	3.687
Splitting Tensile Strength (f_t)	MPa	2.114 ±	1.726 ±	2.681 ±	2.644 ±
		0.153	0.026	0.367	0.115

3.1.1 The Mass

For HPFC1 we notice a very remarkable increase in mass (Figure 3) compared to the two other fiber-reinforced concretes, despite the fact that the concrete contains less fiber. This can be explained by the location of the fibers without any replacement of the constituents of the matrix.

The HPFC2 of 0.18% of polypropylene fibers also marked an increase in the mass compared to the mass of the control HPC, and a decrease of the latter compared to the HPFC1 of 0.12% of polypropylene fibers. Similarly, the HPFC3 of 0.24% PPF compared to the control HPC, HPFC1, and HPFC2.

It can be concluded that beyond an addition of 0.12% of polypropylene fibers the mass decreases as a function of the percentage of fibers, to reach the mass of the control HPC at a percentage to be determined. In addition, it can be also said that the fibers above this percentage replace a certain volume of the matrix.

3.1.2 The Dynamic Elastic Modulus

The incorporation of 0.18% of polypropylene fiber reduces the dynamic elastic modulus E_d by 12.62% to that of the control HPC.

On the other hand, the incorporation of 0.12% and 0.24% of polypropylene fiber reduces the dynamic elasticity modulus by 6.37% and 7.03% respectively to that of the control HPC (Figure 4).

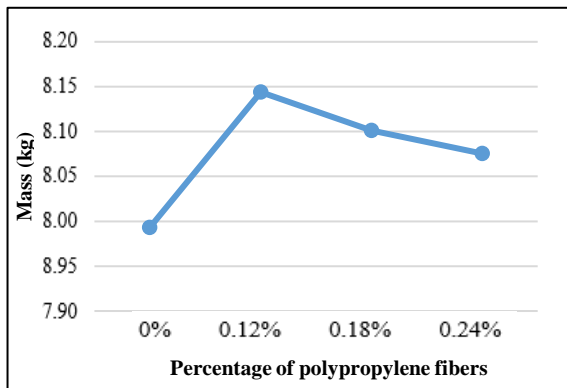


Figure 3: Evolution of the mass ($m_{20^{\circ}\text{C}}$) as a function of the percentage of polypropylene fibers

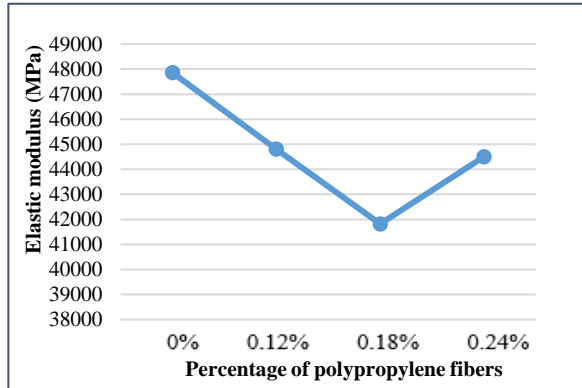


Figure 4: Evolution of the dynamic elastic modulus ($E_{d20^{\circ}\text{C}}$) as a function of the percentage of polypropylene fibers

3.1.3 Compressive Strength

The compressive strength f_c dropped slightly (2.42%) for the incorporation of 0.12% of polypropylene fiber, in contrast to the incorporation of 0.18% PPF, where the drop in resistance is very remarkable, 35.95%, compared to the compressive strength of the control concrete HPC. The fall in compression resistance of HPFC3 is 10.59% compared to that of control concrete HPC (Figure 5).

Regarding the rupture of the matrix, we noticed a rupture even with aggregates according to the literature [16] for the four concretes, with the presence of fibers like hair threads that hold the pieces of fiber concrete together after rupture (Figure 7).

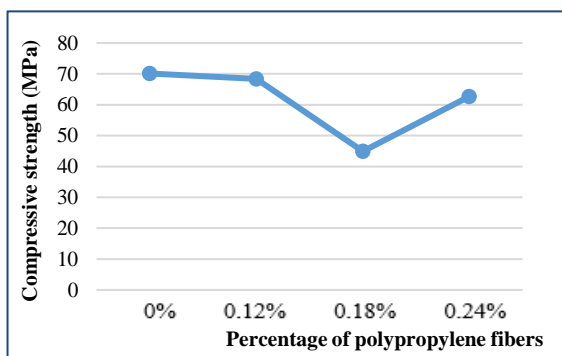


Figure 5: Evolution of the compressive strength ($f_{c20^{\circ}\text{C}}$) as a function of the percentage of polypropylene fibers

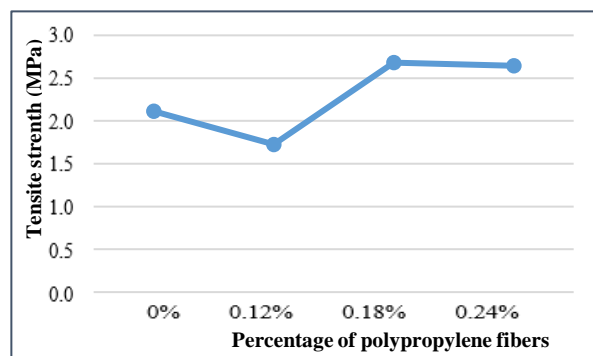


Figure 6: Evolution of the tensile strength ($f_{t20^{\circ}\text{C}}$) as a function of the percentage of polypropylene fibers

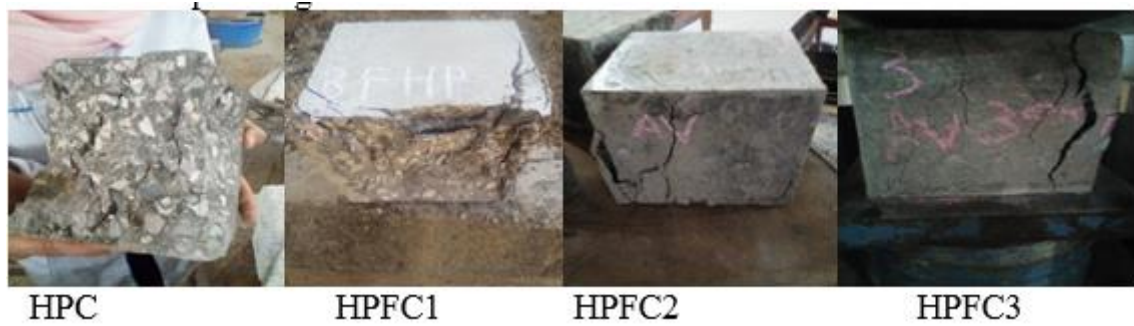


Figure 7: Failure of the compression specimens of the various concrete at 20°C

3.1.4 Tensile Strength

The incorporation of 0.12% polypropylene fiber HPFC1 decreased the tensile strength by 18.35% compared to that of the control concrete (HPC). On the other hand, the incorporation of 0.18% of PPF into the HPFC2 increased the resistance by 26.82%, compared to the tensile strength of the control concrete. It is caused by the high tensile strength of polypropylene fibers. A slight decrease in the tensile strength is observed, compared to HPFC2 of an order of 1.38%, compared to HPFC2, when incorporating 0.24% of PPF to create the HPFC3 (Figure 6). Concerning the rupture of the matrix, the same remark as quoted above is observed for the resistance to compression (Figure 8).



Figure 8: Failure of tensile test pieces by splitting different concrete at 20°C

3.2 The Effect of Temperature

For a better interpretation, the results are presented in the form of reports of the different properties at the temperature studied (250 °C) and compared to the results of the reference concrete at (20 °C). The reports obtained are grouped in Table 5 and illustrated in the figures below (Figures 9, 10, 11, and 12). The results are then compared to the normative results of Eurocode EC2 [17] and the Unified Document DTU [18] at the study temperature.

Table 5: Report of the different residual properties as a function of the percentage of polypropylene fibers

Properties at 250°C/ Properties at 20°C	HPC	HPFC 1	HPFC 2	HPFC 3	DTU	EC2 (silica send)	EC2 (limestone sand)
m (kg)	0.988 ± 0.003	0.9917 ± 0.034	0.9913 ± 0.007	0.9912 ± 0.005			

E_{dyn} (MPa)	0.941 ± 0.105	1.007 ± 0.034	1.088 ± 0.076	1.050 ± 0.040	0.45	0.39	
f_c (MPa)	0.719 ± 0.148	0.786 ± 0.147	1.560 ± 0.224	0.872 ± 0.186	1	0.9	0.94
f_t (MPa)	0.937 ± 0.317	1.860 ± 0.054	1.458 ± 0.000	1.557 ± 0.274	0.58	0.7	

3.2.1 The Mass

The mass loss of 0.62% in HPC is the smallest compared to other fiber-reinforced concretes. HPFC2 and HPFC3 have almost the same mass loss of 0.76% and 0.74%, respectively. On the other hand, HPFC1 has a loss of 1.10% (Figure 9). This can be explained by the free water content of the test pieces before heating. Also, a favorable effect of PPF for transporting moisture can be a contributing factor.

The mass loss of the four concretes is almost zero at 250 °C, so it did not exceed 2%. This value is a little less than that found by [19], which is due to the better compactness of these concretes and their very low porosity resulting from a low (Water/Binder) ratio.

3.2.2 The Modulus of Elasticity

The decrease in the dynamic elastic modulus E_d at 250 °C reached 5.9% for HPC. This decrease in the dynamic modulus of elasticity down to this temperature is twice that of the ultrasonic velocity respecting the proportionality with the ultrasonic velocity, in accordance with the results of [6] but with different values.

Still, the three types of fiber-reinforced concrete have an increased dynamic elastic modulus at 250 °C (Figure 10) of 0.7%, 8.8%, and 5% for HPFC1, HPFC2, and HPFC3, respectively. The results differ from the results of Sideris et al. [20] who observed a linear decrease in the modulus of elasticity up to 300 °C.

All ratios determined for the four types of concrete have higher values than those of DTU [18] and EC2 [17] at a temperature of 250 °C, in fact, even more than double. However, it should be noted that elastic modulus is deduced from ultrasonic velocities (dynamic modulus), so the results also depend on the procedures and formulas used as indicated by Pimienta et al. [21].

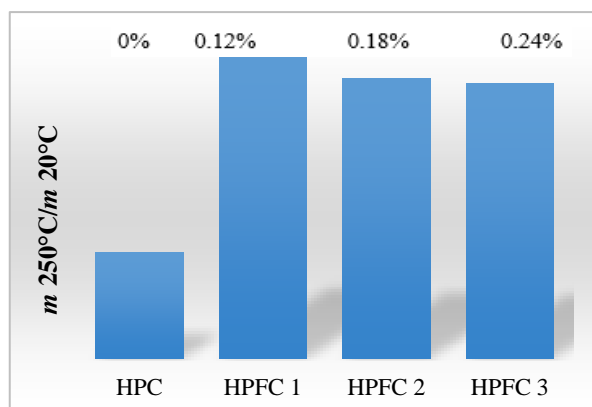


Figure 9: Evolution on the mass ratio as a function of the percentage of polypropylene fibers

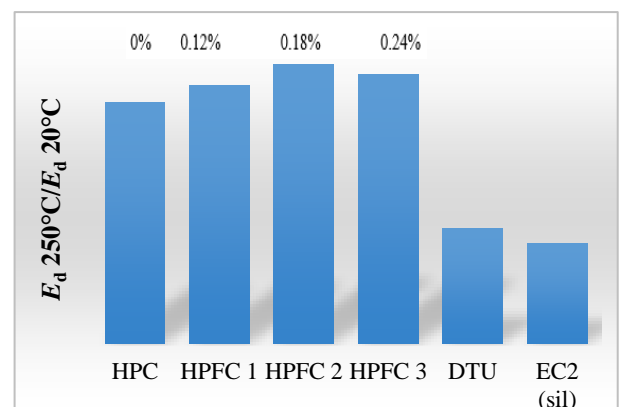


Figure 10: Evolution of the dynamic elastic modulus ratio as a function of the percentage of polypropylene fibers

3.2.3 Compressive Strength

Three types of concrete have relatively low compressive strength f_c at 250 °C for this temperature level. They reach 28.1% for the control HPC sample, 21.4% for HPFC1, and 12.8% for HPFC3 (Figure 11). This drop in the compressive strength is relatively close to those suggested by the Eurocode, where they do not exceed 25%. On the other hand, HPFC2 presents a remarkable improvement of 56% at the tested temperature and with the incorporation of 0.18% of PPF. So, the effect of adding 0.18% of PPF is more favorable after a cycle of 250 °C than that at 20 °C. The results are in contrast to the results of [22, 23] on polypropylene fiber concrete with an addition of 1 kg/m³ i.e., 0.2%, where there is no significant improvement in compressive strength with temperature changes. The change as a function of percentage (PPF) of the compressive strength after 250°C underwent a slight increase on the plateau (0% to 0.12%), then a jump at the point of (0.18%) of (PPF), to fall to (0.24%) of (PPF). The values of the ratios determined for the three types of concrete are around and lower than the values of DTU [18] and EC2 [17] (siliceous or limestone). After reaching 250 °C, the polypropylene fibers behave as an adhesive, which was noticed after different ruptures of the test pieces (Figure 13). Yagoub indicates that PPF melts at around 160 °C [10].

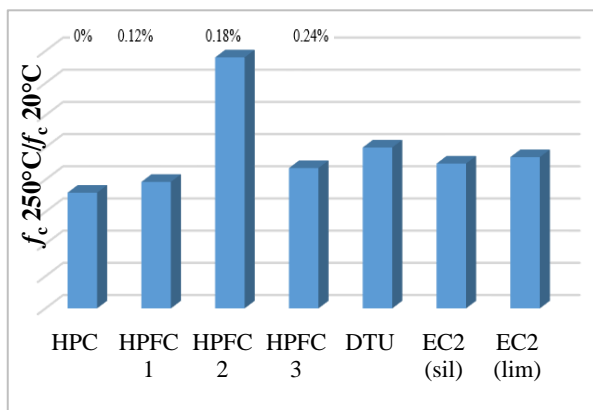


Figure 11: Evolution of the compressive strength ratio as a function of the percentage of polypropylene fibers

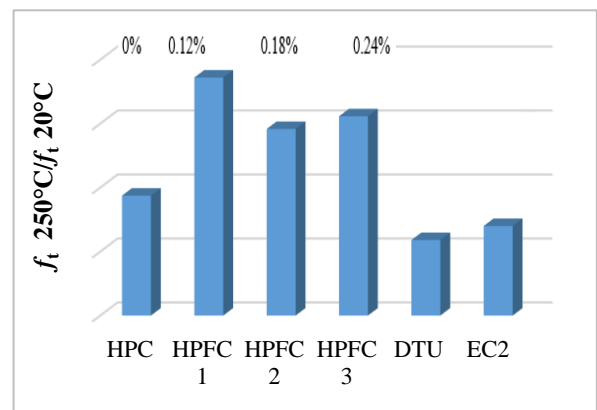


Figure 12: Evolution of the tensile strength ratio as a function of the percentage of polypropylene fibers



Figure 13: Rupture of test specimens by compression exposed to 250°C

3.2.4 Tensile Strength

The decrease in tensile strength f_t for HPC is 6.3% at 250 °C. It is relatively similar to that in compression (Figure 12). On the other hand, the three types of fiber-reinforced concrete have undergone remarkable increases, on average by 50%. The increases are respectively 86%, 45.8%, and 55.7% for HPFC1, HPFC2, and HPFC3, which converges to the results of Pilya [24] for ordinary concretes with polypropylene fibers but not for high performance concretes with polypropylene fibers (HPCF) between 150 °C and 450 °C. Pilya attributed this improvement in resistance to the melting of polypropylene which fills the pores of the concrete and re-solidifies during the cooling phase. The contact forces and the connections between the different grains thus improve. The concretes tested have values much higher than those of DTU [18] and EC2 [17].

4 Effect of Temperature and Fibers on the Relationships Between the Properties of Concrete

The relationships between the resistances (compression and tensile) and between the compressive strengths and the elasticity moduli can be influenced by the rise in temperature and even the incorporation of fibers. It was proved through the results that these properties can have different values. In this part of the work, we explore the effect of temperature and fibers on these relationships, between compressive and tensile strengths on the one hand and between the compression strength and elastic modulus on the other. These relations between properties also go in relation to those given by the regulations DTU [18] and EC2 [17].

4.1 The Relationships between Compressive Strengths and Tensile Strengths

The previous curves show the f_t-f_c relationships for HPFC with 0%, 0.12%, 0.18%, and 0.24% of PPF at 20 °C and 250 °C. Note that the difference between the regulatory curves and the experimental curve of HPFC at 250 °C is not as large as at 20 °C (Figures 14 and 15). On the other hand, we notice the quality reverse of the f_t-f_c regression $R^2 = 0.5273$ at 20 °C and $R^2 = 0.3828$.

At the two temperatures: 20 °C and 250 °C, the f_t-f_c relationships for HPFC always give underestimated values, but at 250 °C, the f_t-f_c relationships have the same appearance as those of the regulations BAEL [18] and EC [17]. In addition, at 20 °C the f_t-f_c relationships begin to wane, decreasing beyond 40 MPa. We can see that the f_t-f_c relationships were influenced by the percentage of PPF fiber incorporation.

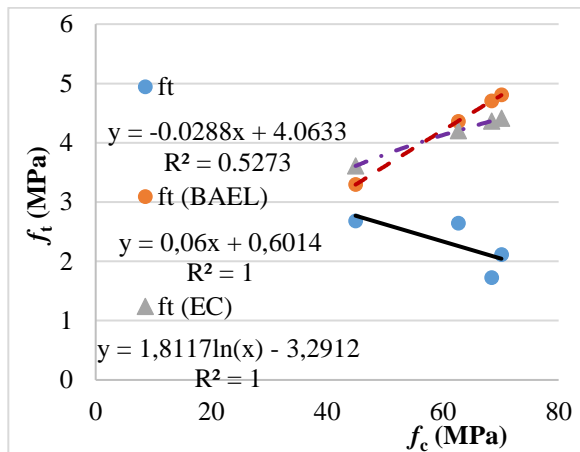


Figure 14: Relations between compressive strengths and tensile strengths at 20 °C

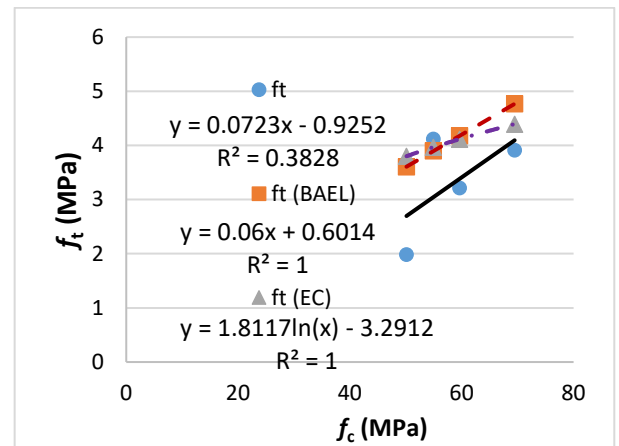


Figure 15: Relationships between compressive strengths and tensile strengths at 250 °C

4.2 The Relationships between Compressive Strengths and Elastic Modulus

We can notice that the majority of the points connecting E_d to f_c (Figures 16 and 17) at either 20 °C or 250 °C are located above the curves given by the regulations (BAEL [18] and EC [17]).

On the other hand, at 20°C, there is an improvement in the relationship for the HPFC ($R^2 = 0.780$), with a rapprochement of the estimate of E_d with those of the regulations for compressive strengths around 65 MPa. But despite the fact that the E_d - f_c relationship at 250 °C tends to become confused with that of EC, its quality of regression is very small ($R^2 = 0.003$).

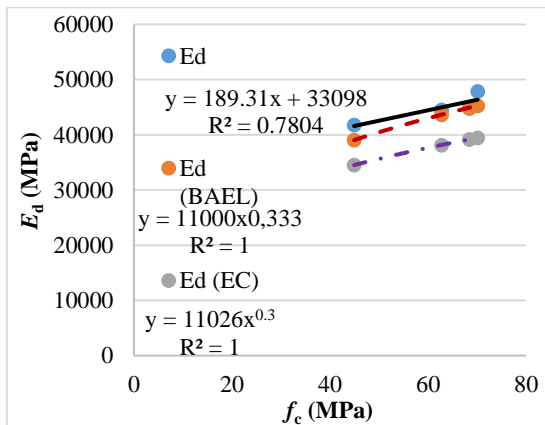


Figure 16: Relationships between compressive strengths and dynamic elastic modulus at 20 °C

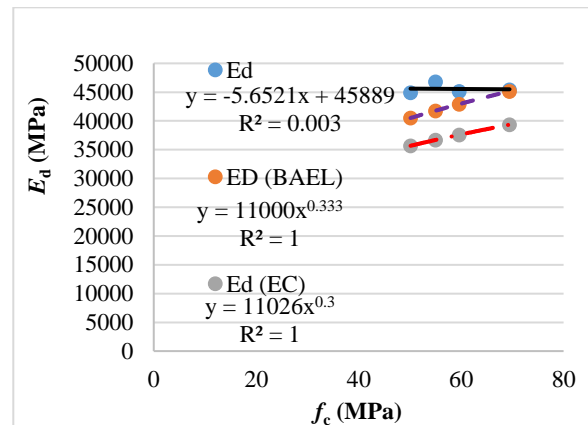


Figure 17: Relationships between compressive strengths and dynamic elastic modulus at 250 °C

5 Conclusion

This study highlighted the difference in behavior with respect to high temperatures of 250 °C between high-performance concrete and three types of concrete with polypropylene fibers. The former is much more influenced by the increase in temperature compared to the latter.

The decrease in compressive strength has exceeded 28% for HPC, while it is between 12% to 22% for HPFC with 0.12 and 0.24% of PPF. An increase of 56% in f_c was observed for HPFC with 0.18% PPF.

In traction, the improvement reaches on average 50% for HPFC. This implies that the tensile strength for HPFC is improved with the rise of temperature than is the compressive strength.

The increase in dynamic elasticity modulus E_d is between 0.5% and 9% for HPFC and the decrease reached almost 6% for HPC. Thus, up to this temperature, the dynamic modulus of elasticity of HPFCs is more improved by the rise of temperature than it is in the case of HPCs. We conclude that the residual mechanical properties of HPFC concretes are higher than the properties of the HPC control sample.

In general, the mechanical performance of the concretes studied and the physical characteristic, which is the mass, are positively influencing by the incorporation of PPF fibers. However, the most remarkable thing is that these incorporated fibers improved all the residual properties studied after the exposure of these concretes to the thermal cycle studied. These results are due to the chemical transformations, which have undergone the PPF under temperature. The relationships between compressive strength and tensile strength at 20 °C and 250 °C taking into account the presence of PPFs were underestimated compared to those of normative documents, therefore we can note that PPFs influence these relationships even at the atmospheric temperature.

The relationships between compressive strength and dynamic elastic modulus present were estimated as higher than those of normative documents.

References

- [1] Kheddache, L., Chahour, K. and Safi, B. "Effet de la répartition des fibres sur le comportement mécanique en flexion des mortiers autoplaçants" *Articles scientifiques sélectionnés - Journal of Civil Engineering*, vol.15, no.1, 2020, pp.129-148. <https://doi.org/10.1515/sspjce-2020-0012>
- [2] Lakhel, R. (2011) *Elaboration des bétons à hautes performances a base des sous-produit locaux formulation et caractérisation physico-mécanique.*» Mémoire de magister, Université Badji Mokhtar, Annaba. .
- [3] Kalifa, P., Menneteau, F-D., Quenard, D. (2000) Spalling and pore pressure in HPC at high temperatures. *Cement and Concrete Research*. 30 (12), 1915-1927.
- [4] Noumowé, A. (1995) *Effect of high temperatures (20-600°C) on concrete. Special case of high concrete.* PhD thesis. France. National Institute of Applied Sciences of Lyon.
- [5] Hager, I. (2004) *High temperature behavior of high performance concretes - evolution of the main ones.* PhD Thesis. France. National School of Bridges and Roads and the School.
- [6] Mindeguia, J. (2009) *Experimental contribution to understanding the risks of thermal instability in concretes.* PhD thesis. France. University of Pau and the Adour countries.
- [7] Aidoud, A., Benouis, A.H. (2018) *Investigation of the Evolving Relationship Between the Properties of Ordinary Concrete and High Performance Concrete at High Temperatures.* *Journal of Materials and Environmental Sciences* 9 (4), 1335-1342.

- [8] Kalifa, P., Chéné, G., Gallé, C. (2001) High-temperature behaviour of HPC with polypropylene fibres - From. Cement and Concrete Research. 30 (10), 1487-1499.
- [9] Yermak, N., Pliya, P., Beaucour, A-L., Simon, A., Noumowé, A. (2017) Influence of steel and/or polypropylene fibres on the behaviour of concrete at high temperature: Spalling, transfer and mechanical properties. Construction and Building Materials. 132, 240–250.
- [10] Yagoub, M. (2009) Assessment of the quality of fiber concrete in situ case of self-placing concrete with mixed fibers. Masters thesis. Algeria. Mohamed Khider University - Biskra.
- [11] Hager, I. (2013) Behaviour of cement concrete at high temperature. Bulletin of the Polish Academy of Sciences 61 (1), 145-154.
- [12] Technical manual (MEDAPLAST- SP 40 (GRANITEX)), available at: <https://fr.scribd.com/document/427211373/Medaplast-Sp-40#>
- [13] EN (2003) European Standard 12309-3. Tests for hardened concrete - part 3: Resistance to compression of test pieces. CEN. 02.
- [14] NF (2005) EN standar. NF 12504-4. Sonic auscultation test. AFNOR.
- [15] CONTROLS (2002) Instruction Manual: Ultrasonic Pulse Velocity tester. Mod. 58-E0048.
- [16] <https://www.holcim.be/fr/les-betons-speciaux-beton-a-hautes-performances>
- [17] Eurocode 2 (2001) (ENV 1992-1-2): Design of concrete structures, Part 1-2: General rules - calculation of fire behavior. February.
- [18] BAEL 91 rules (DTU P 18-702) (revised February 99, 2000) Technical rules for the design and calculation of reinforced concrete structures and structures using the limit states method Fascicle 62, title 1 of the CCTG - Works section 1: reinforced concrete 1.
- [19] Chouiter, Y (2016) Study of the behavior of a high performance concrete (HPC) with glass fibers subjected to high temperature. Master memory. Algeria. Materials. M'sila: Mohamed Boudiaf University.
- [20] Sideris, KK; Manita, P; Chaniotakis, E (2009) Performance of thermally damaged fiber reinforced concretes. Construction and Building Materials 23 (3), 1232-1239.
- [21] Pimienta, P; Mindeguia, JC; Simon, A; Behloul, M; Felicetti, R; Bamonte, R; Gambarova, PG (2012) Performance of concrete subjected to high temperature, from material to structure. Symposium Cergy-Pontoise University. France. 23 October.
- [22] Khaliq, W; Kodur, V (2011) Thermal and Mechanical Properties of Fiber Reinforced HighPerformance Self-Consolidating Concrete at Elevated Temperatures. Cement and Concrete Research. 41 (11), 1112-1122.
- [23] Behnood, A; Ghandehari, M (2009) Comparison of compressive and splitting tensile strength of high-strength concrete with and without polypropylene fibers heated to high temperature. Fire Safety Journal. 44 (8), 1015-1022.
- [24] Pliya, P (2010) Contribution of polypropylene and metallic fibers to improving the behavior of concrete subjected to high temperature. PhD thesis. France. University of Cergy Pontoise.

Seismic Response of Concrete Gravity Dams Considering Hydrodynamic Effects

Aouadj Linda^{1*}, Abdelkrim Kadid²

¹ Department of Hydraulics, University of Batna, Algeria

² Department of Civil Engineering, University of Batna, Algeria

*e-mail: linda_hydro@yahoo.fr

Abstract

This paper presents a dynamic analytical study to assess the effect of dam height as well as fluid compressibility on the gravity response of a concrete dam, considering the effects of hydrodynamic interaction. The analysis is carried out using the ADINA Finite Element software for empty and full reservoir conditions by considering several models. In the first model, the mass of fluid is taken into account by the concept of Westergaard added mass, in the second model; an acoustic fluid element is used to simulate the effect of water on the reservoir. The height of the dam is one of the main factors affecting the seismic response of gravity dams; because the change in height provides different responses depending on the natural periods, displacements and stresses obtained from static and dynamic analyses. The numerical results showed that the effect of interaction between the dam and the reservoir plays an important role in the precise estimation of the dynamic response of gravity dams. The hydrodynamic water pressure from the reservoir increases stresses in the dam body and horizontal displacements at the crest. The seismic response obtained by the incompressible water model (Westergaard) is compared with that of the compressible water model.

Keywords: added masses, dynamic analysis, Fluid-structure interaction, Finite Element Method, gravity dam, hydrodynamic

1 Introduction

Concrete gravity dams are very important structures that can be implemented in high-seismicity areas and whose security must be ensured. In this work, we intend to perform a seismic analysis to evaluate the linear response of concrete gravity dams considering different models.

The study of the behavior of dams under seismic loads is a key factor for the safety requirements of dams and to ensure this safety, a lot of research has been conducted to determine how dams behave under seismic loads. It is evident that the presence of fluid in the reservoir affects the response of dams under seismic excitation. Indeed, when the interaction of the reservoir is considered, the movement of the structure is influenced by the fluid flow

through the forces transmitted to the interface, and reciprocally, the movement of the structure influences the fluid flow through the displacements of the interface which drives the fluid in its movement. For this reason, the dynamic interaction between a fluid and a structure is an important concern in the field of safety evaluation of concrete dams. Earthquake-induced hydrodynamic pressures on the upstream face of a dam are important design factors.

The works of Westergaard and Zangar [1, 2] provided methods for simplified modeling of the dam-reservoir interaction. The most recent works allow more refined modeling of the dam-reservoir interaction. Various authors such as Tiliouine and Seghir [3], Bouaanani et al [4], Lotfi [5], Dey and Sawant [6], Mandal and Maity [7] taken into account the hydrodynamic interaction effects in the dynamic calculations by the Finite Element Method (FEM) in the time domain of reservoir-dam, foundation-structure and foundation-dam-reservoir systems.

Mohan Rao and Shaik [8] or Silveira and Pedroso [9] studied the influence of foundation and reservoir on the dynamic behavior of concrete gravity dams in terms of their parameters in terms of natural frequencies, periods, mode shapes, crest displacement, base reactions and stress distributions. Ouzandja et al. [10], Ravindran and Jacob [11], Zeidan [12], Varughese and Nikithan [13] studied different dynamic modeling problems of a concrete gravity dam, with various field problems using the FEM. Salamone et al. [14] attempted to generate Finite Element results using various methods to determine the earthquake-induced hydrodynamic loads on the concrete arch dam. Millan et al. [15] studied the effects of reservoir geometry on the seismic response of gravity dams. For this purpose, a Boundary Element Method (BEM) model in the frequency domain was used to evaluate the influence of the reservoir geometry on the hydrodynamic dam response. Important conceptual conclusions about the dam-reservoir system behavior show that the reservoir shape influences the seismic response of the dam. Bayraktar et al [16] investigated the effect of reservoir length on the seismic performance of gravity dams to near and far-fault ground motions. Folsom Gravity dam is selected for a numerical example, and it is modeled considering four reservoir lengths and a foundation.

Dams of different heights of 100 m, 84 m, 60 m and 46 m were analyzed, and the results were obtained in terms of natural periods, stresses, and displacements at the crest of the dams for empty and full reservoir conditions.

The results obtained to allow a better understanding of the influence of different parameters considered on the seismic analysis of concrete gravity dams.

2 Fluid-Structure Interactions

The Finite Element Method (FEM) is a technique for obtaining a numerical solution to a specific problem, presented clearly, both in digital and graphic form; by defining the field problem, material properties, geometric properties, network model, boundary conditions, and element types. Usually, at this point, we will simplify the problem as much as possible to get fast and accurate results. Figure 1 Phases of the Finite Element.

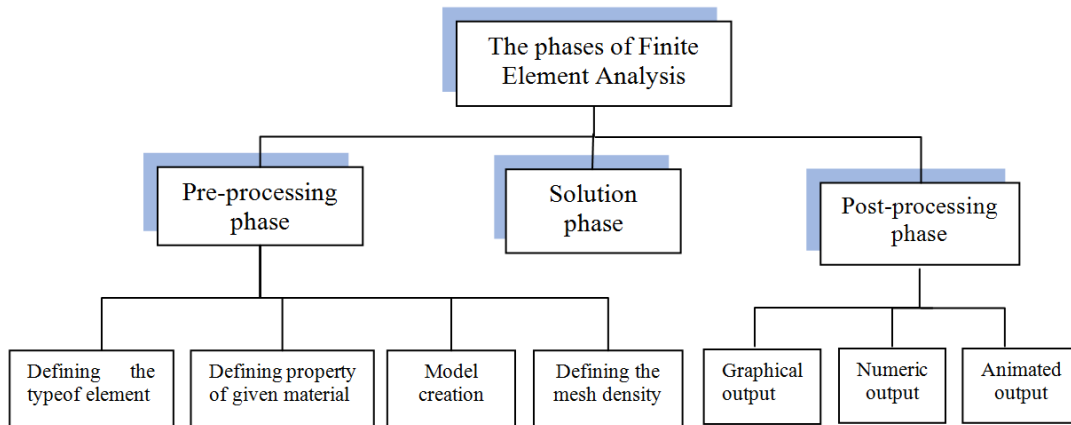


Figure 1: Phases of the Finite Element Analysis

2.1 Westergaard Method (Added Mass Method)

The generalized formula of Westergaard's theoretical solution to simulate the hydrodynamic pressure of reservoir water can be expressed using the added mass by Equation 1.

$$M_{ai} = 7/8 \rho_w A_i \sqrt{H_i (H_i - Z_i)} \lambda_i^T \lambda_i \quad (1)$$

Where i is a node on the structural surface subjected to hydrodynamic pressure, ρ_w is the mass density of water, A_i is the effective area of i , H_i is the total water depth of the vertical surface at which i is located, Z_i is the height from i to the bottom of the structural surface subjected to hydrodynamic pressure, and λ_i is the normal vector of i ,

$$\lambda_i = \{\lambda_{ix}, \lambda_{iy}, \lambda_{iz}\} \quad (2)$$

2.2 Potential-Based Fluid Formulation

We appreciate the comments, we have rewritten the sentence: “The assumptions made for the Potential-Based Fluid Elements in the program of Finite Element Analysis ADINA (Automatic Dynamic Incremental Nonlinear Analysis) are: inviscous, irrotational flow with no heat transfer; slightly compressible or almost incompressible flow; relatively small displacement of the fluid boundary; actual fluid flow with velocities below the sound speed or no actual fluid flow.”

The structure–fluid interaction is described as follows.

$$\begin{bmatrix} 0 & 0 \\ 0 & -M_{FF} \end{bmatrix} \begin{Bmatrix} \Delta \ddot{u} \\ \Delta \ddot{\phi} \end{Bmatrix} + \begin{bmatrix} C_{UU} & C_{UF} \\ C_{FU} & -(C_{FF} + (C_{FF})_S) \end{bmatrix} \begin{Bmatrix} \Delta \dot{u} \\ \Delta \dot{\phi} \end{Bmatrix} + \begin{bmatrix} K_{UU} & K_{UF} \\ K_{FU} & -(K_{FF} + (K_{FF})_S) \end{bmatrix} \begin{Bmatrix} \Delta u \\ \Delta \phi \end{Bmatrix} = \begin{bmatrix} 0 \\ 0 \end{bmatrix} - \begin{bmatrix} F_U \\ F_F + (F_F)_S \end{bmatrix} \quad (3)$$

where Δu is the unknown displacement vector increment; $\Delta \phi$ is the increment of the unknown potential vector; M_{FF} is the fluid element mass matrix; C_{UU} , C_{FU} , C_{UF} , C_{FF} are the damping matrices of the structure, the fluid caused by the structure, the structure caused by the fluid, and the fluid on the fluid-solid coupling interface, respectively; K_{UU} , K_{FU} , K_{UF} , K_{FF} are the stiffness matrices of the structure, the fluid caused by the structure, the structure caused by the fluid, and the fluid on the fluid-solid coupling interface, respectively; F_U , F_F , $(F_F)_S$ are the

fluid pressure on the structure boundary, the volume integral term, and the area integral term corresponding to the fluid continuity equation, respectively.

Equation 3 does not include any structural system matrices, and only gives the contribution of the potential-based Fluid Elements to the system matrices. The contribution of the structural term is added to Equation 3 to obtain the finite element equation of motion for fluid-structure interaction, as follows:

$$\begin{bmatrix} M_{SS} & 0 \\ 0 & -M_{FF} \end{bmatrix} \begin{Bmatrix} \Delta \ddot{u} \\ \Delta \ddot{\Phi} \end{Bmatrix} + \begin{bmatrix} C_{UU} + C_{SS} & C_{UF} \\ C_{FU} & -(C_{FF} + (C_{FF})_S) \end{bmatrix} \begin{Bmatrix} \Delta \dot{u} \\ \Delta \dot{\Phi} \end{Bmatrix} + \begin{bmatrix} K_{UU} + K_{SS} & K_{UF} \\ K_{FU} & -(K_{FF} + (K_{FF})_S) \end{bmatrix} \begin{Bmatrix} \Delta u \\ \Delta \Phi \end{Bmatrix} = \begin{bmatrix} 0 \\ 0 \end{bmatrix} - \begin{bmatrix} F_U \\ F_F + (F_F)_S \end{bmatrix} \quad (4)$$

In Equation 4, the structural element matrix of mass, damping, and stiffness, and the load vector, can be defined as:

$$M_{SS} = \int_{V_S} \rho_s \bar{N}^T \bar{N} dV, C_{SS} = M_{SS} \alpha + \beta K_{SS}, K_{SS} = \int_{V_S} B^T D B dV, \quad (5)$$

$$F_S = \int_{V_S} \bar{N}^T P dV + \int_S \bar{N}^T \bar{T} dS$$

where V_S is the solid region of the calculation; ρ_s is the density of the solid region; N is the nodal shape function of the solid region; α and β are the structural mass and stiffness matrix coefficients, respectively; B and D are the displacement-strain matrix and the elastic stiffness matrix of the solid region, respectively; P , T , and S are the physical force, surface force and boundary surface of the solid region, respectively.

2.3 Boundary Conditions

Reservoir Upstream Boundary

With the vibration of the dam, volumetric hydrodynamic pressure waves are created in the reservoir and propagate upstream. If the length of the reservoir is assumed to be infinity, then these waves would start to vanish. It should be noted that the length of the reservoir is assumed as a finite length, L , in numerical modeling. Hence, an artificial boundary is applied to simulate the effect of the infinite reservoir. This boundary is modeled based on the Sommerfeld boundary:

$$\partial p / \partial n (x, y, z) = -1 / C (\partial p / \partial t) (x, y, z) \quad (6)$$

The Bottom of the Reservoir

According to the rigidity of the reservoir bottom, by assuming the horizontal movement of the Earth, the pressure gradient is neglected:

$$\partial p / \partial n (x, y, z) = 0 \quad (7)$$

The Free Surface of the Reservoir

By neglecting the effects of surface waves, the governing boundary condition is as follows:

$$p(x, y, z) = 0 \quad (8)$$

Fluid-Structure Interface

In the common boundary between the reservoir and the dam body, an interaction between these two occurs which the result of inertia force is caused by the movement of the dam body. Hence, the applied pressure on the reservoir face caused by the inertial force is as follows:

$$\partial p / \partial n(x, y, z) = -\rho \cdot \ddot{u}_n(x, y, z) \quad (9)$$

In which ρ is the density of the fluid and \ddot{u}_n is the structure's acceleration vector in the direction normal to the common boundary of the fluid and structure.

3 Numerical Results and Discussion

The subject of this article is to present a dynamic computational model by the Finite Element Method for a concrete reservoir-gravity dam system taking into account the hydrodynamic interaction effects. Dams of different heights, 45 m, 60 m, 85 m, and 100 m shown in Figure 2 have been analyzed and the results obtained are compared in order to better understand the dynamic behavior of the concrete gravity dam for the performances analyzed by the Westergaard model (incompressible water) and the acoustic water model (compressible water). Concrete reservoir gravity dam systems are idealized as two-dimensional sections in the plane normal to the dam axis. The dam is assumed to be homogeneous, isotropic, and linearly elastic having a modulus of elasticity (E_d) equal to 24×10^6 kN/m², Poisson's ratio ν of 0.2, density ρ of 2500 kg/m³ and the critical damping percentage $\gamma = 5\%$. The water in the tank is assumed to have a density equal to 1000 kg/m³, and the modulus of compressibility of water $K = 2.2$ MPa. The dam is assumed to be fixed at the base and the reservoir length is taken as two times the depth.

The objective was to study the effect of the geometry of the dams on the frequencies, periods, stresses, and displacements of four concrete gravity dams. The dams taken into consideration are of variable height; they are named A1, A2, A3, and A4. The geometries of dams are presented in Table 1.

Table 1: The geometry of dams

	Height of dam(m)	Base width (m)	Top width(m)	Reservoir Height(m)
Dam A1	100	80	14	95
Dam A2	84	67	12	80
Dam A3	60	48	8	57
Dam A4	46	37	6	44

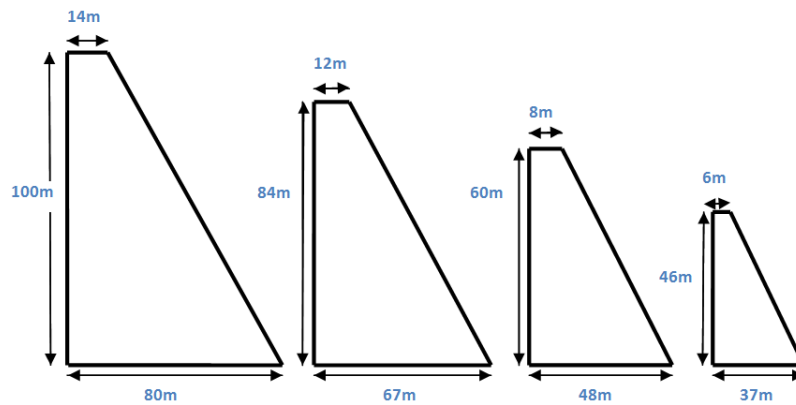


Figure2: Finite element idealization adopted for the four dams

3.1 Modal Analysis of Dam-Reservoir System

3.1.1 Effect of Dam Height on Periods

A modal analysis was performed on the selected family of concrete gravity dams; Figure 3 shows the typical form for the first two positions of each dam. The modal periods of the first six patterns of vibration of the dam reservoir system for different conditions of the dam length are listed in Table 2.

Table 2: First six natural periods of concrete gravity dams with empty reservoirs

Dam	A1	A2	A3	A4
1	0.268	0.226	0.160	0.120
2	0.106	0.090	0.064	0.049
3	0.098	0.082	0.058	0.044
4	0.057	0.048	0.034	0.026
5	0.043	0.036	0.025	0.020
6	0.038	0.032	0.023	0.017

It can be seen that the length of the dam has the main effect of prolonging the periods of vibration of the dam, especially for the highest dam whose values of the periods of vibration are doubled compared to the shortest dam. The period of the dam increases with an increase in height of the dams (for a constant ratio of bottom width to height).

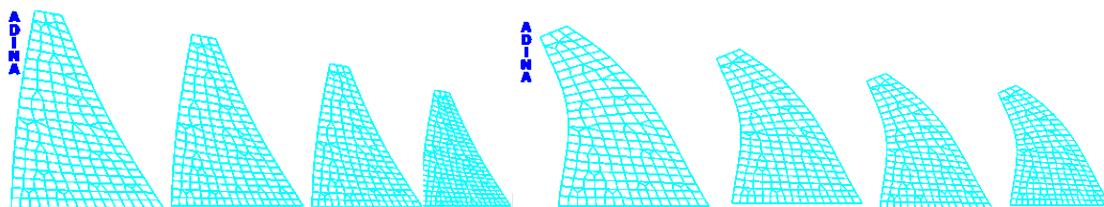


Figure 3: Modal distortions. Modes 1 of the empty dams, Modes 2 of the empty dams

3.1.2 Effect of Fluid Compressibility on Natural Periods

It can be seen in Table 3 below that the FEM using a compressible fluid provides values for periods greater than the Westergaard model of an incompressible fluid.

Table 3: First six natural periods of concrete gravity dams with a full reservoir

Dam Mode	A1		A2		A3		A4	
	Added mass	Acoustic fluid						
1	0.33	0.37	0.28	0.31	0.19	0.22	0.15	0.17
2	0.14	0.21	0.12	0.17	0.08	0.12	0.06	0.10
3	0.11	0.15	0.09	0.12	0.06	0.09	0.05	0.07
4	0.07	0.11	0.06	0.09	0.04	0.07	0.03	0.05
5	0.06	0.10	0.05	0.08	0.03	0.06	0.02	0.05
6	0.05	0.09	0.04	0.08	0.03	0.05	0.02	0.04

The results clearly show that taking into account the compressibility of the water leads to an increase in the periods, especially for the longer dam. This can be explained by the increase in the mass of the coupled fluid-structure system which leads to a smaller frequency and therefore a larger period. It can be noticed that the FEM model using a compressible fluid provides larger period values than the Westergaard added mass model.

3.2 Static Analysis

A static analysis of the dam-reservoir system is first performed to assess its pre-seismic state. This analysis is carried out for the two models considering the self-weight of the dam and the hydrostatic pressure. The following figures show the vertical stresses obtained by static analysis on the empty and full dam.

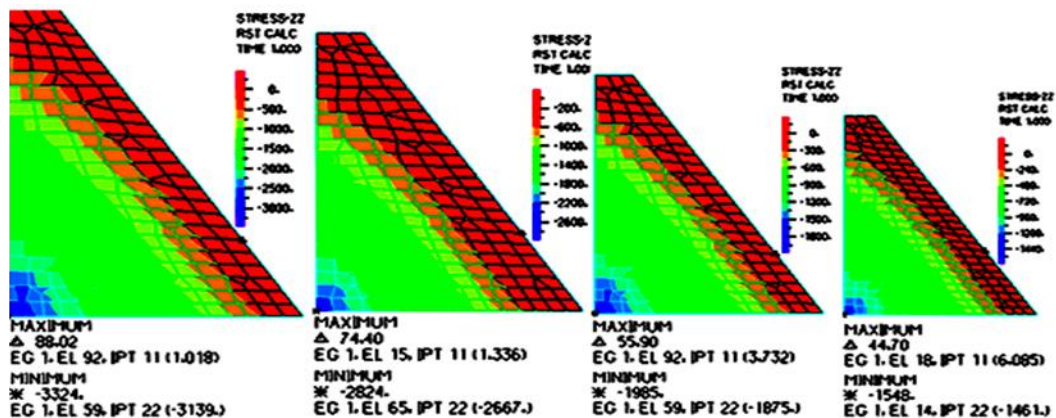


Figure 4: Vertical stresses distribution ZZ of empty dams

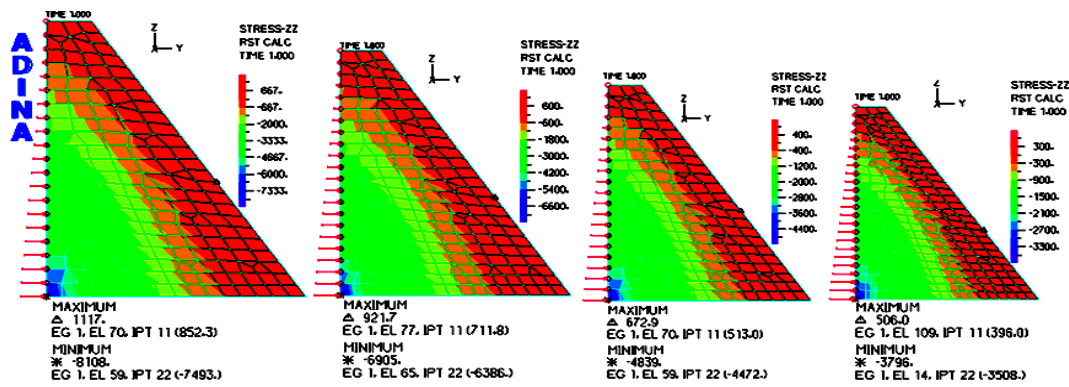


Figure 5: Vertical stresses distribution ZZ of full dams (added mass)

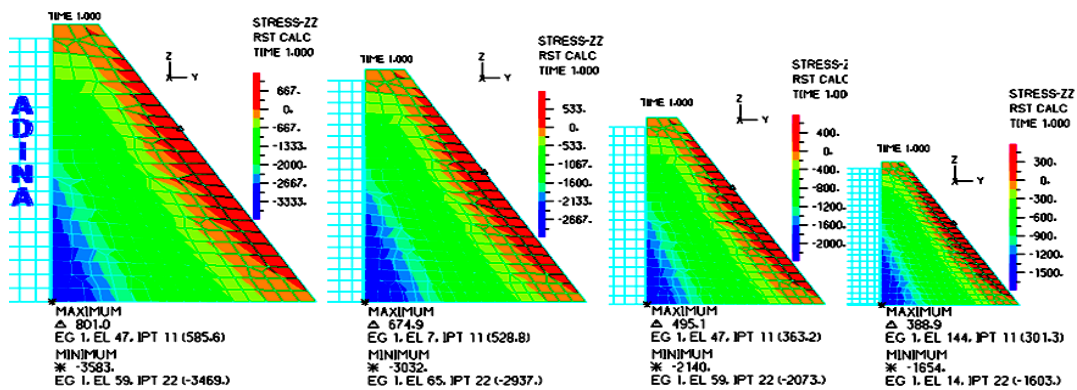


Figure 6: Vertical stresses distribution ZZ of full dams (acoustic fluid)

Figure 4 shows the vertical stress in the static state in the case of an empty reservoir (dam under its weight). The vertical stresses at the base are only the compressive stresses of four dams. Figures 5 and 6 show the vertical stress in the case of the filled reservoir (the hydrostatic state). The compressive stresses increase at the heel level of four dams under the influence of water pressure. The compressive stresses doubled in the case of the added mass with the presence of a tension in the dam toe. Pressures are proportional to the depth of the reservoir, so at the base of the dam, they will have maximum values. The stress distribution of the four dams is identical in all cases, directly proportional to the dam height and stress values.

3.3 Dynamic Analysis

The dynamic excitations considered in this study are represented by the accelerometric recordings of the horizontal component of the Loma Prieta replica from October 18, 1989 (Figure 7). The seismic response of the models is evaluated by analyses that display normal periods, displacements, and stresses. The different results obtained were compared. A summary of the main numerical results obtained is presented below to illustrate the studied effects of various factors on the dynamic response of a coupled system.

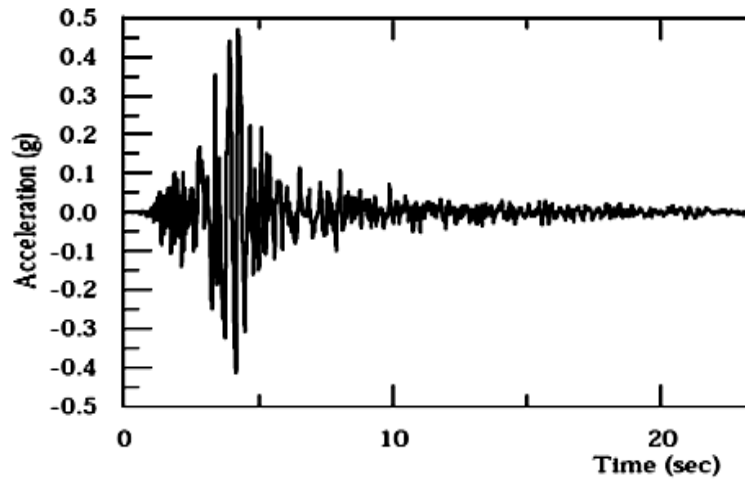


Figure 7: Loma Prieta Accelerogram

The stresses in the four empty dams and with the presence of water under the action of the accelerogram are shown in Figure 8.

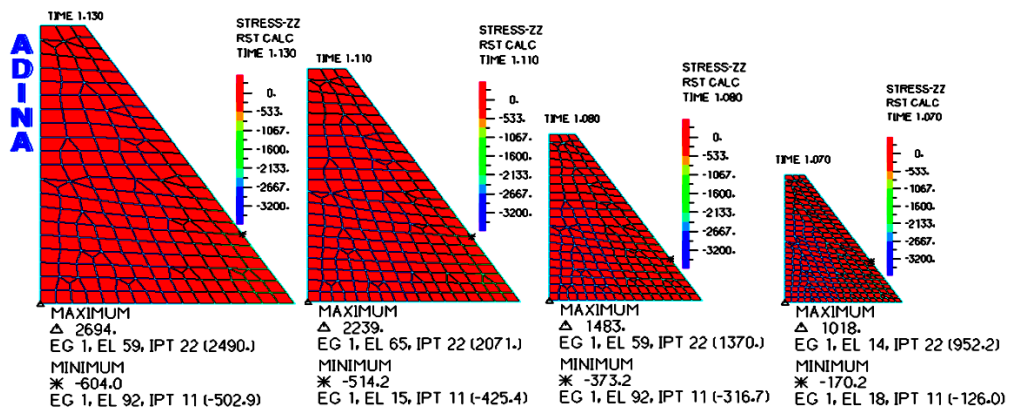


Figure 8: Vertical stresses distribution ZZ of empty dams

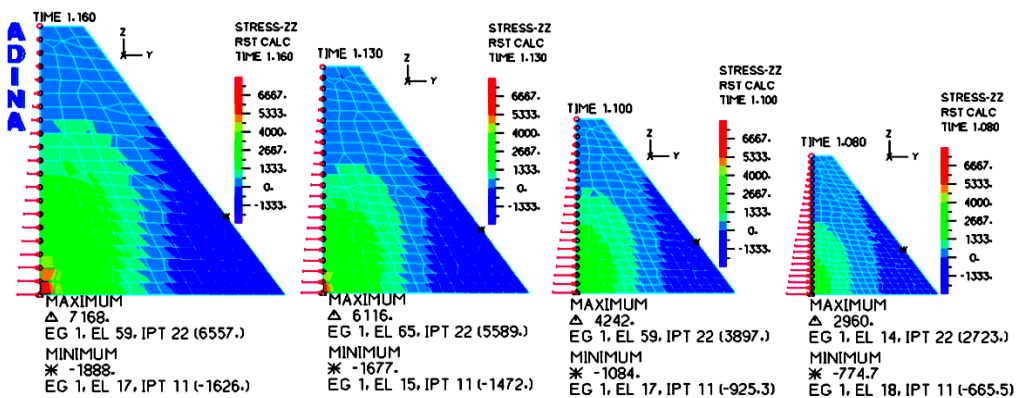


Figure 9: Vertical stresses distribution ZZ of full dams (added mass)

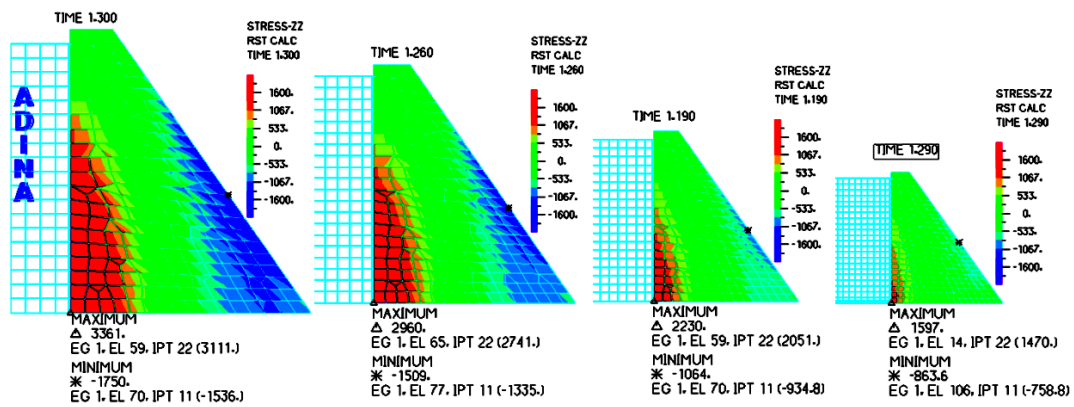


Figure 10: Vertical stresses distribution ZZ of full dams (acoustic fluid)

Vertical tensile stresses start downstream of the dam, then propagate towards the dam body and finally reach the upstream face. Therefore, there's a risk of concrete cracking in these areas because the tensile strength of concrete is low compared to the compressive strength. The stress profiles obtained for the four dams with compressible and incompressible fluids are similar but with different values, highlighting the influence of the height of the dam and the type of fluid in the reservoir. Vertical stress results given in Figures 8, 9, and 10 confirm that as the dam rises, vertical stresses at the dam's heel increase dramatically. Especially for dams with incompressible liquids, we observe unwanted tensile stresses in the heel. Comparisons of vertical stresses (mass added of Westergaard versus acoustic fluid) are shown in Figures 11 and 12.”

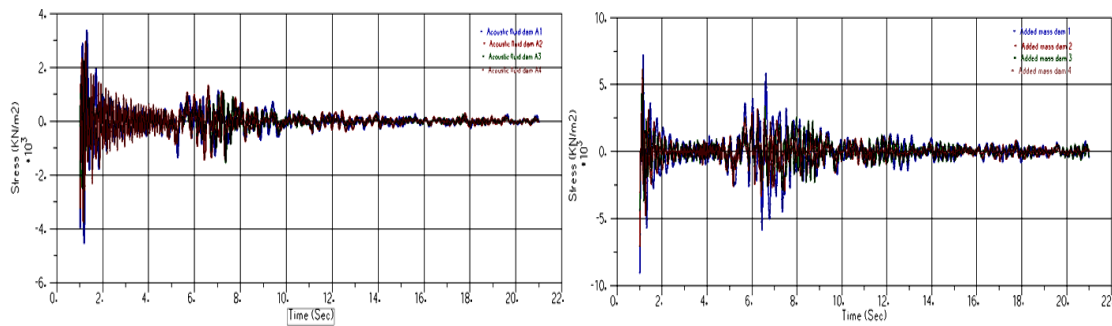
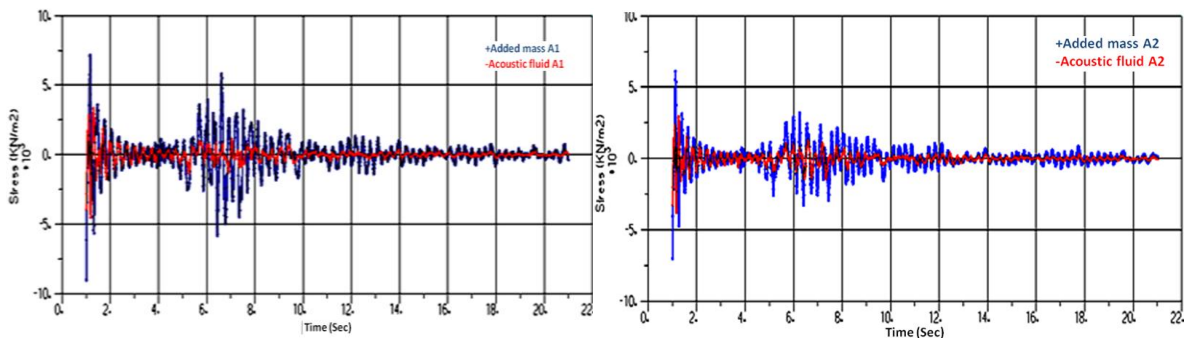


Figure11: Vertical Stresses at dam heel (acousticfluid –added masses) for A1-A4



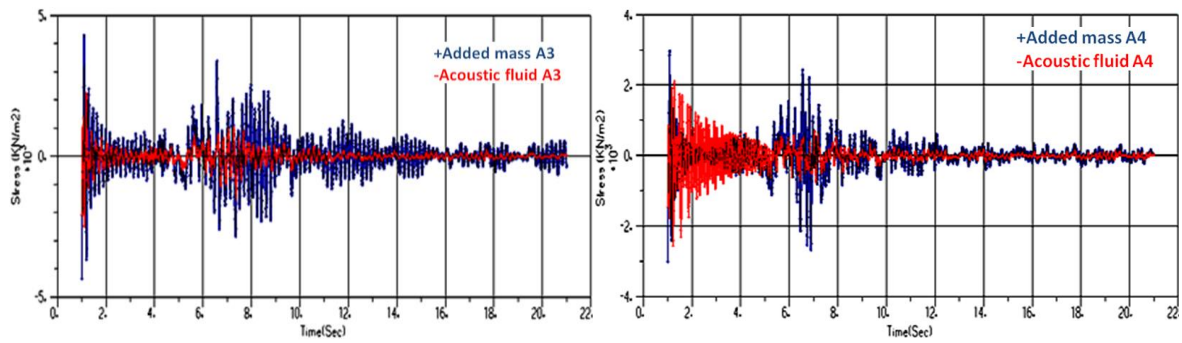


Figure 12: Vertical Stresses at dam heel (added masses vs. acoustic fluid) for A1-A4

The stresses were compared at the heel of the dams. We note that the response of the three highest dams in the first five seconds to the earthquake is the same; the earthquake is the same in the first five seconds, but with double, the values for the incompressible fluid compared to the compressible fluid. In contrast to the lowest dam, the stress values increase after the first to the fifth second in the compressible fluid. Regarding the effect of length on the stresses at the dams' heel for the two fluids, the frequency content is similar, but the vertical stresses increase as the dam height increases with appreciable values in the incompressible fluid. The amplifications and changes in the response of the dam due to the added mass are clearly visible.

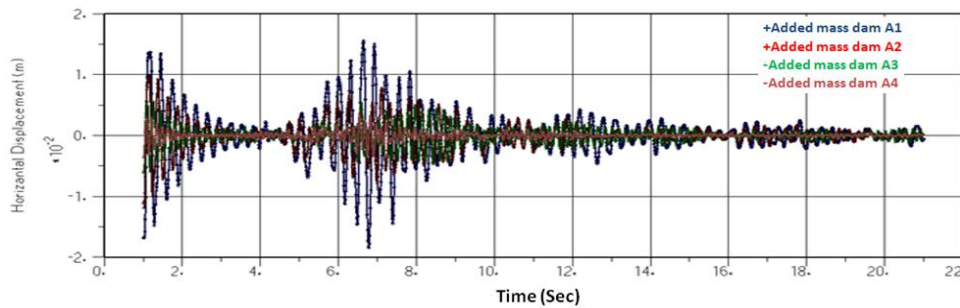


Figure 13: Crest horizontal displacements of full gravity dams (added masses)

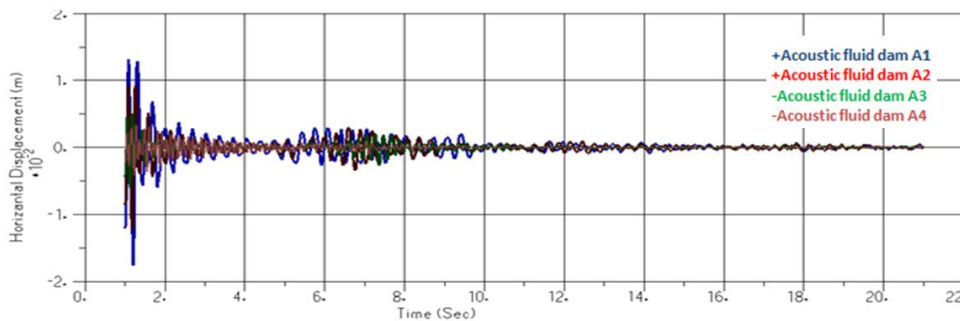


Figure 14: Crest horizontal displacements of full gravity dams (acoustic fluid)

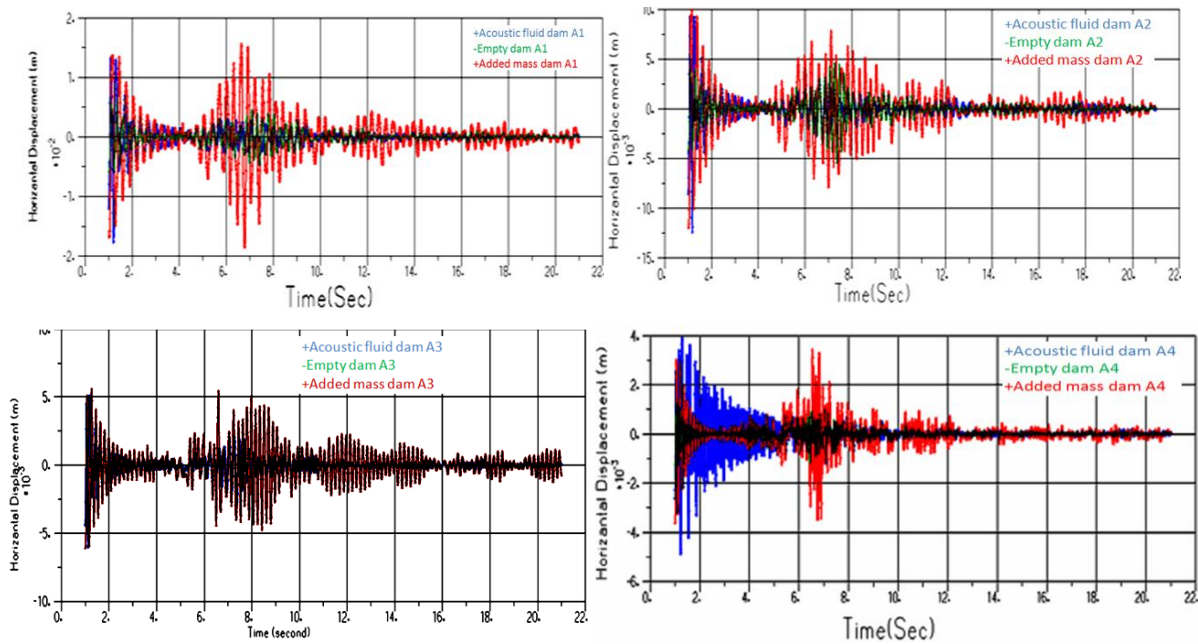


Figure 15: Crest horizontal displacements (added masses vs.acoustic fluid)

Figures 13-15 show the time history of the horizontal displacement at the dam's crest (crest point) upstream of the empty and full reservoir cases. The maximum values of horizontal displacement noted at the dam's crest empty reservoir were 5.87, 5.44, 2.44 and 1.27mm for models A1, A2, A3, and A4, respectively. For the full reservoir, the horizontal displacements noted at this point were 18.46, 11.96, 6.09 and 3.60mm respectively. Therefore, an increase of 68.2, 54.51, 59.93 and, 64.7%, respectively, is observed between the results of an empty and full reservoir (added masses). It is obvious that the horizontal displacements obtained from the full reservoir case are higher than the ones obtained from the empty reservoir case due to the effect of hydrostatic and hydrodynamic pressure of the reservoir water. The maximum values of horizontal displacement noted at this point are 17.76, 12.36, 6.02, and 4.85 mm for the full reservoir (acoustic fluid). Therefore, an increase of 66.94, 55.98, 59.46 and, 73.81%, respectively, is observed between the results of both cases (empty and full reservoir (acoustic fluid)). So, the displacements of the crest in the horizontal direction due to the hydrodynamic effect of an incompressible fluid increases by 5% compared to the horizontal displacements of the crest dams of compressible fluid.

4 Conclusions

In this study, the effect of the hydrodynamic pressure of the reservoir on the response of concrete dams subjected to seismic excitations was studied. The results of the study were obtained in terms of displacement and, stresses. Based on the results, the following conclusions are drawn:

1. The natural period of the dam increases with an increase in height for a constant ratio of the bottom's width to height.
2. The time analysis with an "incompressible fluid" material model provides different results when the compressibility of the fluid is considered.

3. Crest displacement is maximum at the peak of the dam and increases with the height of the dam, hence proper measures should be taken while designing dams.
4. According to the analysis of the vertical stresses, the heel element has the most stress absorption compared to the other parts of the dam.
5. The displacement of the crest in the horizontal direction due to the hydrodynamic effect of an incompressible fluid increases by 5% compared to the horizontal displacement of the crest dams of compressible fluid.
6. Regarding the effect of fluid compression, it was found that for concrete gravity dams, the response of the structure in terms of displacement is not significantly affected; on the other hand, the vertical stresses are particularly amplified at depth.
7. The tensile strength under dynamic loading increases significantly in an incompressible fluid bed. The level of seismic cracking at the base of the dam is likely to be significant. A non-linear analysis is required.

References

- [1] Westergard, H. M. (1933). Waterpressure on dams during earthquakes. Transactions.ASCE. Vol.98.
- [2] Zangar, C.N. (1952). *Hydrodynamic pressures on dams due to horizontal earthquake effects*. Technical Information Office, Denver, Colorado. no. 11.
- [3] Tiliouine, B., Seghir, A. (1997).Influence of the fluid-structure interaction on the seismic behavior of the Oued-Fodda dam (North-West Algeria).CAM97.
- [4] Bouaanani, N., Paultre, P., Proulx, J. (2003). A closed-form formulation for earthquake-induced hydrodynamic pressure on gravity dams. *Journal of Sound and Vibration*. 261, 573–582.[https://doi.org/10.1016/S0022-460X\(02\)01257-9](https://doi.org/10.1016/S0022-460X(02)01257-9)
- [5] Lotfi, V. (2003).Seismic analysis of concrete gravity dams by decoupled modal approach in time domain. *Electronic Journal of Structural Engineering*. 3, 102–116.<https://doi.org/10.56748/ejse.333>
- [6] Dey, A., Sawant, M. B. (2013). Seismic response of a concrete gravity dam considering hydrodynamic effects. In: APCOM & ISCM 11-14th December, 2013. Singapore.
- [7] Mandal, A., Maity, D. (2019). Seismic analysis of dam-foundation-reservoir coupled system using direct coupling method.*Coupled Systems Mechanics*. 8 (5), 393-414.<https://doi.org/10.12989/csm.2019.8.5.393>
- [8] Rao, K.R.M., Shaik, N.N. (2014).Finite Element Modelling and Seismic Response Evaluation of Large Concrete Gravity Dams - An Approach based on Indian Standard Codal Guidelines. *International Journal of Emerging Engineering Research and Technology*. 2 (2), 178-186.
- [9] Silveira, I.V., Pedroso, L.J. (2018). Analysis Of Natural Frequencies And Modes Of Vibration Involving Interaction Dam-Reservoir-Foundation For Concrete Gravity Dams third international dam word. In: Conference BRAZIL.Foz do Iguacu.septembre 17-21.2018.
- [10] Ouzandja, D., Tiliouine, B., Ouzandja T. (2018). *Dynamic Behavior Analysis Of Concrete Gravity Dams Analyse Du Comportement Dynamique Des Barrages-Poids En Béton* » ALGÉRIE EQUIPEMENT N° 58, Janvier 2018. ISSN: 1111-5211.
- [11] Ravindran, A., Jacob, B. (2018). Effects of Dam-Reservoir-Foundation Interaction on Modal Behaviour of Gravity Dam.*International Journal of Advance Engineering and Research Development*. 5(4), 1544–1552.

- [12] Zeidan, B. A. (2014). Finite Element Modeling for Acoustic Reservoir-Dam-Foundation Coupled System. In: International Symposium on Dams In Global Environmental Challenges Bali, Indonesia, June 1ST – 6TH, 2014, Indonesia.
- [13] Varughese, J.A., Nikithan, S. (2016). Seismic behavior of concrete gravity dams. *Advances in Computational Design.1* (2), 195-206.
- [14] Salamon, J., Manie, J. (2017) . Numerical Assessment Of Hydrodynamic Loads Induced During Seismic Interaction between Reservoir and Concrete Dam. In: Blind Prediction Analysis Workshop hosted by the USSD Earthquake Committee, Anaheim, CA.
- [15] Millan, M. A., Young, Y. L., Prevost, J. H. (2007). The effects of reservoir geometry on the seismic response of gravity dams. *Earthquake Engineering Structure Dynamic. 36*, 1441–1459<https://doi.org/10.1002/eqe.688>
- [16] Bayraktar, A., Türker, T., Akköse, M. & Ateş, Ş. (2010). The effect of reservoir length on seismic performance of gravity dams to near- and far-fault ground motions. *Natural Hazards. 52*, 257-275. <https://doi.org/10.1007/s11069-009-9368-1>

Mechanical Properties of Self-compacting Concrete Containing Fine Aggregates from Cement Kiln Dust and Hardened Cement Waste

Leila Kherraf^{1*}, Karim Younes¹, Assia Abdelouahed¹, Mouloud Belachia¹, Houria Hebhoub¹

¹ University of 20 August 1955, Skikda, Algeria,
Department of Civil Engineering
*e-mail: kherrafleila@yahoo.com

Abstract

The aim of this research is to assess the mechanical performance of self-compacting concrete containing different percentages of fine aggregates, produced from the wastes generated by the cement plant industry and construction sites. Eight mixes, incorporating cement kiln dust (CKD) and hardened cement waste with partial fine aggregate replacement of 5%, 10%, 15%, and 20%, were produced and compared with a control mix made with 100% of crushed sand. The workability properties (e.g., flowability, passing ability, and resistance to segregation) and mechanical properties (e.g., compressive, flexural, and splitting tensile strengths) of all mixes were evaluated. The results showed that concretes containing recycled fine aggregates proved to have the best mechanical properties, compared to one made with crushed calcareous sand. However, self-compacting concrete with high mechanical strength could be produced with up to 15% wt. CKD replacement and with 10% wt. hardened cement waste replacement.

Keywords: fine CKD aggregate, fine hardened cement aggregate, self-compacting concrete, mechanical performance

1 Introduction

Self-compacting concretes (SCCs) are very fluid, high-performance concretes, which are placed in the form and compacted under the sole effect of gravity [1]. These concretes are characterised by a formulation containing a high dosage of cement, a large number of fine minerals, a reduced volume of small gravel, rolled or crushed sand, a large dose of superplasticiser, and (sometimes) a viscosity agent. The exact dosages of the constituents depend on the method of formulation chosen [2]. The volume of sand is, generally, 40% of the mortar volume of the concrete [3], which allows it to improve the compactness of the granular skeleton, consequently reducing granular friction and playing a very important role in determining the properties of fresh and hardened SCCs. Crushed or rolled sands have been successfully used in the production of SCCs, crushed sand generally contains a very high content of fine particles, which is considered to be a second source of filler [4]. The angular

shape, the roughness, and the water absorption capacity of the grains promote good adhesion of the grains [5] since they make it possible to increase the paste-sand bonds and densify the layer of these bonds because of the chemical reaction between calcite crystals and cement, to form monocaboaluminate [6]. This reaction is limited to the surface of the aggregates due to the low mobility of the carbonate ions [7]. As a result, the mechanical characteristics of concrete are improved, namely the compressive and tensile strength [8]. The dune sand is fine siliceous sand, characterised by its fineness and a high water absorption capacity. The grain shapes are rounded and spherical, with a smooth surface and almost uniform grain size. Dune sand decreases the fluidity but improves the viscosity of the SCC. Beyond a content of 30%, additional quantities of water and superplasticiser are necessary to satisfy the self-compacting properties [9].

Although it brings many advantages to the world of construction, such as saved time and labour, reduction of noise pollution during its installation, and, of course, very good results in terms of the aesthetic quality of facings, the use of this type of concrete is rapidly becoming popular in developed countries. However, its use is still limited in Algeria, mainly due to its high cost. To this end, we have considered the recovery of waste from the construction sector because it is available and less expensive as an aggregate, in the composition of this type of concrete. This could minimise manufacturing costs and provide interesting properties, perpetuating, and preserving natural resources within the framework of environmental sanitation and the living environment.

In this research, we examine the influence of two types of recycled sand on the rheological and mechanical properties of SCCs, namely: cement kiln dust (CKD) waste sand and hardened cement waste sand.

Cement kiln dust is an industrial by-product formed during the manufacture of cement and is a waste material that is traditionally destined for landfill [10]. This dust, whose composition varies from one clinker production line to another and even from one period to another (within the same line), includes clinker particles and particles resulting from the wearing of the refractory and/or monolithic brick lining of the furnace and associated equipment [11]. CKD has a chemical composition similar to that of conventional Portland cement [12]. Free lime can be found in CKD and its concentration is typically highest in the coarser particles collected closest to the kiln. Finer particles tend to exhibit higher concentrations of sulphates and alkalis [13]. Some of the generated CKD could be reused in a cement kiln as raw feed. However, this is limited by the alkali concentrations in CKD, which may cause the alkali content in cement to exceed the allowable limit [14]. The portion of CKD that is not returned to the cement industry is disposed of, which could pose significant problems. The main environmental problems of CKDs reside in the congestion caused by the increased number of heaps of CKD in the vicinity of cement plants and the pollution of groundwater and water runoff, caused by the leaching of toxic compounds and contamination by soluble substances, such as sulphates, carbonates, chlorides, alkalis, and metals. In addition, CKD affects human health by causing serious health hazards including asthma, skin irritation, and eye problems [15,16].

Current CKD recovery channels are raw feedstock, base stabiliser for pavements, a solidifier and stabiliser for contaminated wastes, and agricultural soil enhancement. It has been in the study phase in the field of construction for several years. The use of CKD as an addition to

Portland cement has been evaluated by a number of researchers. As an indication, Alnahhal et al. [17] investigated the effects of using nano-sized CKD as a partial replacement for Ordinary Portland Cement (OPC) on the strength of cement mortars. A total of 28 concrete mortar mixtures were prepared with four different replacement percentages of nano-CKD (5, 10, 15, and 20%), and seven different milling times. The compressive strengths of all cement mortar mixtures were evaluated after curing periods of 7, 28, and 56 days. The experimental results showed that the partial replacement of OPC with up to 20% nano-CKD resulted in an increase in the compressive strength of cement mortar by about 15 to 30%, compared with normal mortar without CKD. Saleh et al. (2020) [18] concluded that the use of CKD as waste material in concrete makes it economical and it is assumed that the reuse of this waste is the best ecological option to handle the waste disposal problem. At the same time, better performance of light concrete can be achieved in building material applications. Ibrahim Saad Agwa, 2019 [19] studied the potential of using CKD as a cement replacement in self-compacting concrete (SCC). Eight mixes incorporating CKD with a partial cement replacement of 0%, 5%, 10%, 20%, 30%, 40%, 50%, and 75%, in addition to a control mix, were investigated. It was found that the SCC mixture incorporating 5 to 10% CKD was almost similar to that of the control mixture. The workability of SCC concrete decreased as CKD replacement increased. This established the benefits of substituting cement with CKD to make SCC. Khalid B. Najim (2016) [20] investigated the use of CKD as a cement replacement material in producing high-performance/self-compacting concrete. Different percentages of replacement by cement weight were tried, including 10%, 20%, and 30%, whilst keeping other constituent contents constant. The results showed that there was a progressive decrease in flowability and mechanical strength properties with increasing CKD replacement. However, high-strength, self-compacting concrete could be produced with up to 20% wt. CKD replacement, while high-performance/self-compacting concrete was obtained with 30% wt. CKD replacement.

Hardened cement is cementitious waste produced accidentally or through negligence, following the crystallisation of the powder in the event that a bag of cement is in contact with water or a humid environment and becomes unusable on site. Its recovery must be immediate, in order to avoid any kind of possible environmental pollution. The literature review showed that there are no studies concerned with the recovery of this category of waste.

The main objective of this study is to find a substitute for natural aggregate through the incorporation of waste from the cement industry, such as recycled sand, in self-compacting concrete (SCC), illustrating its potential in order to promote the popularisation of its use as a building material in the civil engineering sector.

2 Experimental Program

2.1 Used Materials

- A Portland cement composed of the CEM II/B-L 42.5N type was used, with an absolute density of 3.06 g/cm^3 and the specific surface area of $3190 \text{ cm}^2/\text{g}$.
- The limestone filler (LF) used was prepared by sieving powder recovered from the Ben Azzouz crushing quarry (Skikda-East of Algeria) with an $80 \mu\text{m}$ sieve; the absolute

density was 2.7 g/cm³ and specific surface area was 3200 cm²/gr. The chemical properties of the cement and limestone filler are shown in Table 1.

- Two classes of gravel (G 4/8 and G 8/16) were used during this study, comprising crushed limestone from the ENOF – LAGHEDIR quarry (Skikda-East of Algeria).
- Three types of sand were used as fine aggregates: class 0/4 quarry sand (Q-S) from the ENOF – Laghedir quarry (Skikda-East of Algeria); fine sand from cement kiln dust waste (CKD-S) of class 0/1, from industrial residues recovered by electrostatic filters during the manufacture of clinker at the Hadjar-Soud cement plant in Azzaba (located in Skikda); and fine hardened cement waste sand (HC-S) of class 0/1, recovered from construction sites and obtained after crushing and sieving the rejected hardened cement blocks. The chemical and physical properties of various types of sand and gravel are grouped in Tables 1 and 2, respectively, and their particle size distributions are shown later, in Figure 2.
- A high water-reducing Sikaviscocrete tempo 12 superplasticiser (SP) was used. Its density was 1.06±0.01, its pH was 4.5 and its solid particle concentration was 29%±1.5.
- Tap water (T = 28°C) for mixing.

2.2 Characterization of Materials

2.2.1 Chemical Characteristics

The chemical composition of the cement and the sands were determined by X-ray fluorescence spectroscopy (XRF), according to NF EN ISO 12677:2004. The analysis technique is made from a sample in powder form. The material sample is dried at 105°C at a constant weight and finely ground mechanically. The resulting powder is put in a specific pellet, well compressed, and the surface upper is well smoothed.

Table 1: Chemical composition of cement, limestone filler and sands used

Oxides (%)	CEM II	LF	HC-S	CKD-S	Q-S
CaO	64.02	55.7	63.97	65.04	51.56
Al ₂ O ₃	5.12	0.3	5.43	6.44	0.59
Fe ₂ O ₃	3.3	0.16	3.95	4.24	0.75
SiO ₂	22.05	0.57	21.88	22.43	2.62
MgO	1.25	0.37	1.66	1.2	1.52
Na ₂ O	0.12	0.07	0.08	0.28	0.04
K ₂ O	0.52	0.03	0.53	0.99	0.13
Cl	0.005	0	0.013	0.016	0
SO ₃	1.84	0.01	2.15	0.27	0.3

According to the results illustrated in Table 1, it can be seen that the nature of the sands used is essentially calcareous.

2.2.2 Physical Characteristics

The physical characteristics were determined in accordance with the standards and test results and are presented in Table 2.

Table 2: Physical characteristics of sands and aggregates

Characteristic	HC-S	CKD-S	Q-S	G 3/8	G 8/16	Standards
Bulk density (g/cm ³)	1.50	1.58	1.456	1.53	1.44	NF EN 1097-3
Particle density (g/cm ³)	2.70	2.72	2.683	2.71	2.75	NF EN 1097-6
Sand equivalent (%)	73	83	88	--	--	NF EN 933-8
Water absorption (%)	1.73	1.44	0.783	1.18	0.61	NF EN 1097-6
Fineness modulus	1.70	1.76	2.78	--	--	NF EN 933-1
Fines content (%)	2	1	10.68	--	--	NF EN 933-1
Los Angeles testing (%)	--	--	--	--	24	NF P 18 - 573

It should be noted that:

- The two types of sand HC-S and CKD-S have a similar bulk density. The small difference (about 5%) is attributed to the shape of the sand grains. In addition, Q-S has a value that deviates by 3%, compared to HC-S sand, and 8.5%, compared to CKD-S sand. The angular shape of Q-S sand increases the space between its grains and, therefore, the value of the apparent density decreases.
- The HC-S sand had adequate cleanliness, between 70% and 80%. This indicates that the sand is clean, with a low percentage of clay fines, and perfectly suitable for high-quality concrete. Furthermore, the other two types of sand have cleanliness values greater than 80%, which means that the CKD-S and Q-S sands are very clean.
- CKD-S and HC-S sands are fine sands while Q-S sand is medium and well-spread sand.
- The water absorption capacity A_b (%) of HC-S sand is the highest and is followed by that of CKD-S sand.
- Unlike CKD-S and HC-S sands, Q-S sand contains a large volume of fines $<63 \mu\text{m}$.

2.2.3 Particle Size Analyses

Granulometric analysis of the sands and aggregates used was carried out according to the Standard NF EN 933-1:2012, as shown in Figure 1.

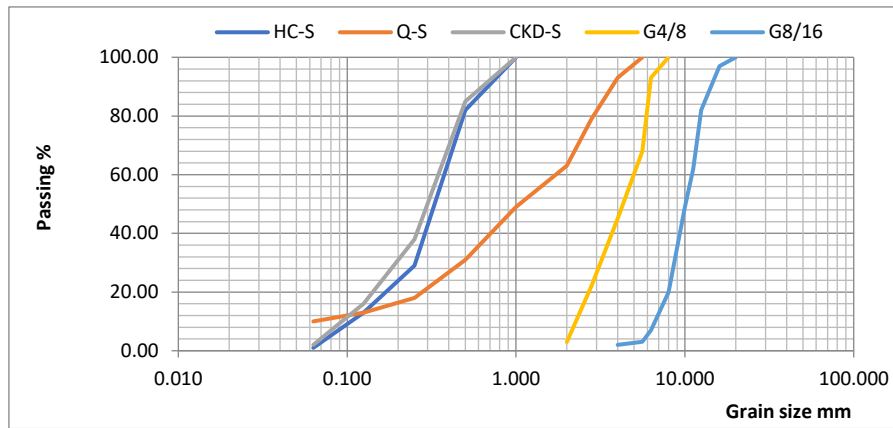


Figure 1: Particle size distribution curves for the sands used

It is noted that the grain size curves of all sands are continuous and relatively comparable for both HC-S and CKD-S sands.

2.2.4 Mixtures and Methods

To achieve the objectives of this study and the required composition of the self-compacting concrete, the quarry sand was successively substituted by a mass fraction of sand from hardened cement waste and CKD sand at rates of 0%, 5%, 10%, 15%, and 20%. The behaviour of the concretes produced in the fresh state, as well as in the hardened state, were evaluated and compared with those of a control concrete, initially composed of 100% crushed sand. The formulation method adopted in the case of this study is an empirical method based on the experience acquired in recent years [21,22]. The proportions of the constituents were determined by trial and error around certain orders of magnitude.

For a rather high cement dosage (the mass of the cement is greater than or equal to the minimum required by the ready-mixed concrete standard (P18 305), i.e., generally 300 to 350 kg/m³), the percentage of additional materials was determined experimentally (superplasticiser, limestone filler). The volume of occluded air was around 2%, and the volume of paste for one cubic meter of concrete was equal to the sum of the volume of cement, superplasticiser, limestone filler, entrained air, and sand, i.e., between 330 and 400 l/m³, and a volume ratio of gravel/sand close to 1.

In fact, the constant parameters for all SCC are cement C = 420 kg/m³, water/binder ratio W/B = 0.37, fillers FC = 74.11 kg/m³, water E = 182.82 l, the superplasticiser SP = 1% (i.e., 4.20 kg/m³), the volume of paste = 370 L/m³, and the gravel/sand volume ratio G/S = 0.9. The only variant was the nature of the sand. The prepared compositions are shown in Table 3 and the notations used are as displayed in Table 4.

Table 3: Compositions of concretes formulated with recycled sand

Concrete	C (kg/m ³)	FC (kg/m ³)	E (l)	S 0/4 (kg/m ³)	HC-S 0/1(kg/m ³)	CKD -S 0/1(kg/m ³)	G4/8 (kg/m ³)	G8/16 (kg/m ³)	Adj (kg/m ³)
SCC1	420	74.11	182.82	878.68	--	--	404.35	410.32	4.20
SCC2	420	74.11	182.82	834.75	43.93	--	404.35	410.32	4.20
SCC3	420	74.11	182.82	790.81	87.87	--	404.35	410.32	4.20
SCC4	420	74.11	182.82	746.88	131.8	--	404.35	410.32	4.20

SCC5	420	74.11	182.82	702.94	175.73	--	404.35	410.32	4.20
SCC6	420	74.11	182.82	834.75	--	43.93	404.35	410.32	4.20
SCC 7	420	74.11	182.82	790.81	--	87.87	404.35	410.32	4.20
SCC 8	420	74.11	182.82	746.88	--	131.8	404.35	410.32	4.20
SCC 9	420	74.11	182.82	702.94	--	175.73	404.35	410.32	4.20

Table 4: Compositions

SCC1: Concrete made with 100% quarry sand			
SCC2	Concrete made with 5% HC-S and 95% Q-S	SCC6	Concrete made with 5% CKD-S and 95% Q-S
SCC3	Concrete made with 10% HC-S and 90% Q-S	SCC7	Concrete made with 10% CKD-S and 90% Q-S
SCC4	Concrete made with 15% HC-S and 85% Q-S	SCC8	Concrete made with 15% CKD-S and 85% Q-S
SCC5	Concrete made with 20% HC-S and 80% Q-S	SCC9	Concrete made with 20% CKD-S and 80% Q-S

An electric cement mixer, with an inclined axis and a capacity of 60 l, was used to make the concretes for the study. All of the materials were mixed, in order to homogenise them, and the total mixing time was 5 minutes, including 2 minutes of dry mixing. At the end of mixing, the concrete was emptied from the mixer into a tank, in order to examine the characteristics of the SCCs in the fresh state, it was then poured into the cubic moulds $15 \times 15 \times 15$ cm, and the $7 \times 7 \times 28$ cm moulds. Unmoulding took place after 24 hours. The test specimens were then kept in water, at an average temperature of $20^{\circ}\text{C} \pm 2^{\circ}\text{C}$ until the end of the test, in accordance with standard NF EN 12390-2: 2012.

3 Results and Discussion

3.1 Characterization Tests of Self-compacting Concrete in the Fresh State

Before defining a composition as being that of self-compacting concrete, it must be ensured that the properties of the concrete in the fresh state comply with certain criteria established by the recommendations of the AFGC (French Association of Civil Engineering).

3.1.1 Slump-Flow Test

The slump flow test was operated according to EN 12350: Part 8-2010 and used to measure the flowability of fresh SCC. Figure 2 shows the results obtained.

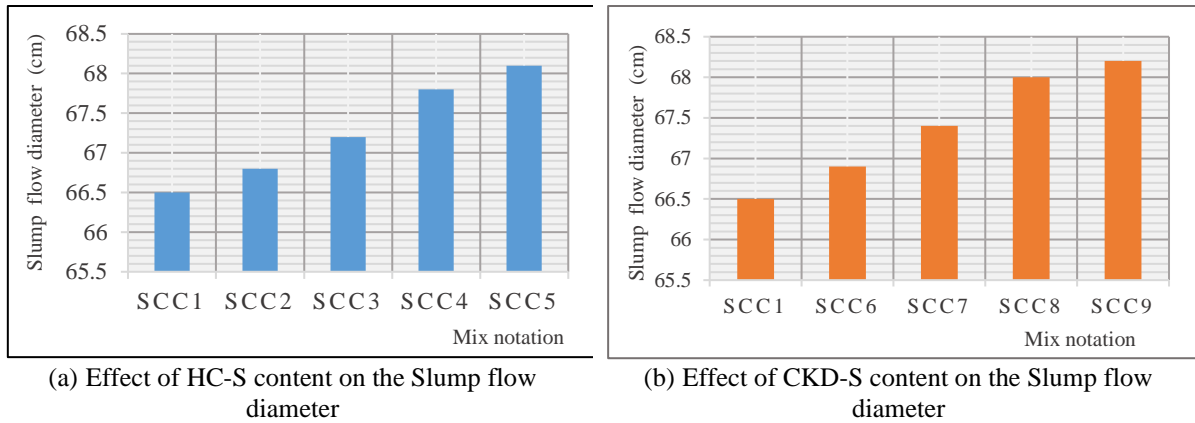


Figure 2: Slump flow diameter of the SCC mixes

Figure 2 shows that the flowability of SCCs, based on hardened cement waste sand or CKD, falls within the range of the SF2 class (660 to 750 mm) defined by the AFGC recommendations [22]. In fact, by increasing the substitution rate of ordinary sand with hardened cement waste sand or CKD sand in the mixtures, the flowability improves remarkably and continuously. However, the values exhibited by CKD-based SCCs are relatively higher than those shown by cement waste sand-based concretes. The maximum slump flow diameter is given by SCC9. It exceeds that of the control by 2.55% and that of SCC5 by 0.14%. All these flowability variations are related to:

- * The use of hardened cement waste sand and CKD sand increased the volume of the paste due to the introduction of a significant number of fine grains which fill the voids available between the aggregates and, as a consequence, the amount of water that occupied the voids is released into the interstitial solution, resulting in better fluidity.

- * The dispersion effect exerted by the superplasticiser used where the molecules of the latter are adsorbed on the surface of the grains of cement, limestone filler, CKD sand and hardened cement sand, causing a kind of coating while preventing water from attaching itself directly to the walls of the grains [23], thus the lubrication of the mixture is all the more noticeable in the case of concrete containing CKD sand.

The difference in behaviour between SCCs with CKD and hardened cement sand depends on the fineness, the absorption ratio, and the compatibility of the superplasticiser with the ternary mixture of cement, limestone filler and fine particles of each of these recycled sands.

3.1.2 L-box Test

The passing ability (PA) of SCCs is characterised by the L-box test, according to EN 12350: Part 10-2010. The results of the variation of the H_2/H_1 ratio are shown in Figure 3. These results clearly show that all the formulations have PA higher than 0.80, which complies with the requirements of the AFGC recommendations.

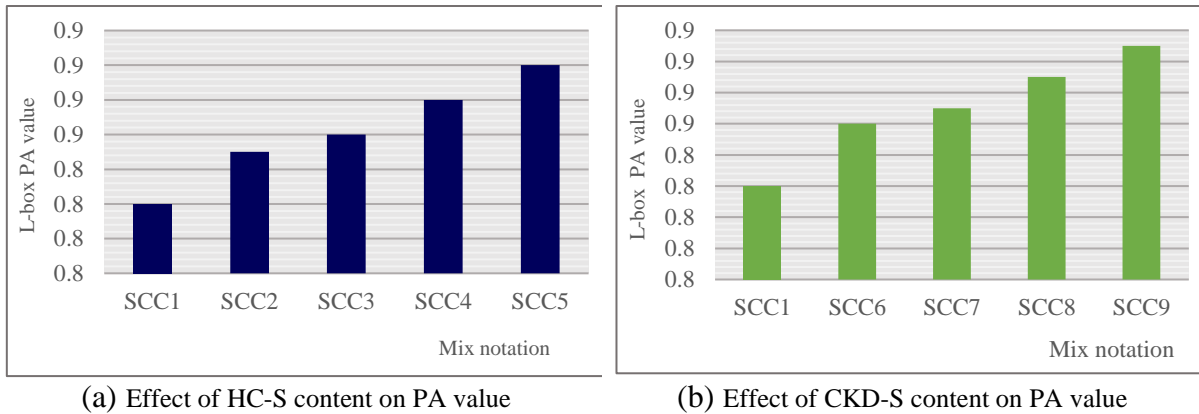


Figure 3: L-box PA values of the SCC mixes

Indeed, the incorporation of increasing rates of hardened cement waste sand and CKD sand in the reference formulation generates a progressive increase in the capacity of the concrete to flow in a confined space. However, compositions based on CKD-S are still the best. This can be attributed to the rounded shape and smooth surface of the grains of CKD sand or hardened cement as well as the presence of several grain sizes and the use of a superplasticiser, which improves the total arrangement of the components in the matrix; the flow of self-compacting concrete is improved by reducing friction between the aggregates.

3.1.3 Seive Segregative Test

Segregation can be defined as the separation of the constituents of a heterogeneous material so that their distribution is no longer uniform. The sieve stability results are presented in histograms in Figure 4. It should be noted that the segregation index is between 10.30% and 13.45%, which is synonymous with satisfactory stability, according to EN 12350-11:2010.

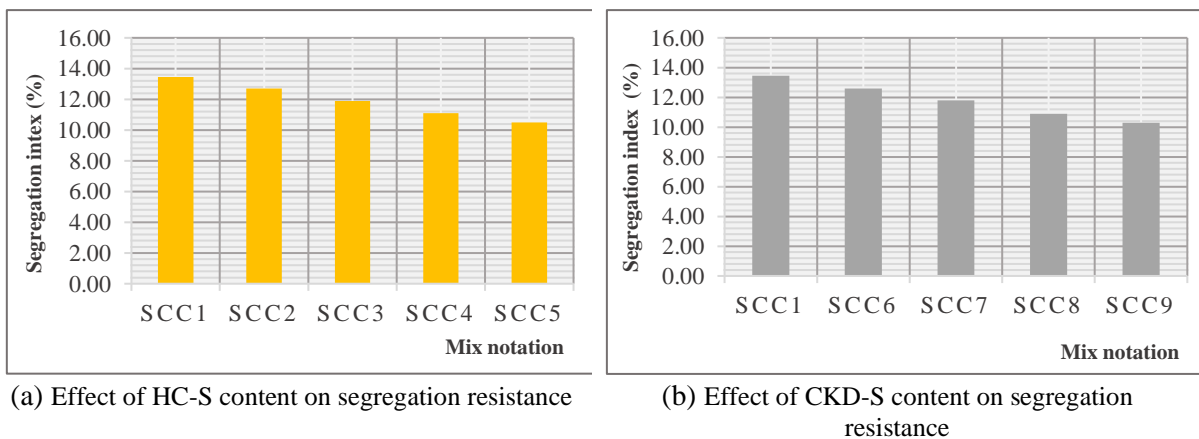


Figure 4: Segregation resistance of self-compacting concrete

The partial incorporation of recycled sand (whether hardened cement or CKD) improves resistance to static segregation and bleeding and there is a proportionality between the increase in the replacement percentage and the improvement of stability. This means that the stability

increases as a result of the increase in the concentration of the solid by volume because the two the types of recycled sand are finer than the quarry sand and well deflocculated by the superplasticiser. The absence of bleeding in concretes based on recycled sands is justified by the presence of alkalis in the composition of CKD and hardened cement is higher than that present in quarry sand because, according to [24], there is less bleeding when the cement contains a high dose of alkali. The reference mixture has the highest amount of laitance (IS=13.45%) compared to the others, which indicates that this composition is of poor homogeneity due to the size of the quarry sand grains, which create more voids between the aggregates. Therefore, at different recycled sand contents, the rheological characteristics are satisfied and below the acceptable performance criteria for SCC.

3.2 Characterization Tests of Self-compacting Concrete in the Hardened State

3.2.1 Compressive Strength

To understand the influence of the fine aggregate replacement ratio on the compressive strength of concrete at 7, 28, and 90 days, the test results are shown in Figure 5. This strength represents the average of the resistances of a series of three cubic specimens of dimensions (15 x 15 x 15) cm³ subjected to crushing according to NF EN 12390-3: 2012.

It can be seen that the compressive strength of all the mixtures is developed at different testing durations. However, the values obtained by the mixtures containing the waste sand are clearly higher than the strength developed by the reference mixture. In fact, the variation in compressive strengths for each series of SCCs is a decreasing function of the replacement percentage of quarry sand by waste sand. As an indication, after seven days, the concrete containing 5% hardened cement waste sand (SSC2) achieves a strength value higher than that of the control concrete by 52%, whereas the composition containing 5% CKD waste (SSC6) illustrates a value superior to the reference value by 57.6%. Moreover, the values displayed by the SCCs containing 20% of HC-S (SSC5) or CKD-S (SSC9) are better than those of the control one by 41.82% and 46.44%, respectively.

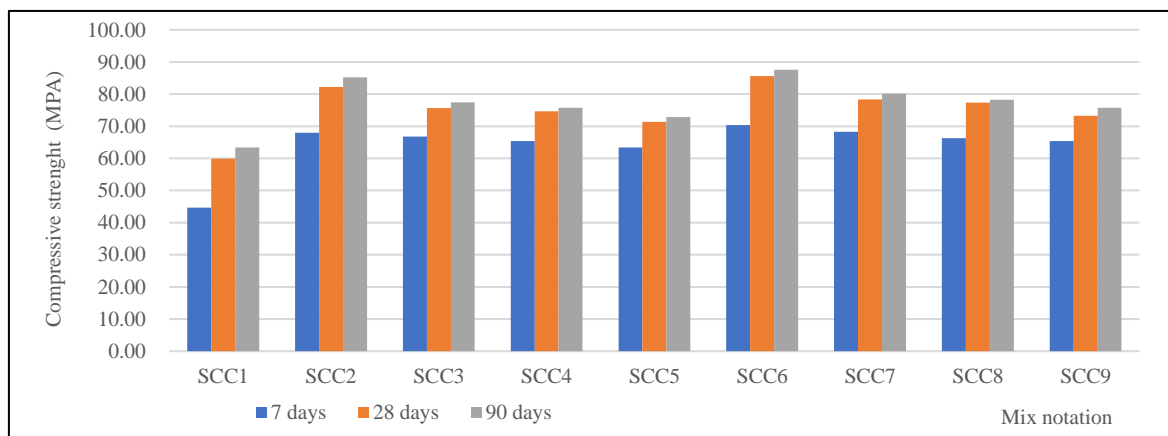


Figure 5: Compressive strength of SCC mixes with different sand content

After 28 days, the trends were almost similar to those on the seventh day. SCCs based on 5% waste sand are the most efficient and the increases in compressive strengths are about: 37.19%

(SSC2) and 42.85% (SSC6) compared to the control mix. Moreover, the concretes incorporating 20% recycled sands exhibit strength which increases by 19.04% (SSC5) and 22.16% (SSC9). In the long term, it should be noted that the improvement in the compressive strengths of the SCCs at 7 and 28 days is reproduced once again. The percentages of variation increase by 34% and 38% of the strength of the reference concrete in the (SSC2), (SSC5), and 14.85 and 19.4% in concretes (SSC6), (SSC9), respectively. The improvement in compressive strength in the case of concretes based on recycled sand is due to the effect of the following parameters:

- * Reduction of the W/C ratio, because the absorption capacity of CKD-S and HC-S is greater than that of quarry sand.

- * The presence of the superplasticiser promotes the hydration of the fine particles of CKD and, as a consequence, the formation of hydrates, which can be qualified as a hydraulic power at a young age [2]. After 90 days, a pozzolanic effect appeared according to the formula (1) [25]:



- * Nucleation sites formed by existing fines in hardened cement sand. The latter contains calcium silicate hydrates (CSH), calcium hydroxide (CH), and hydrated aluminates (CAH), which will accelerate the hydration reaction [26] and densify the microstructure of the long-term cementitious matrix [27].

- * Activation of fine hardened cement particles by the grinding process and by the superplasticifier.

- * The presence of fine particles not yet hydrated (anhydrous phases C_3S , C_2S , C_4AF) in the hardened cement sand contributes to increasing the strength, which results in a long-term pozzolanic effect [28].

- * A filling effect due to the fact that recycled sand is finer than crushed sand, which improves the compactness of the mixtures.

Indeed, the compressive strength of self-compacting concretes prepared with recycled sand depends on the origin of the recycled sand used, the replacement rate, its compatibility with the admixture, and its intrinsic characteristics.

3.2.2 Flexural Strength

The variation in flexural tensile strength of self-compacting concretes at curing times of 7, 28, and 90 days (depending on the type of sand) is shown in Figure 6. The result shown is the average of three measurements, taken from seven prismatic specimens (of dimensions $7 \times 7 \times 28$ cm) for each concrete. The test was performed according to NF EN 12390-6: 2012.

Figure 6 shows that the partial incorporation of hardened cement waste sand or CKD sand into the control concrete leads to an improvement in the flexural strength (after seven days) of the mixtures: SSC2; (SSC3), and SSC6, with a gain of 35.44%, 16.4%, and 10% successively. On the other hand, at 28 days, the mixtures containing up to 15% of waste sand, display an increase in strength in comparison with the control. For example, these improvements have a value of 43.00%, 8.11%, 38.00%, and 1.26% in the four self-compacting concretes SSC2, SSC4; SSC6, and SSC8, respectively.

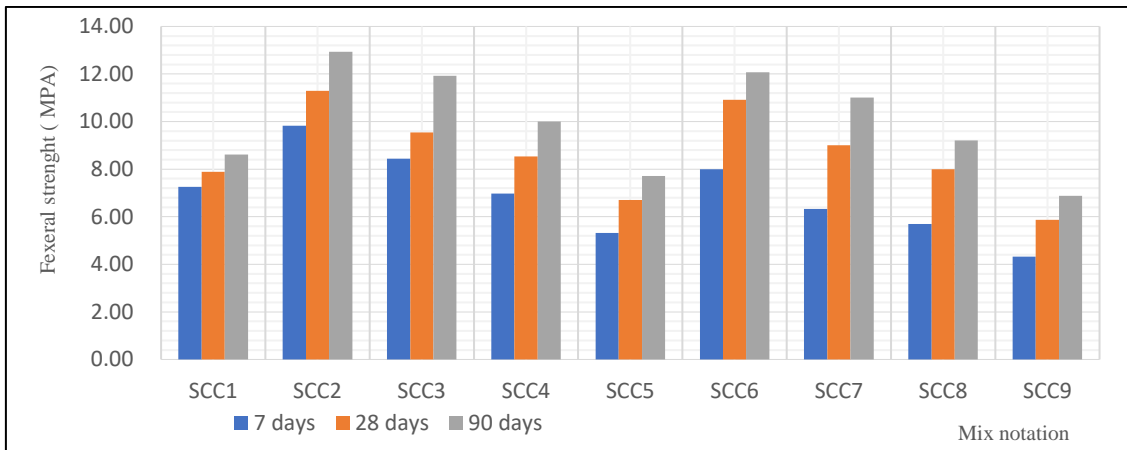


Figure 6: Flexural tensile strength of SCC mixes with different sand content

After 90 days, the best flexural strength is achieved by the self-compacting concrete SCC2, exceeding the reference concrete value by 50%. Furthermore, the SCC5 illustrates a flexural strength gain higher by 40% than the value of the control concrete. In addition, it is clear that the incorporation of up to 15% of recycled sands seems beneficial for the improvement of flexural strength. The cause of this result is that the interfacial transition zone between the grain of hardened cement or CKD-paste is more compact and less porous than that of ordinary sand-paste, due to the existence of more or less reactive fines in the composition of the recycled sand [29].

3.2.3 Split Tensile Strength

The tensile strength is estimated by splitting the $15 \times 15 \times 15$ cm cubic specimens according to NF EN12390-6: 2014. The results obtained are shown in the Figure 7 below.

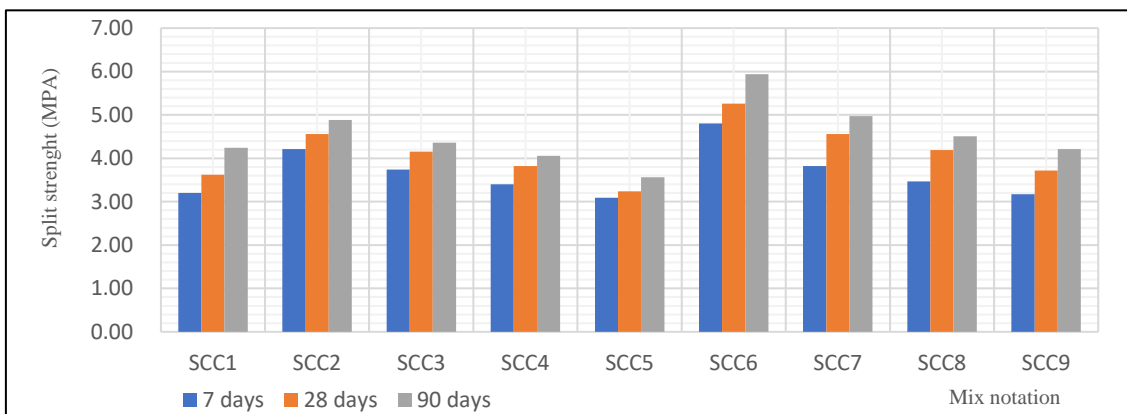


Figure 7: Split tensile strength of SCC mixes with different sand content

By analysing the results illustrated in Figure 7, it can be seen that after seven days, the increase in the amount of CKD sand in the control self-compacting concrete leads to an improvement in the splitting strength of the mixtures incorporating up to 15% waste sand. The rates of increase are around 50.0% (SCC6), 22.5% (SCC7), and 8.4% (SCC8). On the other hand, the incorporation of hardened cement waste sand generates a less significant improvement. The

percentage gains are about 31.56%, 16.87%, and 6.25% for the mixtures SCC1, SCC2, and SCC3, compared to the control concrete.

At 28 days of age, mixtures containing CKD sand remain the most efficient. They illustrate better splitting tensile strengths than those presented by the SCCs, based on hardened cement waste sand and the control mixture. The improvement rates are 25.96% (SCC1); 14.64% (SCC2); 5.52% (SCC3); 45.00% (SCC5); 25.96% (SCC6); 15.74% (SCC7) and 2.76% (SCC9). On the other hand, it should be noted that, after 90 days, the SCCs containing up to 15% CKD sand are still the best, compared to the other mixtures tested. The growth values of these strengths range from 6.3% (SCC7) to 40% (SCC5). However, the two concretes SCC2 and SCC3 display higher strengths than that of the control concrete by 15% and 2.8%, respectively. For some authors, the tensile strength by splitting is conditioned by the adhesion between the aggregates and the cementitious matrix and, generally, the shape of the aggregates is the one that exerts the most influence on the latter. To this end, the weakness of the splitting strengths of SCCs based on cement waste sand, compared to those of SCCs incorporating CKD sand, results from the fact that the grains of the cement waste sand have a smoother surface than those of CKD sand.

4 Conclusion

This research investigates the use of cement kiln dust and hardened cement waste in the production of self-compacting concrete. The properties of fresh and hardened concrete, with different CKD contents, were compared and the following conclusions were obtained:

- All of the concrete met the recommendations of the AFGC.
- Increasing the dosage of recycled sand by up to 20% (substituting quarry sand) positively influences the rheological properties of SCC.
- The introduction of up to 20% hardened cement waste sand or CKD in the control mixture leads to an improvement in the compressive strength at all ages. Nevertheless, the values illustrated by the mixtures based on CKD sand are better than those achieved by the self-compacting concrete containing cement waste sand. 5% CKD-S concrete performed best in both series.
- The flexural tensile strength of self-compacting concretes based on hardened cement waste sand is always better than that of the control and those of concretes based on CKD sand. However, SCCs containing up to 15% recycled sands show acceptable strength.
- The incorporation of CKD sand (up to a rate of 15%) considerably improves the splitting tensile strength of self-compacting concretes. In addition, the rate of 10% hardened cement sand is the optimum for SCCs based on this waste.

Given the results obtained, it can be argued that the use of sands from cement waste in the manufacture of self-compacting concretes can constitute an important economic and technical alternative in certain applications.

References

- [1] Aldikheeli, M., Salih, S., & Al-Zwainy, F. (2018). Physical and mechanical characteristics of sustainable self-consolidating concrete incorporating high volume fly ash and cement kiln dust. *In MATEC Web of Conferences*. 162, 20-25). <https://doi.org/10.1051/mateconf/201816202025>
- [2] Brouwers, H.J.H., Radix, H.J. (2007). Self-compacting concrete: Theoretical and experimental study. *Cem. Concr. Res.* 29, 1–12. doi:10.1016/j.cemconres.2005.06.002.
- [3] Bonen, D., Shah, S.P. (2005). Fresh and hardened properties of self-consolidating concrete, *Prog. Struct. Eng. Mater.* 7 14–26. doi:10.1002/pse.186
- [4] Benabed, B., Kadri, E.H., Azzouz, L., Kenai, S. (2012). Properties of self-compacting mortar made with various types of sand. *Cem. Concr. Compos.* 34, 1167–1173. doi:10.1016/j.cemconcomp.2012.07.007
- [5] De Larrard, F., Belloc, A. (1999). The influence of aggregate on the compressive strength of concretes, *Bull Liaison Des Lab. Des Ponts Chaussées*. 219, 41–52.
- [6] Ramezani pour, A.A., Esmaeili, M., Ghahari, S.A., Najafi, M.H. (2013). Laboratory study on the effect of polypropylene fiber on durability, and physical and mechanical characteristic of concrete for application in sleepers. *Constr. Build. Mater.* 44, 411–418. doi:10.1016/j.conbuildmat.2013.02.076.
- [7] Monteiro, P.J.M., Mehta, P.K., Skalny, C.J.P. (1986). Interaction between carbonate rock and cement paste. *Cem. Concr. Compos.* 16, 127–134. [https://doi.org/10.1016/0008-8846\(86\)90128-6](https://doi.org/10.1016/0008-8846(86)90128-6)
- [8] Lecomte, A., De Larrard, F., Mechling, J.M. (2001). Compressive strength of hydraulic concretes to the unoptimised granular skeleton. Bulletin LPC n° 234, 89-105.
- [9] Rmili, A., Ben Ouedzou, M. (2012). Valorization of the crushed sand and of the desert sand in the composition of the self compacting concrete. *MATEC Web of Conferences*. 2, 1- 9. published by EDP Sciences.
- [10] Elbaz, A. A., Aboufotouh, A. M., Dohdoh, A. M., & Wahba, A. M. (2019). Review of beneficial uses of cement kiln dust (CKD), fly ash (FA) and their mixture. *J. Mater. Environ. Sci.* 10(11), 1062-1073.
- [11] Sreekrishnavilasam, A., Rahardja, S., Kmetz, R., Santagata, M. (2007). Soil treatment using fresh and landfilled cement kiln dust. *Constr. Build. Mater.* 21, 318–327. <https://doi.org/10.1016/j.conbuildmat.2005.08.015>
- [12] Lubna, A. Kh., Salem Al-Mansour. (2012). Stabilization of Dune Sand by Using Cement Kiln Dust (CKD) University College Article.
- [13] Siddique, R. (2006). Utilization of cement kiln dust (CKD) in cement mortar and concrete—an overview. *Resources, Conservation and Recycling*. 48, 315–338. <https://doi.org/10.1016/j.resconrec.2006.03.010>
- [14] Maslehuddin, M., Al-Amoudi, O.S.B., Rahman, M.K., Ali, M.R., Barry, M.S. (2009). Properties of cement kiln dust concrete. *Constr. Build. Mater.* 23, 2357–2361. <https://doi.org/10.1016/j.conbuildmat.2008.11.002>
- [15] Sadek, D. M., El-Attar, M. M., & Ali, A. M. (2017). Physico-mechanical and durability characteristics of concrete paving blocks incorporating cement kiln dust. *Construction and Building Materials*. 157, 300-312. <https://doi.org/10.1016/j.conbuildmat.2017.09.107>

- [16] Yaseri, S., Verki, V.M.& Mahdikhani, M. (2019). Utilization of high volume cement kiln dust and rice husk ash in the production of sustainable geopolymer. *J. Clean. Prod.* 230, 592-602. <https://doi.org/10.1016/j.jclepro.2019.05.056>.
- [17] Alnahhal, W., Taha, R., Al-Nasseri, H., & Nishad, S. (2018). Effect of using Cement Kiln Dust as a nano-material on the strength of cement mortars. *KSCE Journal of Civil Engineering.* 22(4), 1361-1368.
- [18] Saleh, H. M., Salman, A. A., Faheim, A. A., & El-Sayed, A. M. (2020). Sustainable composite of improved lightweight concrete from cement kiln dust with grated poly (styrene). *Journal of Cleaner Production.* 277, 123491. <https://doi.org/10.1016/j.jclepro.2020.123491>
- [19] Agwa, I. S., & Ibrahim, O. M. O. (2019). Fresh and hardened properties of self-compacting concrete containing cement kiln dust. *Challenge Journal of Concrete Research Letters*, 5(1), 13-19. <https://doi.org/10.20528/cjcr.2019.01.003>
- [20] Najim, K. B., Al-Jumaily, I., & Atea, A. M. (2016). Characterization of sustainable high performance/self-compacting concrete produced using CKD as a cement replacement material. *Construction and Building Materials.* 103, 123-129. <https://doi.org/10.1016/j.conbuildmat.2015.11.037>
- [21] Okamura, H., & Ouchi, M. (2003). Self-compacting concrete. *Journal of advanced concrete technology*,1(1), 5-15. <https://doi.org/10.3151/jact.1.5>
- [22] AFGC, 08 : Recommendations pour l'emploi des bétons autoplacants, 2008.
- [23] Flatt, R. J., & Houst, Y. F. (2001). A simplified view on chemical effects perturbing the action of superplasticizers. *Cement and concrete research.* 31(8), 1169-1176. [https://doi.org/10.1016/S0008-8846\(01\)00534-8](https://doi.org/10.1016/S0008-8846(01)00534-8)
- [24] A. Ville, « Propriétés des bétons ». Sherbrooke, Canada, éd. Paris, Eyrolles, 2000.
- [25] R.Bucher, T.Vidal, A. Sellier, and J. Verdier. (2017). Effect of drying on the mechanical properties of cementitious materials, 23rd French Congress of Mechanics, S27- Coupling Sustainability - Mechanical Behavior in Civil Engineering Structures, August 28 - September 1, Lille, France. <http://hdl.handle.net/2042/63477>
- [26] A.M. Soliman, M. L. Nehdi. (2011). Self-Accelerated Reactive Powder Concrete Using Partially Hydrated Cementitious Materials. *ACI Mater Journal.* 108, 596–604.
- [27] Y.Wang, W. Wang, X. Guan. (2011). Physical Filling Effects of Limestone Powders with Different Particle Size. *Advanced Materials Research Journal.* 163-167, 1419–1424. <https://doi.org/10.4028/www.scientific.net/AMR.163-167.1419>
- [28] J. M. Khatib. (2005). Properties of concrete incorporating fine recycled aggregate. *Cem. Concr. Res.* 35(4), 763–769. <https://doi.org/10.1016/j.cemconres.2004.06.017>
- [29] G. Konig, K. Holschemcher, F. Dehn, & D. Weiße. (2001). Self-compacting concrete time development of material properties and bond behaviour. Proceeding of 2nd International RILEM Symposium on Self-Compacting Concrete (Pro 33), Tokio, Japan :507–516.

Experimental Measurements of Drag and Lift Coefficient on Building with an Elliptical Cross-section

Michal Franek^{1*}, Marek Macák², Oľga Hubová³

Slovak University of Technology in Bratislava, Slovakia

¹Faculty of Civil Engineering, Department of Building Structures

² Faculty of Civil Engineering, Department of Mathematics and Descriptive Geometry

³Faculty of Civil Engineering, Department of Structural Mechanics

*e-mail: michal.franek@stuba.sk

Abstract

The characteristics of aerodynamic forces acting on an elliptical cylinder with an aspect ratio of 0.5 with a wind attack angle from 0 to 90° and subjected to the boundary layer wind tunnel were investigated. The model was initially calibrated and compared with the existing work. The aspect ratio of the investigated model was 0.5, and the model was emerging in a turbulent flow. The mean and fluctuating drag and lift coefficients were investigated. The minimum drag coefficient occurred in the wind direction of 0° and the maximum at 90°. The lift coefficient was the largest in the 30° wind direction and the smallest at 0°. Fluctuating coefficients were similar profiles as the mean coefficients. Around the 30° wind direction, an inappropriate phenomenon occurred, caused by the generation of asymmetrical vortices structures and wake instabilities.

Keywords: boundary layer wind tunnel, force sensor, drag coefficient, lift coefficient, elliptical cylinder

1 Introduction

Wind load on unconventional buildings has become more unpredictable. Our article is focused on the bluff body, especially the building with an elliptical cross-section. In engineering practice in Slovakia, no specific procedure for evaluating wind pressure or overall wind loads is mentioned in the code [1]. Therefore, it is necessary to analyze each case individually. Our goal was to treat isolated elliptical buildings in the overall wind loads, which are crucial for designing the support system and foundations.

The first studies of the two-dimensional stationary model with an elliptical cross-section were published by Modi and Wiland [2]. The elliptical cylinder had an eccentricity of 0.8 and 0.6. With a detailed analysis, they experimentally verified the pressure distribution during the organized wake condition. Other work [3] analyzed the wakes behind the elliptical cylinder, which developed shear layer instabilities and unequal wake instabilities. Other researchers [4,5] investigated the wake and streamline pattern for low Reynolds numbers. Zhao and He [6]

investigated the effect of the aspect ratio of elliptical buildings on the pressure distribution. The aspect relationship is the ratio between the major and minor axes, but also the height of the model. Shi, Alam, and Bai analyzed three flow regimes in the unsteady laminar flow, and they found three patterns of wakes [7].

The wind load on the elliptical cylinder is very sensitive to the value of the Reynolds number, which is the ratio of inertial forces to viscous forces within a fluid that is subjected to relative internal movement due to different fluid velocities. The articles only examined the wind loading and flow regime for steady or unstable laminar flow. The buildings in engineering practice are subjected to a turbulent flow. For that purpose, it is necessary to evaluate buildings in Atmospheric Boundary Layer (ABL), which is fully turbulent. Our goal was to measure drag and lift forces in Boundary Layer Wind Tunnel (BLWT).

2 Description of the Boundary Layer Wind Tunnel and Instrumentation Equipment

The experimental investigations were carried out in BLWT Bratislava, where the atmospheric circulation can be reproduced. This is necessary to correctly reproduce the roughness of the Earth's surface that covers different terrain categories according to [1]. Particular devices such as grids, membrane elements, and walls or Counihan vortex generators can be inserted along wind tunnels [8]. These devices simulate the properties of the atmospheric boundary layer as the mean wind velocity and the turbulence intensity. BLWT in Bratislava was designed with an open circuit scheme and two test sections. It is a 26.2 m long low-speed wind tunnel with a working cross-section of 2.6×1.6 m. Tunnel wind velocity was monitored by a static two-pitot tube mounted on the wall behind the inlet part and in front of the measuring area. The 2.4 m diameter turntable helps to investigate many directions of incoming wind. The approaching flow corresponded to the wind flow through the urban terrain with aerodynamic roughness length $z_0 = 0.7$ m on a full scale. The fully turbulent flow was generated using the barrier as a plane wall and a long fetch of roughness elements, simulated by the dimpled membrane. The height of the membrane elements was 20 mm. The mean wind velocity and turbulence intensity profiles are shown in Figure 1. According to the boundary layer characterization, the mean wind velocity at the model roof height was 8.6 m/s, and the turbulence intensity was 18.3 %. The scaling factor of ABL was calculated deterministically from the integral length scale [9], which was 1/390. The velocity scale was 1/5, which means that the target Mean wind velocity was 30.53 m/s at the roof height in full scale. The Reynolds number was set, considering its critical value [10]. The Reynolds number of an experiment ranged from 4.4×10^4 to 8.9×10^4 , depending on the direction of the wind, thus a characteristic dimension of the model.

The models were fixed to the 6-axis force and torque sensor Nordbo Robotics NRS-6050-D50 [11]. The force sensor was strongly screwed into the model with 6 screws, so the movement of the model could be transferred to the sensor. Figure 2 illustrates the position of the force sensor in the wind tunnel. Various bearing systems of the force sensor were used to turn the table to ensure accurate results. The results achieved were compared with measurements made by other authors. The partial goal was to calibrate and find the bearing system method that could partially

dampen the vibration from the wind tunnel and the vortex-induced vibration from the measured model.

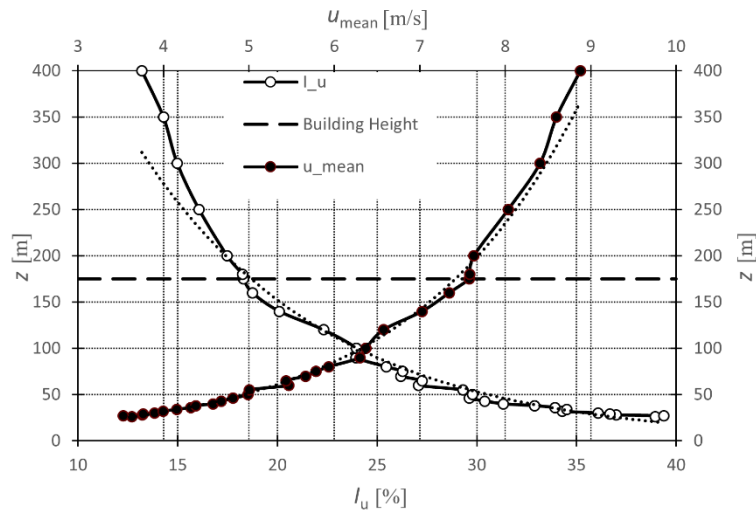


Figure 1: Mean wind velocity (u_{mean}) and turbulence intensity (I_u) profile

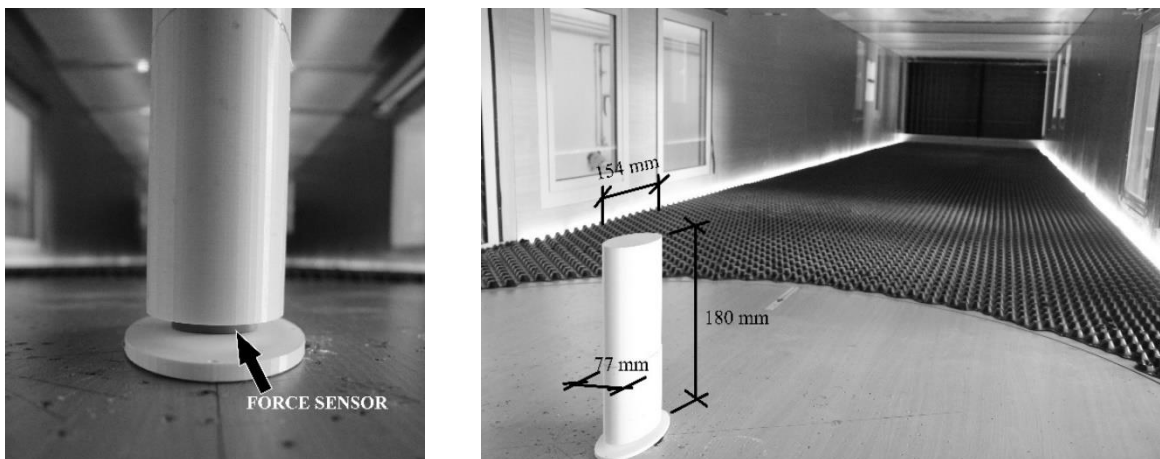


Figure 2: Position of the force sensor and arrangement in the wind tunnel

3 Experimental Model

The experimental model was made from PLA using the 3D printing technique. The dimensions of the cylinder were $77 \times 154 \times 180$ mm (width \times length \times height). The model proportions take into account the existing buildings in our location. Based on the proportions, the aspect ratio was 0.5 (1/2). The scaling factor of the model had to be chosen equal to the ABL scaling, which was 1/390. The model was rotated from 0 to 90° to the wind with rotation increments of 10°.

Three configurations were used to obtain correct results and calibrate with other measurements [12]. The first was the PLA bearing plate, the second was the steel plate, and the third was the

steel plate with a damper in the model. As a damper, the sand filling integrated into the model was chosen.

4 Aerodynamics Coefficients

The main goal was to determine the aerodynamic coefficients on the 180 mm high tower with an elliptical cross-section with an aspect ratio of 0.5. The arrangement and wind direction scheme is illustrated in Figure 3. The model was rotated by 10° steps. The drag coefficient c_d was given as:

$$c_d = \frac{2 \cdot F_d}{\rho_{air} \cdot v_{ref}^2 \cdot A_{ref}} \quad (1)$$

where c_d is the drag coefficient in [-], F_d is the mean drag force in the wind direction in [N], ρ_{air} is the air density in [kg/m³] at the temperature of 18 °C, v_{ref} is the reference wind velocity in the aerodynamic center at 2/3 of the height of the model and A_{ref} is the projected reference area perpendicular to the wind direction in [m²].

The lift coefficient c_l was also measured and given as:

$$c_l = \frac{2 \cdot F_l}{\rho_{air} \cdot v_{ref}^2 \cdot A_{ref}} \quad (2)$$

where c_l is the lift coefficient in [-], F_l is the mean lift force perpendicular to the wind direction in [N], ρ_{air} is the air density in [kg/m³], v_{ref} is the reference wind velocity in the aerodynamic center at 2/3 of the height of the model and A_{ref} is the projected reference area perpendicular to the wind direction in [m²].

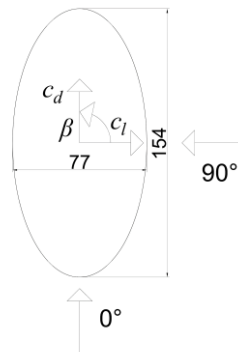


Figure 3: The footprint of the tested tower and the directions of the drag (c_d) and lift (c_l) coefficient

4.1 Calibration for Alternative Bearing System

The first step was to compare existing works with our results to ensure the relevant results and analysis. Our measurements had 3 configurations, as was mentioned in the previous chapter. For the comparison, the publication by Takeuchi et al. [12] was chosen. Their research evaluated the cylinder with an elliptical cross-section with the same aspect ratio. The difference was between the approaching flow. In their research, steady approaching flow with the short-rise-time gusts in the rear section was used. The comparison in Figure 4 showed adequate similarity with the steel plate configuration with sand filling. The results were statistically verified. The

correlation coefficient for the third configuration was 0.991. A minor variation was caused by the approaching flow and roughness of the model, which is common knowledge. Based on the comparison, it could be claimed that the steel bearing plate with the sand filling was adequate for further analysis of the drag and lift coefficient of the elliptical cylinder.

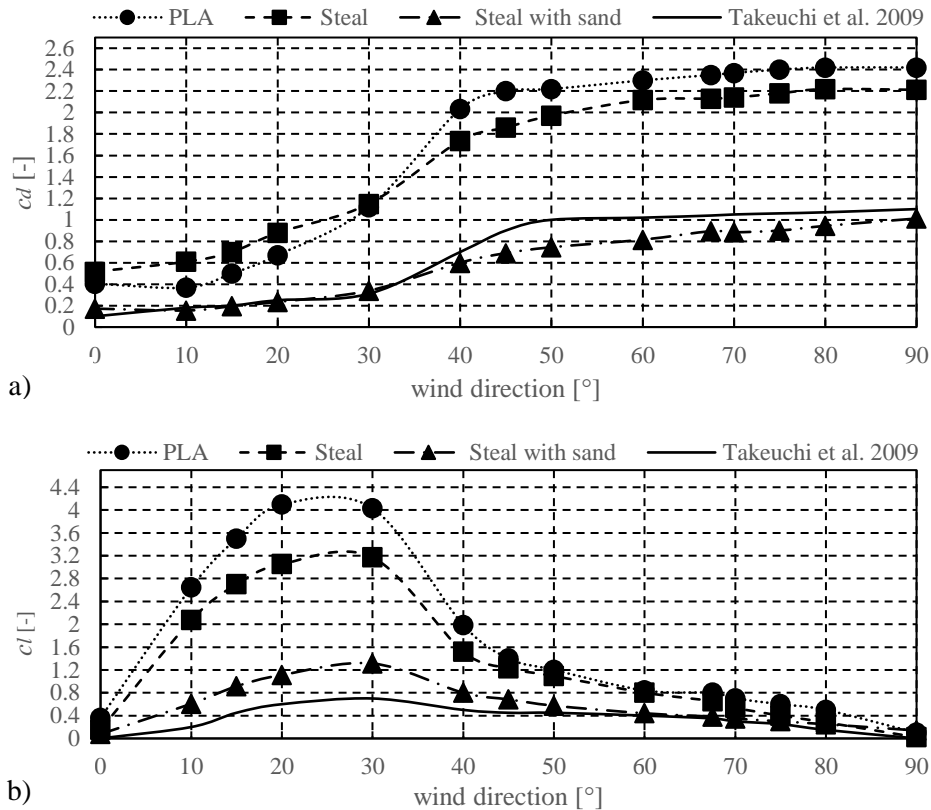


Figure 4: Comparison of variation of mean force coefficients with Takeuchi et al. [12]: a) drag coefficient, b) lift coefficient

5 Results and Discussion

5.1 Mean and Fluctuating Drag and Lift Coefficient

The drag and lift coefficients were measured in the time domain, where the sampling frequency was set to 100 Hz. Each measurement was set to 10 seconds in duration. Coefficients were treated by the mean and fluctuating values. The mean value of the coefficient was obtained as a time-averaging value. The fluctuating value of the coefficient was obtained as a root mean square value. The results were processed into graphs depending on the incident wind, illustrated in Figures 5 and 6.

The mean value of the drag coefficient varied fundamentally according to the direction of the wind. From the perspective of the minimum value of the drag force, the ideal wind direction

was 0 to 15°. It was expected because the area exposed to the wind was the smallest in these directions. The maximum value of the drag force was expected for the direction of the wind at 90°, where the exposed area was the largest. An interesting phenomenon occurred when the wind direction was between 30 and 45°. The most significant increase in the drag coefficient c_d occurred from the value of 0.34 to the value of 0.68. A similar phenomenon occurred for fluctuating values. It could have been caused by flow separation, asymmetrical vortices structures on the sides of the elliptical building, and wake instabilities. Maximum fluctuations occurred for wind direction of 90°. It was caused by the maximum drag force occurring in this direction, generated by the vibrations of the model.

The mean value of the lift coefficient had a different profile than the drag. The minimum value occurred for wind directions 0 and 90°, where the value approached zero. It could have been caused by the stable flow structure without asymmetrical vortices. The maximum lift coefficient occurred around the wind direction of 20 and 30°. Here, we can state that the phenomenon of the generation of asymmetrical vortices structures and wake instabilities caused it. A similar profile of the lift coefficient was observed for the fluctuating value. The maximum force made the vibration go in the same direction.

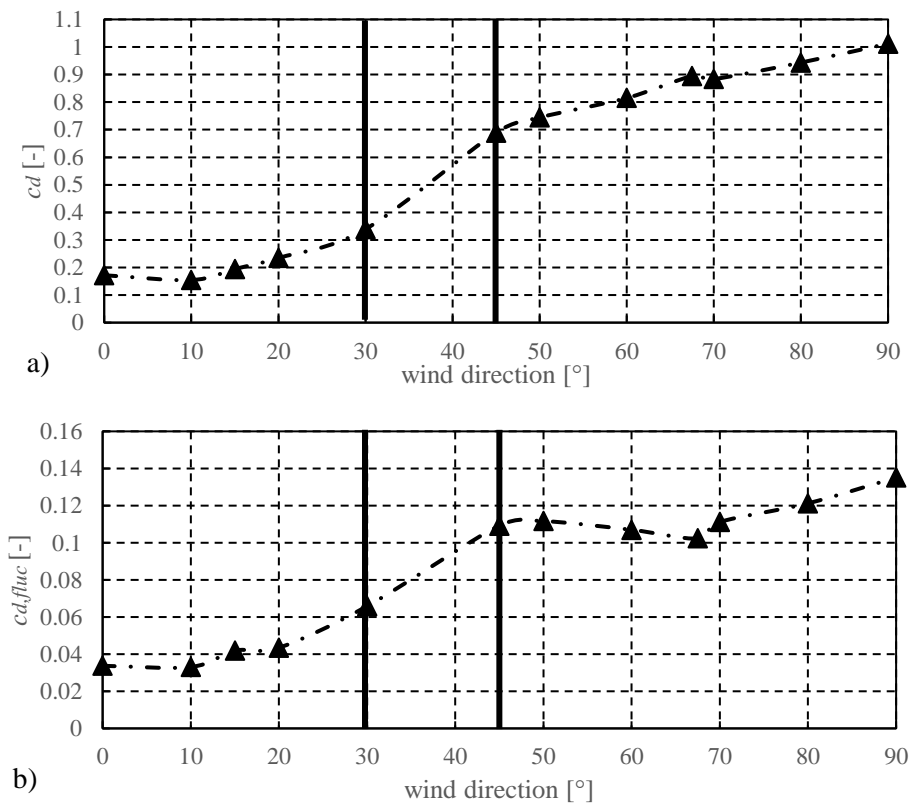


Figure 5: Variation of drag coefficients: a) mean, b) fluctuating

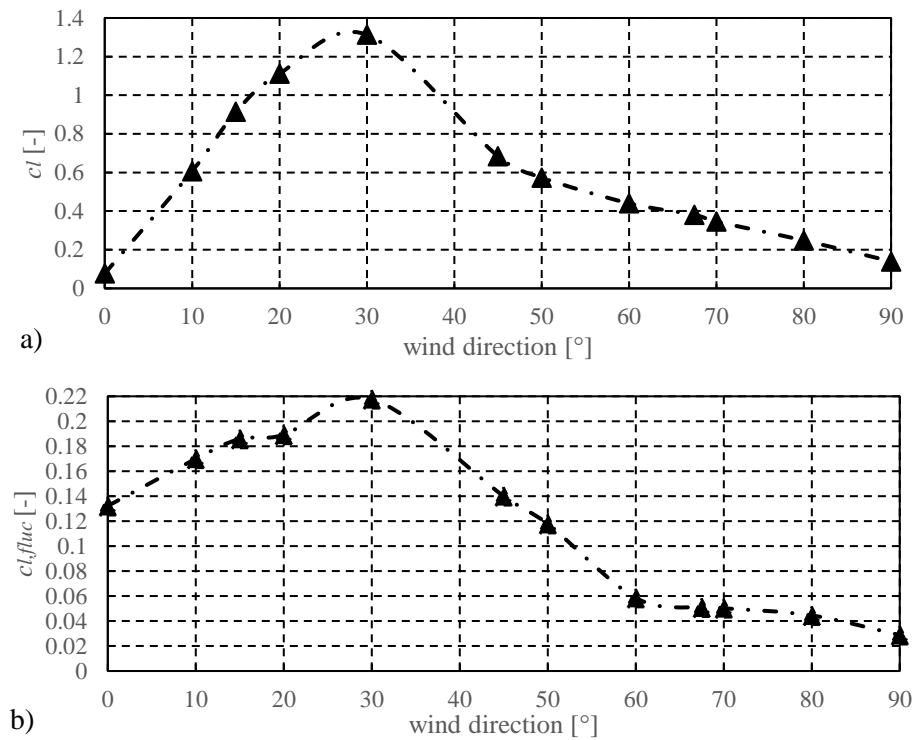


Figure 6: Variation of lift coefficients: a) mean, b) fluctuating

6 Conclusions

This article aimed to find the appropriate method to evaluate and measure the drag and lift coefficient with the force sensor. The main goal was to analyze the free-standing building with the elliptical cross-section for various wind directions. Subsequently, find out the maximum/minimum or optimal/critical value of the drag and lift force.

From the results, the conclusions are as follows:

- the optimal bearing system for the force sensor resulting from the verification with other work [12] was the steal bearing with the sand filling in the model,
- the value of drag and lift coefficient varied fundamentally according to the wind direction,
- the maximum drag occurred in the wind direction of 90° ,
- minimum drag occurred in the wind direction of 10° ,
- maximum lift occurred in the wind direction at 30° ,
- minimum lift occurred in the wind direction 0° ,
- fluctuating coefficients had similar profiles and copied the maximum and minimum wind-induced forces,
- taking into account the overall forces, the optimal wind direction was 0° ,
- the inappropriate wind directions were around 30° ,
- the inappropriate phenomenon was caused by the generation of asymmetrical vortices structures and wake instabilities.

For a better understanding of this phenomenon, future research will suggest additional measuring methods with the help of Computational Fluid Dynamics. To get an overall view of the wind-induced force on the elliptical cylinder.

Acknowledgments

This work was supported by the Scientific Grant Agency MŠVVŠ SR and SAV under VEGA 1/0113/19.

References

- [1] STN EN 1991-1-4. (2007). Eurocode 1: Actions on structures. Part 1-4: General actions. Wind actions. STN EN 1991-1-4. Slovak Office of Standards, Metrology and Testing. Slovak Republic.
- [2] Modi, V. & Wiland, E. (1969). *Unsteady aerodynamics of stationary elliptic cylinders in subcritical flow*. CASI/AIAA Subsonic Aero-and Hydro-Dynamics Meeting, the 30th of August 2022, <https://arc.aiaa.org/doi/10.2514/6.1969-745>. DOI: <https://arc.aiaa.org/doi/10.2514/6.1969-745>.
- [3] Sheard, G.J. (2007). Elliptic cylinders: wake stability cylinders with elliptic cross-section: wake stability with variation in angle of incidence.
- [4] Thompson, M.C., Hourigan, K., Ryan, K. and Sheard, G.J. (2006). Wake transition of two dimensional cylinders and axisymmetric bluff bodies. *Journal of Fluids and Structures*. 22 (6), 793-806. <https://doi.org/10.1016/j.jfluidstructs.2006.05.001>.
- [5] Thompson, M.C., Radi, A., Rao, A., Sheridan, J. and Hourigan, K. (2014). Low Reynolds number wakes of elliptical cylinders: from the circular cylinder to the normal flat plate. *Journal of Fluid Mechanics*. 751, 570-600. <https://doi.org/10.1017/jfm.2014.314>.
- [6] Zhao, D. & He, B. (2017). Effects of architectural shapes on surface wind pressure distribution: case studies of oval shaped tall buildings, *Journal of Building Engineering*. 12, 219-228. <https://doi.org/10.1016/j.jobe.2017.06.009>.
- [7] Shi, X., Alam, M., & Bai, H. (2020). Wakes of elliptical cylinders at low Reynolds number, *International Journal of Heat and Fluid Flow*. 82, 108553. <https://doi.org/10.1016/j.ijheatfluidflow.2020.108553>.
- [8] ASCE Manual of Practice, no.67. (1998) *Wind tunnel studies of buildings and structures*. USA: American Society of Civil Engineers.
- [9] Cook, N.J. (1978), Determination of the model scale factor in wind tunnel simulations of the adiabatic atmospheric boundary layer. *Journal of Wind Engineering and Industrial Aerodynamics*. 2 (4), 311-321. [https://doi.org/10.1016/0167-6105\(78\)90016-8](https://doi.org/10.1016/0167-6105(78)90016-8).
- [10] Achenbach, E. (1971). Influence of surface roughness on the cross flow around a circular cylinder. *Journal of Fluid Mechanics*. 46 (2), 321-335. <https://doi.org/10.1017/S0022112071000569>.
- [11] Nordbo Robotics. (2020). *Datasheet*. the 30th of August 2022, https://uploads-ssl.webflow.com/625fc7fe419e8aaa239f119c/627a66e6f4477a3e96c1bf8c_NRS-6050-D50.pdf.
- [12] Takeuchi, T., Maeda, J., Hayata, T. & Kawashita, H. (2009). Effects of section size on aerodynamic forces on an elliptical cylinder under short-rise-time gusts. In The Seventh Asia-Pacific Conference on Wind Engineering, November 8-12, 2009 (1-8). Taipei, Taiwan.

Effectiveness Assessment of Superplasticizer Admixtures: Case of Self-compacting Concrete Reinforced with Fine Mineral Fillers

Mehena Oualit^{1*}, Amar Irekti², Brahim Hami¹

¹Unit of Research: Materials, Processes and Environment (UR-MPE); Faculty of Technology, Frantz Fanon city, 35000 Boumerdes university, Algeria

²Chemistry Department, Faculty of Sciences, M'Hamed Bougara university, Boumerdes, 35000, Algeria

*e-mail: m.oualit@univ-boumerdes.dz

Abstract

The use of superplasticizers in concrete production has become a common practice, especially when a high fluidity is required. On the other hand, the risk of segregation and the stability of these mixtures is ensured by the incorporation of a large volume of fine mineral additions. The present investigation is devoted to the study of the influence of three types of superplasticizers of different chemical compositions, namely: Combined Synthetic Polymers (CSP), Poly-Carboxylate Ether (PCE), and Modified Poly-Carboxylate Ether (MPCE) on the rheological behavior of self-compacting concrete (SCC) as well as on the mechanical properties at 3, 7, and 28 days of curing. Natural pozzolana (NP) and ground granulated blast furnace slag (GGBFS) were used as additions to stabilize the mixtures. The results revealed that the ether-based superplasticizer PCE gave the best workability and mechanical performance with low amounts (high efficiency). In addition, blast furnace slag promotes the obtaining of better properties whether in the fresh or hardened state compared to natural pozzolana.

Keywords: self-compacting concrete, superplasticizers, strength, workability, mineral fillers

1 Introduction

Many current structures are characterized by the complexity of their architecture (variable shapes and multiple curvatures), as well as by a high density of reinforcement, which often makes it difficult to use conventional plasticity concrete. In order to adapt the concretes to these structures, research has been carried out in recent years to develop concrete formulations characterized by high workability, while being stable (segregation, spreading and entrained air), with good mechanical properties and durability.

Self-compacting concrete (SCC) represents a new generation of concrete with invaluable properties. Thanks to its high fluidity, the implementation is affected without external vibration. This concrete allows the perfect filling of the formwork without any segregation of its components [1, 2]. In the fresh state, the main characteristics of this material are high flowability, passage capacity, and resistance to segregation [3, 4].

Several additions can be incorporated into the production of self-compacting concrete such as metakaolin (MK) [5, 6], fly ash (FA) [7, 8, 6], and ground granulated blast furnace slag

(GGBFS) [7]. These by-products play a significant role in the development of SCC properties whether in a fresh or hardened state [5, 6]. Thanks to their high specific surface area (higher compared to Portland cement) due to thorough grinding, some of these additions have a pozzolanic effect during cement hydration reactions. Indeed, in the presence of moisture, they can fix the portlandite (CH) to form new calcium hydrosilicates (CSH) thus contributing to the improvement of the mechanical properties of concrete [9, 10].

Natural pozzolana is among the mineral additions used as a cementitious additive to replace Portland cement. The use of natural pozzolana as an addition is motivated by its availability (low cost) as well as its advantageous properties such as reduced heat release, decreased permeability, and high chemical resistance, e.g., to acids [11, 12].

Ground granulated blast furnace slag (GGBFS) is a co-product of the metallurgical industry. This by-product is also used as an additive in concrete due to these multiple technical advantages [13, 14]. The incorporation of GGBFS into self-compacting concrete greatly enhances its compactness and consistency. Moreover, it also contributes to the protection of concrete against sulfate attack and the penetration of chloride ions [15]. Indeed, thanks to the lower density of the GGBFS compared to cement, the equivalent mass substitution gives rise to a larger volume of paste, which will consequently promote resistance to segregation and improve the workability of the concrete mixture. The study carried out by Oner and Akyuz [16] showed that the incorporation of ground granulated blast furnace slag in self-compacting concrete significantly improves the rheological behavior of the mixture. The same authors have shown that its incorporation with an optimal content reduces the water/binder ratio, which increases the compressive strength of the hardened SCC.

The high fluidity of self-compacting concrete mixtures is obtained using superplasticizer admixtures. Despite their incorporation with low contents, the latter have a significant influence on the fresh and hardened properties of SCCs [17, 18]. Depending on their chemical structure, there are several types of superplasticizers; among them the polycarboxylate (PC) based superplasticizer. Three (3) important parts make up its structure: a polyethylene backbone, grafted polyoxyethylene (POE) chains, and carboxylic groups as adsorbents. In the presence of this type of superplasticizer (PC), the dispersion is ensured essentially by the steric hindrance (thanks to the long-grafted side chains) instead of the negatively ionized groups (COO^-) which usually adsorb on the outer surface of cement grains [19].

The chemical structure, anionic monomer type, molecular mass, length of the main chain, and side chains, the ratio of anionic / non-ionic groups, and density of superplasticizers have a significant influence on the properties of cementitious materials. In recent years, the objective of several researchers has been to increase the effectiveness of chemical admixtures by modifying these parameters [20, 21, 22].

Evangelina K and Neelamegam [23] examined the influence of 3 types of superplasticizers, namely Sulfonated Naphthalene Formaldehyde (SNF), Poly-Carboxylate Ether (PCE), and Modified Poly-Carboxylate Ether (MPCE) on mechanical performance and workability of self-compacting concrete. The results showed that the workability retention of concrete with PCE allows a longer fluidity of the concrete. In addition, concrete containing MPCE gives better and longer flowability. Therefore, MPCE was found to be a better superplasticizer than the three other selected superplasticizers considered in the study, considering the characteristic behavior of fresh and hardened concrete.

Zhang et al., [24] developed a mathematical model for predicting the optimal mixture of self-compacting concrete depending on the properties of the cement additives (powders) and the

type of admixture (superplasticizer) used. The effectiveness of superplasticizers has also been tested in alkali-activated materials (geopolymers) [25].

This paper reports a comparative investigation of the effect of natural pozzolana (NP) and ground granulated blast furnace slag (GGBFS) on the fresh and hardened properties of self-compacting concrete (SCC) using three types of superplasticizers; the effectiveness of each admixture is assessed.

2 Materials and Methods

2.1 Raw Materials

2.1.1 Cement

The cement used in the present investigation is CEM II 42.5R containing 20% limestone fillers. The density and fineness of this binder are equal to 3.08 g/cm^3 and $3394 \text{ cm}^2/\text{g}$ respectively. The chemical composition of the cement was carried out through X-ray fluorescence analysis while the mineral contents were calculated using Bogue's formulas. The results are displayed in Table 1.

Table 1: Chemical and mineralogical compositions of the CEM II 42.5R

Oxide (%)	SiO ₂	Al ₂ O ₃	Fe ₂ O ₃	CaO	MgO	K ₂ O	Na ₂ O	SO ₃	CaO _f	L.O.I
	15.71	4.15	2.52	60.71	2.38	0.59	0.18	1.79	1.42	1.63
Mineral (%)	C ₂ S	C ₃ S		C ₃ A						
	21	55		7						

2.1.2 Aggregates

Crushed coarse aggregates (3/8 and 8/15 mm) with a density equal to 2.73 g/cm^3 were used in this study. Their water absorption is estimated at 0.45%. River sand with a density of 2.67 g/cm^3 is used as a fine aggregate.

2.1.3 Mineral Additions

The mineral additions used in this study are natural pozzolana (NP) and ground granulated blast furnace slag (GGBFS). Their chemical compositions were obtained by XFR analysis and some of their characteristics are given in Table 2.

Table 2: Chemical compositions and characteristics of the additions used

Parameter Chemical composition	Natural pozzolana (NP) (%)	Ground granulated Blast furnace slag (GGBFS) (%)
SiO ₂	43.67	50.76
Al ₂ O ₃	14.30	9.90
Fe ₂ O ₃	9.64	1.43
CaO	11.33	30.06

MgO	9.89	3.01
K ₂ O	1.60	1.47
Na ₂ O	3.10	1.37
P ₂ O ₅	0.54	0.02
TiO ₂	2.05	0.20
Loss on ignition (L.O.I)	3.72	1.65
Characteristics		
Fineness (cm ² /g)	5367	5847
Activity index at 28 days (%)	63.39	74.76
Density (g/cm ³)	2.70	2.67

2.1.4 Admixtures

Three different types of superplasticizers namely: Poly Carboxylate Ether (PCE); Modified Poly Carboxylate Ether (MPCE) and Combined Synthetic Polymers (CSP) were used in this experimental investigation. These admixtures were recovered from the GRANITEX Company. According to the product data sheets, their characteristics are given in Table 3.

Table 3: Characteristics of the admixtures (superplasticizers) used

Superplasticizer	Form	Color	Density (g/cm ³)	pH	Active ingredient content (%)	Trade name
PCE	Liquid	Light brown	1.07	6 - 6.5	30	Medaflow 30
MPCE	Liquid	Light brown	1.06	5 - 6	30	Medaflow 145
CSP	Liquid	Brown	1.12	6.5 - 7.5	36	Medaflow 113

2.2 Preparation, Optimization, and Storage of Samples

The volume of the paste is considered a basic factor when preparing the different SCC mixtures. European guidelines for the production of self-compacting concrete have been followed [26]. Using a Water/Powder (W/P) ratio of 0.35, six (6) concrete mixes were prepared. The total mass of powder considered in the formulation is around 450 kg/m³. The content of the mineral additions, either natural pozzolana or ground granulated blast furnace slag (GGBFS) represents a ratio of 10% relative to the mass of cement. The proportions of the concrete mixtures are summarized in Table 4.

Table 4: Mix proportions

W/P ratio	Water (L/m ³)	Cement (kg/m ³)	Addition (kg/m ³)	Sand (kg/m ³)	Coarse aggregate 3/8 (kg/m ³)	Coarse aggregate 8/15 (kg/m ³)
0.35	157.85	410	41	926	289.83	566.8

The following codes (abbreviations) are assigned to the different mixtures according to:

- Self-compacting concrete type;
- The first letter of the addition incorporated, and
- The type of superplasticizer (SP) used.

SCC-P-PCE: Self-Compacting Concrete with Pozzolana and Poly Carboxylate Ether.

SCC-P-MPCE: Self-Compacting Concrete with Pozzolana and Modified Poly Carboxylate Ether.

SCC-P-CSP: Self-Compacting Concrete with Pozzolana and Combined Synthetic Polymers.

SCC-G-PCE: Self-Compacting Concrete with Ground Granulated blast furnace slag and Poly Carboxylate Ether.

SCC-G-MPCE: Self-Compacting Concrete with Ground Granulated blast furnace slag and Modified Poly Carboxylate Ether.

SCC-G-CSP: Self-Compacting Concrete with Ground Granulated blast furnace slag and Combined Synthetic Polymers.

Optimization and dosage of superplasticizers are based on the slump flow test (Figure 1(a)). The optimal dosage of each superplasticizer, called saturation dosage allows the concrete to reach a slump diameter of 710 mm as shown in Figure 1(b). The recorded saturation dosages are given in Table 5.



Figure 1: a) Slump flow test, b) Slump diameter measurement

Table 5: Optimal (saturation) dosage of each superplasticizer according to the SCC mixture

SCCs	Superplasticizer dosage (%)	
	SCC-P	SCC-G
PCE	1.6	1.5
MPCE	2.5	2
CSP	3.3	2.6

The adsorbed content of each superplasticizer on the binder grains was evaluated using Altun et al. procedure [27]. A Total Organic Carbon (TOC) analyzer was employed. The adsorbed content was calculated using the formula (1):

$$Ad = \frac{(C_0 + C_c - C_1)V/x}{m} \quad (1)$$

Where Ad is the adsorbed content of the superplasticizer on binder (mg/l), C_0 is the TOC content of the superplasticizer solution without a binder (mg TOC/l), C_c is the TOC content of

the binder solution (mg TOC/l), C_l is the TOC content of the superplasticizer solution when the latter is equivalently adsorbed on the binder surface (mg TOC/l), x is the mass TOC content of superplasticizer (mg TOC/mg), V is the superplasticizer solution volume (in l), and m is the mass of binder (in g).

The preparation of the samples intended for the mechanical tests is carried out by pouring the fresh concrete into molds of standard dimensions (160 mm × 320 mm), (either cylindrical or prismatic). The demolding is done after 24 hours; all the specimens obtained were stored in a climatic chamber ($T = 20\text{ }^\circ\text{C}$; relative humidity $\text{RH} = 90\% \pm 5$) until testing. These controlled conditions ensure the protection of concrete specimens against desiccation.

2.3 Concrete Test Procedures

2.3.1 Fresh Concrete Tests

In order to evaluate the filling ability of the different fresh-state concretes, the slump-flow test and the T_{50} flow time were carried out according to British-adopted European standards [28]. Moreover, the L-box test and sieve segregation tests were performed according to SB EN 12350: 2010: Part 10 and Part 11 [29].

2.3.2 Hardened Concrete Tests

Mechanical characterization of the hardened SCCs was carried out after 2, 7, and 28 days of curing. Compressive strength, splitting tensile strength, and flexural tests were performed according to BS EN 12390 standards [30]. The samples intended for the compressive and tensile strengths are cylindrical specimens with a diameter of 160 mm and a height of 320 mm while those assigned for flexural tests are of prismatic shape having dimensions of 70 mm × 70 mm × 280 mm. The selected result represents the average of three trials.

3 Results and Discussion

3.1 Adsorption Content of Superplasticizers

The content of each superplasticizer (admixture) adsorbed on the cement particles is mentioned in Table 6.

Table 6: Content of superplasticizers adsorbed on cement grains

Superplasticizer (admixture)	Content of adsorption (mg/g binder)
PCE	0.927
MPCE	0.819
CSP	0.704

It can be seen from the results displayed in Table 6 that the amount of PCE adsorbed on the cement grains is higher than with the other two superplasticizers (MPCE and CSP). Generally, the adsorption characteristic of the superplasticizer on the cementitious particles is strongly related to the length of the main and side chains of the admixture. According to the literature [22, 31], the adsorption performance of the admixture improves with the decrease in the

length of the side chain; on the other hand, the steric hindrance effect becomes weaker. Also, as the main chain length increases, the number of anionic functional groups increases, and hence the electrostatic effect increases.

However, the elongation of the main chain of the superplasticizer leads to limited interaction with the cement and consequently low adsorption, due to the intertwining of the long main chains [22, 31].

3.2 Correlation of Superplasticizer Dosages

Figure 2 highlights the correlation between the optimal superplasticizer dosages obtained when the spreading diameter has reached 710 mm, and this, according to the mineral addition (pozzolana or granulated slag) contained in the SCC mixture.

It can be noted that the superplasticizer dosages are lower in the mixtures of SCCs containing granulated blast furnace slag compared to those containing natural pozzolana, and this is valid for all types of superplasticizers used. The dosage increases in a quasi-linear manner and the regression analysis gave a coefficient of determination R^2 equal to 0.992, which means that the established linear mathematical model is almost perfect.

It should be noted that the saturation dosages of superplasticizers obtained using the slump flow test depend on the type of mineral addition contained in the SCC mixture. Indeed, low dosages were recorded with SCCs formulated with granulated slag compared to those of natural pozzolana. Thus, the lowest dosage was recorded with the poly-carboxylate ether (PCE) with a minimum amount of 1.5%; this is due to its important dispersing effect.

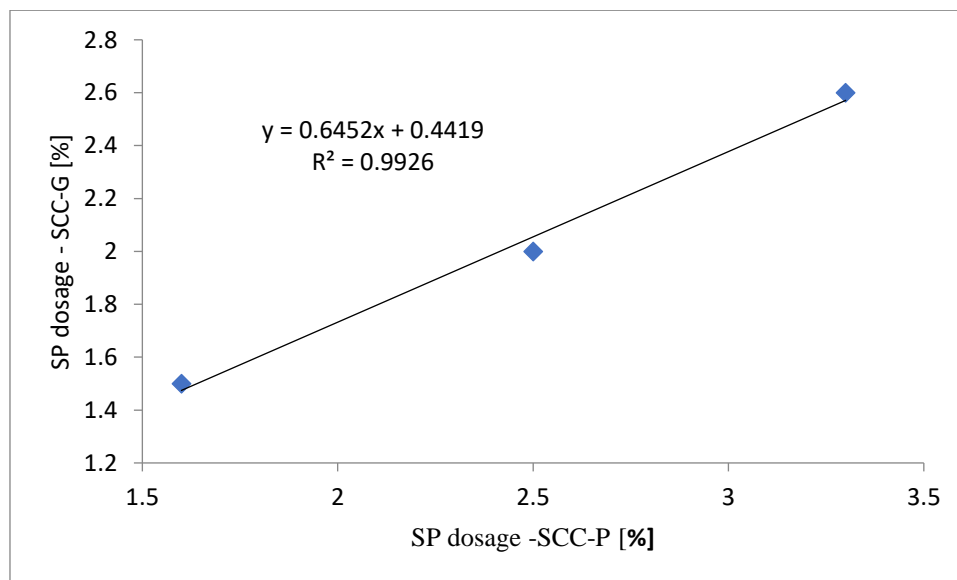


Figure 2: Relationship between the saturation dosages of superplasticizers according to the mineral addition contained in the SCC mixture

3.3 Fresh Properties of Concrete

The evaluation of the rheological properties (fresh state) of the different mixtures of self-compacting concretes is carried out using standard tests, namely L-box, sieve segregation and T₅₀ time tests. The results are given in Table 7.

Table 7: Results of tests in the fresh state

	L-box test			Sieve segregation test (%)			T ₅₀₀ test (s)		
	PCE	MPCE	CSP	PCE	MPCE	CSP	PCE	MPCE	CSP
SCC-P	H ₁ /H ₂ = 0.84	H ₁ /H ₂ = 0.87	H ₁ /H ₂ = 0.83	6.29	6.17	3.54	2	2	2.06
SCC-G	H ₁ /H ₂ = 0.88	H ₁ /H ₂ = 0.88	H ₁ /H ₂ = 0.90	4.5	4.6	5.9	2	2.26	2.18

The results of the L-Box tests showed that all concrete mixtures exhibit high height ratios (H₁/H₂), exceeding the minimum value of 0.80 required by EFNARC [32]. In addition, it can be seen that the best results are obtained with SCC containing ground granulated blast furnace slag as an additive.

For self-compacting concrete formulated with natural pozzolana, it can be noted that the best results (lowest risk of segregation) are obtained in concrete mixtures dosed with the combined synthetic polymer CSP, then MPCE, and finally PCE. On the other hand, opposite results were recorded in the concrete mixtures based on granulated blast furnace slag. The lowest rate (4.5%) was obtained in the concrete containing PCE.

Overall, the results obtained by the sieve segregation test make it possible to qualify all the compositions of the self-compacting concretes as stable because the values were in the range (0 to 15%) recommended by EFNARC [32], which means a minimum risk of segregation. This good stability recorded for all SCCs is probably due to a large amount of paste (cement + addition) contained in the concrete and eventually to the percentage of viscosity agent incorporated in the superplasticizer during its synthesis. Furthermore, it is useful to point out that better stability is obtained with the ground granulated blast furnace slag concrete compared with those containing natural pozzolana. This can be partly explained by the high specific surface of the GGBFS.

From the results displayed in Table 7, it is observed that the time (T₅₀) measured for the concrete to reach a spreading diameter of 500 mm is almost the same for all the compositions. The average recorded value is about two (2) seconds, a common slump time, often recorded in self-compacting concretes. The results obtained for all SCC mixtures are in line with the European guidelines for self-compacting concrete [26, 32].

3.4 Hardened Properties of Concrete

3.4.1 Compressive Strength

The results of the compressive strength of the different self-compacting concrete at 3, 7, and 28 days of curing are presented in Figure 3.

At curing ages of 3 and 7 days, it can be noted that all the self-compacting concretes dosed with MPCE superplasticizer give the best compressive strength, followed in the second

position by those dosed with PCE and finally the samples containing CSP admixture. On the other hand, at 28 days of curing, the concrete dosed with PCE admixture showed the highest value estimated at 58.90 MPa. CSP-based concretes often recorded the lowest values at all curing ages.

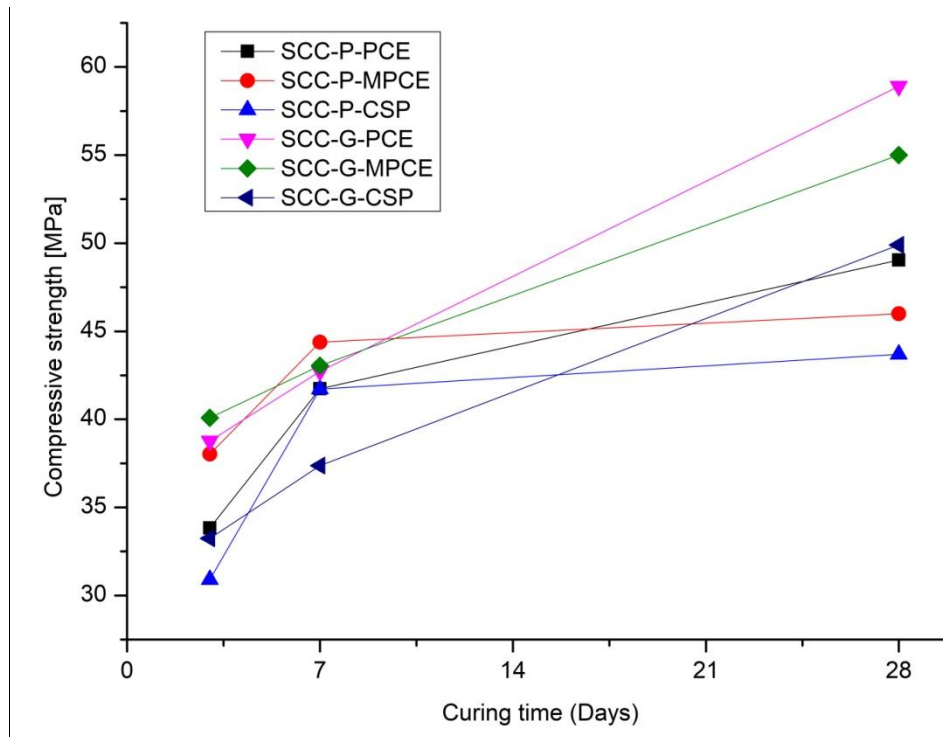


Figure 3: Compressive strength results at different curing times

On another register, except at 7 days of curing, where the compressive strengths are almost similar, it can be noted that the self-compacting concrete produced with blast furnace slag gives better mechanical performances compared with the concrete formulated with natural pozzolana. This can be explained by the filling effect (very fine particles which are inserted between the cement grains thus decreasing the porosity). This densification of the structure is valid for the two mineral additions. However, the blast furnace slag also improves the compressive strengths of concrete through the pozzolanic effect (ability to fix to the lime) [33]. Indeed, the calcium hydroxide (CH) formed during the cement hydration process reacts with the GGBS to produce secondary hydration which will again form CSH gel thus improving the mechanical resistance of the samples [34]. This reaction is favored by the large amount (more than 50%) of the silicon oxide present in the GGBFS as well as its high activity index (74.76%). In addition, the high specific surface of the slag, in particular, because of, the thorough grinding, contributes effectively to improve its reactivity.

3.4.2 Flexural Strength

The results obtained for the flexural strength at different curing ages are given in Figure 4. It can be noted that the values of the flexural strength of the different samples are lower than those recorded by the compressive strength tests. However, the trend of the evolution of these

two mechanical properties (flexural and compression) is practically similar, and this is valid for all the variants studied (according to the type of superplasticizer and the addition used).

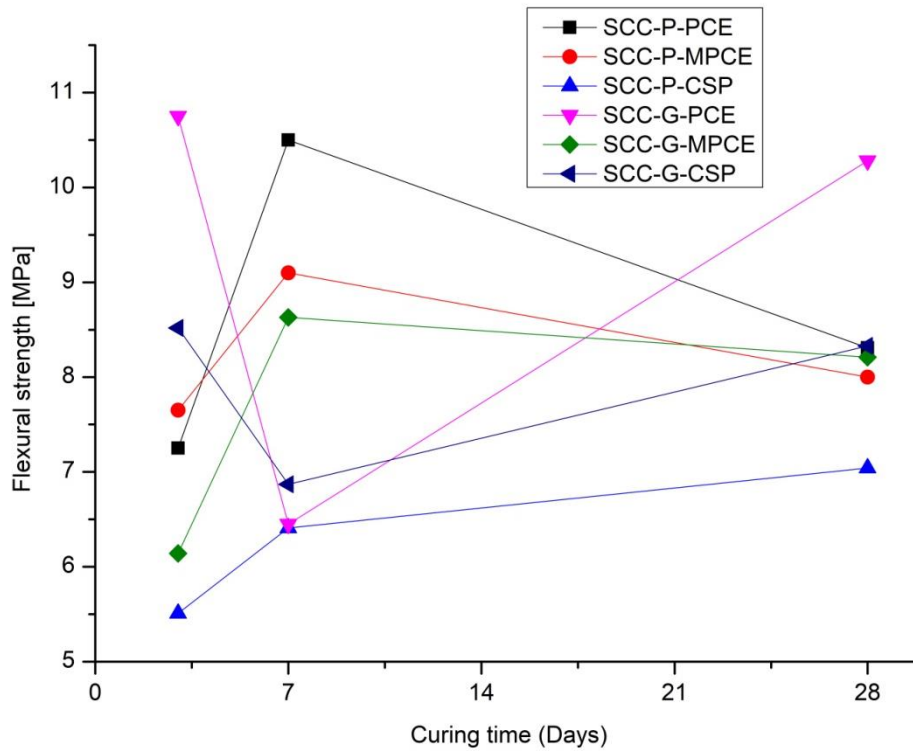


Figure 4: Flexural strength results at different curing ages

3.4.3 Splitting Tensile Strength

The results of the tensile splitting test are shown in Figure 5.

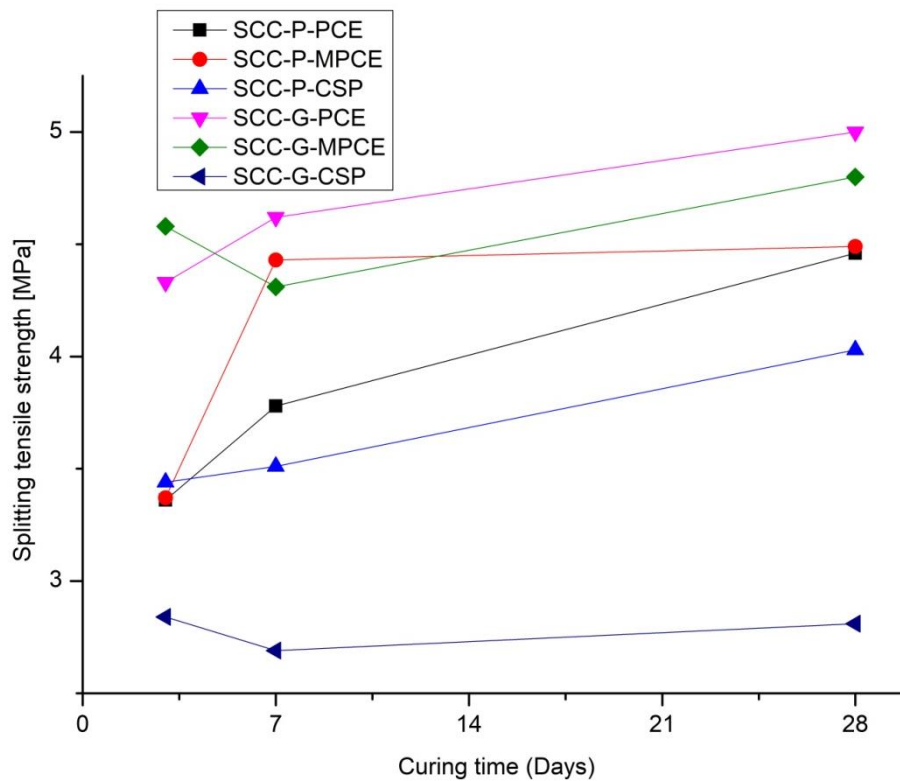


Figure 5: Splitting tensile strength results at different curing times

From the results, it can be deduced that concretes containing ground blast-furnace slag give better resistance to splitting compared to natural pozzolana concretes, especially at 3 and 28 days of curing. On the other hand, low splitting resistance was recorded at all curing ages (3, 7, and 28 days) for the samples where slag addition and CSP admixture are combined.

For concretes blended with natural pozzolana, the best splitting tensile strength is given by concrete containing MPCE admixture at all curing ages; however, for concretes containing GGBS, the use of PCE admixture gave the best performance except after 3 days of curing.

3.5 Relationship between Compressive and Flexural Strength

To highlight the relationship between the compressive and flexural strength of SCCs, the experimental values of the strengths obtained from the different samples at 28 days of curing were exploited. Trend curves were plotted and presented in Figure 6. A regression analysis is performed, and mathematical models (linear and polynomial) have been established.

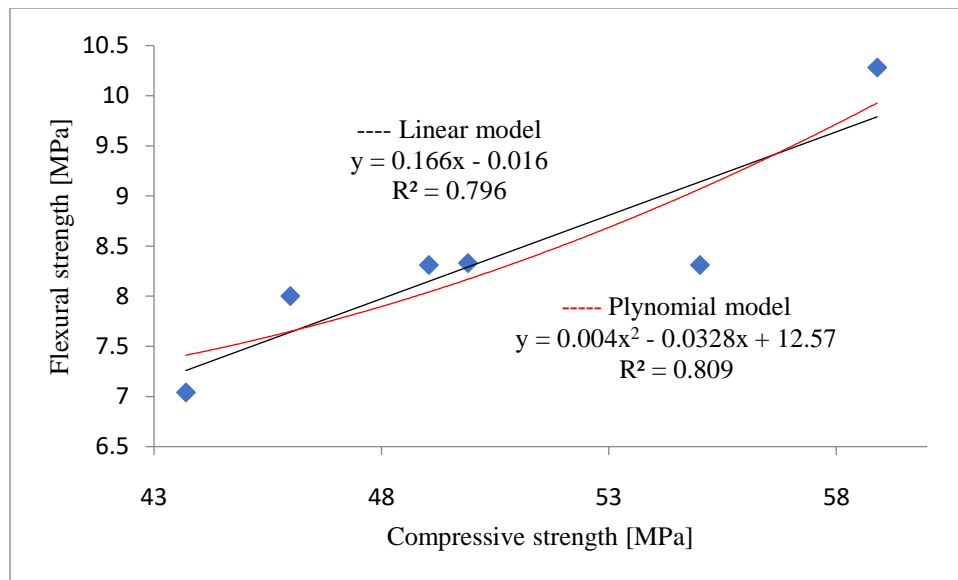


Figure 6: Relationship between compressive and flexural strength at 28 days of curing

The regression analyses, shown in Figure 6, highlight a positive correlation between the two mechanical properties. Indeed, the two properties evolve in the same direction, in other words, the compressive strength increases with the increase in flexural strength.

In order to link these two mechanical properties by equations, two mathematical models were designed according to the trend curves. The results of the calculation of their coefficients of determination R^2 show that the polynomial model is slightly more accurate than the linear model. However, the two models remain relatively imprecise given the value of R^2 which is quite far from 1.

4 Conclusions

The main conclusions from the present experimental study can be summarized as follows:

- Ground granulated blast furnace slag and natural pozzolana can be used as mineral additions in the production of self-compacting concrete (SCC). Their incorporation at 10% by weight relative to the mass of cement has made it possible to achieve properties that meet the standards required for SCCs, whether in the fresh or hardened state.
- Poly Carboxylate Ether (PCE) proved to be the most effective superplasticizer when compared to MPCE and CSP. Moreover, its use with low dosage enabled a better rheological behavior of SCC mixtures.
- The TOC analysis results revealed that Poly Carboxylate Ether (PCE) showed the highest adsorption on the cement particles, while the adsorption of CSP was the lowest. This can be explained by the structure of their main and side chains.
- The saturation dosage of the admixtures varies according to the mineral addition present in the self-compacting concrete mixture, in fact, the lowest saturation dosages

have been recorded in the SCCs containing granulated blast furnace slag as an additive, and this compared to natural pozzolana.

- Self-compacting concretes based on granulated blast furnace slag give better rheological and mechanical properties compared to concretes containing natural pozzolana as mineral addition.
- Compared to PCE and CSP admixtures, Modified Poly Carboxylate Ether (MPCE) makes it possible to obtain high mechanical properties of SCCs at curing ages of 3 and 7 days (short term).
- Our future research direction is to study the effect of these superplasticizers on the different properties of self-compacting concretes in the long term (durability).

References

- [1] BS EN 206-9, Concrete, Part 9 (2010), Additional rules for self-compacting concrete (SCC), British Standards publication.
- [2] Concrete Society, BRE. Technical Report N°.62 (2005), Self-compacting Concrete: A Review, in: R.T.U. Day, I.X. Holton (Ed.), Camberley, UK, Concrete Society, Surrey GU17 9AB, UK.
- [3] Ozawa, K., Maekawa, K., Kunishima, M., Okamura, H. (1989). Development of high performance concrete based on the durability design of concrete structures. In: Proceedings of the 2nd East-Asia and Pacific Conference on Structural Engineering and Construction (EASEC-2), pp. 445-450.
- [4] Thrane, L., Szabo, P., Geiker, M., Glavind, M., Stang, H. (2004). Simulation of the test method ‘L-box’ for self-compacting concrete. *Ann. Trans. Nordic Rheol. Soc.* 12, 47–54.
- [5] Ding, J.T., Li, Z. (2002). Effects of metakaolin and silica fume on properties of concrete. *ACI Mater. J.* 99 (4), 393–398.
- [6] Bai, J., Wild, S. (2002). Investigation of the temperature change and heat evolution of mortar incorporating PFA and metakaolin. *Cem. Concr. Compos.* 24 (2), 201–209.
- [7] Kovler, K., Roussel, N. (2011). Properties of fresh and hardened concrete. *Cem. Concr. Res.* 41, 775–792.
- [8] Bai, J., Sabir, B.B., Wild, S., Kinuthia, J.M. (2000). Strength development in concrete incorporating PFA and Metakaolin. *Mag. Concr. Res.* 52 (3), 153–162.
- [9] Lewis, R., Sear L., Wainwright, P., Ryle, R. (2003). Cementitious Additions. In J. Newman, B.S. Choo (Eds.), *Advanced concrete technology- constituent materials* (pp. 96–159). Elsevier Ltd, Oxford.
- [10] Domone, P.L., Illston, J.M. (2010). *Construction Materials: Their Nature and Behaviour*. Fourth ed.. Taylor and Francis Group, CRC Press, London. ISBN 041546515X.
- [11] Mehta, P.K. (1981). Studies on blended Portland cements containing Santorin earth. *Cem. Concr. Res.* 11 (4), 507–518.
- [12] Ghrici, M., Kenai, S., Meziane, E. (2006). Mechanical and durability properties of cement mortar with Algerian natural pozzolana. *J Mater. Sci.* 41, 6965–6972.
- [13] Uysal, M., Sumer, M. (2011). Performance of self-compacting concrete containing different mineral admixtures. *Constr. Build. Mater.* 25 (11), 4112–4120.

- [14] Dinakar, P., Sethy, K.P., Sahoo, U.C. (2013). Design of self-compacting concrete with ground granulated blast furnace slag. *Mater. Des.* 43, 161–169.
- [15] Russel, W.B., (1997). High performance concrete-from buildings to bridges. *Concr. Int.* 19 (8), 62–63.
- [16] Oner, A, Akyuz, S. (2007). An experimental study on optimum usage of GGBS for the compressive strength of concrete. *Cem. Concr. Compos.* 29 (6), 505–514.
- [17] Felekoglu, B, Sarikahya, H. (2008). Effect of chemical structure of polycarboxylate-based superplasticizers on workability retention of self-compacting concrete. *Constr. Build. Mater.* 22 (9), 1972–80.
- [18] Sahmaran, M, Christianto, H.A, Yaman, I.Ö. (2006). The effect of chemical admixtures and mineral additives on the properties of self-compacting mortars. *Cem. Concr. Compos.* 28 (5), 432–440.
- [19] Shi, C. (2009). Recent developments of PC superplasticizers. In: 2nd International Symposium on design, performance and use of self consolidating concrete. Beijing, China
- [20] Mardani-Aghabaglou, A. (2016). Investigation of Cement-Superplasticizer Admixture Compatibility. PhD thesis, Ege University, Institute of Science and Engineering, Izmir, Turkey.
- [21] Mardani-Aghabaglou, A., Felekoglu, B., Ramyar, K. (2017). Effect of cement C₃A content on properties of cementitious systems containing high-range water-reducing admixture. *J. of Mater. In Civ. Engi.* 29 (8), 04017066.
- [22] Özen, S., Altun, M.G., Mardani-Aghabaglou, A., Ramyar, K. (2022). Multi-effect of superplasticisers main and side-chain length on cementitious systems with fly ash. *Mag. of Concr. Res.* 74 (14), 727-739. <https://doi.org/10.1680/jmacr.21.00134>
- [23] Evangeline, K., Neelamegam, M. (2011). Effect of Super-plasticizer on Workability and Mechanical Properties of Self-Compacting Concrete. In National Conference on Advances in Traffic, Construction Materials and Environmental Engineering.
- [24] Zhang, J., Han, G., Shen, D., An, X., Meye, S.M. (2022). A new model to predict the optimal mix design of self-compacting concrete considering powder properties and superplasticizer type. *J. Mater. Res. Technol.* 19, 3980-3993.
- [25] Xiong, G., Guo, X. (2022). Effects and mechanism of superplasticizers and precursor proportions on the fresh properties of fly ash – slag powder based geopolymers. *Constr. Build. Mater.* 350, 128734.
- [26] The European Guidelines for Self-Compacting Concrete, (2005) -Specification, Production and Use, Self-compacting concrete European project group; 2005.
- [27] Altun, M.G., Özen, S., Mardani-Aghabaglou, A. (2020). Effect of side chain length change of polycarboxylate-ether based high range water reducing admixture on properties of self-compacting concrete. *Constr. Build. Mater.* 246, 118427.
- [28] SB EN 12350-8: (2019): Testing fresh concrete. Self-compacting concrete. Slump-flow test.
- [29] SB EN 12350: (2010): Part 10: Testing fresh concrete-Self compacting concrete- L box test. Part 11: Testing fresh concrete-Self compacting concrete- Sieve segregation test.
- [30] BS EN 12390: Testing hardened concrete. Part 3: Compressive strength and test specimens. Part 5: Flexural strength of test specimens. Part 6: Tensile splitting strength of test specimens.
- [31] Plank, J., Hirsch, C. (2007). Impact of zeta potential of early cement hydration phases on superplasticizer adsorption. *Cem. Concr. Res.* 37 (4), 537–542.

- [32] EFNARC (2002). Specification and guidelines for self-compacting concrete. European Federation of Producers and Applicators of Specialist Products for Structures, 2002.
- [33] Boukendakdji, O., Kenai, S., Kadri, E., Rouis, F. (2009). Effect of slag on the rheology of fresh self-compacted concrete. *Constr. Build. Mater.* 23 (7), 2593–2598.
- [34] Vanyo, S., Petar, A., Vili, L., Victoria, V. (1996). Effect of the “Pozzolit” active mineral admixture on the properties of cement mortars and concrete. Part 1: Physical and Mechanical properties. *Cem. Concr. Res.* 26 (7), 1065-1071.



On the Practical Use of Advanced Constitutive Laws in Finite Element Underground Structures Analysis

Amrane Moussa^{1*}, Messast Salah², Laouar Mohamed Salah³

¹Department of Civil Engineering, Laboratory LGC-ROI, University of Batna 2, 53,
Road of Constantine Fesdis, 05078 Batna, Algeria

²Department of Civil Engineering, Laboratory LMGHU, University of Skikda, BP 26,
Road Elhadeik, Skikda, 21000, Algeria

³Mining Laboratory, Civil Engineering Department, LarbiTebessi University, 12002, Tebessa, Algeria

*e-mail: moussa.amrane@univ-batna2.dz

Abstract

This article emphasizes the value of applying sophisticated constitutive soil models in numerical modeling as daily geotechnical practice. The capabilities of two different constitutive relations for the modeling of the second Heinenoord bored tunnel are compared. The hypoplastic model of Wolffersdorff for granular materials (Hypo) is a relatively simple model without recourse to yield surface or plastic potential based on rational mechanics, whereas the chosen elastoplastic model, the Hardening Soil Model (HSM) belongs to the non-associative plasticity with double hardening. A modification of the hypoplastic model with improved intergranular strain (IGS) was tested, leading to improve model behavior. Comparisons between numerical simulations and experimental values demonstrate the advantages of using the hypoplastic model with improved intergranular strain (IGS).

Keywords: tunneling, numerical modeling, interaction, hypoplasticity, HSM

Introduction

The term hypoplasticity appeared about 30 years ago as an alternative to elasto–plasticity for the description of the irreversible behavior of soils and has since then attracted the attention of many geotechnical scholars [1-3]. The theory is based on nonlinear tensorial functions and is created without using Elasto-plastic theory ideas like yield surface, flow rule, and breakdown of deformation into elastic and plastic portions. Without the application of numerical methods, substantial progress in understanding the behavior of geomaterials would not have been possible [4-7]. The evolution of digital modeling, and soil behavior, in particular, is intimately tied to advances in the domain of numerical analysis [8,9], which employs several approaches such as the Finite Element Method, or the Finite Difference Method.

The contact of existing structures and tunnels is a complex process [9], with the behavior of the surrounding soil being one of the most important factors to consider [10].

Therefore, the choice of ground behavior model is a crucial task to better estimate the magnitude and distribution of deformations.

Different physical mechanisms, e.g., consolidation processes, creep or progressive failure, cause deformations with different displacement patterns. Likewise, different constitutive models provide varying responses concerning displacement behavior because of their mathematical formulations [11].

In this article, two constitutive models with improved levels of complexity are used to simulate the behavior of soil around the second Heinenoord tunnel. The first is a model with hardening (Hardening Soil Model, or HSM); the second is a hypoplastic model (HYPO) [6] with an evolution of this model taking into account the improvement of intergranular strain (IGS) [12].

The HSM model is available in the library of Plaxis software, while the second (HYPO) model is a subroutine, user-defined model [6].

Comparing the results of numerical simulations in this study to in-situ measurements in the second Heinenoord tunnel [13, 14] for settlements and horizontal displacements shows good adaptation and benefits of the use of the hypoplastic model with improved intergranular strain (IGS).

Soil Models

Hardening Soil Model (HSM)

The Hardening Soil Model (HSM) can be considered as an advanced model for soil behavior. This model is a derivative of the Duncan-Chang hyperbolic model. The stress-strain relationship, due to the primary loading, is assumed to be a hyperbolic curve in the HSM. The hyperbolic function, as given by [15], for the drained triaxial test can be formulated as:

$$\varepsilon_1 = \frac{q_a - q}{2E_{50} q_a - q} \text{ pour } q < q_f \quad (1)$$

where ε_1 is the axial strain, and q is the deviatoric stress. The ultimate deviatoric stress (q_f) is defined as:

$$q_f = \frac{6 \sin \varphi}{3 - \sin \varphi} (p + c \cot \varphi) \quad (2)$$

where the quantity (q_a) is the asymptotic value of the shear strength, in which $q_a = \frac{q_f}{R_f}$. The R_f is the failure ratio.

Figure 1 illustrates a stress-strain representation by the HSM model. Three different stiffnesses are used to explain the soil behavior:

triaxial loading stiffness E_{50} , triaxial unloading stiffness E_{ur} and the oedometer loading stiffness E_{oed} .

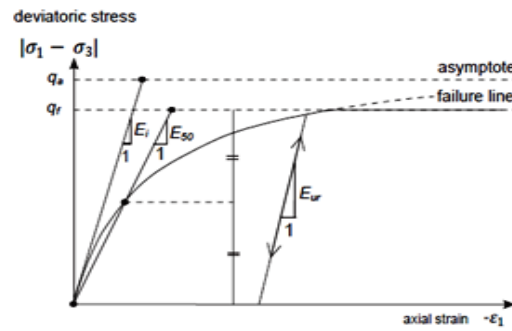


Figure 1: Hyperbolic stress–strain in HS model [16].

The expressions of these three modules are given by Equations 3, 4 and 5.

$$E_{oed} = E_{oed}^{ref} \left(\frac{\sigma}{p^{ref}} \right)^m \quad (3)$$

$$E_{50} = E_{50}^{ref} \left(\frac{c \cdot \cos \varphi + \sigma_3 \cdot \sin \varphi}{c \cdot \cos \varphi + p^{ref} \cdot \sin \varphi} \right)^m \quad (4)$$

$$E_{ur} = E_{ur}^{ref} \left(\frac{c \cdot \cos \varphi + c \cdot \cot \varphi}{\sigma^{ref} + c \cdot \cot \varphi} \right)^m \quad (5)$$

where E_{50}^{ref} is a reference stiffness modulus corresponding to the reference stress p^{ref} (100 kN/m²). E_{ur}^{ref} is the reference modulus for unloading and reloading, which corresponds to the reference pressure p^{ref} . The reference oedometer modulus (E_{oed}^{ref}), is used to control the magnitude of the plastic volumetric strains that originate from the yield cap. In a similar manner to the triaxial moduli, the oedometer modulus (E_{oed}) obeys the stress dependency law.

More explanation of the Hardening-soil model is in [18, 16, 19].

Hypoplastic Model (HYPO)

The hypoplastic model (HYPO), developed by Kolymbas [20] in 1985, describes the stress-strain behavior of granular materials in rate form. It is derived from the stress rate, which is expressed as a function of the stress tensor and strain rate. Later, other researchers [21, 22, 23, 24...] added the void ratio as an additional state variable. This model's simplicity is a significant advantage, as is its ability to express inelastic deformation without the use of any additional concepts such as yield surface or plastic potential [25, 26, 27, 28, 29, 30].

Later, Niemunis and Herle [12] introduce the concept of intergranular strain, which allows for the accounting of small deformation.

This research is limited to sand applications using Von Wolffersdorff's constitutive law [31] with improved intergranular strain (IGS).

Constitutive Equation

The general form of the hypoplastic model is expressed by Equation 6:

$$\dot{T} = F(T, e, D) \quad (6)$$

where:

\dot{T} is the stress rate.

T is the current Cauchy stress.

e is the void ratio.

D is the stretching tensor.

Equation 7 expresses Von Wolffersdorff's modified constitutive equation:

$$\dot{T} = f_b f_e \frac{1}{tr(\hat{T}^2)} \{F^2 D + a^2 tr(\hat{T}D)\hat{T} + f_d a F(\hat{T} + \hat{T}^*) \|D\|\} \quad (7)$$

in which:

$$a = \frac{\sqrt{3}(3 - \sin \varphi_c)}{2\sqrt{2} \sin \varphi_c} \quad (8)$$

The factor F is a function of \hat{T}^*

$$F = \sqrt{\frac{1}{8} \tan^2 \Psi + \frac{2 - \tan^2 \Psi}{2 + 2 \tan \Psi \cos 3\theta} - \frac{1}{2\sqrt{2} \tan \Psi}} \quad (9)$$

$$\tan \Psi = \sqrt{3} \|\hat{T}^*\|; \cos 3\theta = -\sqrt{6} \frac{tr(\hat{T}^{*3})}{[tr(\hat{T}^{*2})]^{\frac{3}{2}}} \quad (10)$$

Herein, $\hat{T}^* = \hat{T} - \frac{1}{3}I$ is the deviatoric part of the stress ratio tensor \hat{T} .

I is the unit tensor and $\hat{T} = \frac{T}{tr T}$, $p_s = -tr \frac{T}{3}$

$$f_b = \left(\frac{e_i}{e_c}\right)^\beta \frac{h_s}{n} \frac{1+e_i}{e_i} \left(\frac{-tr T}{h_s}\right)^{1-n} \left[3 + a^2 - a\sqrt{3} \left(\frac{e_{i0} - e_{d0}}{e_{c0} - e_{d0}}\right)^\alpha\right]^{-1} \quad (11)$$

$$f_d = \left(\frac{e - e_d}{e_c - e_d}\right)^\alpha \quad (12)$$

$$f_e = \left(\frac{e_c}{e}\right)^\beta \quad (13)$$

where:

h_s : Granular hardness.

n : Exponent relates to the sensitivity of granular skeleton to changes of pressure.

α : Exponent describes the transition between peak and critical stress.

β : Exponent represents the change of stiffness at current density.

e_i : maximum void ratio,

e_c : void ratio at the critical state.

e_d : void ratio at a state of maximum density.

Intergranular Strain (IGS)

The original hypoplastic model [21, 22, 31] has a shortcoming in the region of small stress cycles as an excessive accumulation of deformation occurs and therefore the displacements are overpredicted [12]. According to the experimental measurements [32, 33], soil stiffness at a given state defined by stress and void ratio depends strongly on the history of deformation and the direction of strain rate.

Niemunis and Herle [12] proposed a new state variable called the intergranular strain, h , to improve the performance of the hypoplastic model in the range of small load cycles. This tensorial state variable is supposed to account for the deformation of the intergranular interface layer and particle rearrangement when small strains are applied.

It necessitates the use of five parameters that govern the behavior of the soil under small deformations:

R_{max} : The size of the elastic range (in the strain space);

β et χ : Control the rate of degradation of the initial shear modulus G_0 ;

mR : Control the constant value of G_0 ;

mT : Control the value of G beyond neutral stresses.

Parameter Calibrations

The hypoplastic model was calibrated so that the curves, stress-strain of numerical oedometer tests, and numerical triaxial standard tests align the best with the curves of the HSM model. It turned out that the hypoplastic model reacts as expected, insensitive to changes in these physical constants. Therefore, we need only a small number of parameters of the dataset to be changed slightly [34]. However, the biggest impact of the hypoplastic model is to determine the initial values of two state variables' void ratio e_0 and intergranular strain h . In Figure 2, the stress-strain oedometric curves are represented by two models (HSM and HYPO). The HSM is unable to accurately represent unloading and reloading cycles. Hysteretic effects cannot be predicted using a model formulation with a single unloading-reloading modulus E_{ur} . Hysteretic effects can be seen in the stress-strain curve of the HYPO with IGS. The loading-unloading-reloading cycles are modeled better beside the effect of over consolidation.

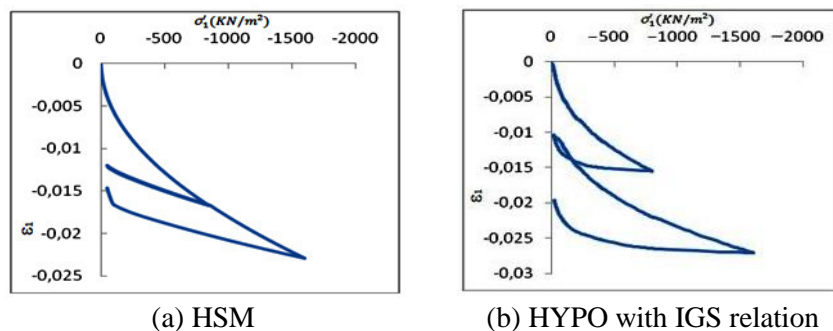


Figure 2: Numerical Oedometer test

Figure 3 shows the stress-strain curves of standard shear triaxial tests under three different confining pressures for both models (HSM and HYPO).

Overall, it is estimated that curves hypoplasticity and elastoplasticity presented in Figures 2 and 3 are in good agreement.

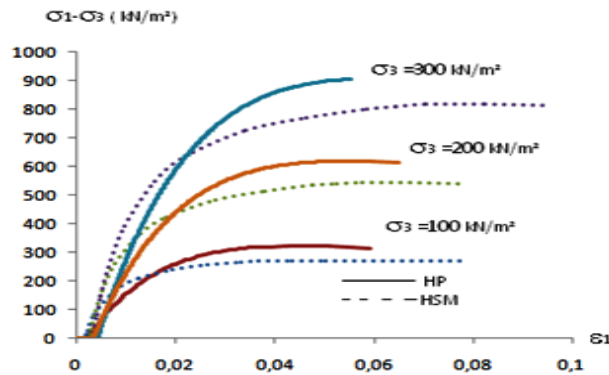


Figure 3: Numerical triaxial tests

Numerical Simulations

Numerical simulations of tunnel boring were carried out by a calculation using the Finite Element software Plaxis, adopting a plane strain model. Figure 4 shows the model geometry and geological section of the site where the Heinenoord tunnel south of Rotterdam is excavated [12, 13], to a depth of 27.5m. The groundwater table is considered at a level of -1.5 m.

Tables 1 and 2 summarize the parameters characterizing such soils according to HSM and HYPO models. Heinenoord tunnel is the circular shape of diameter $D = 8.3$ m; the wall is modeled with linear elastic members with $EA=3.75 \times 10^6$ kN, $EI=1.95 \times 10^4$ kN.m², $\nu = 0.2$ and $\gamma=25$ kN/m³. Several methods of numerical simulation for Heinenoord tunnel analysis can be found in the literature [35, 37, 38, 39]. An overview of these methods is given by Moller [5].

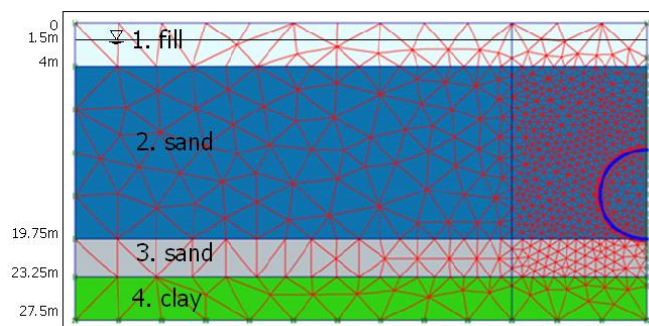


Figure 4: Geological section of the area of Heinenoord tunnel [35], Finite Element geometry and mesh

Table 1: The parameters used for the model HSM [35]

Layers	C' (kPa)	ϕ' (°)	Ψ (°)	E_{oed}^{ref} (MPa)	E_{50}^{ref} (MPa)	E_{ur}^{ref} (MPa)	ν_{ur}	m	K_0^{nc0}
1 / Fill	3	27	0	14	14	42	0.2	0.5	0.58
2 / Sand	0.01	35	5	35	35	105	0.2	0.5	0.47
3 / Sand	0.01	35	5	35	35	105	0.2	0.5	0.47
4 / Clay	7	31	1	7	12	35	0.2	0.9	0.55

Table 2: The parameters used for the model HYPO

Layers	ϕ_c (°)	H_s (MPa)	N	$ed0$	$ec0$	$ei0$	α	β	$Rmax$	βr	χ	mR	mT
2/Sand	30	$2.4 E^3$	0.28	0.55	0.95	1.05	0.25	1.5	$1E^{-4}$	0.5	6	5	2

The implementation was realized with the hypoplastic model via the interface " User_Mod " [19].

Results and Discussions

Deterministic Results

The simulation of the second Heinenoord tunnel is performed using HSM and HYPO models. The results are illustrated in Figures 5 - 8.

Deformed Mesh

After the construction of the tunnel, we noted that a movement of ground occurred at the level of the natural surface, and the level of the excavation (in clay).

The Finite Elements Mesh (Figure 5) clearly shows the existence of a bowl caused by the construction of the tunnel.

We also noted a certain shortening of the lining of the tunnel that is due to the various phases of construction.

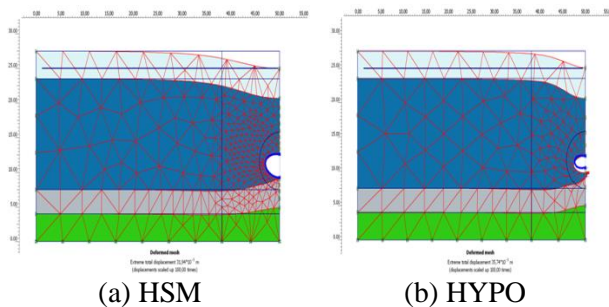
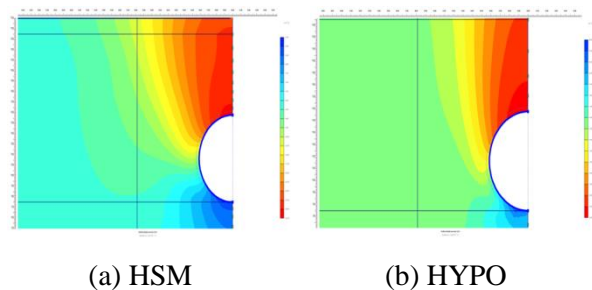


Figure 5: Deformed Mesh


 Figure 6: Vertical displacement U_y

Vertical Displacement U_y

According to several authors, it appears that the displacements would probably not be significant on surfaces, but in the key of the tunnel, they become more extensive. In Figure 6,

we note a certain maximum displacement (for Hypo $U_{y_{max}}= 35.744$ mm; for HSM $U_{y_{max}}= 31.944$ mm), is just near the top of the tunnel.

Horizontal Displacement U_x

The horizontal displacements obtained after the construction of the tunnel are presented in Figure 7.

Figure 7 shows that horizontal displacements are almost null at the lower part of the tunnel and that maximum displacement is present at the level of the sides of the tunnel. This phenomenon can be explained by the effort exerted by the shield which tends to push back the ground at the level of the sides of the tunnel.

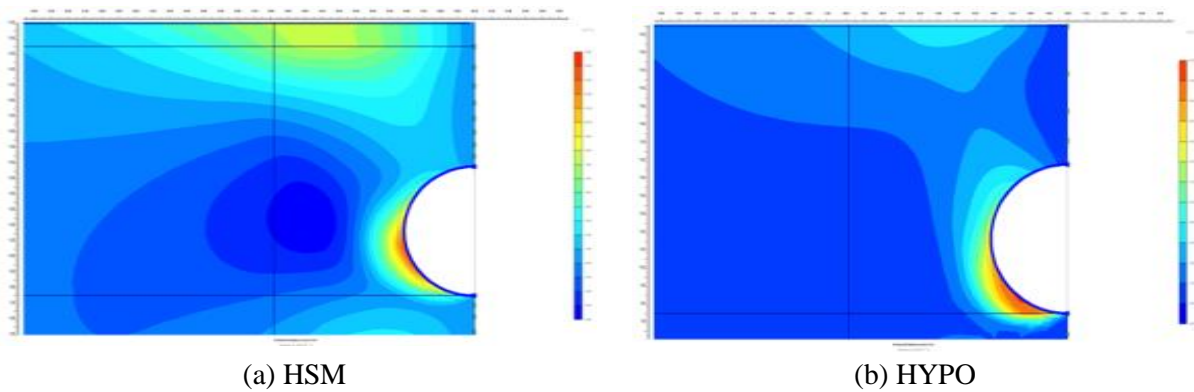


Figure 7: Horizontal displacement U_x

Total Deviatoric Strain γ_{xy}

Figure 8 shows the total deviatoric strain γ_{xy} .

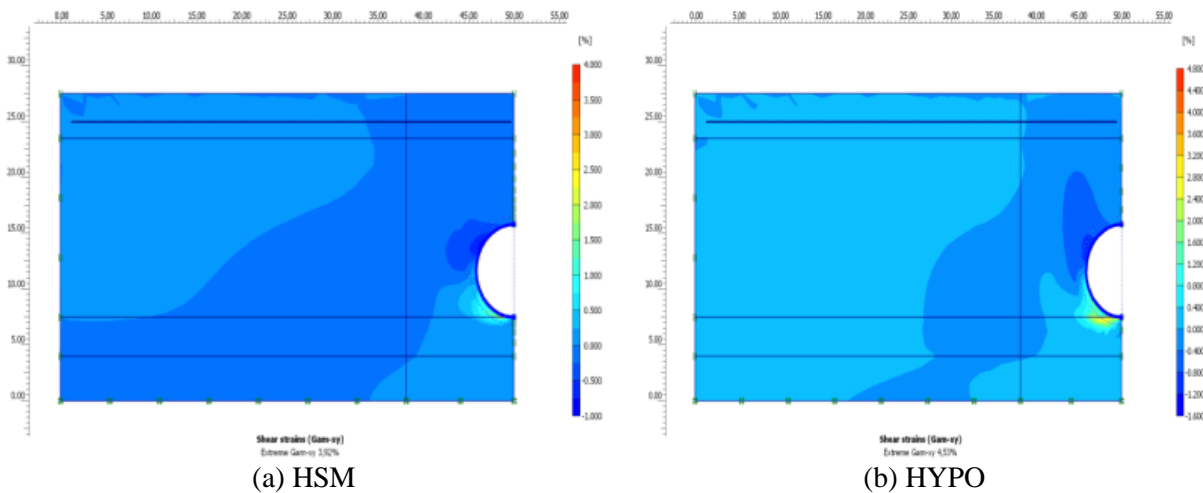


Figure 8: Total deviatoric strain γ_{xy}

Comparison of Load-Settlement Curve from in-Situ Observations and Plaxis

Figures 9 and 10 show that settlement curves and horizontal displacements nearest in situ observations are those relating to numerical simulations taken as soil behavior hypoplastic model incorporating the soil’s small strain stiffness behavior in the analysis of displacement. This finding supports the conclusion that the hypoplastic model is best suited to this type of problem.

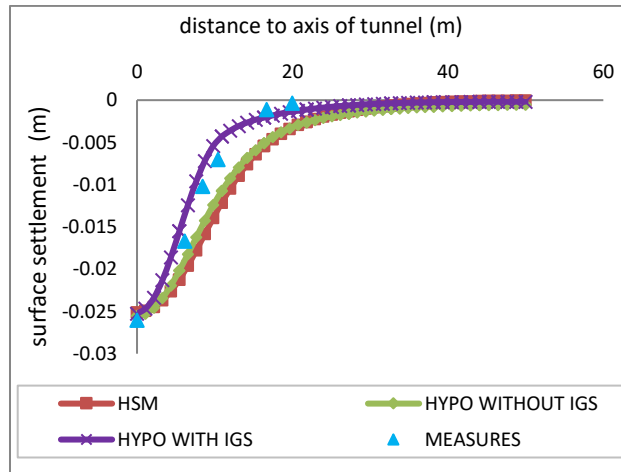


Figure 9: Surface settlements above Heinenoord tunnel, according to various constitutive models

Parametric Study

This part is devoted to a parametric study showing the effect of some parameters on settlements and horizontal displacements.

We vary the stiffness parameters of model HSM by $\pm 25\%$ and reduce the initial void ratio for the simulations with the hypoplastic model HYPO by 15% and then increase it by 15%.

Figures 11 to 14 present the results of the parametric studies.

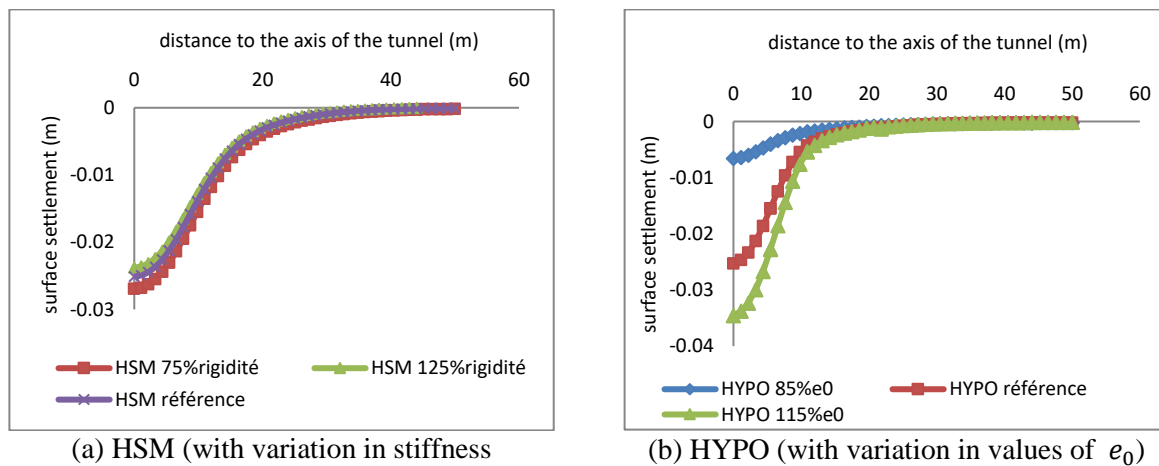


Figure 10: Surface settlement of Heinenoord tunnel

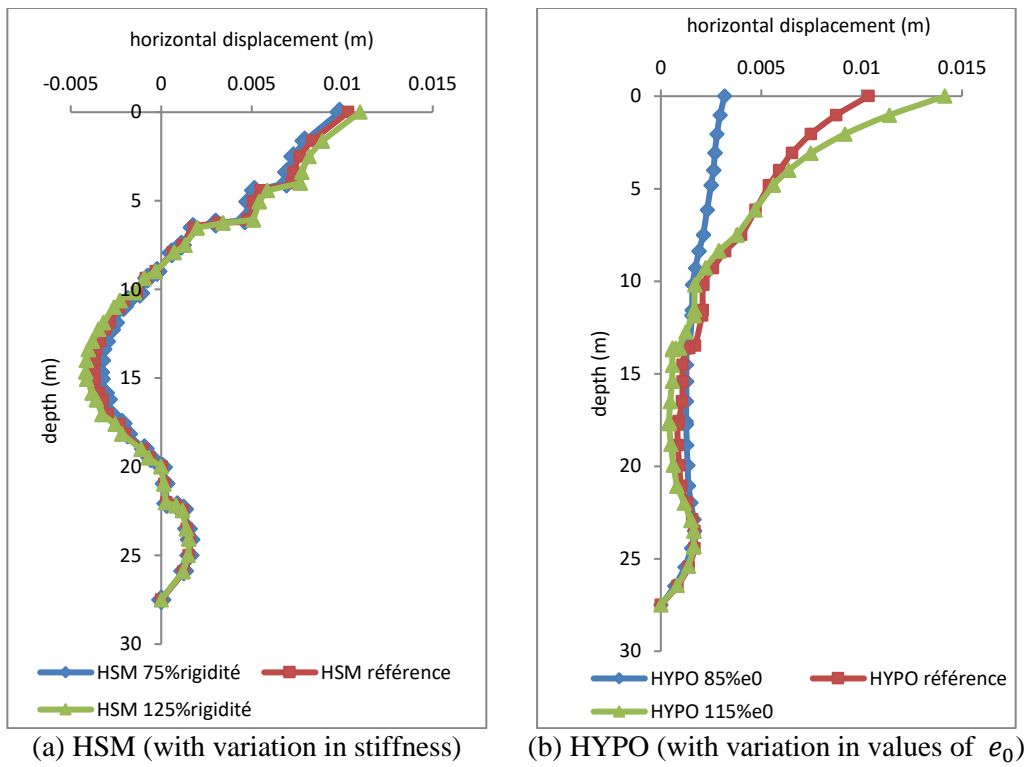


Figure 13: Horizontal displacement from the axis to 10 m

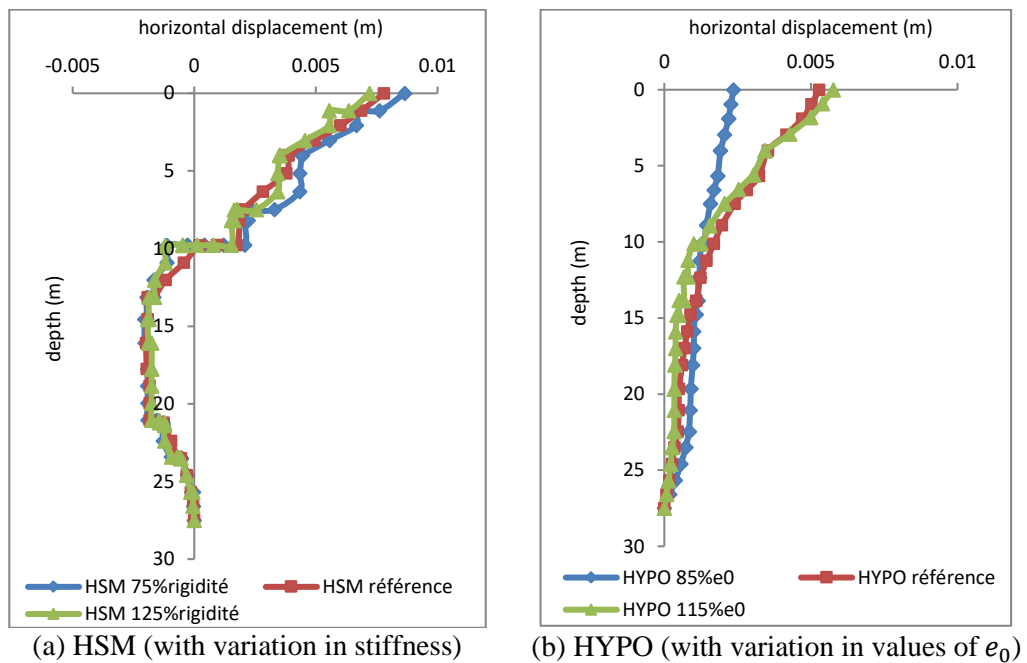


Figure 14: Horizontal displacement from the axis up to 16 m

Note that the settlements and horizontal displacements determined by simulations using the hypoplastic model are more sensitive to fluctuations of a 15% void ratio than the sensitivity of results calculated using the HSM model to a fluctuation in the stiffness of 25%.

This parametric study has shown that the fluctuations of the void ratio in the calculation of hypoplasticity can have a significant impact on calculation results [36, 40].

Conclusion

This study presents a numerical calculation using FEM software Plaxis for modeling the second Heinenoord bored tunnel.

The influence of the type of the model of soil behavior on the response of the tunnel is tested by using two models of behavior, namely: the HSM model and the HYPO model with the improvement of intergranular strain (IGS).

Comparing the results of this study to measurements for settlement at the free surface and horizontal displacements shows the best adaptation of the hypoplastic model with the improvement of intergranular strain (IGS).

A parametric study was conducted to highlight the influence of various parameters on the behavior of the tunnel, and according to this study, the following conclusions should be noted:

- The void ratio, initial e_0 influences soil behavior because it is a state variable in the hypoplastic model.
- A reduction in the rate of void ratio leads to a significant increase in the rigidity and strength of the soil.
- A higher dilatancy also occurs at a reduction in the initial void ratio.

References

- [1] Amrane, M. (2018). Modélisation du Comportement des Ouvrages Géotechniques avec la Loi de J. Lemaitre, PhD thesis, University of Skikda, Algeria.
<http://ftech.univ-skikda.dz/doc2/2018/THESE%20Amrane%20Moussa.pdf>
- [2] Amrane, M. & Messast, S. (2018). Modeling the Behavior of Geotechnical Constructions Under Cyclic Loading with a Numerical Approach Based on J. Lemaitre Model. *Indian Geotech J.* 48, 520–528. <https://doi.org/10.1007/s40098-017-0275-1>
- [3] Moussa, A., Salah, M. & Rafik, D. (2020). Improvement of a Hypoplastic Model for Granular Materials Under High-Confining Pressures. *Geotech Geol Eng.* 38, 3761–3771. <https://doi.org/10.1007/s10706-020-01256-y>
- [4] Chatra, A. S. & Dadagoudar, G. R. (2010). Numerical simulation of hypoplastic constitutive model for sand. In Indian Geotechnical Conference – 2010, GEOTrendz December 16–18, 2010 IGS Mumbai Chapter & IIT Bombay
- [5] Reyes, D.K., Rodriguez-Marek, A., & Lizcano, A. (2009). A hypoplastic model for site response analysis. *Soil Dynamic and Earthquake Engineering.* 29 (1), 173-184.
- [6] Gudehus, G., Amorosi, A., Gens, A., Herle, I., Kolymbas, D., Masin, D., Muir Wood, D., Nova, R., Niemunis, A., Pastor, M., Tamagnini, C. & G. Viggiani, G. (2008). The soilmodels.info project. *International Journal for Numerical and Analytical Methods in Geomechanics.* 32 (12),1571-1572, [Letter PDF].
- [7] Said, I., Gennaro, D.V., & Frank, R. (2009). Axisymmetric finite element analysis of pile loading tests. *Computers and Geotechnics.* 36 (1-2), 6-19.
- [8] Zidan, A.F. & Ramadan, O.M.O. (2014). Three Dimensional Numerical Analysis of the Effects of Tunnelling Near Piled Structures. *KSCE Journal of Civil Engineering.* 19 (4), 917-928.

- [9] Mathew, G.V & Lehane, B.M. (2014). Measured and Back Analysed Soil Structure Interaction Effects in a Layered Stratigraphy During Tunnel Boring. *Geotech Geol Eng.* 32 (4), 873-884.
- [10] Bonini, M., Lancellotta, G., & Barla, G. (2013). State of Stress in Tunnel Lining in Squeezing Rock Conditions. *Rock Mech Rock Eng.* 46, 405–411.
- [11] Ng, C.W.W., Sun, H.S., Lei, G.H., Shi, J.W., Mašin, D. (2015). Ability of three different soil constitutive models to predict a tunnel's response to basement excavation. *Revue canadienne de géotechnique.* 52 (11), 1637-1648.
- [12] Niemunis, A. & Herle, I. (1997). Hypoplastic model for cohesionless soils with elastic strain range. *Mechanics of Cohesive-Frictional Material.* 2, 279-299.
- [13] CUR / COB (1999). Monitoring bij de TweedeHeineneoordtunnel, verslag van eengrootschaligpraktijkonderzoeknaargeboorde tunnels. Final report COB committee K100. CUR / COB, Gouda.
- [14] CUR / COB (2000). Toetsingsrichtlijn voor het ontwerp van boortunnelsvoorweg-enrailinfrastructuur. Final report COB committee L500. CUR / COB, Gouda.
- [15] Schanz, T., Vermeer, P.A. & Bonnier, P.G. (1999). The hardening soil model: Formulation and verification. *Beyond 2000 in Computational Geotechnics.* Balkema, Rotterdam, ISBN 90 5809 040 X”.
- [16] Brinkgreve, R.B.J. et. al. (2002). Plaxis 2D Version 8. A. A. Balkema Publ., Lisse, Abingdon, Exton (PA), Tokyo.
- [17] Janbu, N. (1963). Soil compressibility as determined by oedometer and triaxial tests. European conf on soil mechanics and foundation engineering. Wiesbaden, Germany. 1, 19-25.
- [18] Brinkgreve, R.B.J. et. al. (2001). Plaxis 3D Tunnel Version 1. A. A. Balkema Publ., Lisse, Abingdon, Exton (PA), Tokyo.
- [19] Marcher, T., Vermeer, P.A. & von Wolffersdorff, P.-A. (2000). Hypoplastic and elastoplastic modeling – a comparison with test Data, Proc. III. Euroconference on Constitutive Modeling of Granular Materials, Horton (Greece), S. 353–374, Springer-Verlag Berlin Heidelberg New York, 2000.
- [20] Kolymbas, D. (1985). A generalized hypoelastic constitutive law. Proceeding of International Conference on Soil Mechanics and Foundation Engineering. A. A. Balkema, Rotterdam; Brookfield
- [21] Gudehus, G. (1996). A comprehensive constitutive equation for granular materials. *Soils and Foundations.* 36 (1), 1-12.
- [22] Bauer, E. (1996). Calibration of a comprehensive hypoplastic model for granular materials. *Soils and Foundations.* 36 (1), 13-26.
- [23] Herle, I. (2008). On basic features of constitutive models for geomaterials. *Journal of Theoretical and Applied Mechanics.* Sofia, 38, Nos 1-2, 61-80.
- [24] Bom, L.B.T. & Modaressi-Farahmand-Azavi, A. (2014). Constitutive model for granular materials considering grain breakage in finite deformations. *European Journal of Environmental and Civil Engineering.* 20, 971-1003. <https://doi.org/10.1080/19648189.2014.960101>.
- [25] Kolymbas, D. (1999). *Introduction to hypaplasticity.* - *Advances in Geotechnical Engineering and Tunnelling.* CRC Press, London.
- [26] Lanier, J., Caillerie, D., Chambon, R., Viggiani, G., B´esuelle, P. & Desrues, J. (2004). A general formulation of hypoplasticity. *International Journal for Numerical and Analytical Methods in Geomechanics.* 28, 1461–1478.
- [27] Anaraki, K. E. (2008). Hypoplasticity investigated parameter determination and numerical simulation. MS Thesis, Delft University of Technology, Delft.
- [28] Masin. D. (2010). Hypoplasticity for practical applications – PhD course. <http://web.natur.cuni.cz/uhigug/masin/hypocourse>.
- [29] Mašin, D. (2015). Hypoplasticity for Practical Applications Part 4: Determination of material parameters course on hypoplasticity Zhejiang University, June 2015.

- [30] Engin, H.K. & Jostad, H.P. (2014). On the modelling of grain crushing in hypoplasticity. Numerical Methods in Geotechnical Engineering – Hicks, Brinkgreve & Rohe (Eds), 2014 Taylor & Francis Group, London, 978-1-138-00146-6.
- [31] Von Wolffersdorff, P.A. (1996). A hypoplastic relation for granular materials with a predefined limit state surface. *Mechanics of Cohesive-Frictional Material. 1*, 251-271.
- [32] Atkinson, J., Richardson, D., & Stallebrass, S. (1990). Effect of recent stress history on the stiffness of overconsolidated soil. *Geotechnique. 40*, 531-540.
- [33] Puzrin, M. & Burland, J. (1998). Non-linear model of small strain behavior of soils. *Geotechnique. 48*, 217-233.
- [34] Mayer, P.-M. (2000). Verformungen und Spannungsänderungendurch Schlitzwandherstellung und Baugrubenaushub. Veröff. Inst. Boden- u. Felsmechanik, Universität, Fridericiana Karlsruhe 2000, H.151.
- [35] Moller, S.C. (2006). Tunnel induced settlements and structural forces in linings. PhD Thesis, Universität Stuttgart.
- [36] Gudehus, G. (2004). Prognosen bei Beobachtungsmethoden, *Bautechnik. 81* (1), 1–8.
- [37] Bakker, K.J., van Schelt, W. & Plekkenpol, J.W. (1996). Predictions and a monitoring scheme with respect to the boring of the Second Heinenoord Tunnel. In: Geotechnical aspects of underground construction in soft ground, (eds: R.J.Mair and R.N. Taylor). Balkema, Rotterdam. 459-464.
- [38] Möller, S.C. & Vermeer, P.A. (2008). On numerical simulation of tunnel installation. *Tunnelling and Underground Space Technology. 23*, 461–475.
- [39] Bakker, K.J. (2000). Soil Retaining Structures; development of models for structural analysis. Dissertation (Delft University of Technology). Balkema, Rotterdam.
- [40] Herle, I. & Gudehus, G. (1999). Determination of parameters of a hypoplastic constitutive model from properties of grain assemblies. *Mechanics of Cohesive Frictional Materials. 4*, 461–486.

Theoretical Analysis on Reinforced Concrete Bridge from Non-linear Temperature Effect

Michal Tomko^{1*}, Ivo Demjan¹

¹Technical University of Košice, Slovakia
Civil Engineering Faculty, Institute of Structural Engineering
*e-mail: michal.tomko@tuke.sk

Abstract

The paper presents a theoretical analysis that models the effects of temperature load induced on a two-pole, two-box reinforced concrete bridge. Implemented was theoretical analysis of thermodynamic effects, which was performed on a closed double-box reinforced concrete bridge structure. The modelling and analysis only considered the upper part of the load-bearing bridge structure. This type of bridge was selected to present the results of this study which analysed the worst effects of temperature acting on the bridge structure.

Keywords: bridge, modelling, temperature

1 Introduction

In recent years, increased attention has been paid to professional public law consistent with the modelling of structures and the effects of operating loads. The aim of this paper is that the knowledge gained from the study will be subsequently applied to future design methodology, regulations, and standards [1, 2].

It can be stated that in the case of large bridge structures, the effect of accidental long-term effects becomes a decisive factor in the dimensioning of the bridge. A self-targeted analysis of individual load effects presupposes a good overall design of the bridge from a combination of individual effects. At present, social practice has required a more accurate analysis of the effects of climate change, especially the recent effects of temperature changes, etc., [3, 4, 5, 6, 7, 8, 9, 10, 11, 12].

In this case, a theoretical analysis was performed focused on a reinforced concrete closed two-chamber bridge object loaded by the effects of temperature. Only the supporting structure of the upper part of the bridge was modelled and analysed. The choice of the type of bridge object was chosen so that the presented results of this study analyse the most unfavourable effect of temperature on the bridge object in question.

2 Concrete Chamber Beam

The hollow chamber cross-section is characterized by torsional rigidity even at large spans, it is economical in terms of reinforcement consumption, but in terms of production, they are more laborious than slab bridges. The construction height of the bridge deck is always greater than with slab bridges. The chamber cross-section provides a very good possibility of use as a deck bridge, but the precondition is to achieve sufficient rigidity, i.e., non-deformability of the cross-section above the support because the cross brace cannot be realized. All load-bearing parts of chambered concrete bridges are monolithically connected, i.e., they form one unit. The most accurate picture of the stress at any point in the bridge is obtained when the structure is considered as a whole.

3 Heat Transfer in the Bridge Structures

When solving a specific calculation of a bridge structure subjected to temperature effects, an appropriate analysis of the suitability of the use of a particular method, procedure and simplifying assumptions must be preceded. The standard [13] provides guidance for determining the load of buildings and civil engineering works due to the effects of temperature resulting from climatic and operating conditions. The standard gives alternative procedures, values, and recommendations for classification in cases marked with a note stating that a national selection may be made, i.e., a national annex. In the case of bridges, the national annex specifies whether general non-linear or simplified linear temperature components are used in the design calculations. The standard [13] is intended for use in conjunction with EN 1990, other parts of EN 1991 and EN 1992 to 1999 for structural design. In standards [13, 14, 15], a one-dimensional linear vertical temperature drop of heat propagation along the cross-sectional height of the bridge structure is considered, which is sufficient in certain cases. For important buildings, the model is not satisfactory, and a non-linear (linearization by parts) vertical temperature drop of heat propagation along the height of the cross-section of the bridge object is recommended.

The standard [13] considers heat dissipation only in the cross-sectional plane of the bridge structure, i.e., in general, it can be stated that this is a dominant effect of temperature. In the presented study, the propagation of heat is considered even along the length of the bridge structure, which more realistically represents the actual effect of temperature.

In the walls of a closed chamber concrete profile, which is a static indeterminate element, the temperature drop depends on the individual temperatures between the outer and inner sides of the wall and on the interconnection of the individual walls. Standard EN 1991-1-5 states in the article:

6.1.4.4 Components of the temperature gradient in the walls of a concrete chamber beam

(1) When designing large concrete chamber bridges, it is necessary to pay attention to the possible occurrence of significant temperature differences in such structures between the inner and outer walls.

The bridge structure has two poles with a length of individual fields of 63.0 m and is placed on two sliding supports and one pinned support (Figure 1). The supporting structure of the bridge consists of a closed profile (Figure 3).

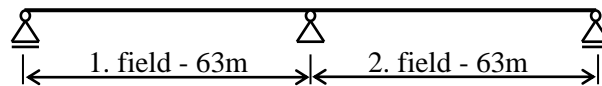


Figure 1: Schematic representation of a bridge object

In the ANSYS program, a FEM model of the bridge structure was created, and a temperature analysis was performed, which was focused on two-dimensional heat transfer in the bridge structure. The heat distribution obtained the heat dissipation along the thickness of the individual walls of the closed cross-section and along the length of the bridge structure. The values of the temperatures around the circumference, i.e., on the walls, the loaded individual profiles of the bridge structure are taken from the standard [13].

The course of temperatures after the cross-section was subsequently transformed into a loading state, ie. the bridge object was burdened by the effects of temperature. The bridge object model was analyzed by "structural stress thermal FEM analysis". Transformations, relative deformations, and stresses were observed in the "structural stress thermal FEM analysis" of the two-pole bridge.

The FEM model of the bridge structure consisting of a closed single-chamber profile is created in the ANSYS program and has 38 123 elements, the BRICK SOLID 70 volume element used (Figure 2).



Figure 2: FEM bridge model

The effects of two-dimensional temperature propagation in the construction of a bridge formed by a closed profile were considered in three variants:

- 1) the temperature drop is considered only in the vertical direction - warming (Figure 3);
- 2) the temperature drop is considered only in the vertical direction - cooling (Figure 8);

3) the temperature drop is considered in the vertical and horizontal direction - warming (Figure 11).
Some results of the temperature analysis are shown in Figure 3 to Figure 15.

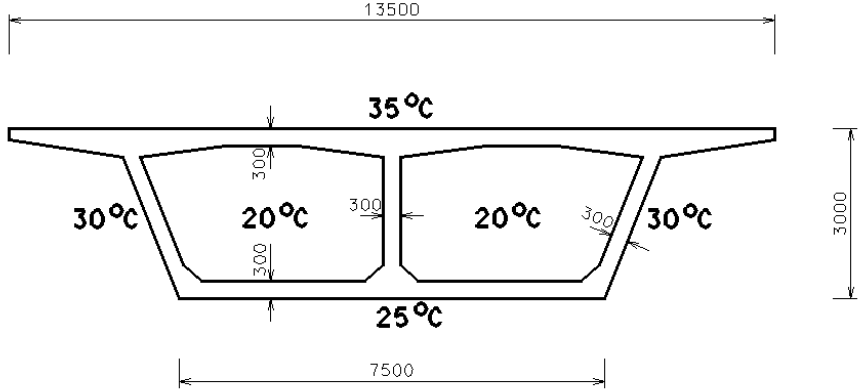


Figure 3: Cross-section of the bridge (cross-section), heating in the vertical direction

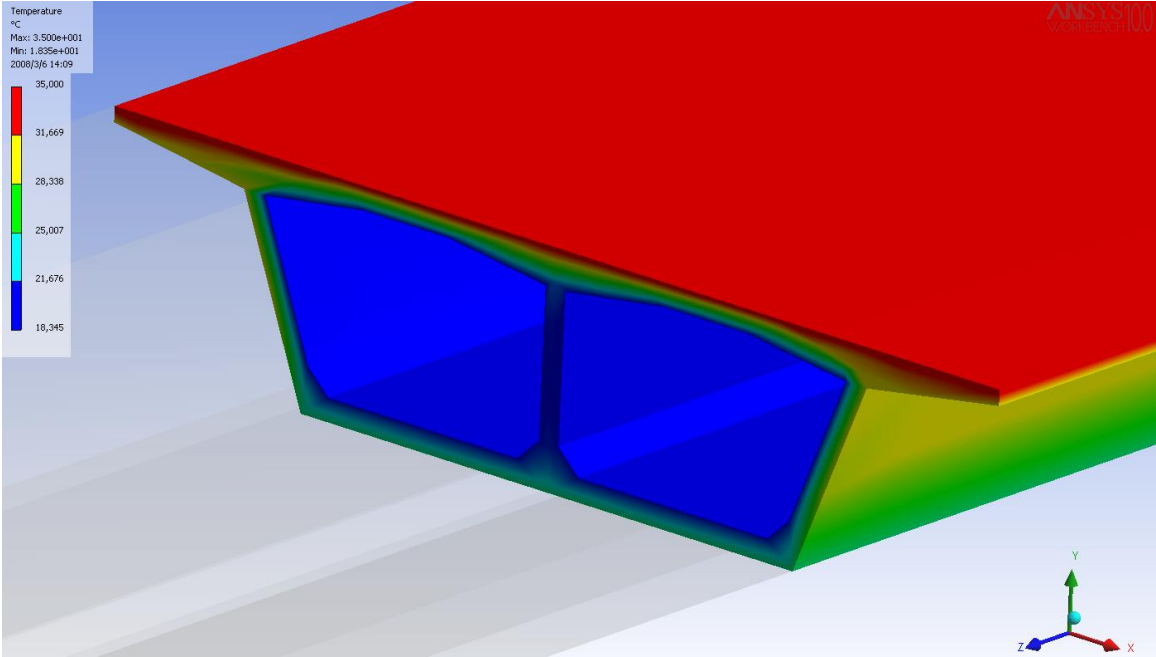


Figure 4: Heat transfer through the cross-section of the bridge (in the middle of the 2nd field), warming in the vertical direction

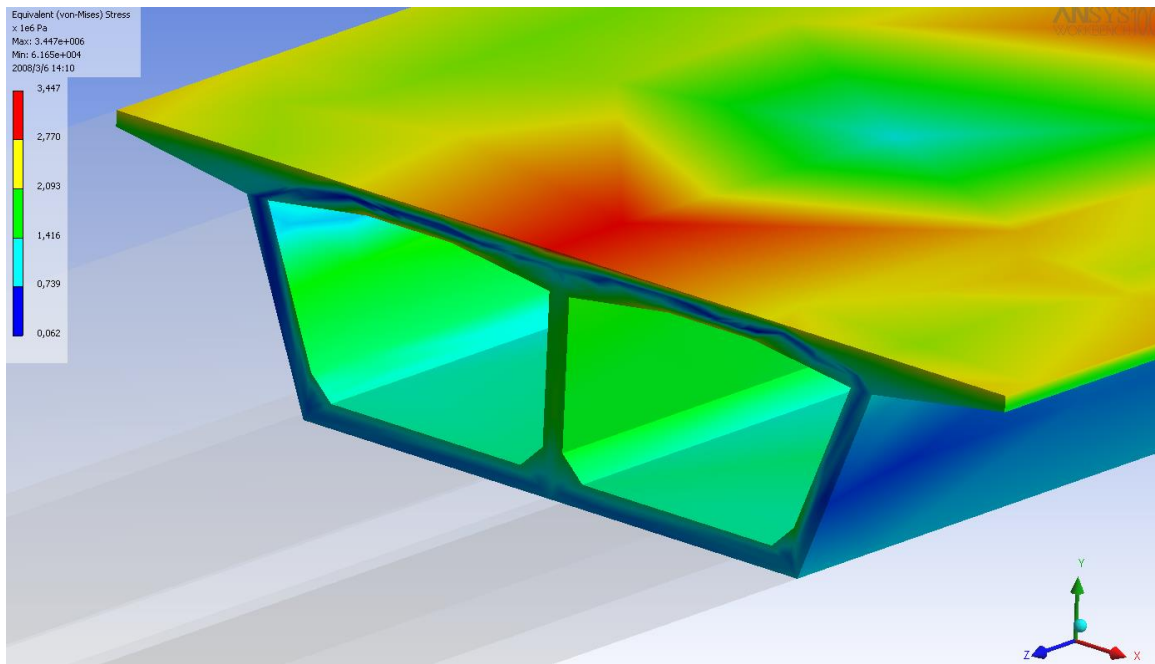


Figure 5: Equivalent stress corresponding to the applied thermal effect (in the middle of the 2nd field)

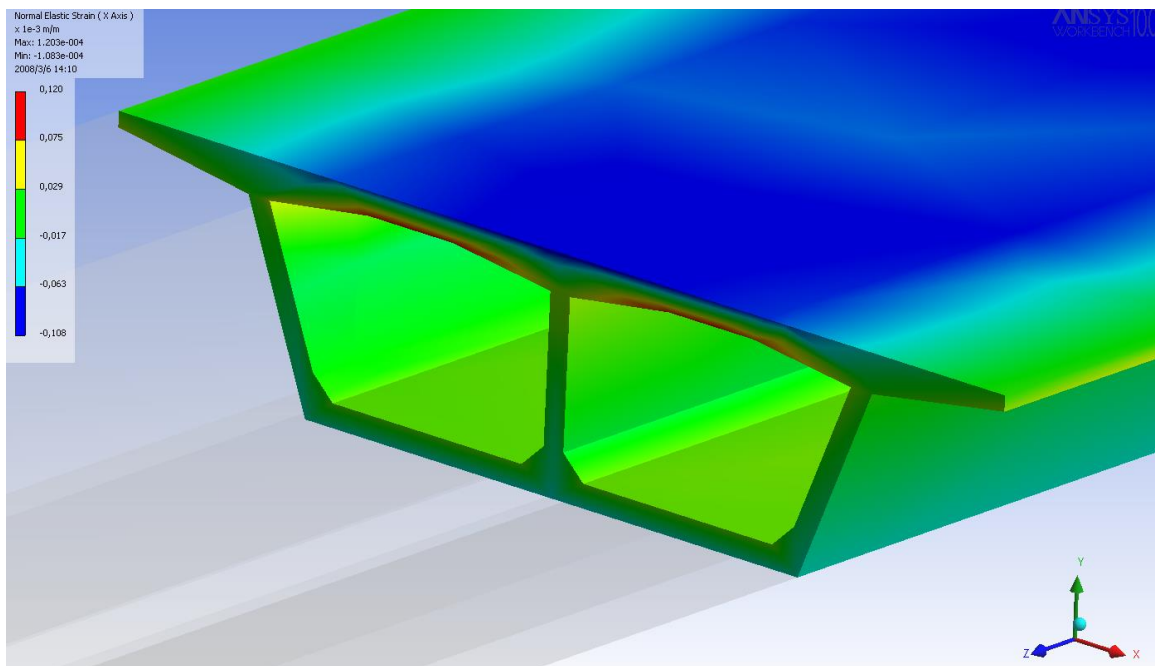


Figure 6: Deformation of the bridge (δ_z [mm]) in the direction of the Z axis (in the middle of the 2nd field)

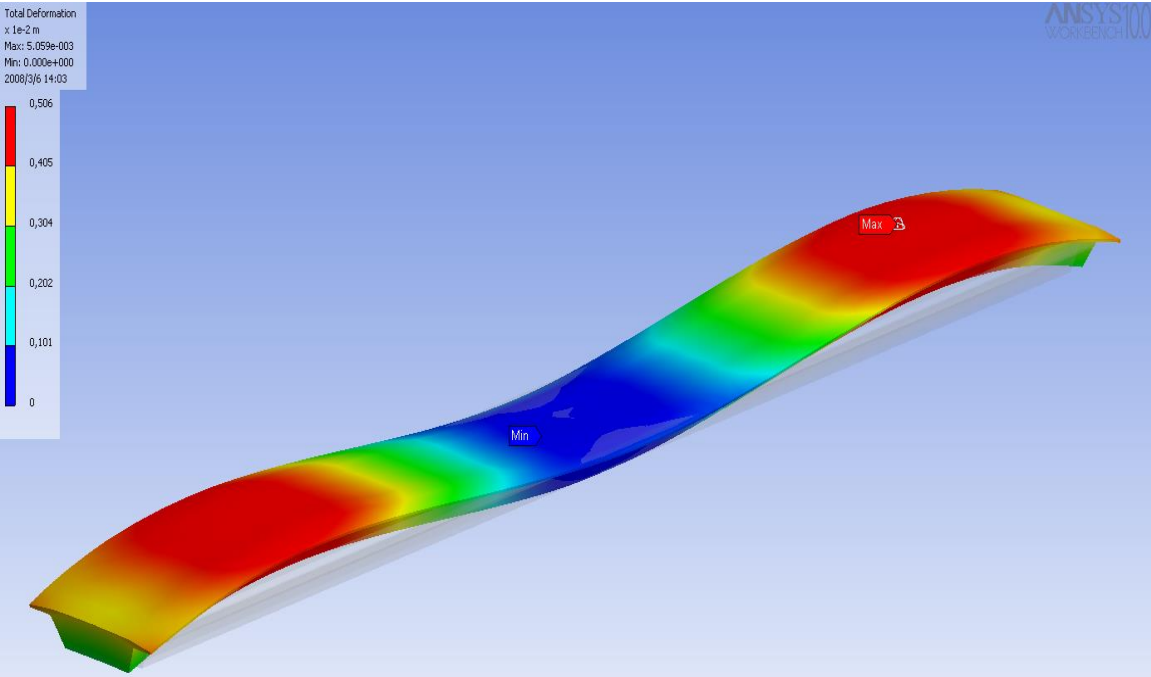


Figure 7: Total deformation of the bridge

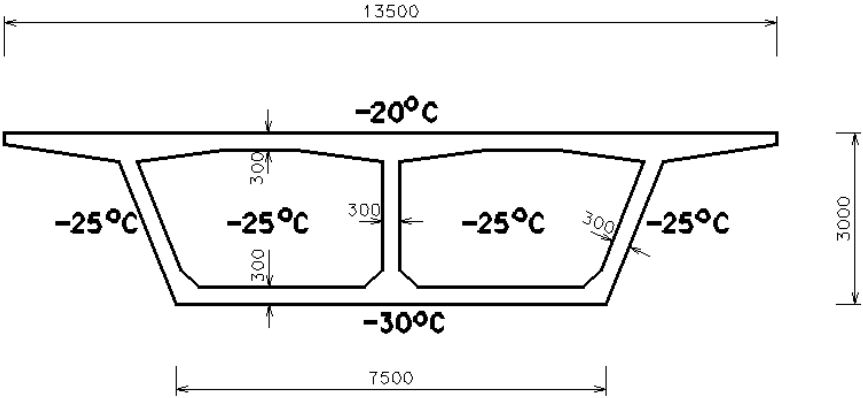


Figure 8: Cross-section of the bridge (cross-section), cooling in the vertical direction

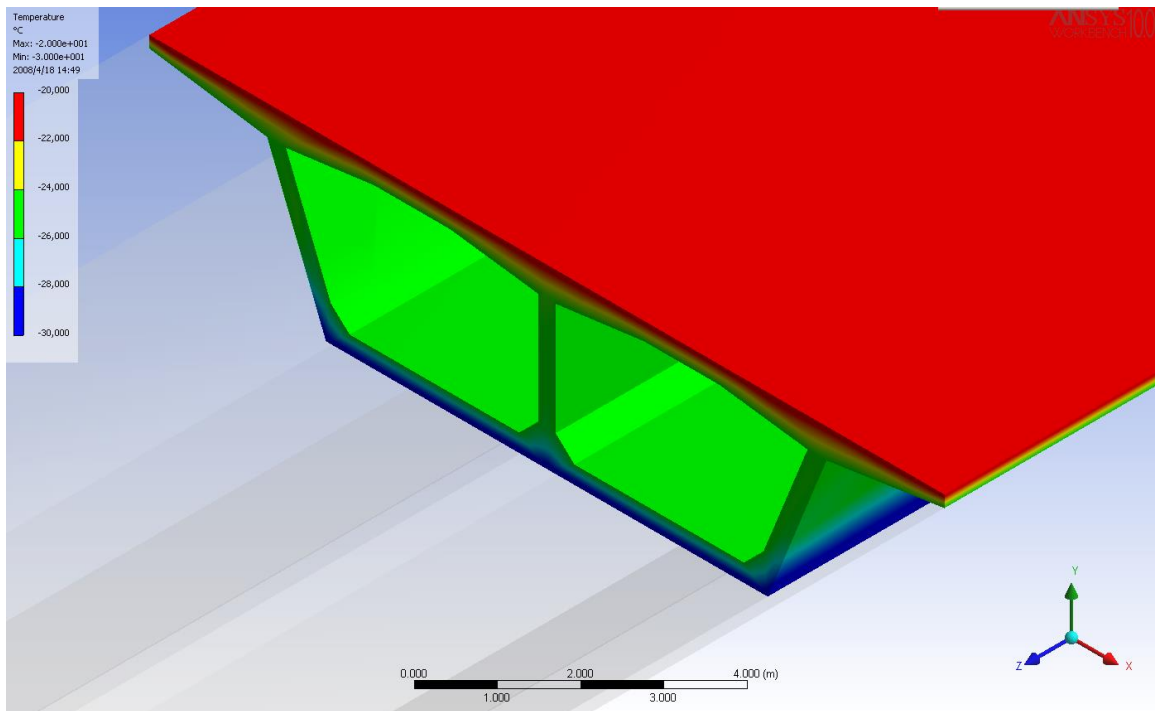


Figure 9: Heat transfer through the cross-section of the bridge (in the middle of the 2nd field), cooling in the vertical direction

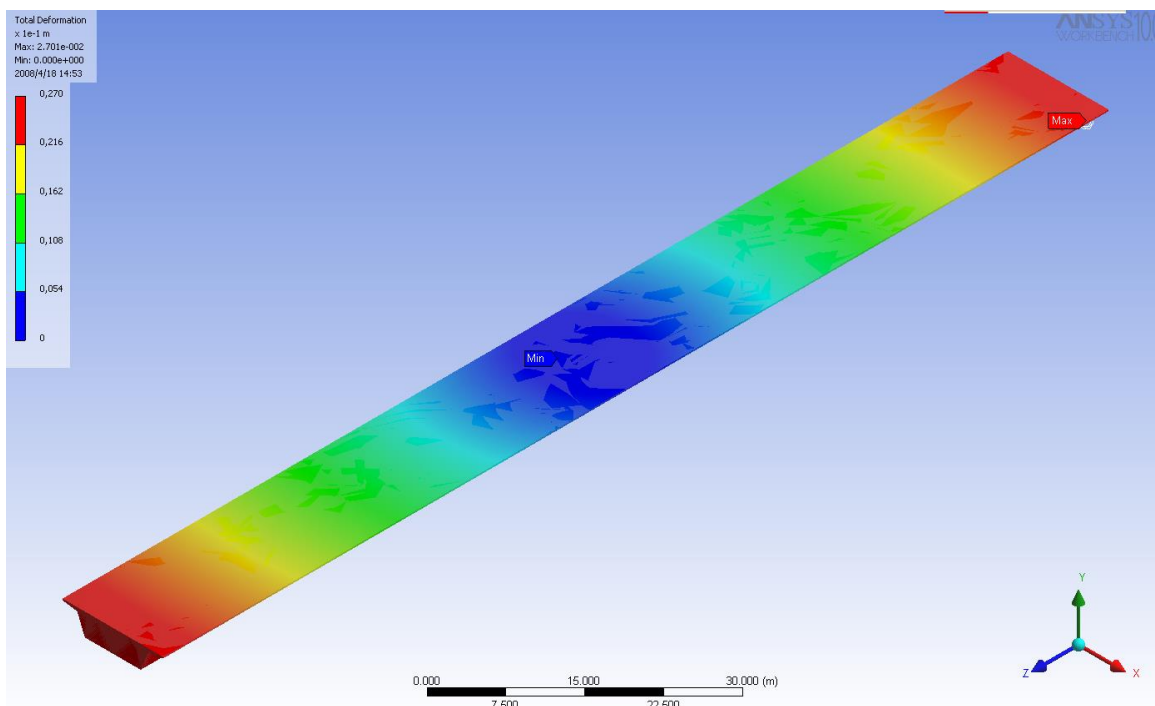


Figure 10: Total deformation of the bridge

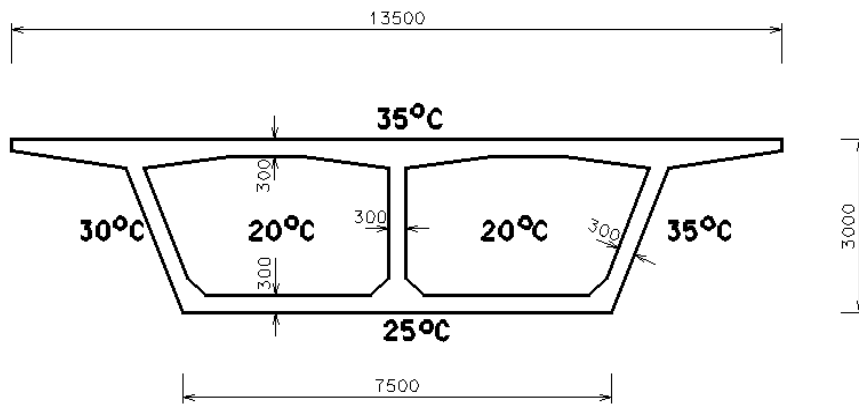


Figure 11: Cross-section of the bridge (cross-section), vertical and horizontal warming

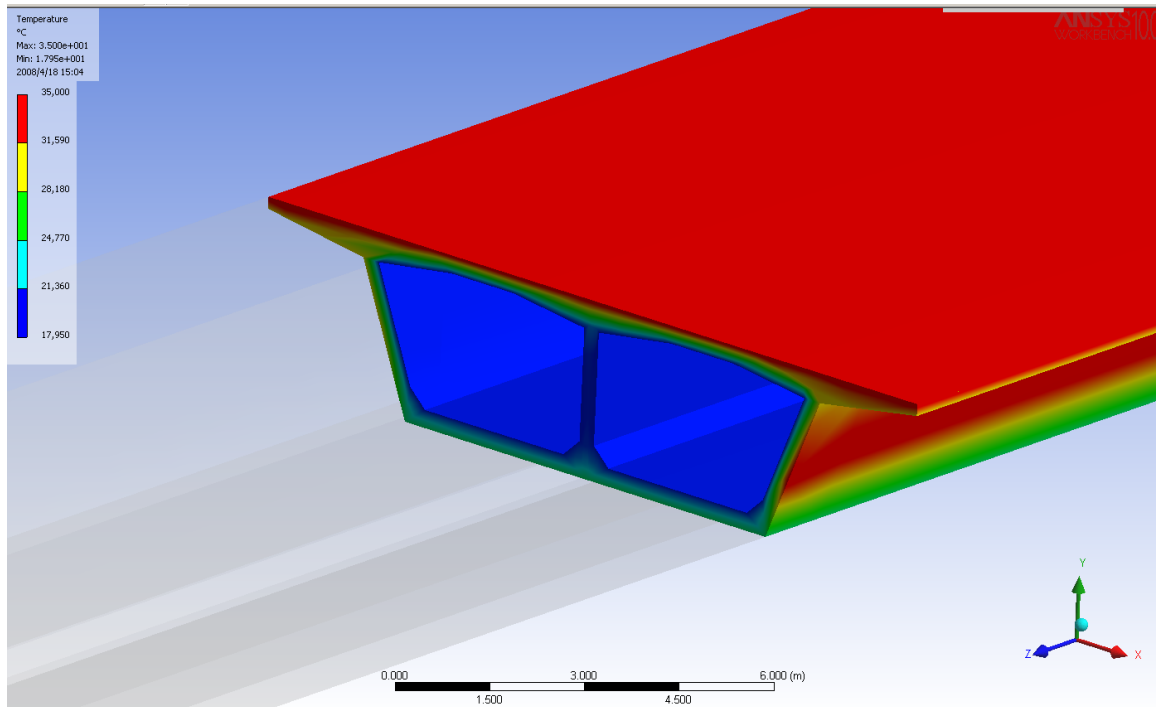


Figure 12: Heat transfer through the cross-section of the bridge (in the middle of the 2nd field), vertical and horizontal warming

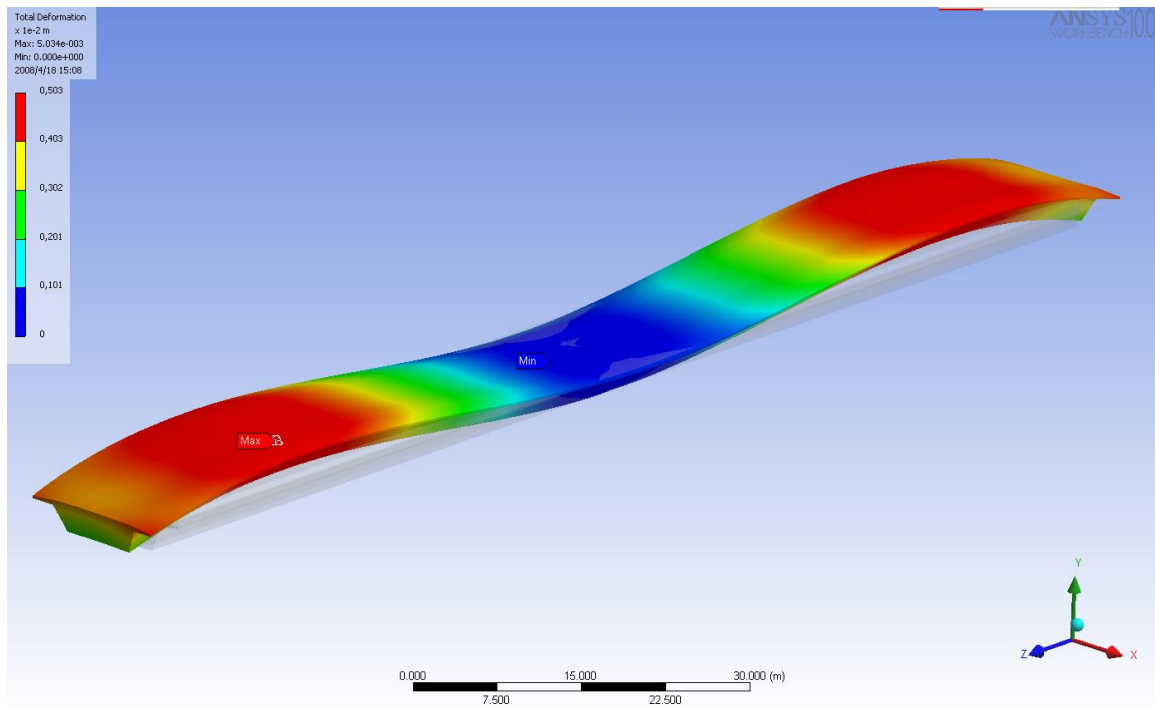


Figure 13: Total deformation of the bridge

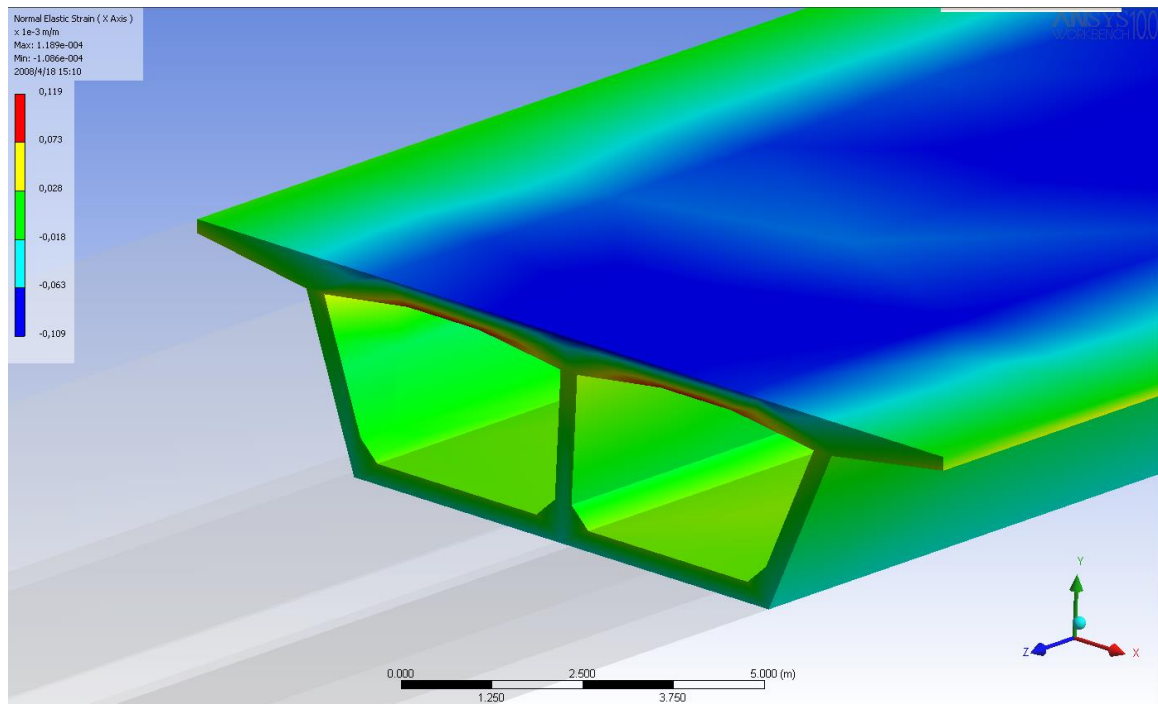


Figure 14: Relative deformation of the bridge (δ_x [mm]) in the direction of the X axis (in the middle of the 2nd field)

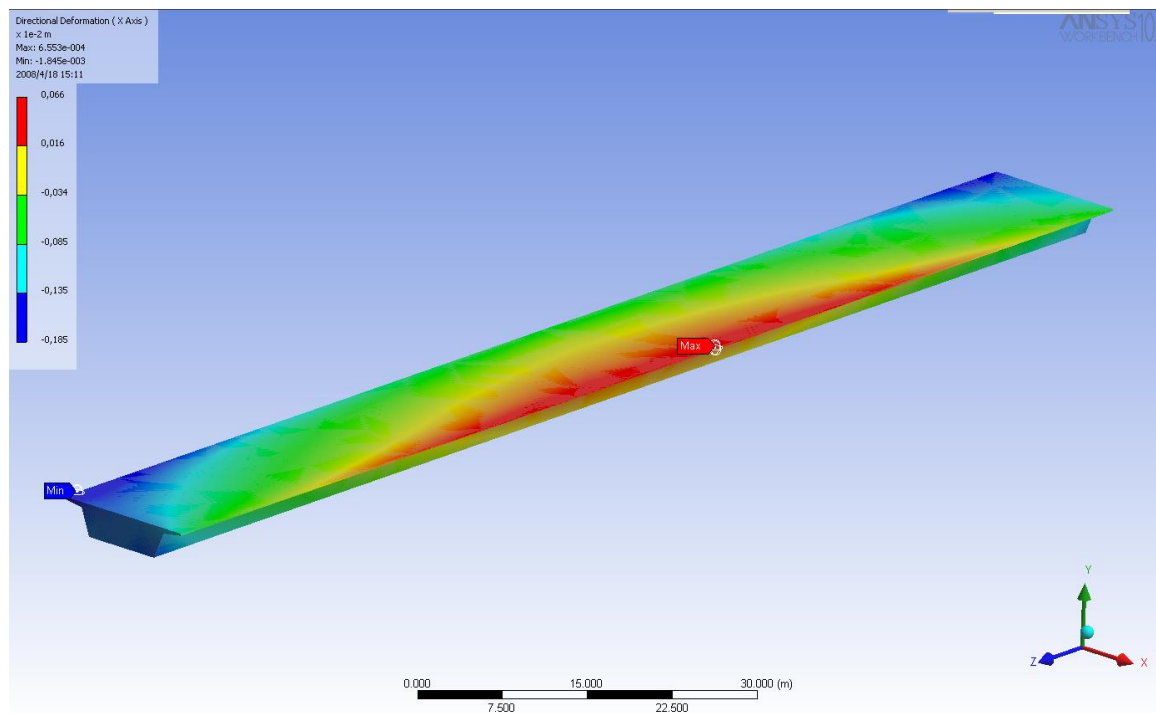


Figure 15: Deformation of the bridge (δ_x [mm]) in the direction of the X axis

4 Analysis of the Results

Deformations, relative deformations, and normal stresses were observed in the "structural stress thermal FEM analysis" of a two-pole two-chamber bridge. In the standard [15], the load effect from the influence of temperature is defined in only one direction, ie. linear action of the temperature effect in the axis of the wall of the chamber bridge, Figure 16. The temperature acting in the axis of the circumferential walls of the closed chamber bridge for the individual temperature effects is shown in Figure 17.

The results of the "structural stress thermal FEM analysis" of two-dimensional heat dissipation of a two-pole bridge with a two-chamber cross-section are compared with the values given in [13]. The presented results of heat dissipation point to temperature differences in individual points in the range of 2.6 ~ 25%.

When considering the effect of temperature in two dimensions, the temperature drop is considered in the vertical and horizontal directions, there is also a horizontal bending effect in the horizontal plane of the bridge object, which acts on the walls of the profile of the closed chamber beam. From the presented results it is clear that the nonlinear effect of temperature propagated in two directions affects the normal stresses and deformations in the bridge structure. This fact should be taken into account when designing a bridge structure, especially for massive bridge structures with a larger span of fields.

For large-span chamber bridges, additional conditions and influences need to be considered, which may ultimately affect the results to some extent. The environmental conditions (air temperature, solar radiation, radiation emitted from the bridge structure, wind speed), the structural arrangement of the bridge (geometric characteristics, method of laying the bridge

(statically definite/indeterminate, continuous girder, etc.)) have the greatest influence on the bridge temperature, the shape of the bridge (directional guidance of the bridge straight, in the arch, etc.), used material of the bridge, etc.

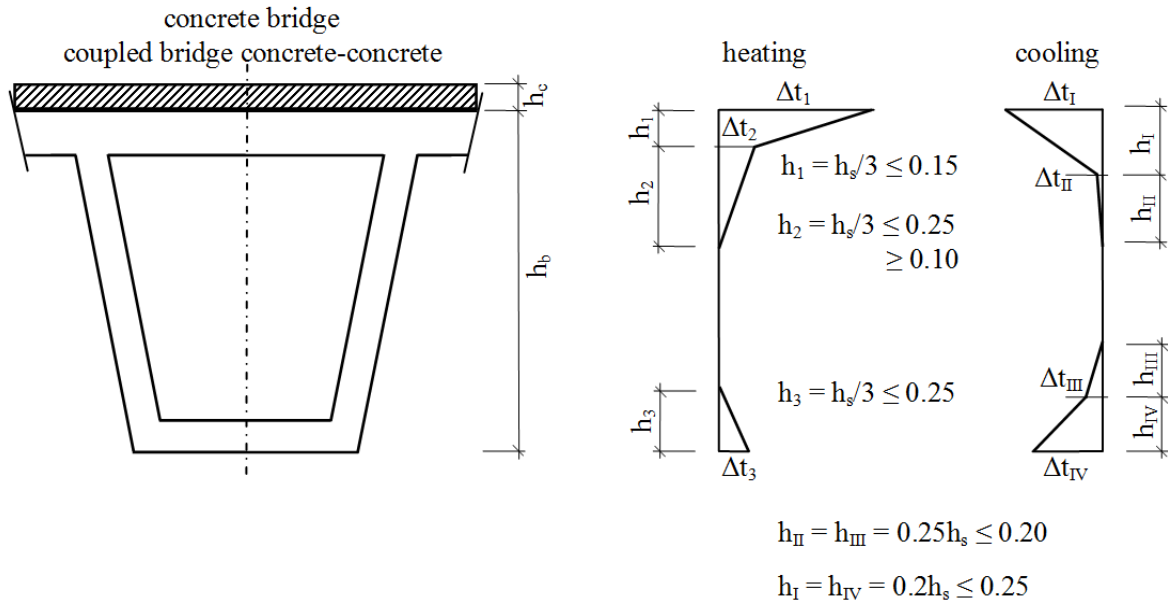


Figure 16: One-dimensional heat dissipation in a concrete chamber beam according to standard [15]

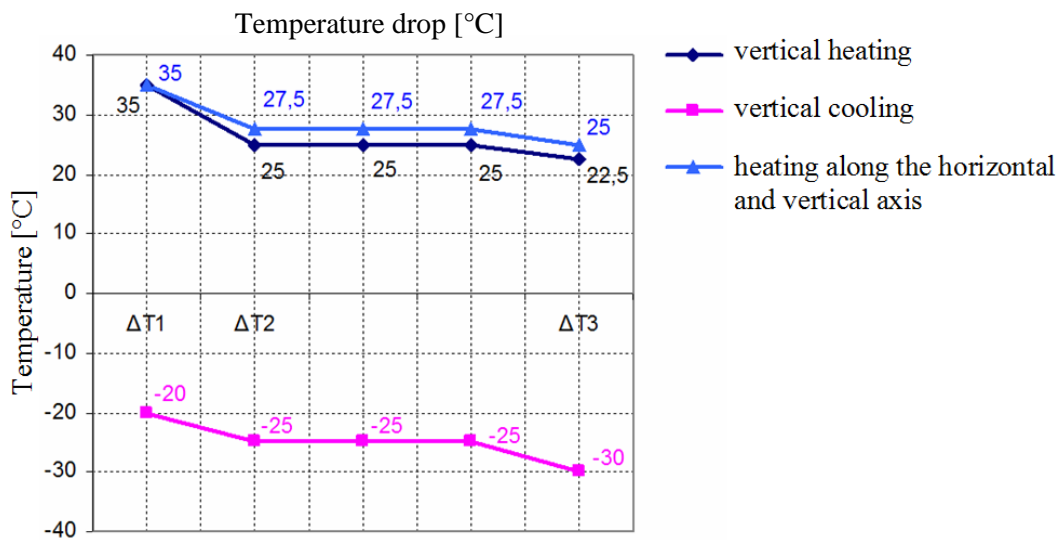


Figure 17: Temperature acting in the axis of the walls of the chamber concrete bridge

5 Conclusion

The basic precondition for a good evaluation of the influence of temperature on a bridge object is knowledge of the nature of thermal effects, values of the magnitudes of the acting temperature, structural-physical and physical-mechanical properties of the bridge structure, i.e., parameters that should also be included in the theoretical calculation model. The real behavior of the bridge structure should reflect the theoretical response of the computational model. At present, in professional publications as well as in international standards, it is recommended to perform calculations of significant structures on a spatial model, taking into account the actual decomposed mass, the rigidity of the building and the actual load in space. The deformation and stress characteristics of the chamber reinforced concrete beam calculated by the theoretical approach from the effect of temperature are influenced by the method of thermal load simulation, the choice of the calculation model, but also by the conditions of the model placement.

For practical needs, it would be appropriate to extend the described theoretical procedures for modeling the temperature effect on a two-chamber bridge structure to other types of bridge structures and their computational models. Based on the above, it can be stated that the presented procedures and the achieved results of the simulation of nonlinear modeling of the effect of the temperature effect on the bridge provide useful information for technical construction practice.

Acknowledgements

This work was supported by The Slovak Research and Development Agency under the contract No. APVV-15-0777 and by The Slovak Scientific Grant Agency under the contract No. VEGA 1/0129/20.

References

- [1] Kvočák, V. & Dubecký, D. (2013). Experimental stiffness verification of composite beams (ASEM 13). In *Advances in Structural Engineering and Mechanics*. World Congress on Advances: International Convention Center Jeju, Jeju. Techno-Press. p. 3171-3178. ISBN 978-89-89693-37-6.
- [2] Kvočák, V., Dubecký, D., Kocúrová, R., Beke, P. & Al Ali, M. (2014). Evaluation and analysis of bridges with encased filler beams. In *Civil Engineering and Urban Planning 3: Proceedings of the 3rd International Conference on Civil Engineering and Urban Planning: CEUP 2014: Wuhan, China*. London: Taylor and Francis Group, p. 150-153. ISBN 978-1-138-00125-1.
- [3] Yun, L., Jiantao, W. & Jun, C. (2014). Mechanical properties of a waterproofing adhesive layer used on concrete bridges under heavy traffic and temperature loading. *International Journal of Adhesion and Adhesives*. 48, 102-109.
- [4] Kyong-Ku, Y. & Pangil, C. (2014). Causes and controls of cracking at bridge deck overlay with very-early strength latex-modified concrete. *Construction and Building Materials*. 56, 53-62.
- [5] Si, X. T., Francis Au, T. K. & Li, Z. H. (2013). Capturing the long-term dynamic properties of concrete cable-stayed bridges. *Engineering Structures*. 57, 502-511.
- [6] Pagani, R., Bocciarelli, M., Carvelli, V. & Pisani, M. A. (2014). Modelling high temperature effects on bridge slabs reinforced with GFRP rebars. *Engineering Structures*. 81, 318-326.

- [7] Giussani, F. (2009). The effects of temperature variations on the long-term behaviour of composite steel-concrete beams. *Engineering Structures*. 31 (10), 2392-2406.
- [8] Kovaľaková, M., Fričová, O., Hronský, V., Olčák, D., Mandula, J. & Salaiová, B. (2013). Characterisation of crumb rubber modifier using solid-state nuclear magnetic resonance spectroscopy. *Road Materials and Pavement Design*. 14 (4), 946-958. <https://doi.org/10.1080/14680629.2013.837835>
- [9] Mandula, J., Salaiová, B. & Kovaľaková, M. (2002). Prediction of noise from trams. *Applied acoustics*. 63 (4), 373-389. [https://doi.org/10.1016/S0003-682X\(01\)00047-0](https://doi.org/10.1016/S0003-682X(01)00047-0)
- [10] Wang, Z. C., Zha, G. P., Ren, W. X., Hu, K. & Yang, H. (2018). Nonlinear boundary parameter identification of bridges based on temperature-induced strains. *Structural Engineering and Mechanics*. 68 (5), 563-573. <https://doi.org/10.12989/sem.2018.68.5.563>.
- [11] Abdel-Fattah, M. T. & Abdel-Fattah, T. T. (2019). Behavior of Integral Frame Abutment Bridges Due to Cyclic Thermal Loading: Nonlinear Finite-Element Analysis. *Journal of Bridge Engineering*. 24 (5). [https://doi.org/10.1061/\(ASCE\)BE.1943-5592.0001394](https://doi.org/10.1061/(ASCE)BE.1943-5592.0001394)
- [12] Wedel, F. & Marx, S. (2022). Application of machine learning methods on real bridge monitoring data. *Engineering Structures*. 250, 113365. <https://doi.org/10.1016/j.engstruct.2021.113365>.
- [13] EN 1991-1-5 (2007). Eurocode 1: Actions on structures - Part 1-5: General actions - Thermal actions.
- [14] EN 1991-2-5 (2000). Eurocode 1: Actions on structures - Part 2: Traffic loads on bridges.
- [15] CSN 73 6203 (1986). Loads on bridges.

Deformation Properties of Stone Columns Back-calculated from Static Load Tests

Houman Soleimani Fard ^{1*}

¹ Keller - Middle East and Africa, PO Box 111323, Dubai, UAE

*e-mail: houman.fard@keller.com

Abstract

The stone column is a cost-effective, sustainable, and technically sound ground improvement solution for enhancing bearing capacity, minimizing settlement, and mitigating the liquefaction potential of a wide range of soils. In this study, the main methods of stone column execution are briefly explained, design approaches are discussed, and testing procedures are elaborated on in more detail. The results of plate load tests (PLT) are numerically simulated to back-calculate stone column properties. In this research, the Hardening Soil model (HS) is selected to simulate stone columns and soil profiles. The outcomes of this modelling and the adopted calculation approach are verified by three-zone load tests (ZLT) performed on grounds reinforced by stone columns in various projects. Reasonably good matches are observed between experimental and numerical results, approving parameters back-analyzed from PLTs and the employed calculation methodology. Finally, a widely used analytical approach of the calculation of stone columns (Priebe method) is compared with the numerical and experimental results of the studied ZLTs. The comparison confirmed that the Priebe method could practically calculate the settlement of grounds treated by stone columns although settlements were slightly higher than experimentally observed values. In the end, the advantages and limitations of each method are discussed.

Keywords: Stone Column, Plate Load Test (PLT), Zone Load Test (ZLT), Numerical Modelling, Hardening Soil Model (HS)

1 Introduction

The Vibro Stone Column technique, as one of the most widely implemented ground improvement solutions, consists of the installation of pile shape elements, usually made of gravel, into the natural subsoil to enhance the bearing capacity of the ground for low-rise buildings or road and transportation projects and to improve the shear strength parameters for slope stability purposes. Regarding the nature of the employed materials, stone columns are among environmentally friendly and cost-efficient solutions compared to the cementitious and/or reinforced alternative techniques. Stone columns are typically designed as per homogenization or unit cell approaches, considering equivalent parameters for the improved ground instead of considering them as individual columns [4], [13], [15], [16]. The most famous calculation method based on the unit cell approach was proposed by Priebe (1976) [17] and later updated and modified by [18], [19],[20], [21], [22]. Although for more complicated

conditions, it is recommended to simulate the ground improvement in the Finite Element Method (FEM) analysis (e.g., [1], [5], [7], [14], [23]). [30] optimized the design of stone columns using Monte Carlo simulation.

[8] and [29] modelled geotextile-encased sand columns. The latter studied the effect of column arrangement by modelling single and group columns and concluded that the structural performance of group columns is about 11% better than single columns.

The key factors for designing and calculating a stone column project are the improvement design (i.e., depth, diameter, and the spacing of stone columns), loading intensity and type, footing dimension and groundwater table, and stone column and soil properties. Except for stone column properties, all others are not highly complicated to measure or correlate from design or soil investigation reports. On the other hand, there have always been debates on the properties of stone columns among researchers and designers in the field of ground improvement and more importantly, on the stiffness of the executed columns.

The quality of stone columns is typically a function of the natural surrounding soils (among others); therefore, their geotechnical properties should always be deemed as site-specific parameters and -if possible- measured on the field to be able to conduct reliable, safe and as the same time cost and environmentally efficient design. Accordingly, this study aims to back-calculate the stiffness of stone columns (as the modulus of deformation) from numerous static load tests conducted on the top side of the stone columns. For this purpose, tests are numerically simulated using the FEM analysis and the results are compared to the field data. Finally, the material properties of stone columns together with the corresponding calculation approach are proposed and verified in the modelling of the large-scale loading tests in different projects. The Priebe method, as the most common calculation approach for stone columns, is evaluated and compared with the FEM method.

2 Vibro Replacement (VR)

Vibro replacement technique (VR) or stone column installation is widely employed to improve the bearing capacity, control settlement, and mitigate liquefaction susceptibility. In many practical projects, VR has been accepted as a cost-effective and time-efficient alternative to piling where loads and/or structural requirements are in a moderate range. Moreover, VR is a sustainable and environmentally-friendly product since no cement or steel is required in the production process.

Two main technologies exist for installing stone columns, namely top- and bottom-feed methods (sometimes referred to as wet or dry methods, respectively). The methods are schematically shown in Figure 1.

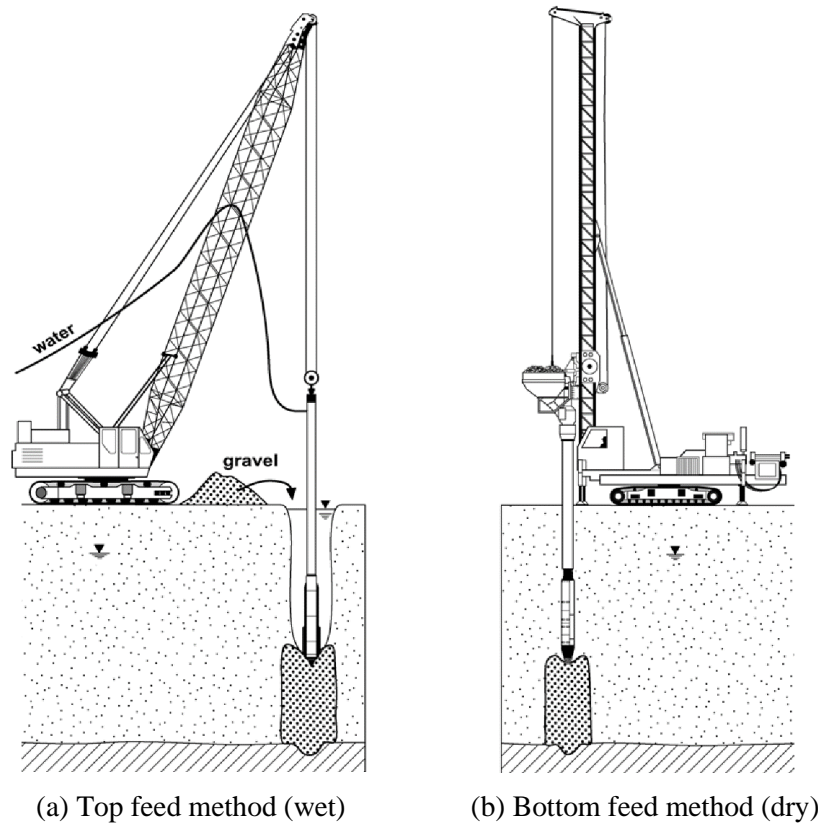


Figure 1: Stone column installation methods [11]

In the wet method, a depth vibrator (a long heavy tube shape equipped with eccentric weights driven by an electric motor connected to power and water sources) is suspended from a crane. The vibrator penetrates the ground using electric power and a high-pressure jet of water. By vibration and high water jet pressure, the soil surrounding the vibrator is liquefied assisting in penetration and creating a cavity around the vibrator and its holding tube. The cavity is then filled with aggregates while the vibrator is at its maximum depth. Next, the stone column is formed in steps in which the aggregate is laterally pressed into the soil by pushing the vibrator downward.

Regarding the dry process, the vibrator and the extension tube are equipped with a channel through which aggregates can reach the tip of the vibrator by the pressurized air. When the vibrator is penetrated down to the design depth, the aggregates are fed into a funnel and transported through the channel. During the withdrawal steps, aggregates run from the vibrator tip into the created annular space and then are compacted and pressed into the surrounding soil during the following re-penetration step.

2.1 Priebe Method

The design procedure proposed by [20] is widely accepted for the analysis of stone columns in which the unit cell approximation is implemented. In this method of calculation, a single cell out of the grid is considered, comprising the column and its associated tributary surrounding soil that is closely approximated as an equivalent circle having the same total area whether

having a triangular or rectangular pattern (Figure 2). Other assumptions of the Priebe method are as follows: the column is based on a rigid layer, the column material is incompressible, and the unit weight of the column and the soil is negligible.

If stone columns are installed on a relatively large area with uniform spacing, the unit cell approach of Priebe can be employed to estimate the settlement of foundations constructed over the treated area.

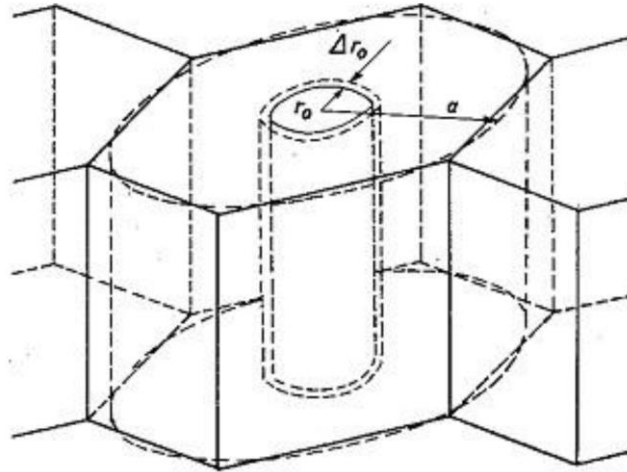


Figure 2: Unit cell of an infinite triangular grid. Source: [17]

The volume of the in situ soil replaced by the stone column within a unit cell can be quantified by the area replacement ratio a_s , which is defined as the ratio of the area of the stone column after execution (A_c) to the total area within the unit cell (A) (Equation 1).

$$a_s = A_c/A \quad (1)$$

When the stone column reinforced ground is loaded, the stress further concentrates in the column, leading to a reduction in stress in the surrounding less stiff soil. The distribution of the vertical stress within a unit cell can be expressed by a stress concentration factor (n_0), which is defined as the ratio of the stress in the stone column (σ_c) to the stress in the surrounding soil (σ_s). The magnitude of the stress concentration depends on the relative stiffness of the stone column and the surrounding soil. In typical stone column projects, the value of n_0 generally lies between 2 and 6. The stress concentration factor increases with the time of consolidation. For a given n_0 value, the stress on the surrounding soil can be determined by Equation 2:

$$\sigma_t = \sigma_c a_s + \sigma_s (1 - a_s) \quad (2)$$

where σ_t is the total stress, σ_c and σ_s are the stresses in the stone column and the surrounding soil, respectively, and a_s is the replacement ratio.

The improvement of the soil relies on the assumption that the column material shears from the beginning, whereas the surrounding soil behaves elastically. The soil displacement due to column installation occurs to the extent that the coefficient of earth pressure (K_s) equals 1.0. Assuming a Poisson's ratio $\nu = 1/3$, the improvement factor (i.e., the ratio of settlement with and without a column) is represented by Equation 3 and in Figure 3:

$$n_0 = 1 + \frac{A_c}{A} \left[\frac{5 - \frac{A_c}{A}}{4K_{ac}(1 - \frac{A_c}{A})} - 1 \right] \quad (3)$$

where K_{ac} denotes the coefficient of active Earth pressure calculated as $\tan^2(45^\circ - \varphi_c/2)$ and φ_c is the internal friction angle of stone columns. The improvement factor is plotted versus the inverse area ratio (A/A_c) in Figure 3.

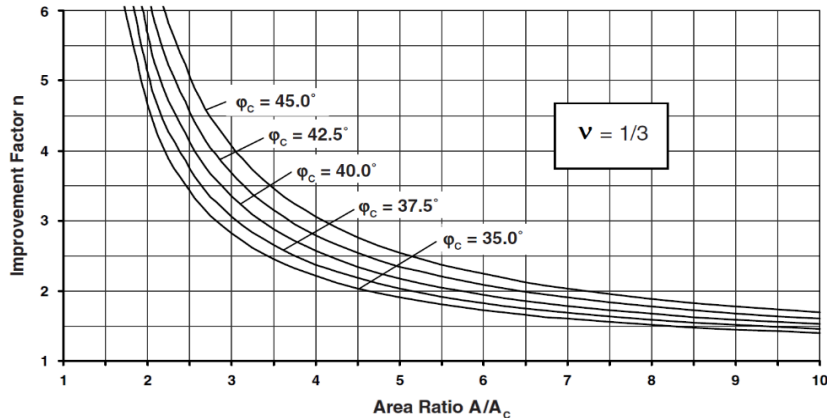


Figure 3: Design chart for Vibro replacement. Source: [20]

The method was later improved for taking into account the compressibility of stone columns, the depth factor (the weight of the soil and the column), and foundations with limited dimensions. Interested readers can refer to [17], [18], [20], [21], [22] for further detail on the Priebe approach. [6] discussed the limitations of the Priebe method and compared the results with other approaches in three-stone-column projects.

3 Static Load Tests

3.1 Plate Load Test (PLT)

The most common confirmatory measure for controlling the quality of stone columns is PLT, in which the stone column shall be concentrically loaded using a plate of at least 25 mm thickness and 152-762 mm in diameter (Figure 4). The applied load and the plate settlement should be measured with a load cell and at least three deflection transducers (or dial gauges) uniformly installed around the plate and fixed on datum beams. Depending on the load level, a heavy vehicle or kentledge with enough dead load can be used as a counterweight. Additionally, the applied load can be in the range of 100-200% of the foundation working load and the test may contain more than one cycle of loading/unloading if necessary. The details of PLT are provided in ASTM D 1195 [2].



Figure 4: Plate load tests on stone columns

PLT results can be interpreted and converted to the modulus of elasticity of the stone column in different ways, typically as per the elastic deformation theory with Boussinesq approximation, Equation 4, or similar classic elastic methods:

$$E' = \frac{qBI(1-\nu^2)}{S} \quad (4)$$

where S , q , B , I , ν and E' are monitored settlement, applied load, plate diameter, influence factor (for circular footing $\pi/4$), the Poisson ratio, and the modulus of the elasticity (Young modulus) of the tested stone column, respectively.

One of the fundamental assumptions of the above-mentioned methods is that the ground is semi-infinite, homogeneous, and elastic while the VR-treated ground is a composite system consisting of the stone column surrounded by the in situ soil which makes the Boussinesq theory theoretically inapplicable. Moreover, deeper parts of the stone column are expected to demonstrate higher stiffness compared to shallower parts since the lateral confining pressure increases by depth.

Despite these shortcomings and limitations, this method, thanks to its simplicity, is widely used in the interpretation of PLT results, which is practically accepted by many engineers. However, more accurate material properties should be employed for projects with sensitive applications or complicated conditions.

3.2 Zone Load Test (ZLT)

In the ZLT, a squared footing of 1×1 to 4×4 m (rarely larger) is usually loaded for observing the settlement process of a shallow foundation of similar size and load. The footing is typically loaded by a hydraulic jack pushing the footing against a counterweight or kentledge beams that are fixed on reaction piles. The maximum load can be 100-250% of the design load. It is recommended to apply the load in steps not larger than 25% of the maximum load. Similar to the PLT, the applied load and the resulting deformation are measured with a load cell and deflection transducers. The stress distribution in the ground depends on the interaction between the footing and the ground, along with the subsoil profile.

In the case of the homogenous ground, the elasticity theory, with the assumptions of Equation 4, is often used to illustrate the settlement and stress distributions in the subsurface due to footing pressure. On the other hand, this method is invalid for the ground treated by stone columns and thus a more accurate calculation procedure is necessary (e.g., unit cell homogenization or FEM analyses). Nevertheless, in most practical applications as a quality control tool, the ZLT settlement is simply compared against the maximum allowable short-term

settlement of the project. The schematic setup of ZLT on stone columns is depicted in Figure 5.

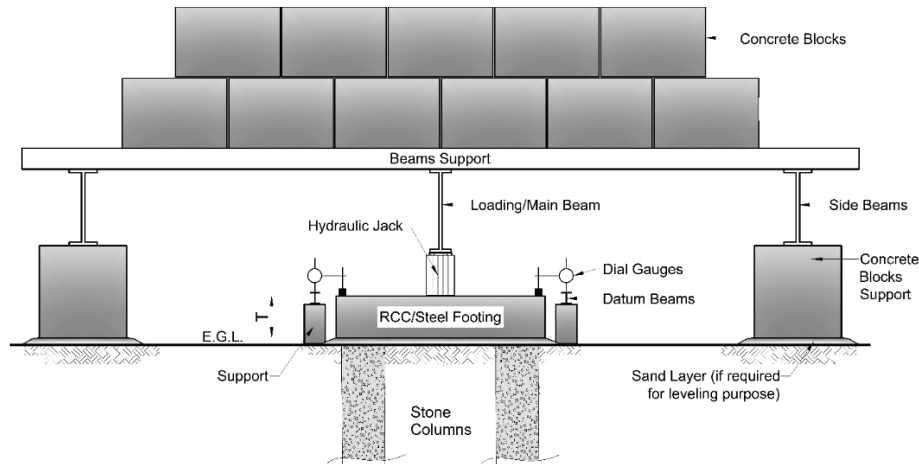


Figure 5: Schematic setup of ZLT on stone columns

4 Interpretation of CPT Results

Many empirical correlations have been introduced in the literature, guidelines, and standards to interpret the characteristics of soils from Cone Penetration Test (CPT) results. Here the correlations used in this study are presented.

[12] suggested Equation 5 for friction angle φ' of sand:

$$\varphi' = 17.6 + 11 \log(q_{t1}) \quad (5)$$

where q_{t1} is normalized cone resistance:

$$q_{t1} = \frac{q_t}{(p_a \cdot \sigma'_{v0})^{0.5}} \quad (6)$$

$$q_t = q_c + u_a(1 - a) \quad (7)$$

p_a , q_c , q_t , u_a , σ'_{v0} and a represent atmospheric pressure, CPT cone resistance, corrected CPT cone resistance, pore water pressure, in situ effective vertical stress and the net area ratio (from laboratory calibration), respectively.

The total unit weight of the soil, γ , is estimated as per [26] as follows:

$$\frac{\gamma}{\gamma_w} = 0.27 \log(R_f) + 0.36 \log\left(\frac{q_t}{p_a}\right) + 1.236 \quad (8)$$

where R_f is friction ratio, the ratio of sleeve friction, f_s , over cone resistance, q_c , and γ_w is the unit weight of water.

[9], [24], and later [25] introduced and modified an iterative procedure (as summarized below) to calculate the soil behaviour type index, I_c , which is used in estimation of several soil parameters.

$$I_c = [(3.47 - \log Q_{tn})^2 + (1.22 + \log F_r)^2]^{0.5} \quad (9)$$

$$Q_{tn} = \left(\frac{q_t - \sigma_{v0}}{p_a}\right) \cdot \left(\frac{p_a}{\sigma'_{v0}}\right)^n \quad (10)$$

$$F_r = \frac{f_s}{q_t - \sigma_{v0}} \times 100\% \quad (11)$$

$$n = 0.381I_c + 0.05 \frac{\sigma'_{v0}}{p_a} - 0.15 \leq 1.0 \quad (12)$$

where Q_{tn} , F_r , σ_{v0} and n denote normalized CPT cone resistance and sleeve friction (with respect to the effective overburden pressure), in situ total vertical stress and stress exponent. [25] proposed the following correlations to estimate the Young modulus, E' , from CPT results for uncemented sand.

$$E' = \alpha_E (q_t - \sigma_{v0}) \quad (13)$$

$$\alpha_E = 0.015 \times 10^{(0.55I_c + 1.68)} \quad (14)$$

Although this correlation is recommended to be implemented for a 0.1% strain level, in this paper it is employed to estimate the modulus of elasticity of soil layers. In this research, the calculated strains of the case study PLT and ZLTs were in the range of 0.1% to 0.3%.

5 Case Study Project

The designated ground for a tank farm project in Egypt was not capable enough to carry heavily loaded foundations and satisfy the requirements of the project, therefore, the subsoil was treated by the stone columns to improve the load-bearing capacity while reducing the settlement to acceptable limits. The diameters and loads of the tanks were in the range of 38-55 m and 250-316 kPa, respectively.

As shown in the CPT results in Figure 6, the top 12-14 m of the in situ ground is mainly a sandy material. The CPTs were performed before the installation of stone columns from the elevation of +4.0 m. It should be noted that PLTs (and later ZLT) were conducted at the elevation of +2.0 m (after the excavation of the top clayey layer) which was the design level for the bottom of the foundation. The groundwater table is around the elevation of +0.5 m.

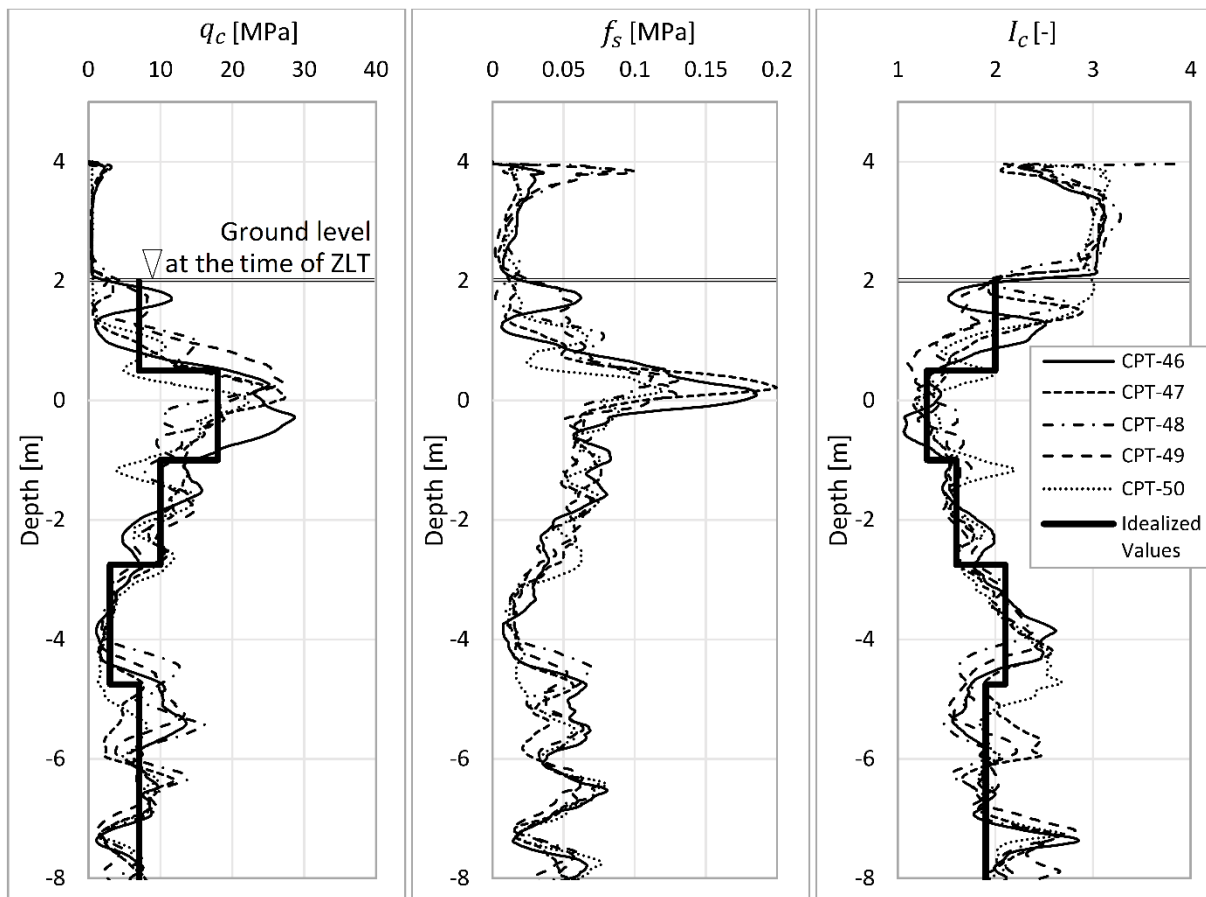


Figure 6: CPT tip resistance (q_c), sleeve friction (f_s) and soil behaviour index (I_c) of the PLT area and ZLT case A

The installed stone columns in this project were executed with the top feed (wet) method using crushed stones with 25-100 mm grading and a maximum of 40% Los Angeles Abrasion (conducted as per ASTM C 131 [3]). The properties of stone column material (the final compacted product) are provided in Table 1. The executed stone columns under all tanks were all 1 m in diameter while the spacing of the columns varied from 1.2 to 2.5 m in different tanks and various parts of the tanks.

The quality control tests of the ground improvement works were PLT and ZLT in addition to typical quality assurance procedures (e.g., production protocols, aggregate consumption, etc.). However, the interpretation of the load test results was challenging. Unlike conventional laboratory tests (e.g., triaxial and oedometer), PLT and ZLT do not directly provide the mechanical characteristics of the column, but they shall be converted to parameters employed in designing and calculating the ground improvement.

Table 1: HS parameters of the in situ soil and the applied stone column material in the PLAXIS model for PLT and ZLT Case A

Parameter	Unit	Soil A1	Soil A2	Soil A3	Soil A4	Soil A5	Stone Column
Elevation	[m]	+2.00 to +0.50	+0.50 to -1.00	-1.00 to -2.75	-2.75 to -4.78	-4.75 to -9.00	NA

q_c (average)	[MPa]	7.0	18.0	10.0	3.0	7.0	NA
I_c (average)	[-]	2.0	1.3	1.6	2.1	1.9	NA
α_E	[-]	9.04	3.72	5.45	10.26	7.96	NA
γ_{unsat}	[kN/m ³]	18.5	19.5	18.5	17.5	18.5	22.0
γ_{sat}	[kN/m ³]	19.0	20.0	19.0	18.0	19.0	22.0
c	[kPa]	0	0	0	0	0	0
φ	[°]	42.0	42.0	41.0	34.0	38.0	47.5
E_{50}^{ref}	[kN/m ²]	62.8	66.8	53.9	29.57	54.5	120.0
ψ	[°]	12.0	12.0	11.0	4.0	8.0	17.5
p^{ref}	[kN/m ²]	13.9	40.0	55.4	71.3	98.3	16.5

6 Numerical Simulations of PLT

As mentioned earlier, the standard procedures of deriving soil stiffness may not be the appropriate method when the PLT is performed on the stone column. Therefore, in this study, the conducted PLTs on the case study project were analyzed using PLAXIS 3D V20 software by considering the actual surrounding soil parameters as well as geometry and loading sequences. Nonetheless, the stiffness of the stone column is fine-tuned in such a way that the calculated settlement meets the average monitored settlements in PLTs.

The modelled condition consists of a 25-mm-thick plate with 0.7 m in diameter sitting at the centre of a 1-m-diameter stone column on the top surface. The load increases up to 250 kPa in 5 increments of 50 kPa each with a holding time of 15 minutes for the interim and 2 hours for the last step (250 kPa). The unloading path has the same loads and holding time but in descending order.

Considering that the material properties of the stone column are assessed at extremely shallow depths and under low confining pressure, a single stiffness value constant over depth should not be assigned to the full length of columns, but more realistically, it should be a function of depth (or effective stress). To observe this effect, the Hardening Soil (HS) constitutive model ([27] and [28]) was selected for the surrounding soil and stone column materials in this study. In this model, stiffness is a non-linear function of confining pressure ([27] and [28]). This is in accordance with the principles of soil mechanics. The stiffness moduli of HS model are presented by Equations 15 to 17.

$$E_{50} = E_{50}^{ref} \left(\frac{c \cdot \cos \varphi - \sigma'_3 \cdot \sin \varphi}{c \cdot \cos \varphi + p^{ref} \cdot \sin \varphi} \right)^m \quad (15)$$

$$E_{ur} = E_{ur}^{ref} \left(\frac{c \cdot \cos \varphi - \sigma'_3 \cdot \sin \varphi}{c \cdot \cos \varphi + p^{ref} \cdot \sin \varphi} \right)^m \quad (16)$$

$$E_{oed} = E_{oed}^{ref} \left(\frac{c \cdot \cos \varphi - \frac{\sigma'_3}{K_{\sigma'_3}} \cdot \sin \varphi}{c \cdot \cos \varphi + p^{ref} \cdot \sin \varphi} \right)^m \quad (17)$$

where E_{50}^{ref} and E_{50} ; and E_{ur} and E_{ur}^{ref} are the secant moduli at 50% of maximum strength and the unloading/reloading moduli in triaxial test at confining pressures of p^{ref} and σ'_3 , respectively. Similarly, E_{oed} and E_{oed}^{ref} are and oedometer stiffnesses at pressure levels of p^{ref}

and σ'_3 , respectively. The exponent m represents the stress level dependency of stiffness. Further, K_0^{nc} , c and φ are the coefficient of lateral earth pressure for a normally consolidated stress state, cohesion and friction angle. Figure 7 schematically displays the introduced moduli in triaxial and oedometer tests.

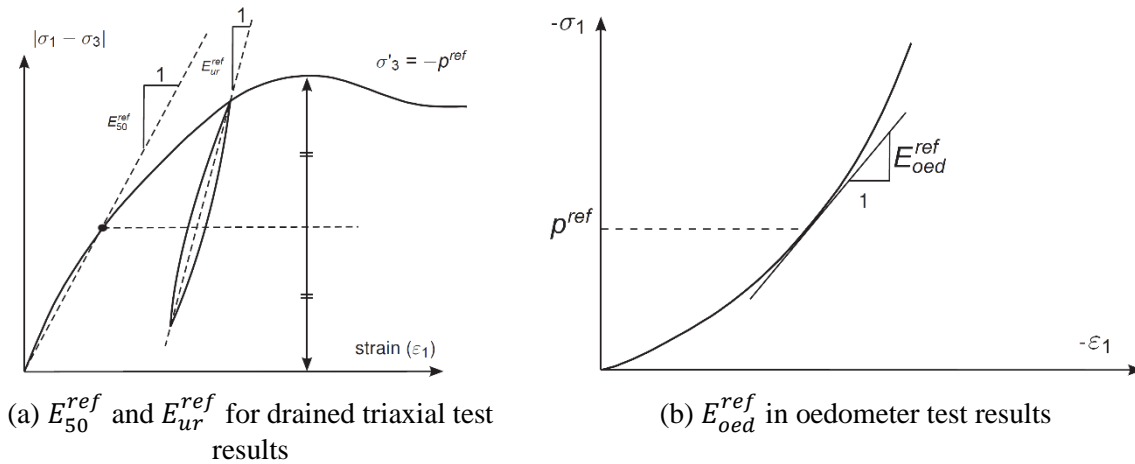


Figure 7: The deformation moduli used in HS model. Source: PLAXIS manual

In the absence of triaxial and oedometer tests, CPT and PLT test results should be converted to required parameters in the numerical modelling in order to derive the deformation parameters of the in situ soil and the stone column material. For the natural soil, the adopted correlation of E_{50}^{ref} from the CPT tip resistance (q_c) is as in Equation 13.

As approximately shown by the thick solid lines in Figure 6, the q_c values of each subsoil layer (soils A1 to A5) are averaged over the thickness of the sublayers. The average tip resistances and assigned E_{50}^{ref} values are provided in Table 1.

Given that E_{50}^{ref} values are correlated with average q_c over the actual depths of the soils, the corresponding p^{ref} values should also represent the stress level at nearly the same depths. In this study, the p^{ref} of the in situ soils is assumed to be the effective vertical ground pressure at the average depth of the concerned layer at the time of CPT by taking into account the groundwater table and soil densities (Table 1).

For the stone column material, E_{50}^{ref} is back-calculated from numerical simulation of the PLTs, in which a p^{ref} the value should also be assigned representing the initial stress level over the PLT influence depth, here assumed approximately 2 times of plate diameter (i.e., ~ 1.5 m). In this study, the same concept of adopting effective ground pressure as p^{ref} is used for the stone column material as well, but averaged over the PLT influence depth, hence, $p^{ref} = (1.5 \text{ m}/2) \times 22 \text{ kN/m}^3 = 16.5 \text{ kPa}$.

The approach of using effective stress as p^{ref} in the HS model is a simplified method to incorporate the influence of the stress level on stiffness in the simulations where no laboratory test is available. However, the classic definition of p^{ref} as per the HS model is different. Table 1 summarizes the considered HS parameters for the modelled soil and the stone column.

In this study, the following assumptions were considered for all materials (see Table 1); $E_{oed}^{ref} = E_{50}^{ref}$, $E_{ur}^{ref} = 3 \times E_{50}^{ref}$, $m = 0.5$, and ψ (dilatancy angle) = $\phi - 30^\circ$.

It should be noted that the E_{50}^{ref} of the stone column (and consequently, the E_{ur}^{ref}) has been back-analyzed to reach a calculated settlement equal to the average observed settlements in the PLTs. Figure 8 shows the numerically simulated PLT results plotted with experimentally captured results. The back-calculation procedure aimed to settle in the range of the actual PLT settlement. One similar PLT test from another project, but on a stone column installed with the same execution method and material, is also plotted in Figure 8 (denoted as AE1, the only PLT result in this Figure with the unloading path) which is also reasonably close to the other PLTs and the numerical results.

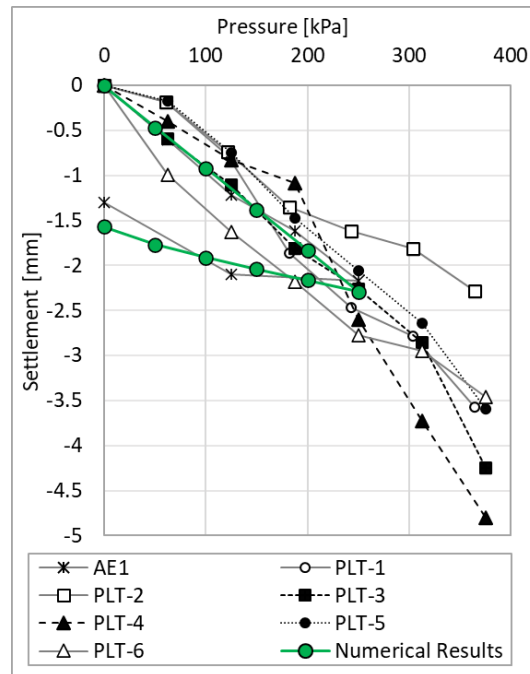


Figure 8: Results of executed and simulated PLTs on stone columns in the case study project

The model geometry and the generated mesh are illustrated in Figure 9. The loading plate is modelled by a 0.7-m-diameter and 25-mm-thick steel plate. Only one-quarter of the full geometry is simulated in the software. Figure 10 depicts the total vertical effective stress and deformation at the highest load step (250 kPa).

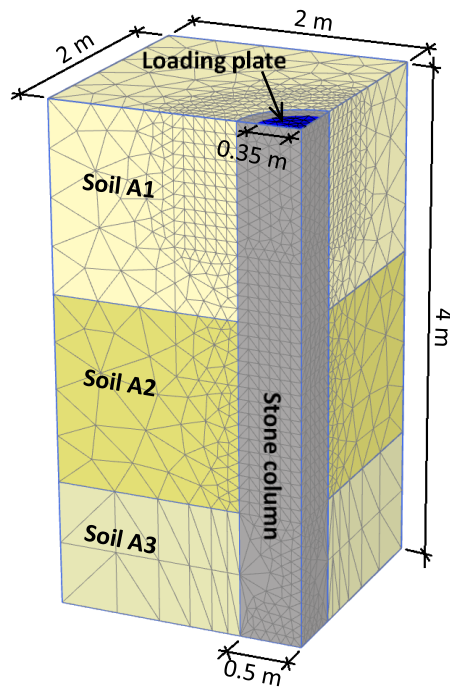
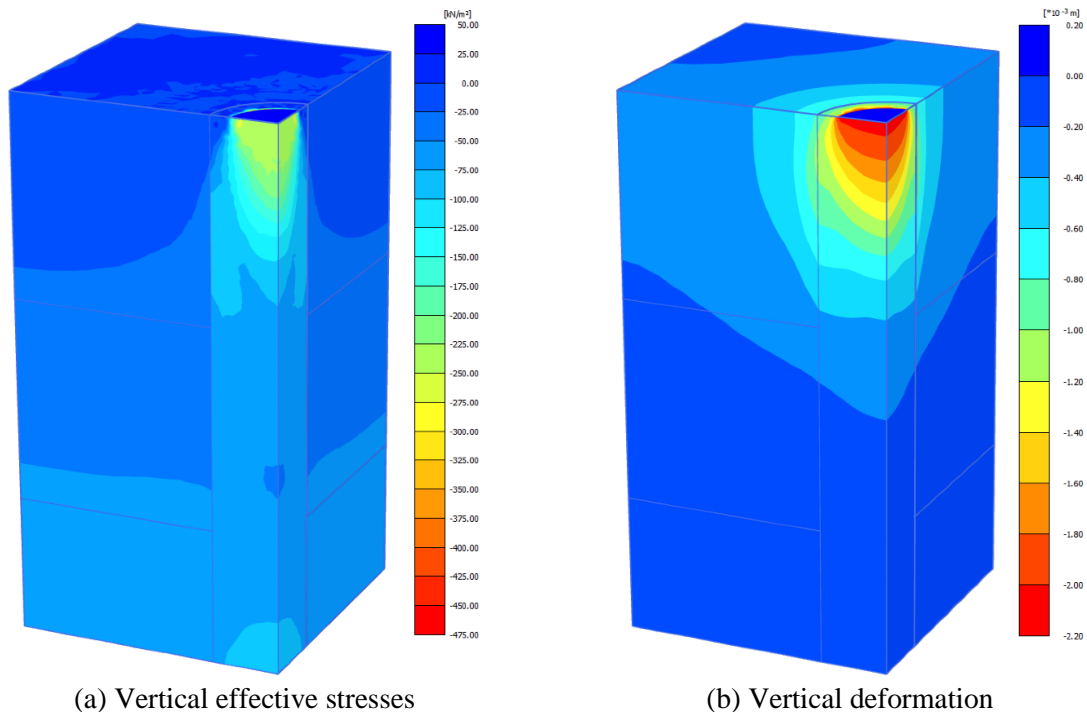


Figure 9: Model geometry and generated mesh



(a) Vertical effective stresses (b) Vertical deformation
 Figure 10: Results of numerical modelling of PLT at the maximum load (250 kPa)

It is worth mentioning that the back-calculated modulus of deformation for stone columns would be valid only with the other assumed calculation procedures (i.e., the adopted constitutive model, p^{ref} values, etc.). Therefore, if other assumptions change, this parameter should be reassessed.

7 Verification of the Introduced Approach

To verify the above-mentioned calculation approach and the interpretations of CPT and PLT tests, three ZLTs conducted on grounds treated by stone columns were modelled in PLAXIS. The ZLTs (which are referred to as A, B, and C cases) are selected in a way to cover various stone column spacings and layouts, and improvement of depth and loading levels. They were performed in different projects in various countries although stone columns were installed with the same technique (the top feed method as described above). The ground improvement and testing schemes of the three cases are summarized in Table 2.

Table 2. Summary of the stone column and the testing schemes of the studied ZLTs

		Case A	Case B	Case C
Stone column design	Diameter	1.0 m	1.0 m	0.8 m
	Length	>20.0 m	3.0 and 5.8 m*	4.5 m
	Spacing	1.5×1.5 m rectangular	2.5×2.5 m circular	2×2 m triangular
Footing size		3×3 m	3×3 m	2.5×2.5 m
Maximum load		400.0 kPa	487.5 kPa	800.0 kPa
* Short and long columns				

In all three cases, the ZLTs were directly conducted on top of the stone columns with no additional engineering fill layer which is usually constructed between stone columns and building foundations. The test setup is schematically illustrated in Figure 5. Figure 11 displays the heads of stone columns and the ZLT.



Figure 11: ZLT on the ground treated by stone columns

The material properties of the applied in situ soil in the modelling of ZLTs were correlated from CPT results according to the proposed procedure for PLT simulations. The material properties of stone columns are considered to be exactly the same as back-calculated from the PLT analysis

in this study. The loading footings of all cases are modelled as a 0.6-m-thick concrete body using the linear elastic material with a 30-GPa Young's modulus.

7.1 Case A

Case A was the same case study project of PLT tests (i.e., the tank farm in Egypt). The columns were installed to various depths although they were in the range of 20 m or above for the concerned area, which is much deeper than the influence depth of PLT and ZLT. As illustrated in Figure 12, the soil is idealized into five layers. The soil profile and correlated material properties are presented in Figure 6 and Table 1.

The pattern of the stone columns was rectangular with 1.5 m spacing (Figure 12). The ZLT footing was 3×3 m in size and loaded as per the schedule presented in Table 3. In this test, four columns were loaded equally while some other columns were not directly under the footing but were affected by the load.

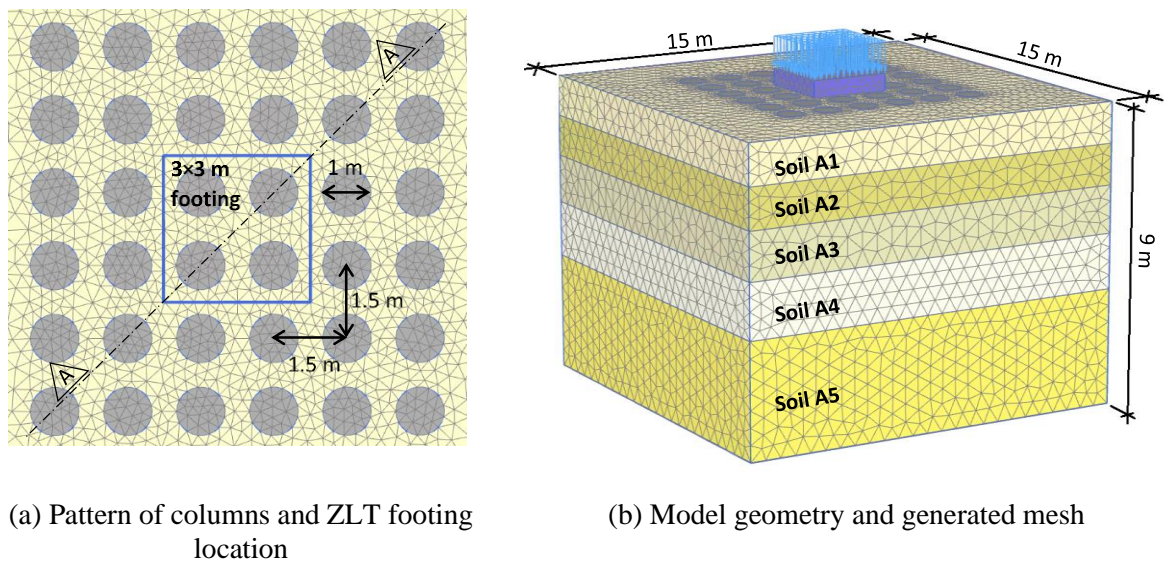


Figure 12: Simulation of case A

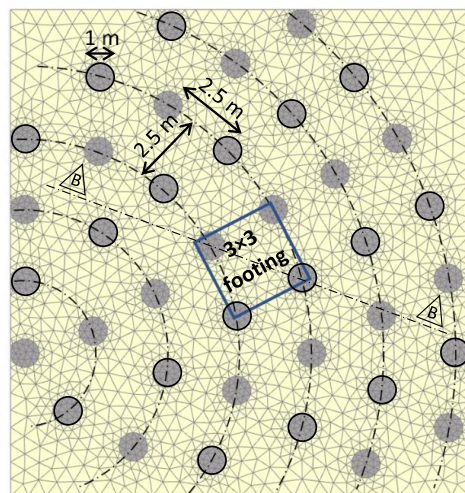
Table 3. Loading and unloading schedule of ZLT for Cases A, B, and C

Case A		Case B		Case C	
Footing load [kPa]	Holding time [min]	Footing load [kPa]	Holding time [min]	Footing load [kPa]	Holding time [min]
0	-	0	-	0	-
100	60	81.3	15	80	15
200	60	162.5	15	160	15
300	60	243.8	30	240	15
400	360	325	60	320	120
300	15	406.3	60	400	15
200	15	487.5	360	480	15
100	15	325	15	560	15
0	60	162.5	15	640	15

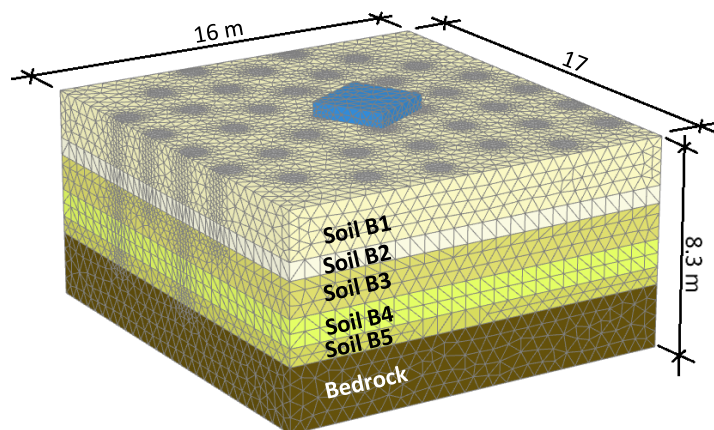
0	60	720	15
		800	1,440
		720	15
		640	15
		560	15
		480	15
		400	15
		320	15
		240	15
		160	15
		80	15
		0	120

7.2 Case B

In case B, the ZLT was conducted on a ground improved by stone columns installed in a circular pattern under an oil storage tank (Figure 13). The elevation of the natural surface was around +6.2 m although the top 0.9 m was removed before ground improvement works. The top elevations of the columns and the groundwater table are +5.3 and +4.0 m. The spacing between the stone columns' rows and two adjacent columns are 2.5 m. Moreover, every second column is short and long (3 m and around 5.8 m). In Figure 13, the columns marked by solid black circles are the long ones. As shown, the ZLT footing is situated on two short and two long columns and the position is not symmetrical with respect to the columns. More surrounding columns are also modelled although not all of them are affected by the ZLT load.



(a) Pattern of columns and ZLT footing location



(b) Model geometry and generated mesh

Figure 13: Simulation of case B

The CPT results representing the soil type under the ZLT location of case B are illustrated in Figure 14, which was conducted before removing the topsoil and ground improvement works. The subsoil consists of sandy layers with scattered seams of silty sand in the first 2 meters of the ground (after excavation to +5.3 m). The thick black lines in Figure 14 depict the idealized soil strata selected for the numerical simulation of the ZLT. The material properties of subsoil layers are provided in Table 4. The material properties of stone columns are back-calculated in the modelling of the PLT (Table 1).

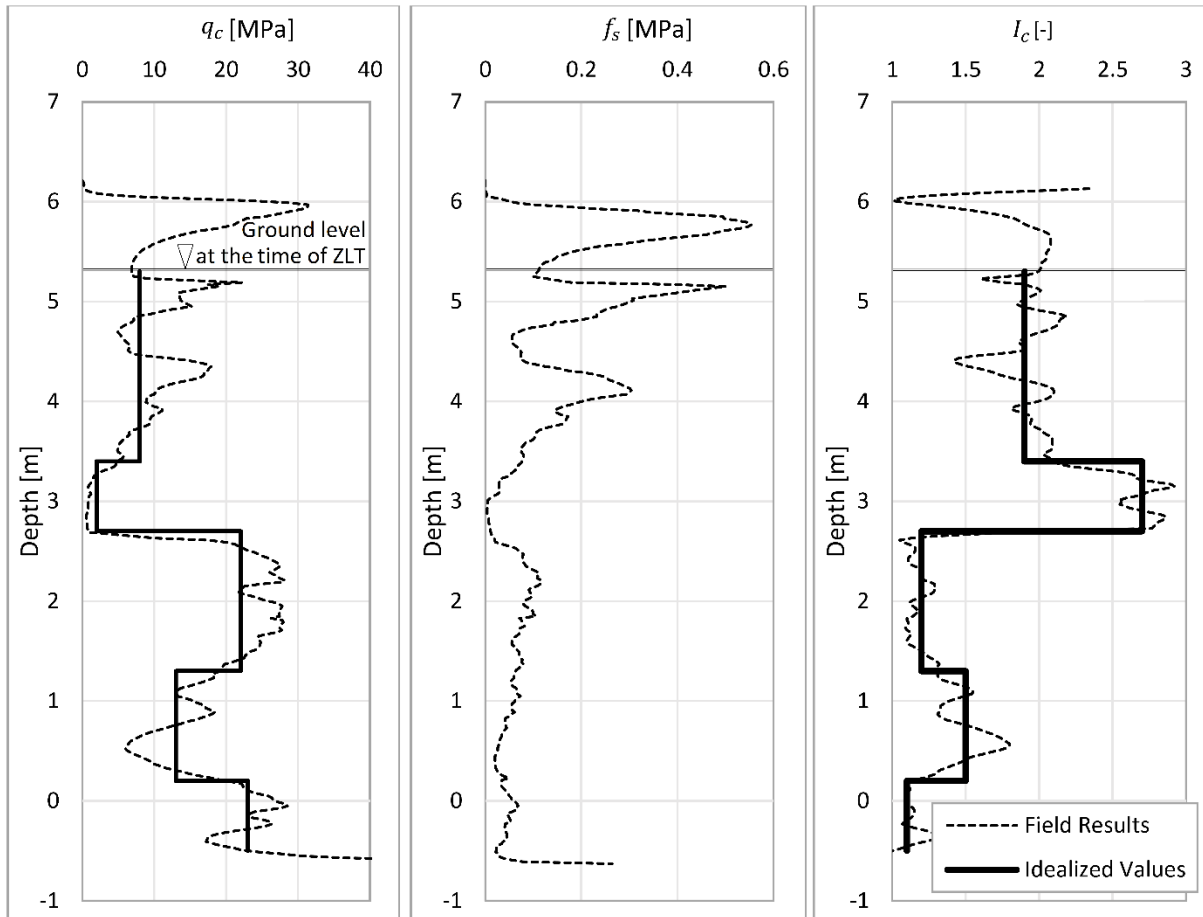


Figure 14: CPT tip resistance (q_c), sleeve friction (f_s) and soil behaviour index (I_c) of the ZLT case B

Table 4: Case B: HS parameters of the applied in situ soils in the PLAXIS model

Parameter	Unit	Soil B1	Soil B2	Soil B3	Soil B4	Soil B5	Bedrock
Elevation	[m]	+5.30 to +3.40	+3.40 to +2.70	+2.70 to +1.30	+1.30 to +0.20	+0.20 to -0.50	below -0.50
q_c (average)	[MPa]	8.0	2.0	22.0	13.0	23.0	NA
I_c (average)	[-]	1.9	2.7	1.2	1.5	1.1	NA
α_E	[-]	7.96	21.93	3.28	4.80	2.89	NA
γ_{unsat}	[kN/m ³]	19.5	18.5	19.5	18.5	19.5	21.0
γ_{sat}	[kN/m ³]	20.0	19.0	20.0	19.0	20.0	21.0
c	[kPa]	0.0	0.0	0.0	0.0	0.0	20.0

φ	[°]	42.0	34.0	42.0	42.0	42.0	35.0
E_{50}^{ref}	[kN/m ²]	63.4	42.5	72.0	62.0	66.3	300.0
ψ	[°]	12.0	4.0	12.0	12.0	12.0	5.0
p^{ref}	[kN/m ²]	18.5	34.5	44.7	56.6	74.1	100

Similar to case A, the loading schedule consisted of one cycle of loading-unloading, but with different maximum loads and holding times. The loading details are listed in Table 3.

7.3 Case C

The ZLT case C was conducted on a ground treated by stone columns in a triangular pattern (Figure 15). The spacing between the columns and the ZLT footing size were 2 and 2.5 m, respectively. The footing was placed and partially covered three columns, in a way that the centre point of the footing was located on the centroid of the three columns underneath. The columns were averagely extended to the elevation of -4.0 m. The subsoil profile is presented in Figure 16 and Table 5.

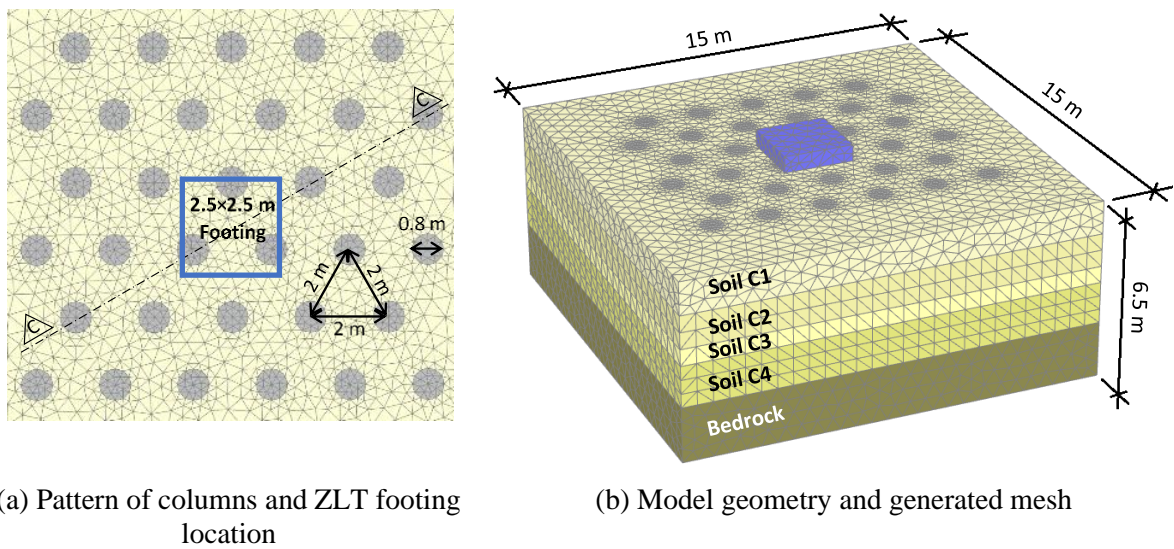


Figure 15: Simulation of case C

Table 5: Case C: HS parameters of the applied in situ soils in the PLAXIS model

Parameter	Unit	Soil C1	Soil C2	Soil C3	Soil C4	Bedrock
Elevation	[m]	+0.50 to -0.70	-0.70 to -1.90	-1.90 to -2.50	-2.50 to -4.00	below -4.00
q_c (average)	[MPa]	10	17	8	40	NA
I_c (average)	[-]	1.6	1.4	1.7	1.1	NA
α_E	[-]	5.45	4.23	6.18	2.89	NA
γ_{unsat}	[kN/m ³]	19.0	19.5	18.5	20.5	21.0
γ_{sat}	[kN/m ³]	19.5	20.0	19.0	21.0	21.0
c	[kPa]	0	0	0	0	20
φ	[°]	42.0	42.0	41.0	42.0	35.0

E_{50}^{ref}	[kN/m ²]	54.5	71.7	49.2	115.5	300.0
ψ	[°]	12.0	12.0	11.0	42.0	5.0
p^{ref}	[kN/m ²]	11.4	34.9	52.6	74.4	95.0

Figure 16 shows the CPT results of the ground under ZLT case C. The thick solid lines represent the idealized soil profile. The soil consists of sandy materials to the elevation of around -4.0 m where hard strata (weathered bedrock) begin on which the stone columns are sitting. The groundwater table was observed around -0.5 m.

The loading schedule of case C is provided in Table 3. The maximum load was considerably higher compared to the other two cases and a heavier setup was erected accordingly. The holding time (at the maximum load) was also longer.

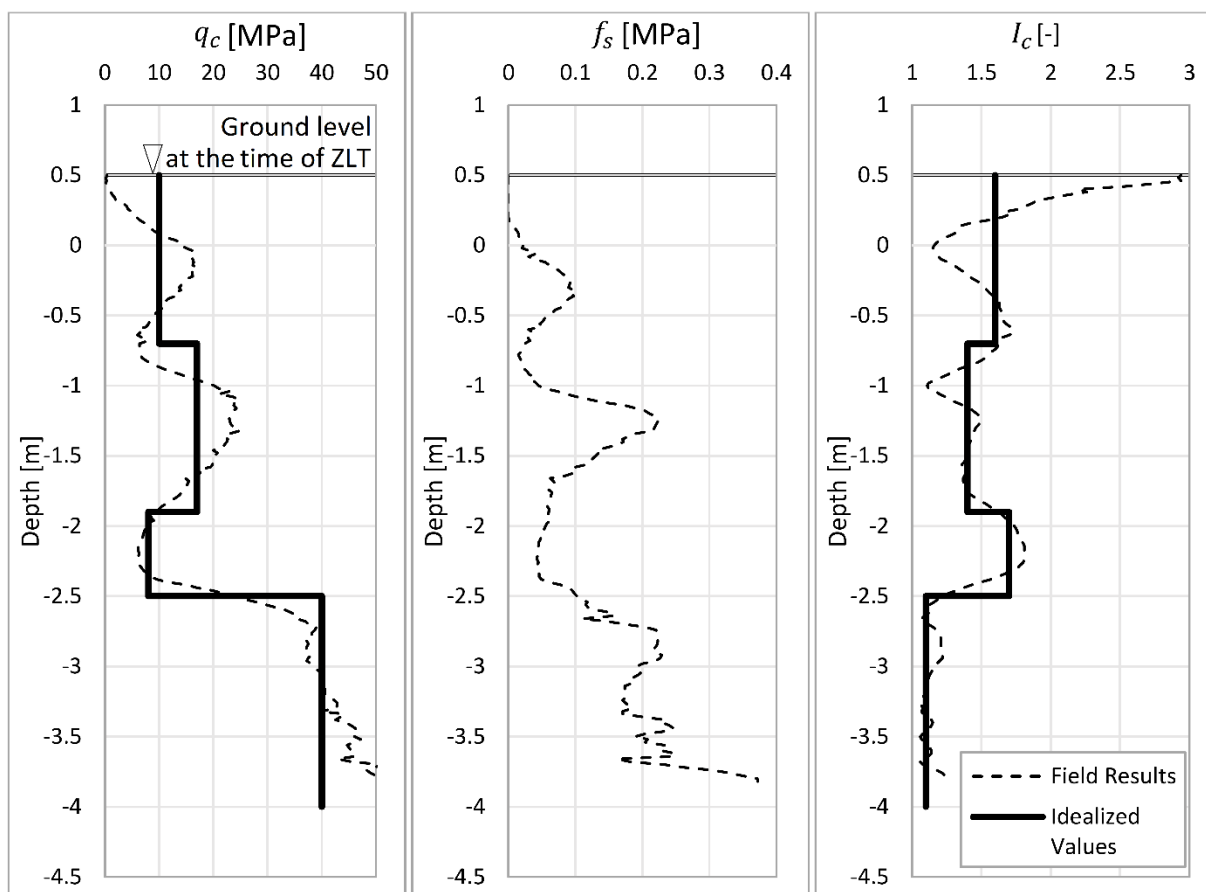


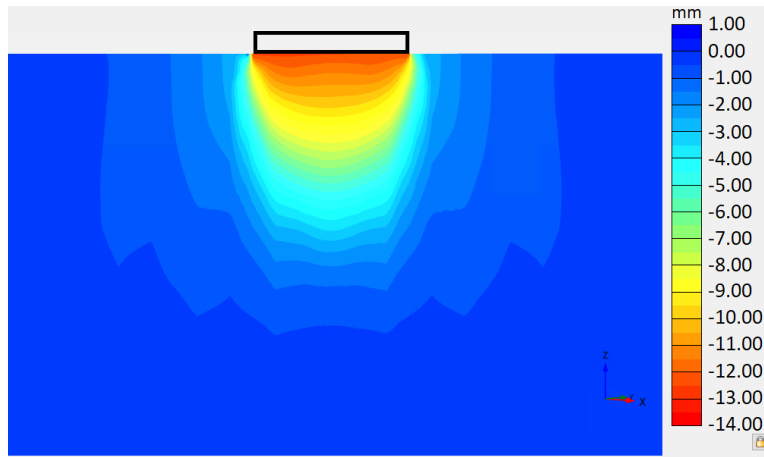
Figure 16: CPT tip resistance (q_c), sleeve friction (f_s) and soil behaviour index (I_c) of the ZLT case C

8 Results and Discussions

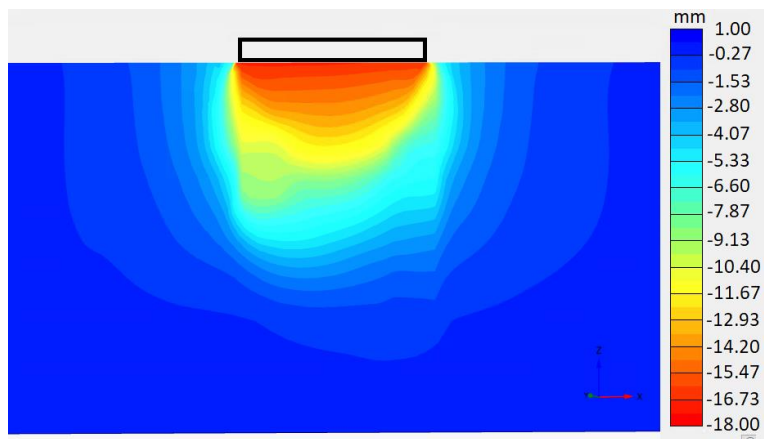
8.1 FEM Analyses Results

As mentioned earlier, the studied ZLTs were modelled in PLAXIS 3D V20 using soil parameters presented in Tables 1, 4 and 5, as well as stone column properties back-calculated from PLT outcomes. Figure 17 shows the calculated deformation of ZLTs at the maximum load

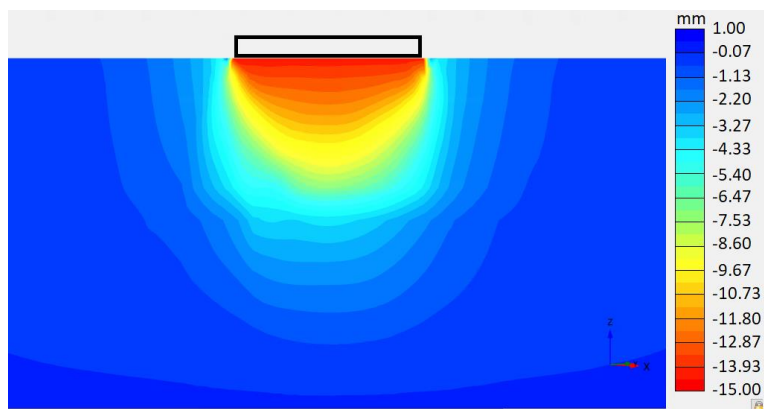
of cases A, B and C. All settlements were acceptably uniform. Even for case B, where the footing is not symmetrically placed on the stone columns, the differential settlement is only 1 mm.



(a) Case A



(b) Case B



(c) Case C

Figure 17: Calculated deformations at the maximum applied load on the cross-section diagonally connecting two corners of the footings

The settlement of the footings against the test loads is plotted in Figure 18 for all three cases. As shown, the results demonstrate relatively good matches between calculated and experimental settlements, especially at the maximum applied load. However, the calculated settlements at the interim loading stages were more than experimental values (especially in Case C), which could be due to the significantly short holding time of the load for those steps. As mentioned in Table 3 the holding times for the interim loading steps were in the range of 15 minutes to one hour, whereas those of maximum loads were six hours for cases A and B and 24 hours for case C. Figure 19 displays the settlement vs. time. In short holding times (marked by solid arrows in Figure 19) the settlements have not reached an equilibrium; consequently, larger settlements could be recorded for these loading steps if longer holding times were maintained, and hence the experimental settlements could be closer to the calculated values. On the other hand, the loads were kept for a longer period at their maximum values, resulting in (or getting close to) the completion of the immediate settlement as shown in Figure 19 by hollow arrows.

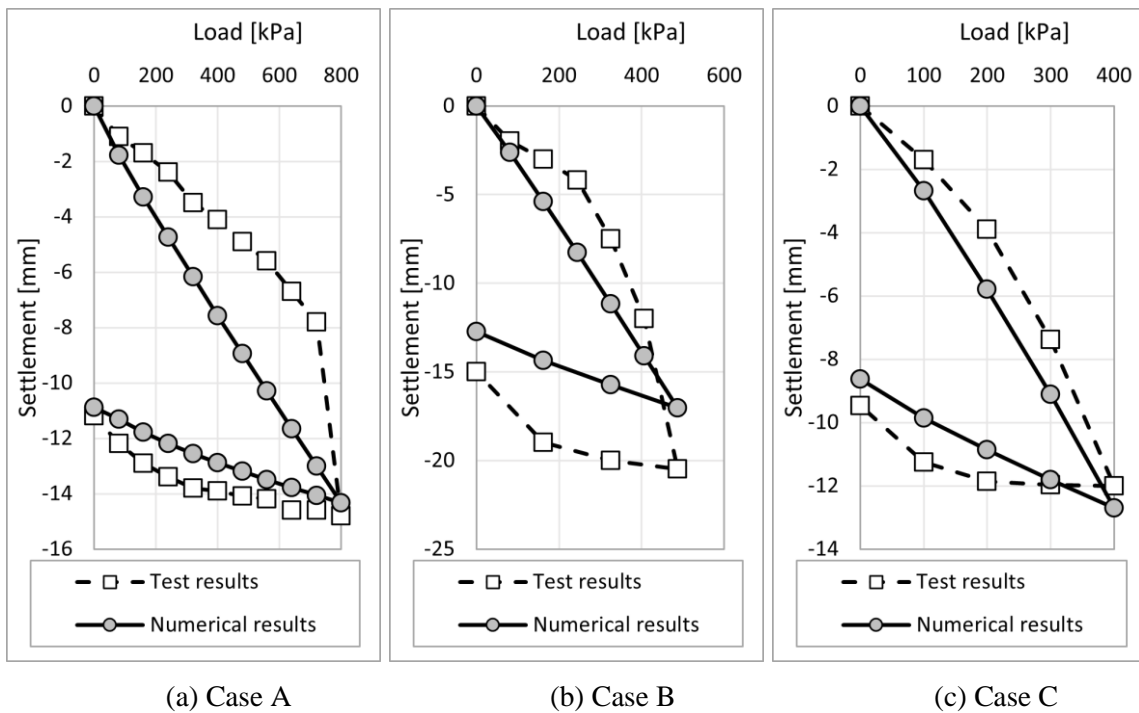


Figure 18: Maximum calculated deformation and settlements monitored during ZLTs

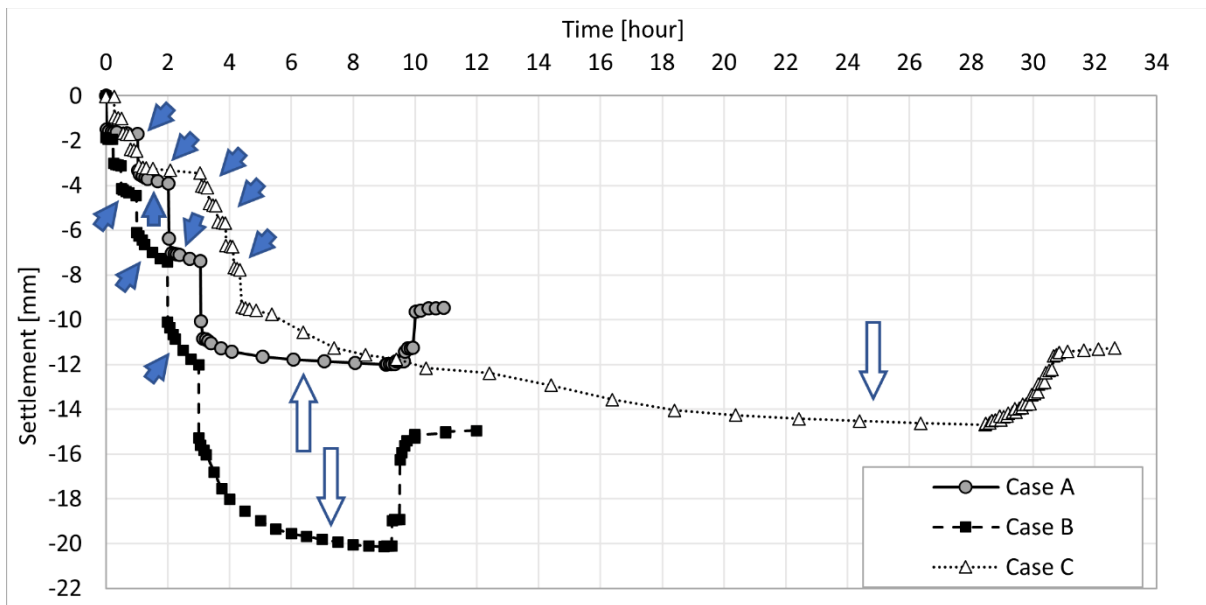


Figure 19: Settlement of ZLTs vs. time

8.2 Unit cell calculations (Priebe method)

In this study, the same three ZLT cases were evaluated by the unit cell approach (the Priebe method) as well. First, the equivalent moduli of the elasticity of the grounds treated by the infinite grid of stone columns are calculated. Next, the ZLT footings are modelled on the grounds consisting of different sublayers (Tables 1, 4, and 5) with enhanced moduli of elasticity. The whole procedure is incorporated into KID software, the in-house program Keller.

One of the basic assumptions of the Priebe method is having an infinite stone column grid and loaded area, therefore, the method proposes the use of constrained modulus (E_{oed}) as the input parameter for stiffness. However, the same applied correlation for deriving the moduli of deformation (E_{50}^{ref} in the HS model) from CPT was also employed in this study to estimate the E_{oed} (Equations (13) and (14)). Similarly, for stone column material the modulus of elasticity of 120 MPa was considered as the constrained modulus in Priebe calculations. Figure 20 shows the settlement calculation using the KID program for ZLT case C.

The monitored settlements are compared with the calculated settlements as per Priebe and FEM methods in Figure 21. As shown, FEM analyses could reasonably predict experimental settlements while the Priebe method overestimated the results in an acceptable range.

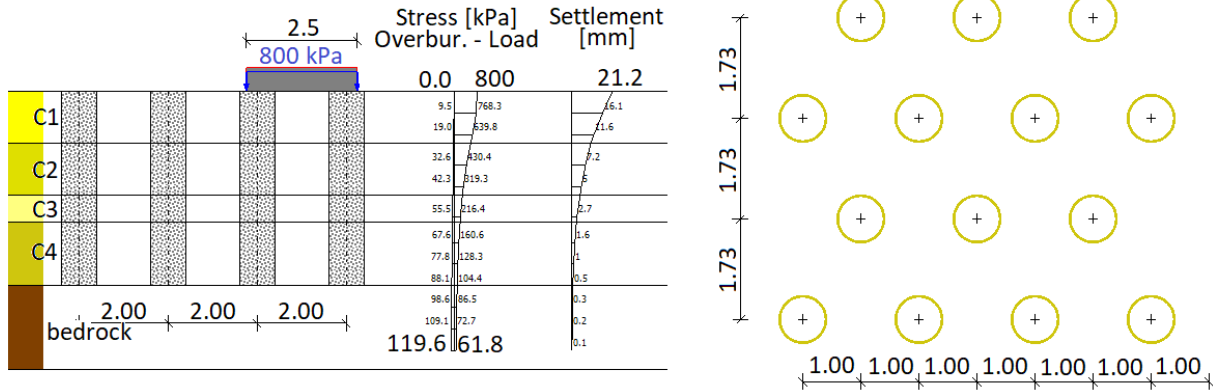


Figure 20: Settlement calculations using KID software (for case C)

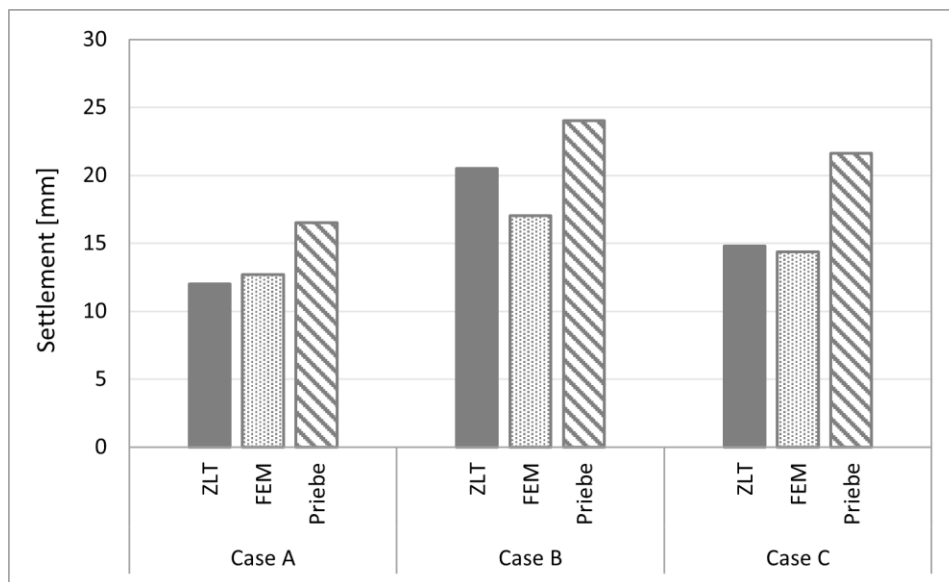


Figure 21: Comparison of experimental and calculated settlements using FEM and Priebe methods

9 Conclusion

The static load tests (i.e., PLT and ZLT), as the most commonly implemented quality control measures in the Vibro stone column projects, were assessed in more detail using FEM and Priebe methods and the results were compared with experimental data. A good match between experimental observations and numerical analyses confirmed that the assumptions and the selected calculation methodology could simulate the studied conditions to an acceptable extent. Although ZLT settlements under the highest load were properly modelled in PLAXIS, the settlements of the interim loading steps were not simulated accurately. The reason probably lies in the loading time. For the largest loading step, a typically longer holding time is maintained (as in the studied cases), allowing the settlement to reach its final value or continue at a negligible rate (this settlement is what numerical simulation considers), while a shorter holding time is allowed for interim steps and the applied load usually goes to the next stage when the settlement of the previous stage is still ongoing. Therefore, all remaining settlements are

accumulated in the last loading stage where enough time is given in this regard. To capture settlements in extremely short periods, more detailed investigations on material properties are required which can be the topic for the next phase of this study.

Despite its simplicity, the Priebe method provided reliable results reasonably close to experimental values but on the safe side. Except for special conditions (e.g., complicated geometry, heterogenous soil profile, sensitive structures, etc.), the Priebe method can be applied for designing and calculating stone column projects.

The soil parameters were derived from CPTs performed prior to installing stone columns. However, it is widely accepted that the installation procedure also improves the in situ soil for non-cohesive soils. Therefore, the considered alpha factors should represent the post-improvement condition of the natural soil based on pre-VR CPTs. Needless to say, in real projects, post-VR CPTs are not available in the design stage of stone columns; therefore, conservatively the pre-VR CPTs are taken as the design soil profile. Nevertheless, more studies are needed to investigate the influence of stone column installation on the in situ soil between the columns.

References

- [1] Ambily, A.P. & Gandhi, S.R. (2007) Behavior of stone columns based on experimental and FEM analysis. *J. Geotech. Geoenviron. Eng.* 133 (4), 405-415. [http://dx.doi.org/10.1061/\(ASCE\)1090-0241\(2007\)133:4\(405\)](http://dx.doi.org/10.1061/(ASCE)1090-0241(2007)133:4(405))
- [2] ASTM D 1195. Standard Test Method for Repetitive Static Plate Load Tests of Soils and Flexible Pavement Components, for Use in Evaluation and Design of Airport and Highway Pavements.
- [3] ASTM C 131. Standard Test Method for Resistance to Degradation of Small-Size Coarse Aggregate by Abrasion and Impact in the Los Angeles Machine.
- [4] Babu, M.D., Nayak, S. & Shivashankar, R. (2013) A critical review of construction, analysis and behavior of stone columns. *Geotech. Geol. Eng.* 31 (1), 1-22. <http://dx.doi.org/10.1007/s10706-012-9555-9>
- [5] Benmebarek, S., Remadna, A. & Benmebarek, N. (2018) Numerical Modelling of Stone Column Installation Effects on Performance of Circular Footing. *Int. J. of Geosynth. and Ground Eng.* 4, 23. <http://dx.doi.org/10.1007/s40891-018-0140-z>
- [6] Ellouze, S., Bouassida, M., Hazzar, L. & Mroueh, H. (2010) On settlement of stone column foundation by Priebe's method. *Proceedings of the Institution of Civil Engineers - Ground Improvement.* 163 (2), 101-107. <https://doi.org/10.1680/grim.2010.163.2.101>
- [7] Elsayy, M.B. & El-Garhy, B. (2017) Performance of granular piles improved soft ground under raft foundation: a numerical study. *Int. J. Geosynth. Ground Eng.* 3 (4), 36. <http://dx.doi.org/10.1007/s40891-017-0113-7>
- [8] Fattah, M.Y. Zabar, B.S. & Hassan, H.A. (2015) Soil arching analysis in embankments on soft clays reinforced by stone columns. *Structural Engineering and Mechanics.* 56 (4), 507-534. <https://doi.org/10.12989/SEM.2015.56.4.507>

- [9] Jefferies, M.G. & Davies, M. (1993) Use of the CPTu to Estimate Equivalent SPT N60. *Geotech. Testing J., GTJODJ.* 16 (4), 458-468.
- [10] Killeen, M.M. & McCabe, B.A. (2014) Settlement performance of pad footings on soft clay supported by stone columns: a numerical study. *Soils Found.* 54 (4), 760-776.
<http://dx.doi.org/10.1016/j.sandf.2014.06.011>
- [11] Kirsch, K. & Kirsch, F. (2010) *Ground Improvement by Deep Vibratory Methods*. Spon Press, London and New York.
- [12] Kulhawy, F.H. & Mayne, P.H. (1990) Manual on estimating soil properties for foundation design. Report EL-6800 Electric Power Research Institute; EPRI, August 1990.
- [13] Maheshwari, P. & Khatri, S. (2012) Nonlinear analysis of infinite beams on granular bed-stone column-enforced earth beds under moving loads. *Soils Found.* 52 (1), 114-125,
<http://dx.doi.org/10.1016/j.sandf.2012.01.004>
- [14] Mohanty, P., & Samanta, M. (2015). Experimental and Numerical Studies on Response of the Stone Column in Layered Soil. *Int. J. of Geosynth. and Ground Eng.* 1, 27.
<http://dx.doi.org/10.1007/s40891-015-0029-z>
- [15] Nayak, S., Vibhoosha, M.P. & Bhasi, A. (2019). Effect of Column Configuration on the Performance of Encased Stone Columns with Basal Geogrid Installed in Lithomargic Clay. *Int. J. of Geosynth. and Ground Eng.* 5, 29. <http://dx.doi.org/10.1007/s40891-019-0181-y>
- [16] Ng, K.S. & Tan, S.A. (2015). Stress Transfer Mechanism in 2D and 3D Unit Cell Models for Stone Column Improved Ground. *Int. J. of Geosynth. and Ground Eng.* 1, 3.
<http://dx.doi.org/10.1007/s40891-014-0003-1>
- [17] Priebe, H.J. (1976). Abschätzung des Setzungsverhaltens eines durch Stopfverdichtung verbesserten Baugrundes. *Die Bautechnik*, 53 (8).
- [18] Priebe, H.J. (1987). Abschätzung des Scherwiderstandes eines durch Stopfverdichtung verbesserten Baugrundes. *Die Bautechnik*, 55 (8).
- [19] Priebe, H.J. (1988). Zur Abschätzung des Setzungsverhaltens eines durch Stopfverdichtung verbesserten Baugrundes. *Die Bautechnik*, 65 (1).
- [20] Priebe, H.J. (1995). Die Bemessung von Rüttelstopfverdichtungen. *Die Bautechnik*, 72 (3).
- [21] Priebe, H.J. (1998). *Vibro replacement to prevent earthquake induced liquefaction*. Ground Engineering, London.
- [22] Priebe, H.J. (2003). Zur Bemessung von Rüttelstopfverdichtungen – Anwendung des Verfahrens bei extrem weichen Böden, bei schwimmenden Gründungen und beim Nachweis der Sicherheit gegen Gelände – oder Böschungsbruch. *Die Bautechnik*, 80.
- [23] Remadna, A., Benmebarek, S. & Benmebarek, N. (2020). Numerical Analyses of the Optimum Length for Stone Column Reinforced Foundation. *Int. J. of Geosynth. and Ground Eng.* 6, 34.
<http://dx.doi.org/10.1007/s40891-020-00218-x>

- [24] Robertson, P.K. & Wride, C. (1998). Evaluating cyclic liquefaction potential using the CPT. *Can. Geotech. J.* 35 (3), 442-459.
- [25] Robertson, P.K. (2009). Interpretation of cone penetration tests – a unified approach, *Canadian Geotech. J.* 46 (11), 1337-1355. <http://dx.doi.org/10.1139/T09-065>
- [26] Robertson, P.K. (2010). Estimating soil unit weight from CPT. 2nd International Symposium on Cone Penetration Testing. Huntington Beach, CA, USA, May 2010.
- [27] Schanz, T. (1998). *Zur Modellierung des Mechanischen Verhaltens von Reibungsmaterialien*. Habilitation. Stuttgart Universität.
- [28] Schanz, T., Vermeer, P.A., & Bonnier, P.G. (1999). The hardening-soil model: Formulation and verification. In R.B.J. Brinkgreve, *Beyond 2000 in Computational Geotechnics*, Balkema, Rotterdam. 281-290, <http://dx.doi.org/10.1201/9781315138206-27>
- [29] Shamsi, M., Ghanbari, A. & Nazariafshar, J. (2019). Behavior of sand columns reinforced by vertical geotextile encasement and horizontal geotextile layers. *Geomech. and Eng.* 19 (4), 329-342. <http://dx.doi.org/10.12989/GAE.2019.19.4.329>
- [30] Yu. Y., Wang, Z. & Sun, H. (2020). Optimal design of stone columns reinforced soft clay foundation considering design robustness. *Geomech. and Eng.* 22 (4), 305-318. <http://dx.doi.org/10.12989/gae.2020.22.4.305>



Identification of Soil Mechanical Parameters by Inverse Analysis Using Stochastic Methods

Moussaoui Moufida ^{1*}, Rehab Bekkouche Souhila ², Kamouche Houda ², Benayoun Fadila ³, Goudjil Kamel ⁴

¹Department of Hydraulics, Faculty of Technology, University Badji Mokhtar Annaba, Algeria

²Department of Civil Engineering, University 20 Août 1955 Skikda, LMGHU Laboratory, Algeria

³Department of Civil Engineering, Faculty of Sciences and Applied Sciences, University Oum El Bouaghi, Algeria

⁴Department of Civil Engineering, Faculty of Sciences and Technology, University of Souk Ahras, Algeria

*e-mail: moussaouigc@yahoo.fr

Abstract

The mechanical parameters of the soil that must be introduced into geotechnical calculations, in particular those carried out by the Finite Element Method, are often poorly understood. The search for the numerical values of these parameters so that the models best reflect the observed reality constitutes the inverse analysis approach. In this article, we are interested in the identification of the mechanical parameters of the soil based on the principle of inverse analysis using the two methods of stochastic optimization, the genetic algorithm and the hybrid genetic algorithm with Tabu search. Soil behavior is represented by the constitutive soil Mohr-Coulomb model. The identification relates to the following two parameters: The shear modulus (G) and the friction angle (φ). The validation of these two stochastic optimization methods is done on the experimental sheet pile wall of Hochstetten in Germany. The results obtained by applying the genetic algorithm method and the hybrid genetic algorithm method for the identification of the two Mohr-Coulomb parameters (G , φ) show that the hybridization process of the genetic algorithm combined with the Tabu search method accelerated the convergence of the algorithm to the exact solution of the problem whereas the genetic algorithm alone takes a much longer computation time to reach the exact solution of the problem.

Keywords: inverse analysis, identification of parameters, stochastic methods, numerical modeling, sheet piling

1 Introduction

The mechanical parameters of the soil that must be introduced into the geotechnical calculations are often poorly known. The search for the numerical values of these parameters, so that the models best reflect the observed reality, constitutes the inverse analysis approach [1]. This form of inverse analysis consists of calibrating a numerical soil model on experimental data by iterative modifications of the values of the input parameters of the model until the output values reproduce the observed data as close as possible, i.e., until the error function, which quantifies the difference between the experimental and numerical results, is minimal. Parameter adjustment boils down to a stochastic optimization problem [2, 3, 4].

The objective of this work is to apply the principle of inverse analysis using two methods of stochastic optimization, the genetic algorithm and the hybrid genetic algorithm with the Tabu search method to identify two parameters of the constitutive soil Mohr-Coulomb model, the shear modulus (G) and the friction angle (φ). In order to test the convergence and the efficiency of the two stochastic methods, we have developed two programs under Matlab 07. The first program uses the genetic algorithm method and the second uses the hybrid genetic algorithm method with Tabu search, these two programs are validated from an experimental sheet pile wall from Hochstetten in Germany. In 1993, the University of Karlsruhe in Germany built a full-scale experimental retaining structure on the Hochstetten site. This experiment consisted in digging an excavation in front of a wall of braced sheet piles in a sandy environment and in stressing the wall until the limit equilibrium. The experimental sheet pile wall of Hochstetten is therefore a very well instrumented geotechnical structure. It has been the subject of many studies which constitute a large database [1, 5, 6].

Many studies have been devoted to the determination of the mechanical properties of soils from the experimental sheet pile wall of Hochstetten. This structure has been the subject of numerous studies which constitute an important database such as the research work of Mestat and Arafati [5], Von Wolffersdorff [6] and Levasseur [1]. We propose to complete this research work by studying an optimization problem on a finite dimensional space. The goal of the optimization problem is to identify the best sets of soil parameters (G, φ) that minimize the gap between the numerical model and the experiment. Many participants in the forecasting competition chose the Mohr-Coulomb soil constitutive model. In order to compare the results of the identification method with their predictions. Numerical simulations were carried out using the numerical calculation software Plaxis 08.

2 Optimization Principle

A given optimization problem must first be able to be numerically modeled by a Finite Element Calculation. For this study, we chose the Plaxis software. Depending on the stresses imposed on the model and the parameters assumed for a constitutive soil model, a numerical answer is calculated. The numerical answer obtained is then compared to the available experimental data. This comparison results in the calculation of the difference between the observed data and the calculated values, i.e., the calculation of the error function (F_{err}). This difference is then minimized by two stochastic optimization algorithms. From this optimization are deduced new values for the parameters of the constitutive soil model [1]. The process repeats until the difference between the calculated values and the measured data is minimal (Figure 1).

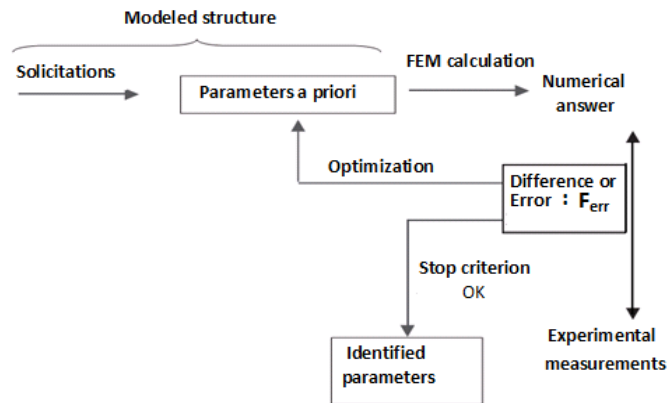


Figure 1: Optimization principle

2.1 The Error Function

The choice of the error function (F_{err}) is crucial in inverse analysis. Often in geotechnical engineering, the error function evaluates the difference between a numerically calculated curve, described by U_{ni} , and an experimental curve measured in situ, described by U_{ei} , as shown in the Equation (1):

$$F_{err} = \left(\frac{1}{N} \sum_{i=1}^N \frac{(U_{ei} - U_{ni})}{(0.01 + U_{ei})} \right) \quad (1)$$

where:

N : is the number of measurement points; U_{ei} : is the experimental displacement at a measurement point i and U_{ni} : is the numerical displacement at a measurement point i .

2.2 Optimization Algorithms

2.2.1 Optimization by Genetic Algorithm

The genetic algorithm operates on a population of individuals, each individual representing a set of parameters. Selection, crossover and mutation operators are applied to generations of individuals (called parents) in order to create new individuals (called children) [7]. The individuals of the new population will be evaluated from the error function to replace a part of the individuals of the current population. The process of optimization by the genetic algorithm is illustrated in Figure 2.

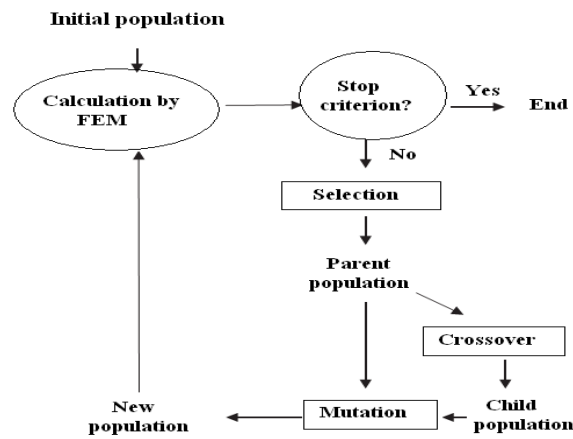


Figure 2: The optimization process by the genetic algorithm

2.2.2 Optimization by Hybrid Genetic Algorithm

Genetic algorithms, although robust, are expensive methods because they do not take local information into account much, so it is interesting to hybridize a genetic algorithm with a local search algorithm such as the Tabu search method which allows carrying out a modular analysis of a problem by agreeing to sacrifice generality to gain efficiency [8]. The Tabu search method is introduced after the crossover operation using the intensification operator to find the best neighbor for each solution found. The result will be a new optimized population that will continue to evolve through further genetic operations to produce new generations better suited to the problem [5, 6]. The process of optimization by the genetic algorithm is illustrated in Figure 3.

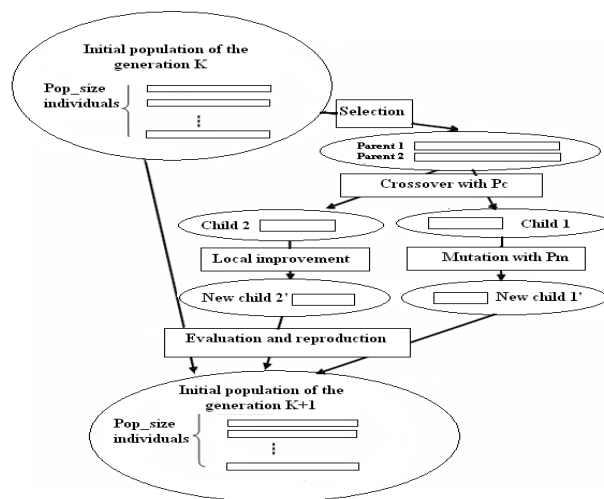


Figure 3: The optimization process by the hybrid genetic algorithm

3 Presentation of the Experimental Device An Instrumentation of the Experimental Sheet Pile Wall

The experiment, shown schematically in Figure 4, concerns a KRUPP KD VI type sheet pile wall 7 m long (experimental wall), installed by vibratory driving up to 6 m deep in a mass of unsaturated sandy soil, and held by a level of buttons. This experimental curtain supports one of the longitudinal walls of a rectangular excavation (7 m long and 4 m wide) whose depth reached 5 m at the end of construction. The props, three in number, are spaced 2.4 m apart over a total length of 7 m. The second curtain of ARBED PU 8 type sheet piles, 8 m deep, forms the support for the opposite wall. The sheet and the inertia of this curtain were chosen so that they did not undergo any displacement during the experiment. The water table is located at the depth of 5.5 m [1, 5].

The execution and testing of the work involved the following six stages:

- Step 1: excavation to a depth of 1.75 m;
- Step 2: installation of three struts spaced horizontally by 2.4 m and located at a depth of 1.25 m. The struts are preloaded with a force of 10kN per strut, i.e., a unit force of around 4.5kN per meter of curtain length;
- Step 3: resumption of excavation to a depth of 4 m;
- Step 4: continue the excavation to a depth of 5 m. The excavations are carried out at the same time as the bracing system and screw jacks are operated so as to prevent any displacement of the bracing level;
- Step 5: application of an overload of 10 kPa, on the surface, on an area located between 1 and 5 m behind the head of the experimental curtain. The overload is exerted through a basin filled with water;
- Step 6: reduction of the strut force by shortening the struts to the limit state of the soil block. This state is reached when the forces in the struts remain approximately constant.

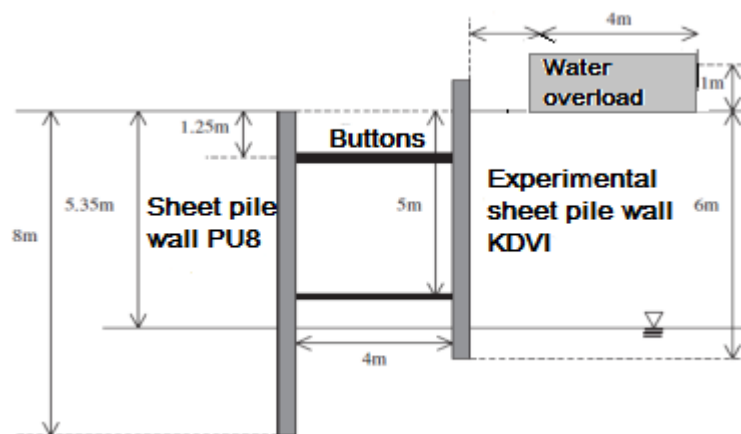


Figure 4: The schematic of the Hochstetten sheet pile wall experiment

3.1 Experimentation Modeling

In this experiment, two sheet pile walls with different characteristics are used: the instrumented wall and the retaining wall. It is therefore necessary to model the two structures.

On the other hand, given the length of the excavation and the small spacing between the struts, it is reasonable to produce the model in plane strain. The model then corresponds to a cross section of the structure [1, 5]. The numerical modeling of this structure is shown in Figure 5. Table 1 gives some geometric and numerical characteristics of this model. The characteristics of the curtains and struts are presented in Table 2. The mechanical behavior of Karlsruhe sand is modeled by the Mohr-Coulomb constitutive law, the values of the parameters of which are given in Table 3. These values are used initially to define the experimental data used for the inverse analysis. The experimental curve, shown in Figure 6, corresponds to the horizontal displacements of the KRUPP KD VI type sheet pile wall (experimental sheet piles).

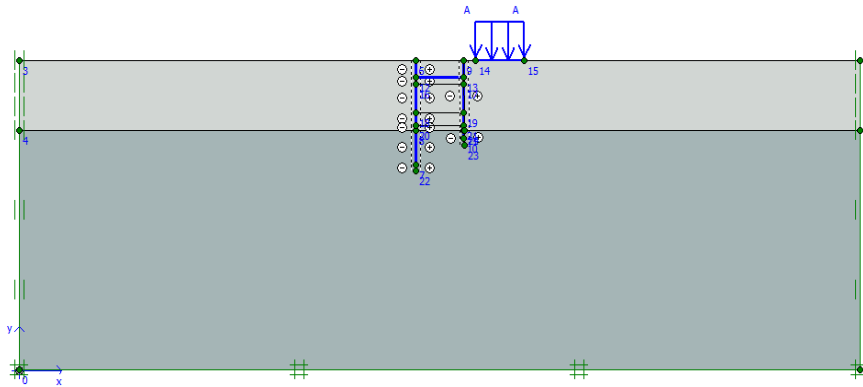


Figure 5: The numerical model

Table 1: Characteristics of the Finite Element Model [5]

Geometric characteristics	
Model size:	$L=70$ m, $H=24$ m
Size of the excavated area:	$h = 5.35$ m, $w = 4$ m
Height of KRUPP KD VI type sheet pile wall (experimental wall):	$hw = 7$ m
Height of the ARBED PU 8 type sheet pile wall (rigid wall):	$hw = 8$ m
Finite element characteristics	
Type of mesh elements:	triangles with 15 nodes
Number of elements:	464
Number of knots:	3987

Table 2: Values of the parameters of the elastic behavior models used to model the sheet pile wall and the struts [5]

Parameter	Name	Value	Unit
Sheet pile wall	<i>KRUPP KD VI</i>		
Normal stiffness	EA	$2.2 \cdot 10^6$	kN/m
Bending stiffness	EI	$2.0 \cdot 10^3$	kN m ² /m
Weight	w	0	kN/m/m
Equivalent thickness	d	0.105	m
Poisson's ratio	ν	0.3	–
Sheet pile wall	<i>ARBED PU 8</i>		
Normal stiffness	EA	$2.2 \cdot 10^6$	kN/m
Bending stiffness	EI	$24.4 \cdot 10^3$	kN m ² /m
Weight	w	0	kN/m/m

Equivalent thickness	d	0.363	m
Poisson's ratio	ν	0.3	–
Buttons			
Normal stiffness	EA	$4.2 \cdot 10^6$	kN/m
Bending stiffness	EI	$1.0 \cdot 10^5$	kN m ² /m
Equivalent thickness	d	0.535	m

Table 3: Values of the parameters of the of the constitutive soil Mohr-Coulomb model for a sand of Karlsruhe [5]

Parameter	Name	Value in the unsaturated layer	Value in the saturated layer
Young's modulus	E (kPa)	30000	45000
Shear modulus	G (kPa)	12000	18000
Poisson's ratio	ν	0.25	0.25
Cohesion	c (kPa)	0	3
Friction angle	φ (°)	41.6	41.6
Dilatancy angle	Ψ (°)	11.6	11.6
Earth coefficient at rest	K_0	0.336	0.336

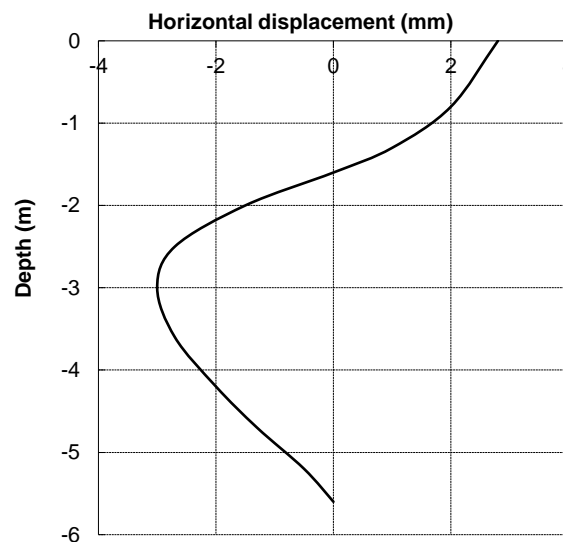


Figure 6: Horizontal displacement of the experimental sheet pile wall according to the depth

(-) Experimental measurements to be optimized

4 Validation of the Optimization Methods

In order to test and evaluate the performance of the proposed optimization methods, we have developed two programs under Matlab environment. The first program uses the genetic algorithm method (*GA*) and the second uses the Hybrid genetic algorithm method (*HGA*) with the Tabu search method. These two programs have been validated on the case of Hochstetten sheet piling in Germany, for the purpose of identifying the parameters of the constitutive soil model Mohr-Coulomb, the shear modulus (G) and the angle of friction (φ). Preliminary values

are given to the unknown parameters to simulate the numerical model, using the numerical calculation code Plaxis 08, until the difference between the result of the numerical calculation (numerical curve) and the experimental data (curve experimental) is minimal.

4.1 Genetic Algorithm Method

To launch the genetic algorithm program several parameters are necessary to give solutions of very good quality with a reasonable calculation time, these parameters are cited in Table 4.

Table 4: Values Parameters of the genetic algorithm

Parameter	Value
Number of individuals	$N = 30$
Number of generations	$K = 100$
Length of the bit chain	$l = 18$ bits
Probability of crossover	$P_c = 0.6$
Probability of mutation	$P_m = 0.08$

4.1.1 Results and Discussion

The optimization method using the genetic algorithm program is tested to identify two parameters of the Mohr-Coulomb model, the shear modulus (G) and the friction angle (φ), from the horizontal displacement of the sheet pile wall depending on the depth. The optimization inside the search space is controlled by the error function (F_{err}). Figure 7 shows the evolution of the individuals composing the parent populations during the process of optimization by genetic algorithm. It appears that starting from an initial population uniformly distributed over the entire parameter search space, from the first iteration a solution zone of the space is identified. Then, as the genetic algorithm iterations progress, the identification is refined around the absolute optimum of the problem. The optimization process ends at iteration 11 on a unique combination of solution parameters of the problem for which the error function is equal to zero. This characterizes the convergence of the algorithm. Finally, after 100 Finite Element Calculations, the identified optimum is the exact optimum of the problem, i.e., the following combination of parameters: $G = 9800$ kPa; $\varphi = 44^\circ$. It can be clearly seen that the numerical answer, corresponding to the parameters identified by the genetic algorithm method, are in good agreement with the experimental curve as illustrated in Figure 8.

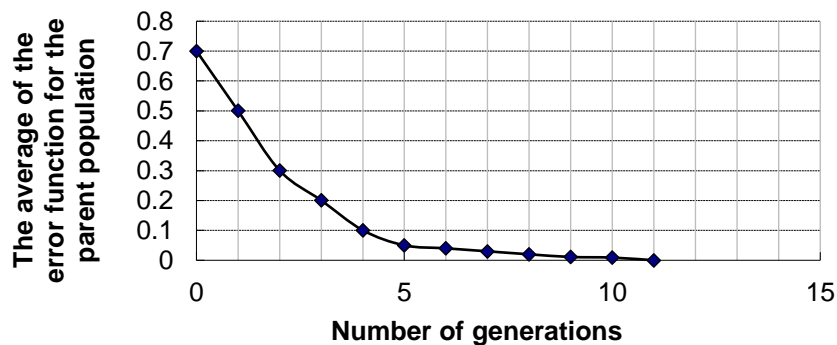


Figure 7: Evolution of the average of the error function on parent population according to the generations of a genetic algorithm

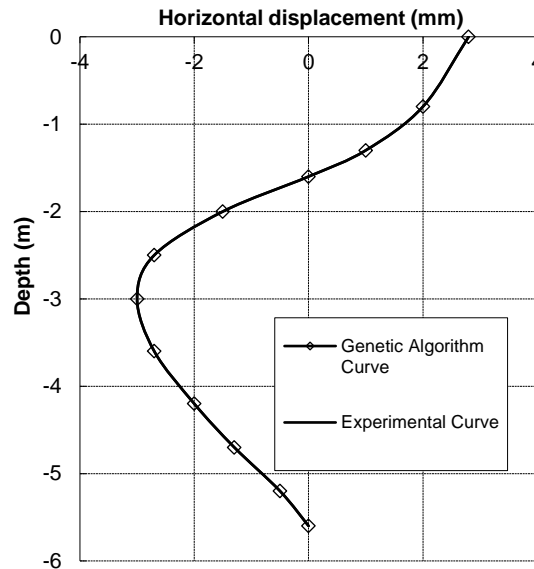


Figure 8: Horizontal displacement of the sheet pile wall according to the depth. (-) Experimental measurements to be optimized; (\diamond): Modeling of measurements after optimization by genetic algorithm

4.2 Hybrid Genetic Method

The tests carried out on the parameters chosen for the hybrid genetic algorithm program have guaranteed the obtaining of a very satisfactory result, these parameters are cited in Table 5.

Table 5: Values Parameters of the hybrid genetic algorithm

Parameter	Value
Number of individuals	$N=30$
Number of generations	$K=100$
Length of the bit chain	$l=18$ bits
Probability of crossover	$P_c = 0.6$
Probability of mutation	$P_m = 0.04$
Size of the tabu list	$T= 3$

4.2.1 Results and Discussion

The hybrid genetic algorithm program that we have implemented to identify the Mohr Coulomb parameters (G and φ) relies mainly on the error function which quantifies the difference between the numerical results and the experimental measurements. Figure 9 presents the evolution of the mean error function on the parent populations of the hybrid genetic algorithm according to the generations of the algorithm. For each of these generations, the evolution of the parent population in the search space shows once again that from an initial population uniformly distributed over the search space, the individuals gradually converge towards the areas of the search space where the error function (F_{err}) equals zero.

After four iterations and 100 Finite Element Calculations, all the parent individuals are equal to the same combination of parameters, the optimization stops. The identification is refined to the exact optimum of the problem which is the following combination of parameters: $G = 9800$ kPa; $\varphi = 44^\circ$. Figure 10 shows that the combinations of parameters obtained allow a very good reproduction of the experimental measurements.

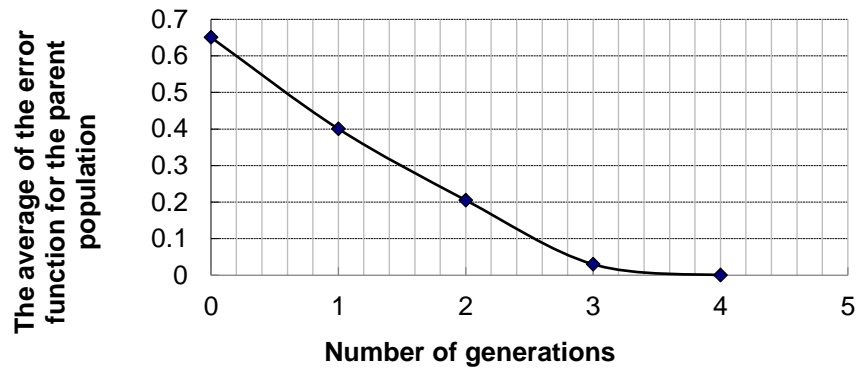


Figure 9: Evolution of the average of the error function on parent population according to the generations of a hybrid genetic algorithm

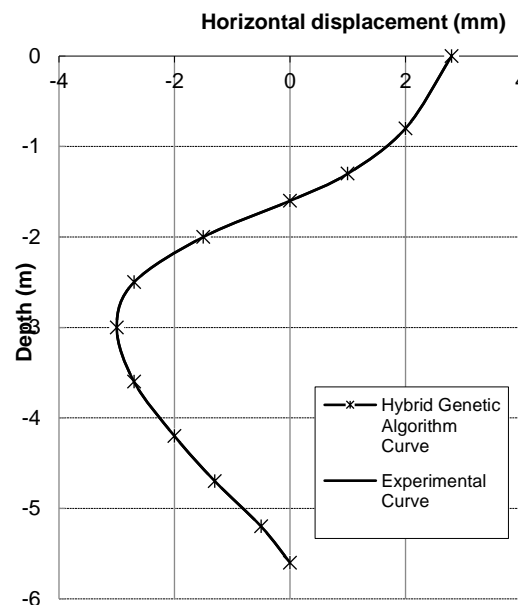


Figure 10: Horizontal displacement of the sheet pile wall according to the depth. (-) Experimental measurements to be optimized; (*): Modeling of measurements after optimization by hybrid genetic algorithm

5 Comparison of Results

The comparison of the horizontal displacements of the sheet pile according to the depth obtained by the two stochastic optimization curves (*GA* and *HGA*) with those obtained experimentally shows good agreement between the measured profiles and those drawn from

the numerical answer corresponding to the parameters identified by the two stochastic optimization methods. This concordance shows that the difference between the experimental curve and the numerical curves which is expressed by the calculation of the error function (F_{err}) is equal to zero. So, the identification of the two soil parameters (G, φ) is refined to the exact optimum of the problem (see Figure 11).

If we compare the results obtained by the genetic algorithm method with those estimated by the hybrid genetic algorithm method, it is clear that these two optimization methods provide the same combinations of solution parameters for this problem. However, while it takes 11 iterations for the genetic algorithm to converge, it only takes 4 for the hybrid genetic algorithm method.

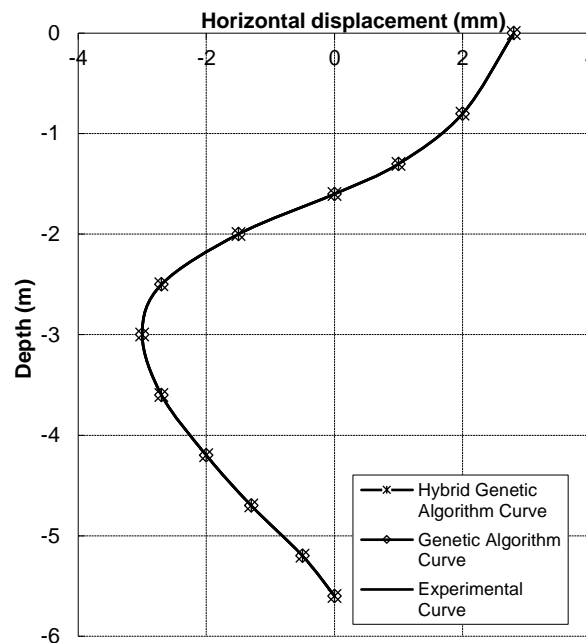


Figure 11: Horizontal displacement of the sheet pile wall according to the depth

(-) Experimental measurements to be optimized; (\diamond): Modeling of measurements after optimization by genetic algorithm; (\ast): Modeling of measurements after optimization by hybrid genetic algorithm

6 Conclusion

In this article, we sought to validate two stochastic optimization methods the genetic algorithm and the hybrid genetic algorithm with the Tabu search based on the inverse method from the study of an experimental sheet pile wall of Hochstetten in Germany. For this application, we tested the capacities of two optimization methods to identify two parameters of the constitutive soil model Mohr-Coulomb (G, φ). The results obtained show that each of these two methods identifies the exact solution of the problem. But the hybridization process of the genetic algorithm with the Tabu search method accelerated the convergence of the

algorithm towards the exact solution of the problem, whereas the genetic algorithm alone takes a much longer computation time to reach the exact solution to the problem.

Despite the large number of evaluations of the objective function required by stochastic methods, these methods constitute a class of approximate methods adaptable to a very large number of optimization problems. They have been shown to be highly effective in providing good quality approximate solutions for a large number of optimization problems and real applications. For this reason, the study of these methods is currently in full development.

References

- [1] Levasseur, S. (2007). *Inverse analysis in geotechnical: development of a method based on genetic algorithms*, PhD thesis. University of Joseph Fourier Grenoble I.
- [2] Cui, L. Sheng, D. (2005). Genetic algorithms in probabilistic finite analysis of geotechnical problems, *Computer and Geotechnics*, vol.32, pp. 555–563.
- [3] Glover, F. (1986). Future paths for integer programming and links to artificial intelligence. *Computers and Operations Research*, vol.13, pp. 533-549.
- [4] Hansen, P. (1986). The steepest Ascent Mildest Descent Heuristic for Combinatorial Programming. *The Congress on Numerical Methods in Combinatorial Optimization, Italy*.
- [5] Mestat, P. Arafati, N. (1998). Finite element modeling of curtain behavior Hochstetten experimental sheet piling. *Bulletin of the Laboratories of Bridges and pavements*. 216:19–39.
- [6] Von Wolffersdorff, P.A (1994). Results of field test and evaluation of the prediction and subsequent calculations. In Workshop Sheet Pile Test Karlsruhe. Technical University of Delft, The Netherland.
- [7] Kajberg, J. Lindkvist, G. (2004). Characterization of materials subjected to large strains by inverse modeling based on in-placed displacement fields. *International Journal of solids and Structures*, vol.41, pp.3439–3459.
- [8] Hao, J. K. Galinier, P. Habib, M. (1999). Méthaheuristiques pour l'optimisation combinatoire et l'allocation sous contraintes. *Journal de l'intelligence artificielle*, vol.13, pp.283–324.

Thermal Study of Traditional Gypsum Plaster Brick Prototypes: The Case of Ouargla

Hachem Chaib ^{1*}, Abdelouahed Kriker ¹

¹Department of Civil Engineering and Hydraulics, University Kasdi Merbah Ouargla, Ouargla30000, Algeria

*e-mail: chaib.hachem.dz@gmail.com

Abstract

This research is oriented towards the valorisation of local materials and the reduction of energy consumption with the aim of judicious use of these materials. In front of the world economic crisis, that also affects our region, it is necessary to solve the problem of pollution and enable important links for the balance with nature. In Algeria, buildings are very inefficient in terms of energy use and therefore remain a major source of energy consumption. To reduce this consumption and improve the thermal comfort of a building and save energy, it is necessary to use particularly high-performance materials that ensure good thermal insulation. The objective set in this work is to study the thermal behaviour of walls of different compositions, in order to identify those that allow the greatest energy savings in the case of air-conditioning for the Saharan context. The results proved that it is possible to use local materials to reduce energy consumption by 50% and save energy, improve the performance of the construction, and ensure the thermal comfort of buildings.

Keywords: brick, traditional gypsum plaster, energy consumption, thermal comfort

1 Introduction

Algeria with its vast surface area encompasses a heterogeneity of local materials, especially those located in the southern region, that should be valorised, namely: sand dunes, clays, tuff, gypsum, and others that are still poorly incorporated into the local building processes. Most of the building materials currently used in the Saharan regions are not well adapted in terms of climatic and environmental conditions, sustainability, and economics.

In order to gain a better understanding of the behaviour of local materials in the field of civil engineering and building construction, it is important to estimate their resources and study their physical, chemical, mechanical, and thermal properties [1,2, 4-11].

In this respect, the objective set in this work is the characterisation and valorisation of local material, the traditional gypsum plaster known as "Timchemt", suggesting the ways of improvement of the of Timchemt-based bricks' mechanical characteristics, and studying the effect of the addition of cement in precise percentages.

1.1 The Ksar of Ouargla Materials

The word "ksar" (plural ksour) is an Arabic term meaning palace, which also designates fortified built ensembles which essentially characterize the Moroccan and Algerian south. The ksar is generally square or rectangular in shape, but it can also be circular (Figure 1).



Figure 1: An aerial view of the ksar of Ouargla

This material is available, it is extracted from the quarry and then tallied as needed and used in the various structural elements [2]. It is a binder that is made using Ouargla stones (red or white). They are of a gypsum nature. The white stone gives a very consistent binder more than the red stone (red stone = el karmouda; white stone = tafza). With the increased quantity of ashes, it gives a very coherent binder [2].

The traditional oven manufacture of Timchemt starts with digging the earth in a circular shape with a depth varying from 1 to 1.5m and then putting the stones one on top of the other:

- 1- Put the stones in the oven.
- 2- Cover the oven with wood and stones.
- 3- Put a palm tree in the middle.
- 4- Light the fire with the palm.
- 5- Leave the stones to cook in the oven for 1 or 2 months, then tap it and sieve it and use it.

1.2 Climate Analysis of Ouargla City

The weather situation of Ouargla (Figure 2), with a limited area in the south by the Sahara with arid climate and in the north with temperate climate, allows to have specific characteristics. According to the classification given by architectural recommendation Ouargla city belongs to the climate zone E4 in summer and H3c in winter, which has two main seasons [2]:

1. Summer: hotter and dry; the difference in temperature is not important.
2. Winter: cold and dry, with a significant difference in temperature.



Figure 2: Geographical situation of the wilaya of Ouargla

1.2.1 Temperature

The region of Ouargla is characterized by very high temperatures; the hottest month is July, with 48.68°C and the average temperature minimum of the coldest month is 15°C in January. The average annual temperature is 30.73°C [2, 3].

1.2.2 The winds

In the region of Ouargla, the winds are very variable during the year. They are mostly northerly and dominate in the region of study in summer and can cause damage, especially in the absence of vegetation cover with a maximum speed of 4.61 m/s . The annual average wind speed is 3.62 m/s [2, 3].

1.3 Energy Consumption of Ouargla City

In the following Table 1, we give statistical data obtained from the mines branch of Ouargla city (2021) [2].

Table 1: Electricity consumption of Ouargla city [2]

The month	January	February	July	August
Number of subscribers	73381	73991	75192	75448
Consumption /subscriber kWh/subscriber	419	345	594	872

We notice an increase in the consumption of electrical energy as a function of the increasing number of consumers. We also notice the peak of electrical energy consumption in the months of July and August.

2 Methods and Materials

2.1 Traditional Gypsum Plaster

Traditional gypsum plaster is burned in traditional ovens (Figure 3). These ovens are rudimentary constructions, built with a thick Timchemt. The vertical oven is 1.5 m high and 1 m in diameter, and the second horizontal oven is 1 m high and 4 m in diameter in a courtyard.



Figure 3: Traditional ovens used for cooking Timchemt

We are studying this material physically and chemically at the civil engineering laboratory of Kasdi Merbah Ouargla University.

The table below presents the results of the physical tests (Table 2):

Table 2: Results of the physical tests on the Timchemt

Tests	Results
Bulk density	1.39 g/cm ³
Absolute density	2.18 g/cm ³
Methylene blue	0.68
Atterberg limit	$W_L = 41.10$
	$W_P = 34.42$
	$I_P = W_L - W_P = 6.68$
Sand equivalent	$E_{sv} = 38.80$
	$E_{sp} = 37.17$

E_{sv} = visual sand equivalent

E_{sp} = plunger sand equivalent

I_P = plasticity index

According to the NF P 94-068 standard, our sample is not very adsorbent, not very plastic, and sensitive to water.

According to Atterberg and Burmister, we can classify our Timchemt by its plasticity index $I_P = 6.68$ the nature of this traditional plaster is not very plastic, with a natural density of 1.51g/cm³ the result belongs to the range 1.4 to 1.8 according to the classifications, this material is classified as loose despite the distinction observed between them.

2.1.1 X-ray diffraction (XRD)

The Mineralogical analysis of Timchemt was made with the aid of X-ray diffraction (XRD) (Figure 4). This technique allows to identify the crystalline phases present in this traditional gypsum plaster and determine the parameters of the mesh associated. These applications are possible thanks to the interference of X-rays with the matter.

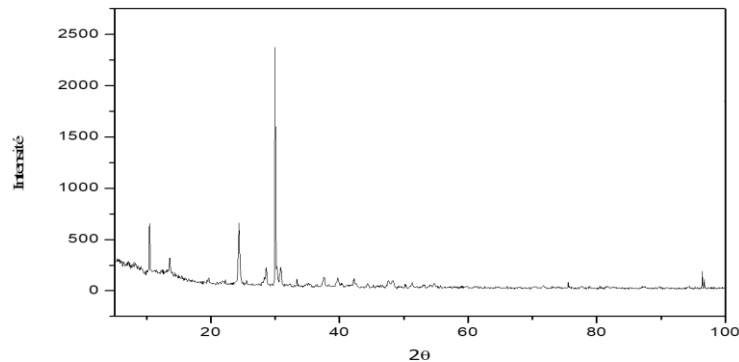


Figure 4: The X-ray diffraction (XRD) of Timchemt

What must be remembered in this diffractogram is that our Timchemt is sulphated throughout the course of the peaks obtained, hence we can see the following:

Sulphate CaSO_4 forms a large part of the minerals with a percentage of 96% NaOH found with low percentages of around 4%.

The results of the chemical analyses are presented above.

Table 3: Chemical analyses of traditional gypsum

	Components	Valuers
Insolubles NF P 15 - 461	Insolubles	27 %
	SO_3^{-2}	14.09 %
Sulfates BS 1377	$\text{Ca SO}_4 / 2\text{H}_2\text{O}$	75.71 %
	SO_4^{-2}	16.93 %
Carbonates NF P 15 - 461	CaCO_3	2 %
Chlorides MOHR method	Cl^-	0.845 %
	NaCl	1.385 %

The table presented shows the elements in the sample of gypsum, where are 75.71% of sulphates with an insoluble compound of 27%, while the levels of sulphates and chlorides are very low.

The experimental study of our work is to determine the thermal characteristics and mechanical characteristics of bricks on basis of Timchemt of Ouargla. In our work, we have prepared tubes and compared them with test reference tubes of raw earth, cinder, and plaster. Various tests have been carried out on the bricks: mechanical tests (resistance to traction by bending, the resistance to compression, speed of propagation of sound), and thermal tests (thermal conductivity (λ), thermal resistance (Rh), specific heat (CP)).

Table 4: The prepared compositions

compositions	C1	C2	C3	C4
Timchemt	100	0	0	0
raw earth	0	100	0	0
cinder block	0	0	100	0
plaster	0	0	0	100

2.2 Energy Consumption

Unit calculations relate to the components of the walls and measurement of the necessary parameters (Equation 1).

$$Q = mC (tf - ti) \quad (1)$$

where Q is the heat [J], m is the mass [g], C is the specific heat capacity [$J \cdot g^{-1} \cdot ^\circ C^{-1}$], and $tf-ti$ is the temperature change [$^\circ C$].

2.3 Testing

After the manufacture of the bricks, we conducted a series of mechanical and thermal tests. The results of these tests are presented in Figures 5-11.

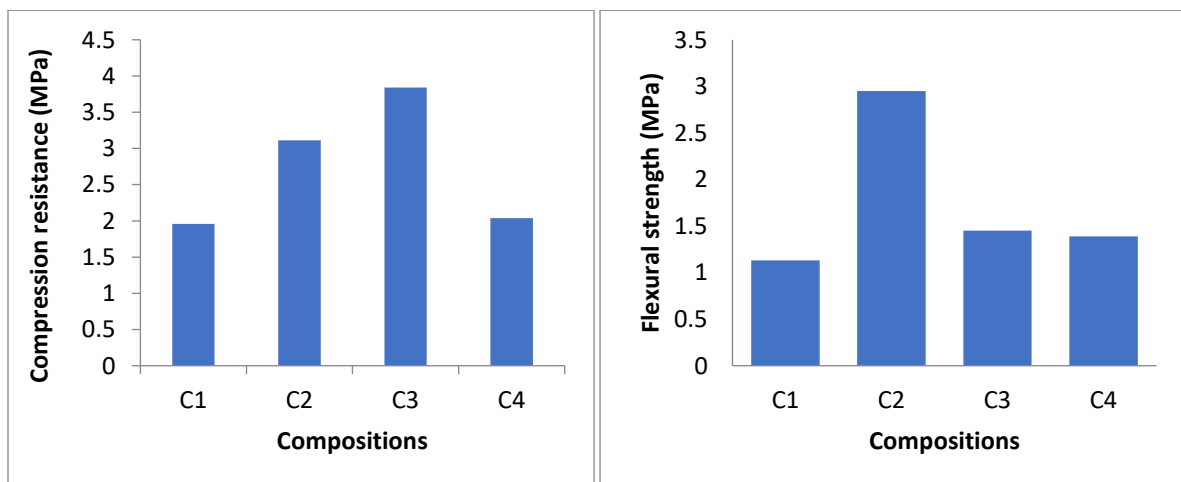


Figure 5: Compression strength (MPa) Figure 6: Flexural strength (MPa)

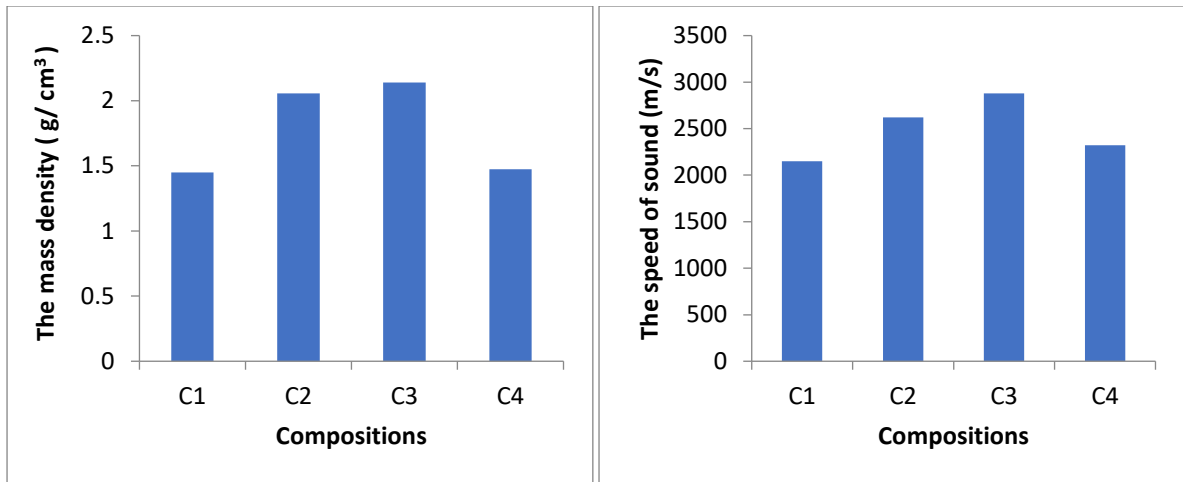


Figure 7: The mass density (g/ cm³) Figure 8: The speed of sound (m/s)

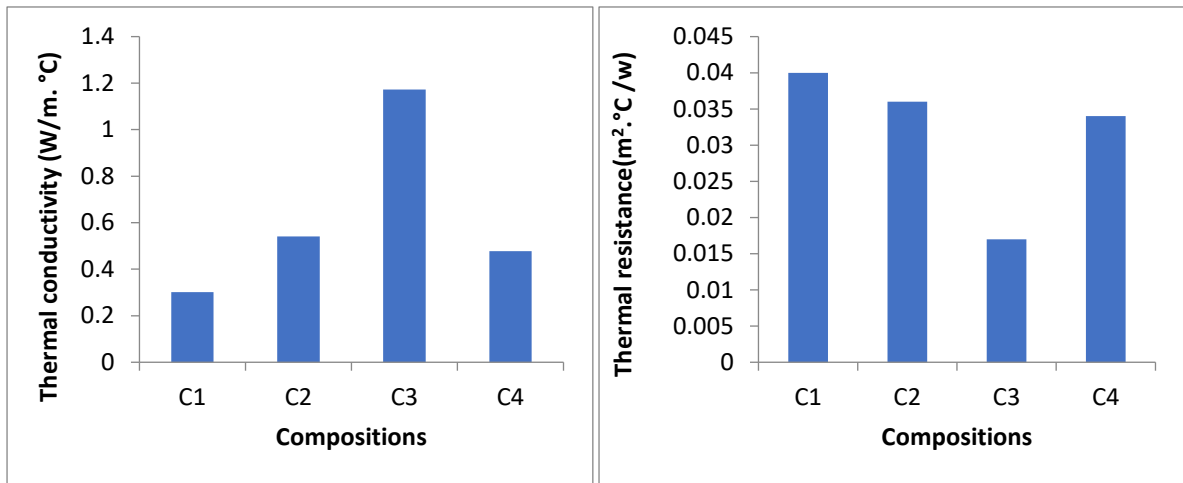


Figure 9: Thermal conductivity (W/m.K) Figure 10: Thermal resistance (m²K/W)

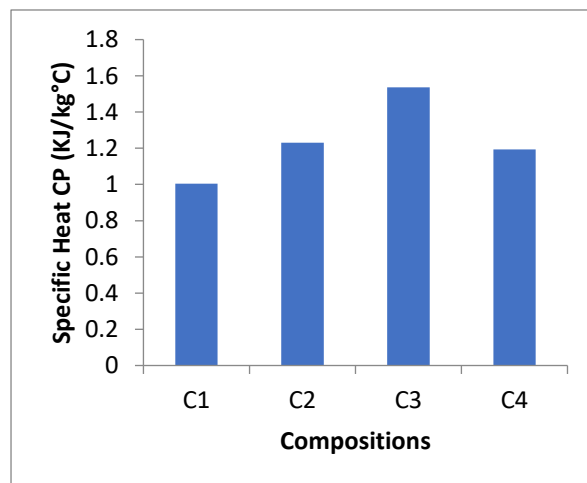


Figure 11: Specific Heat CP kJ/kgK)

According to the thermo-mechanical tests, we can say the following:

1. The density of samples (C₂) and (C₃) is higher than the density of other samples. This is due to the increase in mass of the components of the ash block and the adhesion of the clay grains. A convergence between the density values of Timchemt and gypsum samples is due to the nature of the gypsum and Timchemt.
2. The composition of the plaster C₄ gives the best resistance to bending. The bricks of the raw earth (C₂) give the wrong result which is due to inner contact between the components of the earth flood. On the other hand, we note that the bricks of composition C₂ give the best results in compression tests.
3. The bricks of traditional plaster (Timchemt) give acceptable results from a mechanical point of view (in compression and bending tests).
4. The results of the speed of sound confirm the results mechanical.
5. From the thermal point of view, the bricks of Timchemt marked the best results. This is due to the nature of gypsum Timchemt.
6. The composition of the cinder block gave bad thermal results, like other cementitious products.
7. The thermal conductivity increases when the density increases, because it decreases the proportion of void, in the material.
8. The histograms indicate that the thermal resistance is automatically reduced because it is inversely proportional to the thermal conductivity [2, 5].

3 Results and Discussion

3.1 Realization of Prototypes

In order to enhance the value of our bricks in the construction, we produced several realized prototypes of the bricks which have presented good thermal and mechanical properties. The prototypes are put in the actual conditions in the open air.

The location and directions of the prototypes are N-S-E-W.

We propose the thermal behaviour of the walls of different compositions in order to identify those which allow the largest economy of energy in the case of air conditioning for the Saharan context. The composition of these walls is given in Table 5.

Table 5: The composition of the elements of the prototypes [1]

prototypes	Dimensions	the Slab	Brick
P1	(1x1x1) m ³	concrete	cinder block
P2	(1x1x1) m ³	concrete	raw earth
P3	(1x1x1) m ³	gypsum	Timchemt

We note the studies are carried out in the hottest month (July), at the University of Kasdi Merbah Ouargla.

3.2 Thermal Study Prototypes

After the realization of the prototypes, we measured the outdoor and indoor temperatures and the moisture.

According to recommendations of Algerian DTR [1] thermal regulation of buildings, the requirement for hygrothermal comfort varies between 30% and 60% and the temperatures are $T_{\text{Comfort } T_{\text{min}}} = 24^{\circ}\text{C}$, $T_{\text{Comfort } T_{\text{max}}} = 30^{\circ}\text{C}$. Using a digital thermometer and hygrometer, we measured the climate data during the days of the 20th, 21st, and 22nd of July 2021.

3.2.1 Prototype P1

Figure 12 summarizes the graph of variation of the interior/exterior temperature, and Relative Humidity (RH).

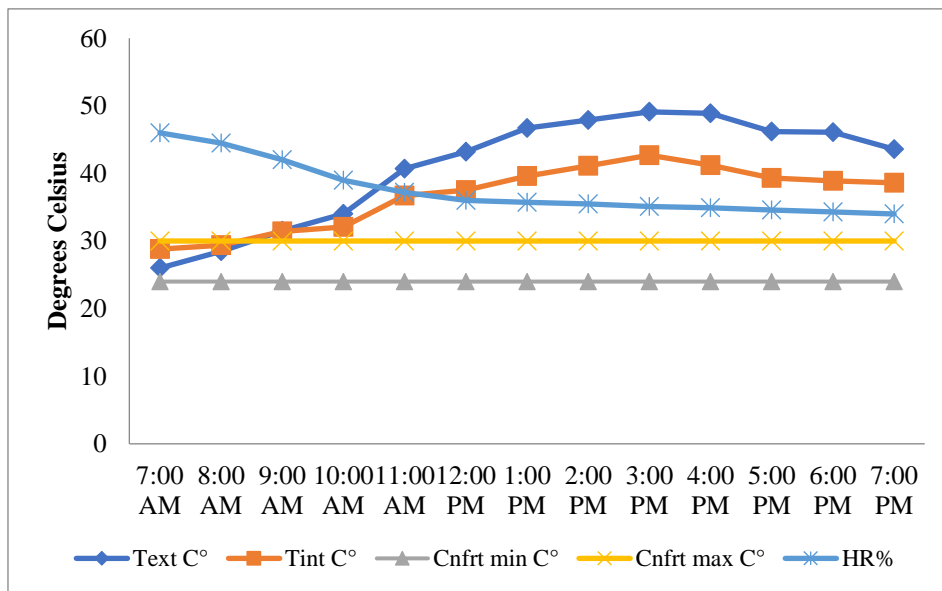


Figure 12: influence of temperature on the prototype P1

Figure 12 shows the curves for the variation of the temperature inside prototype P1, the outside temperature, and the air humidity as a function of time. During the day, we noticed that the difference in indoor and outdoor temperatures exceed 7 °C in the case of the cinder blocks with the concrete slab.

Between 09 am and 7 pm, we found that the interior of the P1 prototype is uncomfortable. The effect of heat storage by the concrete slab affects this prototype; the humidity increases as the temperature drops.

It can be observed that the P1 prototype offers us a considerable thermal gap (the temperature difference in Figure 12), which allows us to conclude that the brick walls have prevented the penetration of heat into the interior, this gap reaches almost 8 °C.

3.2.2 Prototype P2

Figure 13 summarizes the graph of variation of the interior/exterior temperature, and RH.

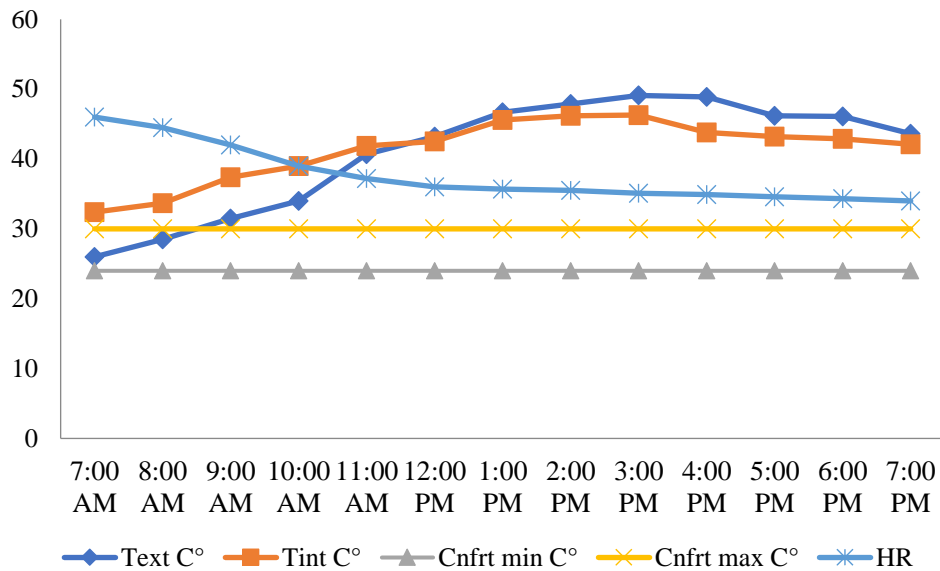


Figure 13: Influence of temperature on the prototype P2

The indoor temperature varies between 32.4 and 46.3°C gradually, following the increase of the outdoor temperature from 26 to 49.1°C. Also, during the first few hours, the indoor temperature is higher than the outdoor temperature because of the concrete slab that retains the heat. When the humidity decreases, the temperature increases.

During the early morning hours, the temperature inside is higher than outside and this is due to the absorption of heat by the concrete slab although the walls are made of cinder blocks.

3.2.3 Prototype P3

Figure14 summarizes the graph of variation of the interior/exterior temperature, and RH.

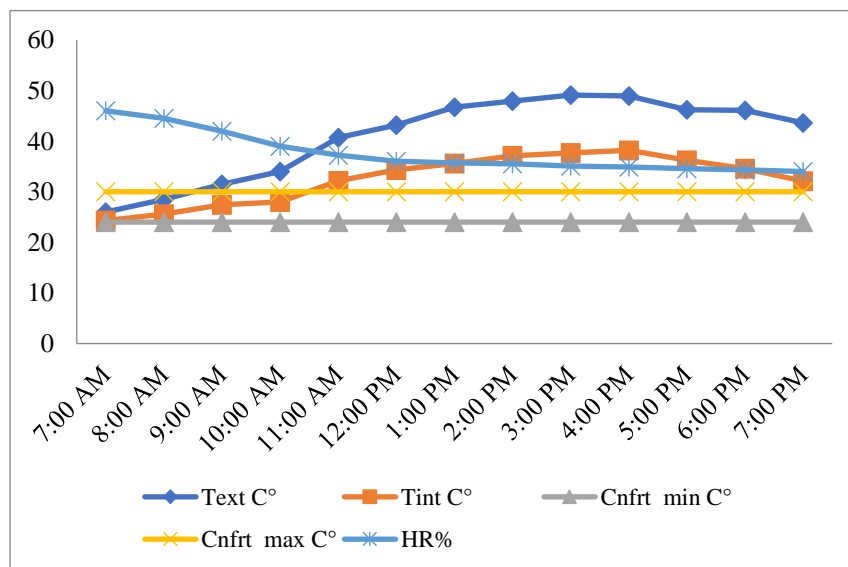


Figure 14: Influence of temperature on the prototype P3

According to the results of Figure 14, we can see from the first morning hours that the indoor temperature of the P3 prototype is lower than the outside temperature. This is directly related to the material used in the realization of this prototype, which shows good thermal insulation behaviour; from 1 pm the temperature difference starts to widen to 11.5 °C around 7 pm, given the insulating capacity of the Timchemt, which allows us to reduce the air-conditioning and save electricity; in this case also the humidity decreases with the increase of the temperature.

In prototype P3 the indoor temperature is always lower than the outside temperature during all the hours of the day, starting with a small difference in the first few hours, but with time the difference widens to more than 11.5 °C, thanks to the good thermal resistance of traditional gypsum bricks.

3.3 Deviation of the Temperature of the Prototypes

To better see the influence of the prototypes on the decrease of the indoor temperature, we present Figure 15 to highlight the differences in temperature between the outside and the inside.

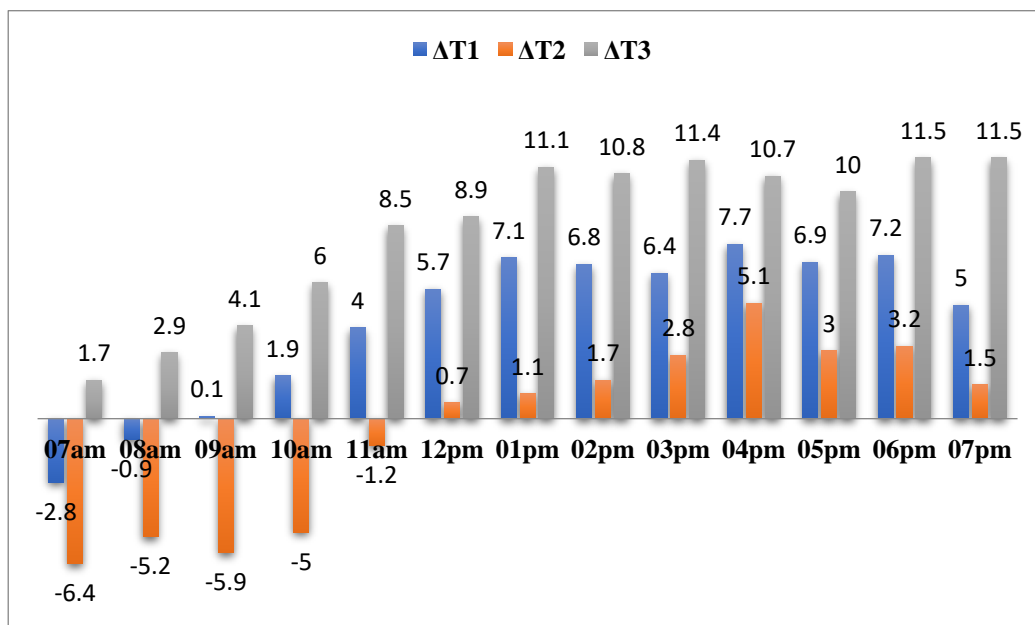


Figure 15: Difference in the temperature of the prototypes (P1 to P3)

Concluding from Figure 15, we record the following points:

3.3.1 Prototype P1

From 7:00 am to 8:00 am the temperature difference is negative: -2.8 to -0.9°C.

From 9:00 am to 7:00 pm the temperature difference is positive and reaches up to +7.7°C.

3.3.2 Prototype P2

From 7:00 am to 11:00 am the temperature difference is negative: -6.4° to -1.2°C.

From 2 pm onwards, a small temperature difference of up to: +5.1°C.

3.3.3 Prototype P3

From 7:00 am to 1:00 pm the temperature difference increases from: 0.7 to 11.1°C.

From 2 pm onwards, the temperature difference stabilizes at an average of 11°C.

The amount of unit energy required to remain in comfort ($T_{\max} = 49.1^{\circ}\text{C}$ maximum temperature in our region and $T_{\text{comfort}} = 30^{\circ}\text{C}$ temperature of human comfort). $Q=16.08\text{kJ}$

The amount of unit energy required to remain in comfort ($T_{\max} = 49.1^{\circ}\text{C}$ and $T_{\text{comfort}} = 30^{\circ}\text{C}$)

$Q = 12.35 \text{ kJ}$. The amount of unit energy required to remain in comfort ($T_{\max} = 49.1^{\circ}\text{C}$ and $T_{\text{comfort}} = 30^{\circ}\text{C}$) $Q = 7.08\text{kJ}$.

After these calculations, we notice that the nature of the material influences the energy consumption of the buildings in the Saharan regions where the temperature exceeds 49°C . Thus, we can say that the Timchemt bricks prove their efficiency.

4 Conclusion

After the experiment, the results obtained showed that:

Traditional gypsum bricks gave good results from a mechanical and thermal point of view.

The thermal study of the prototypes and the study of the energy consumption shows that Timchemt bricks save more than 50% of the electrical energy and improve the performance of the construction and ensure the thermal comfort of the habitat.

The choice of building materials plays an important role in the comfort of the premises. Indeed, the inertia of a building reduces and delays the effect of external conditions and is particularly suited to the climate where the temperature difference between day and night is important.

The objective in the context of this work is the achievement of a level of thermal comfort with lower energy consumption and a mechanical resistance acceptable with a reduced cost.

This study is carried out in order to address this objective.

References

- [1] Mekhermeche A. (2012). *Contribution à l'étude des propriétés mécaniques et thermiques des briques en terre en vue de leur utilisation dans la restauration des Ksours sahariennes*. Master Thesis. University of Ouargla.
- [2] Chaib H. (2017). *Contribution à l'étude des propriétés thermomécaniques des briques en terre confectionnée par des fibres végétales locales*. PhD thesis. University of Ouargla.
- [3] <https://www.dlupal.com/en/load-zones-for-snow-wind-earthquake/wind-dtr-c-2-47.html#¢er=28.414259720498414,1.6575215000000076&zoom=5&marker=36.768,3.054>
- [4] Kriker A. (2005). *Caractérisation des fibres de palmier dattier et propriétés des bétons et mortiers renforcés par ces fibres en climat chaud et sec*. PhD thesis. ENP.
- [5] Chaib H. (2017). *Technique de production des briques en terre*. Paris: éditions Universitaires Européennes.

- [6] Bedzki, AK, Gassan J. (1999). Composites reinforced with cellulose based fibres. *ProgPolymSciVolume* (issue), 24:221-274. DOI:10.1016/S0079-6700(98)00018-5
- [7] Hanifi B, Orhan A, Mehmet N, Erhan A, Selim K. (2007). Thermal isolation and mechanical properties of fibres reinforced mud bricks as wall materials. *Construction and Building materials*.21, 901-906. DOI: 10.1016/j.conbuildmat.2005.11.004
- [8] Abani S. (2003). *Caractérisation des bétons renforcés par des fibres végétales de palmier dattier*. Master Thesis . University of Ouargla.
- [9] Ghavami K, Filho RDT, Barbosa NP. (1999). Behaviour of composite soil reinforced with natural fibres. *CemConcr Compos* ,21(1):39–48. DOI:10.1016/S0958-9465(98)00033-X
- [10] Coutts RSP, Ni Y. (1995). Autoclaved bamboo pulp fibre reinforced cement. *CemConcr Compos*,17(2).99–106. DOI: 10.1016/0958-9465(94)00002-G
- [11] Taallah B., Guettala A., Guettala S, Kriker A. (2014). Mechanical properties and hygrosopicity behavior of compressed earth Block filled by date palm fibers. *Construction and Building Materials* 59. 161–168. DOI: 10.1016/j.conbuildmat.2014.02.058

SSP-JCE Volume 17

Lenka Kabošová^{1*}, Katarína Čákyová²

Technical University of Kosice, Slovakia
Faculty of Civil Engineering, ¹CRIC – Center for Research and Innovation in Construction, ²Institute of
Architectural Engineering,
*e-mail: lenka.kabosova@tuke.sk

Abstract

The building industry, like many other industries, is driven to take a significant turn due to the pressing issue of global climate change. The potential in digital technologies and digital design approaches is pushed forward and exploited in architecture, structural, civil, and geotechnical engineering. The challenges such as the overheating of buildings and urban spaces, lack of drinking water, expensive and environment-aggressive building materials, and many more are investigated in more depth in Volume 17 of the Selected Scientific Papers - Journal of Civil Engineering.

Keywords: building industry, architecture, changing climate

1 Introduction

In the last decade, architectural design and the construction industry are increasingly facing many issues and changes [1]. Undoubtedly, the most significant is climate change, which has significantly affected the construction industry [2]. One of the many issues is the increasingly frequent overheating of cities and buildings themselves during the summer season [3, 4]. As a result, there is a greater need for energy for cooling [5]. Therefore, several studies focus on optimizing and reducing energy consumption for cooling spaces, for example by using different ventilation strategies [6], including the natural ventilation between buildings [7] but also by using intelligent shading, progressive glass systems, or appropriate orientation to the cardinal points [8]. This is also related to room daylight, which has a significant impact on the quality of the indoor environment [9].

The need for sustainability in construction shows the necessity of using recycled materials applicable to the circular economy [10]. We are also observing the development and testing of new building materials that would be less energy-intensive to produce and would replace traditionally energy-intensive materials [11, 12].

The current issue of the SSP magazine also summarizes the trends we observe worldwide in the field of construction. In individual published articles, the authors describe in detail modern design approaches in construction and future technologies, without which the civil engineer of this new era cannot do.

2 Volume 17 Research Topics

2.1 Overheating of Interiors

Overheating mitigation strategies through employing structural elements with greater heat accumulation are investigated in the first article. Although the authors have experimented with heavy-weight structures and window shaders, the interior temperature in the summer, due to the trends of extreme heat waves, did not reach the required level below $<27^{\circ}\text{C}$ throughout the whole day. Further investigations into this topic are planned.

2.2 Recycled Materials

Adding $>1.5\%$ of recycled PET fiber to mortar has a distinctive impact on the physical and mechanical characteristics of the mortar obtained in both fresh and hardened states. For more details, the reader is encouraged to read the second article.

2.3 Water Management

The strategies for minimizing drinking water loss are ranging from computational approaches in designing infrastructure, through changes in directives to attempts for changes in industrial practice. A balanced approach, considering the water leakages, and taking the non-revenue water into consideration, has revealed that the water distribution systems are more sensitive to pressure than has been assumed, according to the third article of the 2022 issue.

2.4 Energy Storage

The thermal energy storage, after it is produced in abundance can be made utilizing bio-based phase change materials such as plastics immersed in coconut oil, as can be read in the fourth article.

2.5 High-performance Concrete

Pozzolan as an additive was immersed in two acids, hydrochloric and sulfuric to experiment with the resulting mechanical properties of concrete. The Ultra-high-performance concrete made from Portland cement substituted with 10% pozzolana has improved mechanical characteristics

2.6 Daylight in the Interior

Two identical rooms with different glazing at the Faculty of Civil Engineering of the Slovak Technical University in Bratislava were investigated regarding the photopic and melanopic daylighting values. As the authors conclude, it is essential to consider the spectral properties of glazing and indoor opaque surfaces. For more information, don't hesitate to dive into article 6.

2.7 Enhancing the Properties of Soil

The effects of different percentages of ground granulated blast-furnace slag with quicklime used as an activator on the immediate behavior of the silty clay are studied and the compressive strength, cohesion, and internal angle of friction are observed. The results of the investigation can be read in article number 7 of the 2022 issue.

2.8 Digital Design of Reinforced Concrete Beams

A Fuzzy Logic Expert System with different types of membership functions as an Artificial Intelligence (AI)-based prediction can be used to predict the deflection behavior of the Near Surface Mounted Reinforced Concrete beams. Based on two inputs (applied load and variable length), the deflection of two types of strengthened RC beams was predicted.

2.9 Estimation of Foundations Deformation

In geotechnical engineering, the deformations of shallow foundations after many (>1000) loading cycles can be predicted digitally with good precision, employing the Finite Element Method as article number 9 explains.

2.10 High-performance Fiber Concrete

At high temperatures, the mechanical properties of concrete deteriorate. The influence of polypropylene fibers and their effect on the deterioration behavior of concrete is studied in the tenth article of volume 17's issue.

2.11 Digital Analysis of a Concrete Dam

The combined effect of dam height with the fluid compressibility on the concrete dam and its dynamic response is investigated in article 11. As the Finite Element analysis showed, the effect of interaction between the dam and the reservoir is important for the precise prediction of the gravity dams' structural behavior.

2.12 Self-compacting Concrete with Recycled Aggregates

Aggregates, produced from the cement production and construction industry wastes proved to have enhanced mechanical properties (high mechanical strength). The use of sands obtained from cement waste opens up a valuable economic and technical alternative in the construction industry.

2.13 The Wind Flow Around Atypically Shaped Buildings

As the aerodynamic forces, induced by the wind flow around buildings of unconventional shapes are not yet well analyzed (as opposed to the box-shaped buildings), an elliptically-shaped high-rise building was investigated employing the wind tunnel in article 13.

2.14 Superplasticizers in Concrete

Article number 14 investigates the influence of three types of superplasticizers of different chemical compositions of concrete (Combined Synthetic Polymers, Poly-Carboxylate Ether, and Modified Poly-Carboxylate Ether) on its rheological behavior and mechanical properties.

2.15 Numerical Modeling in Geotechnical Practice

The study of sophisticated constitutive soil models in numerical modeling of soils proved the adequacy of the use of the hypoplastic model with improved intergranular strain, which was also confirmed by obtained experimental results.

2.16 Digital Analysis of Temperature Loads on a Concrete Bridge

The reinforced concrete bridge was analyzed digitally, regarding the thermodynamic effects on the bridge structure. The thermal effects, the magnitude of the acting temperature, and the mechanical properties of the bridge structure are crucial parameters in the theoretical calculation model affecting its final theoretical behavior, which must reflect the real behavior of the bridge structure, as article 16 explains.

2.17 Stone Columns for Enhancing the Bearing Capacity of Soils

This comprehensive study investigated stone columns as a sustainable solution for enhancing the bearing capacity of soils. Experimental and numerical results are compared, leading to reasonably good matches. For more information, the reader is referred to article number 17.

2.18 Genetic Algorithms for the Prediction of Soil Behavior

Genetic algorithms and hybrid genetic algorithms with Tabu search were investigated in this article to simplify the identification of soil mechanical parameters (shear modulus and friction angle). The authors conclude that the hybrid genetic algorithm enhanced with the Tabu search method indeed accelerated the convergence of the algorithm.

2.19 Valorization of Local Materials in Construction

The ideas for the reduction of energy consumption through utilizing local materials in construction are proposed in the last article. Facing the world economic crisis, it is natural to search for efficient solutions in construction. The thermal comfort of buildings can be enhanced using local materials, leading to savings in energy, as article 19 explains.

3 Conclusion

The articles creating this year's issue covered many topics of civil, structural, and geotechnical engineering. All the manuscripts have been peer-reviewed in the double-blind peer review process. Subsequently, they were corrected by the authors, proofread, and re-evaluated, which

has increased the scientific quality of the 2022 issue. Trends in construction, modern design approaches, and future technologies are discussed, and many questions are raised, crucial for the future evolution of the construction industry.

References

- [1] Hao, H., Bi, K., Chen, W., Pham, T.M., Li, J. (2023). Towards next generation design of sustainable, durable, multi-hazard resistant, resilient, and smart civil engineering structures. *Engineering Structures*. 277, 115477. <https://doi.org/10.1016/j.engstruct.2022.115477>
- [2] Chakraborty, D., Alam, A., Chaudhuri, S., Başağaoğlu, H., Sulbaran, T., Langar, S. (2021). Scenario-based prediction of climate change impacts on building cooling energy consumption with explainable artificial intelligence. *Applied Energy*. 291, 116807. <https://doi.org/10.1016/j.apenergy.2021.116807>
- [3] Hwang, R.-L., Lin, T.-P., Lin, F.-Y. (2020). Evaluation and mapping of building overheating risk and air conditioning use due to the urban heat island effect. *Journal of Building Engineering*. 32, 101726. <https://doi.org/10.1016/j.jobe.2020.101726>
- [4] Martinez, S., Machard, A., Pellegrino, A., Touili, K., Servant, L., Bozonnet, E. (2021). A practical approach to the evaluation of local urban overheating– A coastal city case-study. *Energy and Buildings*. 253, 111522. <https://doi.org/10.1016/j.enbuild.2021.111522>
- [5] Rahif, R., Hamdy, M., Homaei, S., Zhang, C., Holzer, P., Attia, S. (2022). Simulation-based framework to evaluate resistivity of cooling strategies in buildings against overheating impact of climate change. *Building and Environment*. 208, 108599. <https://doi.org/10.1016/j.buildenv.2021.108599>
- [6] Cakyova, K., Figueiredo, A., Oliveira, R., Rebelo, F., Vicente, R., Fokaidis, P. (2021). Simulation of passive ventilation strategies towards indoor CO2 concentration reduction for passive houses. *Journal of Building Engineering*. 43, 103108. <https://doi.org/10.1016/j.jobe.2021.103108>
- [7] Kabošová L, Chronis A, Galanos T. (2022). Fast wind prediction incorporated in urban city planning. *Int J Archit Comput* 147807712211210. <https://doi.org/10.1177/14780771221121034>
- [8] Dolnikova, E., Katunsky, D., Vertal, M., & Zozulak, M. (2020). Influence of Roof Windows Area Changes on the Classroom Indoor Climate in the Attic Space: A Case Study. *Sustainability*, 12(12), 5046.
- [9] Ngarambe, J., Adilkhanova, I., Uwiragiye, B., Yun, G.Y. (2022). A review on the current usage of machine learning tools for daylighting design and control. *Building and Environment*. 223, 109507. <https://doi.org/10.1016/j.buildenv.2022.109507>
- [10] Dokter, G., Thuvander, L., Rahe, U. (2021). How circular is current design practice? Investigating perspectives across industrial design and architecture in the transition towards a circular economy. *Sustainable Production and Consumption*. 26, 692-708. <https://doi.org/10.1016/j.spc.2020.12.032>
- [11] Piccardo, Ch., Hughes, M. (2022). Design strategies to increase the reuse of wood materials in buildings: Lessons from architectural practice. *Journal of Cleaner Production*. 368, 133083. <https://doi.org/10.1016/j.jclepro.2022.133083>
- [12] Ebolor, A., Agarwal, N., Brem, A. (2022). Sustainable development in the construction industry: The role of frugal innovation. *Journal of Cleaner Production*. 380 (2), 134922. <https://doi.org/10.1016/j.jclepro.2022.134922>